

6

AD-A148 355

JOINED WING TRANSONIC DESIGN
AND
TEST VALIDATION



Rockwell International

DTIC FILE COPY

DTIC
ELECTE
DEC 04 1984
S D
E

This document has been approved
for public release and sale; its
distribution is unlimited.

84 11 30 011

NA-84-1434

SERIAL NO.

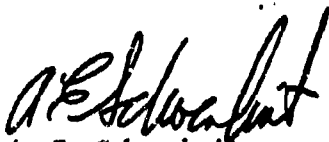
JOINED WING TRANSONIC DESIGN
AND
TEST VALIDATION

PREPARED BY:

J.A. CLYDE, E. BONNER, T.P. GOEBEL AND L. SPACHT

PREPARED FOR

OFFICE OF NAVAL RESEARCH
ARLINGTON, VIRGINIA



A. E. Schoenheit
Manager
Flight Sciences

DATE 22 June 1984

NO. OF PAGES i thru xi plus 142



Rockwell international

North American Aircraft Operations
Rockwell International Corporation
P.O. Box 92098
Los Angeles, California 90009

This document has been approved
for public release and sale; its
distribution is unlimited.

Unclassified

SECURITY CLASSIFICATION OF THIS PAGE (When Data Entered)

REPORT DOCUMENTATION PAGE		READ INSTRUCTIONS BEFORE COMPLETING FORM
1. REPORT NUMBER NA-84-1434	2. GOVT ACCESSION NO. AD-A148 355	3. RECIPIENT'S CATALOG NUMBER
4. TITLE (and Subtitle) Joined Wing Transonic Design and Test Validation		5. TYPE OF REPORT & PERIOD COVERED Final Report 9-30-82 to 5-31-84
		6. PERFORMING ORG. REPORT NUMBER NA-84-1434
7. AUTHOR(s) J.A. Clyde, E. Bonner, T.P. Goebel, and L. Spacht		8. CONTRACT OR GRANT NUMBER(s) N00014-C-0601 <i>js</i>
9. PERFORMING ORGANIZATION NAME AND ADDRESS Rockwell International North American Aircraft Operations Los Angeles, California, 90009		10. PROGRAM ELEMENT, PROJECT, TASK AREA & WORK UNIT NUMBERS 62241N RF--41-411 NR212-276
11. CONTROLLING OFFICE NAME AND ADDRESS Office of Naval Research Mechanics Division, Code 432 Arlington, Va. 22217		12. REPORT DATE 22 June 1984
		13. NUMBER OF PAGES 142
14. MONITORING AGENCY NAME & ADDRESS (if different from Controlling Office)		15. SECURITY CLASS. (of this report) Unclassified
		15a. DECLASSIFICATION/DOWNGRADING SCHEDULE
16. DISTRIBUTION STATEMENT (of this Report) Approved for public release, distribution unlimited		
17. DISTRIBUTION STATEMENT (of the abstract entered in Block 20, if different from Report)		
18. SUPPLEMENTARY NOTES		
19. KEY WORDS (Continue on reverse side if necessary and identify by block number) Joined Wing Forward Sweep Transonic Design Aft Sweep Transonic Test Biplane		
20. ABSTRACT (Continue on reverse side if necessary and identify by block number) A tactical supercritical flow research model was designed to achieve high aerodynamic efficiency at Mach number 0.90 and lift coefficient 0.50 using numerical transonic design procedures. A wind tunnel model was built and tested in the Rockwell International Trisonic Wind Tunnel at Mach numbers of 0.40, 0.85, 0.90, and 0.95. Lift-drag ratio at the design condition compared favorably with theoretical upper bound levels for the test arrangement and		

FOREWORD

This study was conducted by the Los Angeles Aerodynamics group of North American Aircraft Operations, Rockwell International. The work was performed under Contract No. N00014-82-C-0601, Joined Wing Transonic Design and Test Validation. Dr. Robert Whitehead of the Office of Naval Research was Project Monitor. Dr. Julian Wolkovitch acted as technical consultant.

ABSTRACT

A tactical supercritical flow research model was designed to achieve high aerodynamic efficiency at Mach number 0.90 and lift coefficient 0.50 using numerical transonic design procedures. A wind tunnel model was built and tested in the Rockwell International Transonic wind tunnel at Mach numbers of 0.40, 0.85, 0.90, and 0.95. Lift-drag ratio at the design condition compared favorably with theoretical upper bound levels for the test arrangement and conditions. Six component force measurements for the joined wing are well behaved and near linear over an angle-of-attack range of $-4 < \alpha < 10$ degrees. Stable stall is naturally achieved for the arrangement. Weak changes in longitudinal and lateral-directional stability and control with pitch angle exist.

Accession For	
NTIS GRA&I	<input checked="" type="checkbox"/>
DTIC TAB	<input type="checkbox"/>
Unannounced	<input type="checkbox"/>
Justification	
By _____	
Distribution/	
Availability Codes	
Dist	Avail and/or Special
A-1	



TABLE OF CONTENTS

Section		Page
I	INTRODUCTION	1
II	CONFIGURATION DEFINITION	2
III	JOINED WING DESIGN	3
	Linear Initialization	3
	Linear Induction Effects and Effective Twist	4
	Design Pressure Distribution	5
	Candidate Supercritical Airfoils	5
	Transonic Small Disturbance Design	5
	Forward Wing	5
	Aft Wing	7
	Theoretical Design Performance	8
	Transonic Redesign	8
IV	REFERENCE MONOPLANE DESIGN	9
	Linear Initialization	10
	Design Pressure Distribution	10
V	JOINED WING/REFERENCE MONOPLANE COMPARISON	12
VI	JOINED WING COMPARISON WITH THEORY	13
	Force Data	13
	Longitudinal	13
	Lateral-Directional	13
	Longitudinal Control	14
	Lateral Control	14
	Direct Side Force	14
	Summary	16
	Surface Pressure Data	16
VII	CONCLUSIONS	17
	REFERENCES	18
APPENDIX A	AERODYNAMIC METHODOLOGY	A-1
APPENDIX B	VISCOUS DRAG ANALYSIS	B-1

TABLE OF CONTENTS

Section	Page
APPENDIX C MODEL DESIGN AND CONSTRUCTION	C-1
Stress and Flutter Analysis	C-1
Aeroelastic Analysis	C-1
Model Loft Geometry	C-1
Model Fabrication	C-1
Contour Checks	C-2
Aeroelastic Characteristics	C-2

LIST OF ILLUSTRATIONS

<u>Figure No.</u>	<u>Title</u>	<u>Page No.</u>
1	Reference Monoplane Arrangement	25
2	Joined Wing Arrangement	26
3	Joined Wing Linear Finite Analysis Model	27
4	Joined Wing Linear Vortex Drag Optimization Model	29
5	Effect of Longitudinal Stability on Joined Wing Trimmed Span Load Efficiency at $M = 0.9$	31
6	Effect of Longitudinal Stability on Joined Wing Sectional Load Ratio at $M = 0.9$	32
7	Effect of Forward Wing Section Lift Coefficient on Upper Surface Local Mach Number for a Candidate Supercritical Design Pressure Distribution at $M = 0.90$	33
8	Candidate Linear Optimum at $M = 0.9$, $C_L = 0.5$	34
9	Aft Wing Geometric and Effective Twist at $M = 0.90$, $C_L = 0.50$	38
10	Forward Joined Wing Design Pressure Distribution at $M = 0.90$	39
11	Aft Joined Wing Design Pressure Distribution at $M = 0.90$	40
12	Yawed Wing Boundary Layer Analysis of Design Pressure Distribution	41
13	Forward Joined Wing Candidate Streamwise Airfoil	42
14	Aft Joined Wing Candidate Streamwise Airfoil	43
15	Transonic Forward Wing-body Prism Model	44
16	Initial Transonic Forward Wing Analysis Results	46
17	Final Forward Wing Transonic Design Geometry	48
18	Final Forward Wing Transonic Design Flow Quality	52
19	Final Forward Wing Transonic Boundary Layer Displacement Thickness	58
20	Forward Wing Airfoils with/without Boundary Layer Displacement Thickness	60
21	Aft Wing Transonic Model	65
22	Final Aft Wing Transonic Design Geometry	76
23	Final Aft Wing Transonic Design Twist	81
24	Final Aft Wing Transonic Design Flow Quality	82
25	Final Aft Wing Transonic Boundary Layer Displacement Thickness	88
26	Aft Wing Airfoils With/Without Boundary Layer Displacement Thickness	90
27	Joined Wing Estimated Turbulent Friction Drag	93
28	Joined Wing Theoretical Design Performance	94
29	Joined Wing Force Results, First Test Entry, $M = 0.90$	95
30	Joined Wing Oil Flow Photographs, First Test Entry, Forward Wing, $M = 0.90$	96
31	Joined Wing Theoretical Elastic Twist Increments, $M = 0.90$, $C_L = 0.50$, $q = 1120$ psf	97

LIST OF ILLUSTRATIONS (CONCLUDED)

<u>Figure No.</u>	<u>Title</u>	<u>Page No.</u>
32	Joined Wing Linear Spanload for Design and Jig Twist at $M = 0.90$	98
33	Joined Wing Transonic Small Disturbance Pressure Distribution Comparison, Forward Wing, $M = 0.90$	99
34	Joined Wing Full Potential Pressure Distribution Comparison, Forward Wing, $M = 0.90$	100
35	Joined Wing Transonic Small Disturbance and Full Potential Pressure Distribution Comparison, Forward Wing, $M = 0.90$	101
36	Joined Wing Transonic Small Disturbance Pressure Distribution Comparison, Aft Wing $M = 0.90$	102
37	Joined Wing Oil Flow Photographs, First Test Entry, Aft Wing, $M = 0.90$	103
38	Effect of Joined Wing Incidence Change on Linear Spanload Distribution at $M = 0.90$	104
39	Effect of Joined Wing Incidence Change on Predicted Longitudinal Characteristics at $M = 0.90$	105
40	Redesign Full Potential Transonic Flow Quality, $M = 0.90$	106
41	Joined Wing Force Results, Second Test Entry, $M = 0.90$	107
42	Reference Monoplane Linear Finite Element Analysis Model	108
43	Effect of Longitudinal Stability on Reference Monoplane Span Load Efficiency at $M = 0.90$	109
44	Reference Monoplane Wing Sectional Loading at $M = 0.90$, $C_L = 0.50$	110
45	Reference Monoplane Design Pressure Distribution at $M = 0.90$, $C_L = 0.50$	111
46	Upper Bound Joined Wing/Reference Monoplane Lift/ Drag Ratio Comparison	112
47	Joined Wing Lateral-Directional Comparison, First Test Entry, $M = 0.90$	113
48	Joined Wing Lateral-Directional Comparison, Second Test Entry, $M = 0.90$	114
49	Joined Wing Flap Lift Comparison, First Test Entry, $M = 0.90$	115
50	Joined Wing Flap Pitching Moment Comparison, First Test Entry, $M = 0.90$	116
51	Joined Wing Aileron Comparison, First and Second Test Entry, $M = 0.90$	117
52	Comparison of Measured and Full Potential Forward Wing Pressure Distributions at $M = 0.90$, $C_L = 0.50$	118
53	Upper Surface Oil Flow Photographs $M = 0.90$, $\alpha_e = 4.1 \times 10^\circ$, $C_L = 0.507$, $i_w = -1.27$ degrees	121
54	Comparison of Measured and Transonic Small Disturbance Aft Wing Pressure Distribution at $M = 0.90$, $C_L = 0.50$	122

LIST OF TABLES

<u>Table No.</u>	<u>Title</u>	<u>Page No.</u>
I	Aerodynamic Characteristics	19
II	Optimization Results	20
III	Joined Wing Airfoil Design Conditions	21
IV	Longitudinal Characteristics, $\alpha = \beta = 0^\circ$	22
V	Lateral-Directional Stability, $\alpha = 0^\circ$, $-5 < \beta < 5$	22
VI	Lifting Flap Effectiveness, $M = 0.90$, $\alpha = 0^\circ$	23
VII	Pitching Moment Effectiveness, $M = 0.90$, $\alpha = 0^\circ$	23
VIII	Rolling Moment Effectiveness, $M = 0.90$, $\alpha = 0^\circ$	24

NOMENCLATURE

General Symbols

a.c.	Aerodynamic center
AR	Aspect ratio, b^2/S_{ref}
b	Wing span
B.P.	Buttock plane, inches
c	Surface chord
\bar{c} , MAC	Mean aerodynamic chord
CG	Center of gravity
CP	Center of pressure
C_{D_0}	0 Percent suction drag or drag at $C_L = 0$
$C_{D_{100}}$ or $C_{D_{vtx}}$	100 Percent suction or vortex drag
C_{D_i}/C_L^2	Drag due to lift factor
C_l	Sectional lift coefficient, l/qc
C_{L_α}	Lift curve slope, $dC_L/d\alpha$, per degree
C_{L_0}	Lift coefficient at $\alpha = 0$ degrees
C_{M_α}	Pitching moment slope, $dC_M/d\alpha$, per degree
$C_{M_{\alpha=0}}$	Pitching moment at $\alpha = 0$ degrees
$C_{M_{C_L=0}}$	Pitching moment at $C_L = 0$
C_n	Sectional normal force coefficient
C_p	Pressure coefficient, $(P-P_\infty)/q$
C_p^*	Critical pressure coefficient
dC_M/dC_L	Static longitudinal stability
e_{100}	Trefftz plane spanload efficiency
FP	Full potential
F.S.	Fuselage station, inches

i_w	Wing incidence, negative nose down
L/D	Lift to drag ratio, C_L/C_D ,
M	Mach number
M_2	Local upper surface Mach number
P	Static pressure
q	Dynamic pressure, psf
Q	Total velocity
RN, R_e	Reynolds number per foot
R_c	Reynolds number based on mean aerodynamic chord
S	Reference area, ft^2
S_A	Aft wing reference projected trapezoidal wing area
S_F	Forward wing reference projected trapezoidal area
t/c	Wing thickness ratio
TSD	Transonic small disturbance
WP	Water plane, inches
WS	Wing station, inches
X, Y, Z	Cartesian body axis axial, lateral, vertical coordinates

Greek Symbols

α	Angle-of-attack, degrees
β	Angle-of-sideslip, degrees
Δ	Increment
δ	Surface Deflection, perpendicular to hinge line, degrees
ϵ	Downwash angle, degrees
η	Fraction of span, $2y/b$
Λ	Sweep angle, degrees

NOMENCLATURE (CONTINUED)

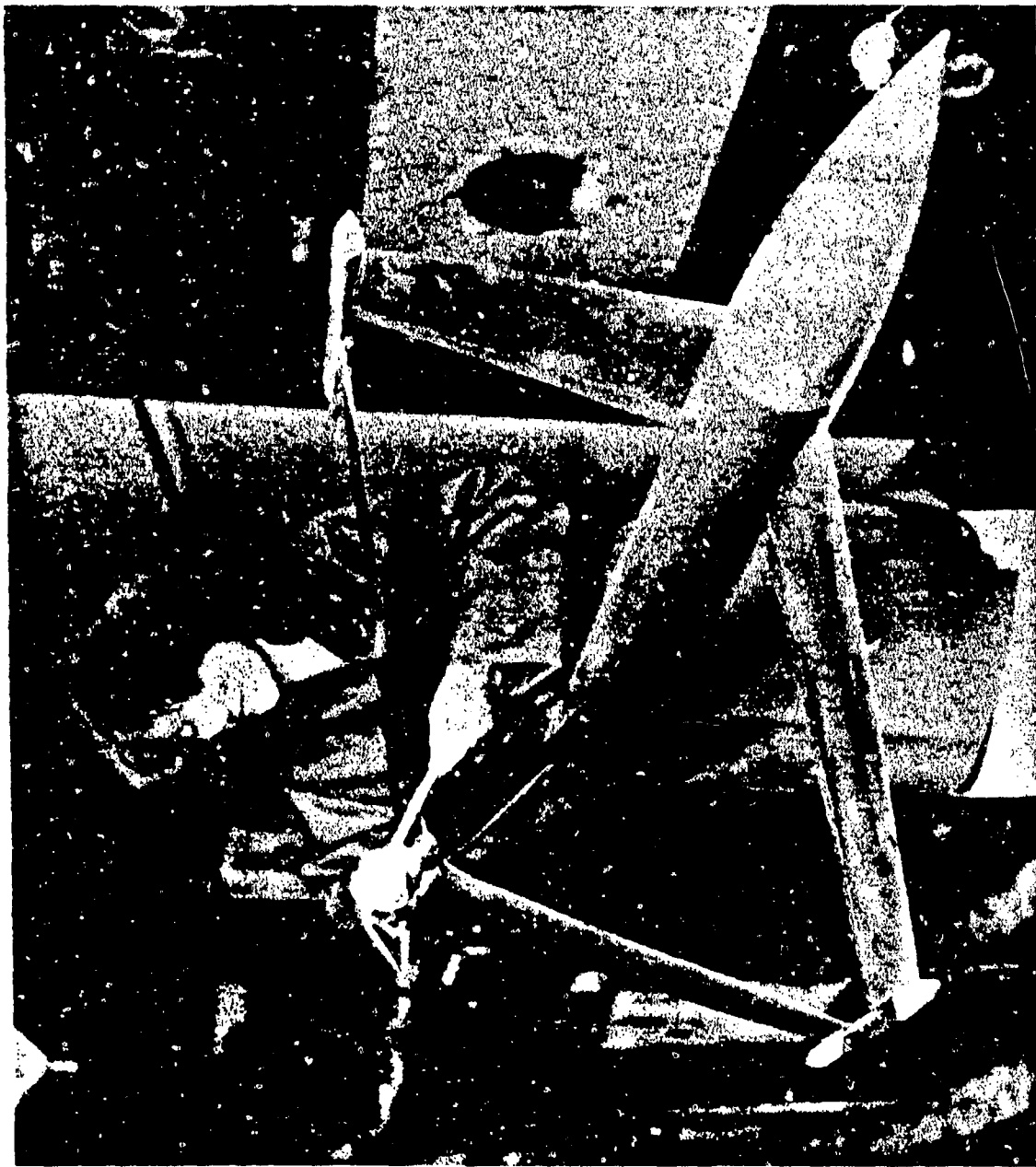
θ	Twist angle, positive nose up
λ	Taper ratio
ψ	Yaw angle, $(-\beta)$, degrees

Coefficients

C_C	Chord force coefficient	$\frac{\text{Chord Force}}{qS}$
C_D	Drag Coefficient,	$\frac{\text{Drag}}{qS}$
C_L	Lift coefficient,	$\frac{\text{Lift}}{qS}$
C_{ℓ}	Rolling moment coefficient,	$\frac{\text{Rolling Moment}}{qSb}$
C_M	Pitching moment coefficient,	$\frac{\text{Pitching Moment}}{qSc}$
C_N	Normal force coefficient,	$\frac{\text{Normal Force}}{qS}$
C_n	Yawing moment coefficient,	$\frac{\text{Yawing Moment}}{qSb}$
C_p	Pressure coefficient,	$\frac{P-P_{\infty}}{q}$
C_y	Side force coefficient,	$\frac{\text{Side Force}}{qS}$

Subscripts

A	Aft wing panel
AL	Attachment line
B	Body axes



Section I
INTRODUCTION

The joined wing is a general concept which combines two wings, a fuselage and a vertical fin. The wings form a diamond shape in both planform and front view. A limited amount of low speed design, wind tunnel test and evaluation, and several structural studies are discussed in reference 1 and in references cited therein. Joined wing aerodynamic technology offers potential for improved induced drag efficiency for transonic flight. An aerodynamic study of the application of the joined wing concept to a fighter can be used to explore this potential and to define the unique characteristics of a joined wing arrangement. A Mach number of 0.90 lift coefficient of 0.50 design point was selected to focus the study and corresponds to a condition between cruise and high g maneuvers. Contour definitions by numerical transonic design, and experimental validation by subsonic/transonic wind tunnel test, are required to validate the highly-nonplanar, strongly-interacting generic joined wing arrangement.

Configuration aerodynamic development, numerical wing design and experimental test validation are described in the text of the report. Specific methodology used, viscous drag analysis and model design and construction details are presented in appendices A, B, and C, respectively.

Section II

CONFIGURATION DEFINITION

Representative geometric data from current fighters (e.g., body length to wing span, body width to wing span, tail volume etc.) were used to define a reference monoplane and a joined-wing configuration. A common body was used for both configurations. Standard longitudinal locations of the aerodynamic surfaces were used for the monoplane.

The joined wing configuration was selected to have the same span as the reference monoplane and a projected total (i.e., to the plane of symmetry) plan area of both panels equal to the total wing area plus exposed horizontal tail area of the reference monoplane. The joined wing panel leading edge sweep was nominally selected to be ± 45 deg, based on transonic perpendicular sectional lift coefficients ($C_{L\perp} = C_L + \cos^2 \Lambda_{c/2}$) and supersonic wave drag considerations. Ten degrees of dihedral and 20 degrees of anhedral were used for the forward and aft wing panels, respectively, to achieve substantial reductions of vortex drag due to nonplanar effects. The vertical tail size was a geometric fallout of the 30 degrees included angle of the joined wing. Nominal thickness ratio $t/c = 0.05$ was selected based on current fighter design practice. Configuration arrangement of the reference monoplane and the joined wing are shown on figures 1 and 2, respectively. Note that the dimensions shown correspond to a 1/10th scale. The wind tunnel model tested was a 1/15th scale as described later.

Arrangement considerations for the joined wing included a level of low speed static longitudinal instability and lateral-directional stability that were similar to the reference monoplane and consistent with current tactical advanced design studies. A comparison of the various linear aerodynamic characteristics computed by the method of reference 2 are presented on table I. The pitch damping derivative, C_{M_q} , is typically twice that of the reference monoplane.

Section III

JOINED WING DESIGN

The numerical aerodynamic design methodology used for the present study is summarized in appendix A.

LINEAR INITIALIZATION

Two linear nonplanar finite element models were used for the study. The analysis model consists of a slender body (not shown), interference shell, forward and rear wings, and a vertical tail as shown in figure 3. Vortex drag minimization (reference 3) uses a flat plate fuselage and forward and aft-wings as shown in figure 4. The vertical tail is not simulated because it has no influence on the optimization. In order to maintain solution consistency between models, 10 uniform chordwise by 10 uniform spanwise panels were used for the forward and aft wings.

Linear vortex drag optimizations were performed to satisfy necessary (far field) design objectives at $M = 0.90$ and $C_L = 0.50$. The following constraints were considered to insure a practical result:

1. $C_M = 0$ at the design C_L
2. High lift stable pitching moment break
3. Moderate supersonic longitudinal stability levels
4. Moderate twist
5. Sectional loadings that are consistent with moderate upper surface supercritical Mach numbers ($M_{\xi} < 1.3$)

Equal joined wing projected panel areas were considered initially (cases 1 through 4 of table II). The impact of longitudinal balance on trimmed span load efficiency and the relative peak sectional lift (cases 1 through 3) are presented on figures 5 and 6 respectively. As shown, unstable balance is indicated which was compatible with low speed stable stall (since the forward wing panel progressively separates from tip to root and is located ahead of the center of gravity) and moderate supersonic longitudinal stability. Attempts to more uniformly balance the loading between the forward and aft panels (case 4), in the interest of reducing the supersonic upper surface Mach number on the forward wing, resulted in unacceptable span load efficiency penalties (figure 5) and excessive twist. Two alternative approaches were examined to reduce the loading on the forward panel:

1. Reduce the sectional design lift coefficient (which is uniquely related to the gross lift coefficient for a given optimum solution).
2. Redistribute wing area to 60 percent on the forward panel and 40 percent to the aft panel (case 5).

The results of the latter trade are presented on figure 5 and indicate penalties on span load efficiency relative to the equal area case. The reduced design C_l option was consequently selected. A local upper surface Mach number of 1.25 on the forward panel was tentatively selected and corresponds to a gross design $C_l = 0.45$ for the 20 percent unstable $M = 0.90$ balance (case 6). Table II presents a summary of the initial optimization cases considered.

The design C_l was subsequently increased to 0.50 to reflect a constant more positive lower surface candidate pressure than originally assumed (see figure 7). As indicated, this revision allows an increase in sectional lift coefficient for a fixed upper surface Mach number.

A series of linear vortex drag optimizations were subsequently performed at $M = 0.90$, $C_l = 0.50$ with a longitudinal instability of 0.20%. Several design refinements were incorporated subject to maintaining the previously derived potential drag due-to-lift. They were: smooth variation of spanwise twist, low root chord incidence, and supercritical type camber on the forward surface. The resulting linear design is presented on figure 8. The impact of the previously cited constraints on span load efficiency was negligible.

LINEAR INDUCTION EFFECTS AND EFFECTIVE TWIST

The method used to account for the wing-wing interaction in the Transonic Small Disturbance (TSD) analysis is an immersion or apparent twist philosophy. The upwash/downwash distribution of the aft wing on the front and the front wing on the aft are calculated with linear theory and then applied as twist increments to the geometry used in the TSD code.

The induction effects are calculated for the candidate linear design case using a mixed boundary condition analysis (reference 3). The process imposes a $C_{p_{net}} = 0$ constraint on the surface where the downwash effects are to be defined, and maintains the design $C_{p_{net}}$'s on the other surface(s). The induction effects of the aft wing on the front wing are negligible. The effects of the front on the rear wing are given on figure 9. Induced camber is negligible for either panel.

DESIGN PRESSURE DISTRIBUTION

Evaluation of $M = 0.90$ candidate sectional supercritical pressure distribution for the forward and aft wing panels was performed for the nominal model test Reynolds number. The design sectional lift coefficients were 0.60 and 0.33 for the forward and aft panels respectively, for a design gross lift coefficient of 0.50. These pressure distributions correspond to midspan values resulting from minimization of the trimmed vortex drag for the full three dimensional arrangement. Flat top upper surface distributions with a linear

recompression beginning at 60 percent chord were initially considered. Local Mach numbers of 1.19 for the swept aft wing and 1.07 for the swept forward panel resulted for the sectional C_p of interest considering representative lower surface pressure distribution² levels. The resulting candidate design pressure distributions are presented on figures 10 and 11. Local sonic and leading edge attachment line (i.e., $Q_{AL} = Q_{\infty} \sin \Lambda_{LE}$) conditions are indicated.

An integral laminar/turbulent yawed wing boundary layer analysis (reference 4) was performed for a joined wing mean aerodynamic chord Reynolds number of 4.1×10^6 which corresponds to a minimum dynamic pressure tunnel operating condition to reduce model stress levels. Transition was enforced at approximately 3.5 percent chord. The results of figure 12 indicate the flow remains fully attached for the forward surface with separation occurring downstream of 95 percent chord on the upper surface of the aft wing. Although the latter panel is more lightly loaded, its higher trailing edge sweep offsets the reduction in adverse pressure gradient.

The results of the viscous analysis indicate the candidate design pressure distributions of figures 10 and 11 satisfy the sufficient condition of good flow quality considering real fluid effects. The potential far field optimization results of figure 3 satisfy the necessary design conditions. Taken together, both necessary and sufficient considerations are met and provide satisfactory initialization of the three dimensional transonic design. The boundary layer displacement thickness growth for the upper and lower surface of figure 12 indicate a candidate airfoil should have a nominal trailing edge thickness of 1.5 percent chord to permit undercutting of the design contour to minimize weak viscous interaction effects on the transonic potential design.

CANDIDATE SUPERCRITICAL AIRFOILS

The nominal airfoil design conditions for $M = 0.90$ $C_L = 0.50$ trimmed condition with a 20 percent longitudinal unstable balance^L and a thickness ratio of 5 percent are summarized on table III. The candidate streamwise airfoil sections for the forward and aft swept wings are presented in figures 13 and 14 respectively. These contours in conjunction with the effective twist distributions of figures 8 and 9 are used to initialize the three dimensional potential transonic small disturbance design of the aft swept wing-body and forward swept wing vertical tail fairing described in the next section.

TRANSONIC SMALL DISTURBANCE DESIGN

FORWARD WING

The transonic small disturbance (TSD) model for the front wing-body combination is shown on figure 15. Figure 15a shows the wing planform and the prism used to satisfy the body boundary conditions. Figure 15b shows the fuselage modeling. The forward wing was initially modeled with the candidate airfoil of figure 13 across the entire span in conjunction with the lesser optimum twist of figure 8. The resulting analysis (reference 5) is shown on figure 16.

To reduce the aft loading of the inboard airfoils the camber was progressively decreased. The inboard span stations have a relatively strong shock at 90 percent chord which required further design work to weaken. The mid-span region developed the desired flat top pressure distribution although terminal upper surface adverse pressure gradients exceed the candidate distribution and required moderation. The outboard region meets the design goal and required no additional refinements.

Further design effort attempted to eliminate the inboard trailing edge shock. The target upper surface pressure coefficient was specified aft of 20 percent chord at each of the inboard TSD defining stations. The resulting airfoils were unrealistic. Subsequent effort was directed at more modest root shock weakening movement of the shock towards the trailing edge. A candidate 5 percent airfoil was derived from inverse analysis (reference 6) in conjunction with twist adjustments to approximate the linear optimum sectional normal force distribution. Comparison of the results indicate:

1. The strength of the inboard shock and adverse pressure gradient has been moderately reduced.
2. The inboard change of airfoil caused a degradation of the flow quality in the midspan region of the wing.
3. The outboard section of the wing was unchanged.

The impact on the center section was not considered serious since subsequent design effort was to be directed at reducing the trailing edge recompression problems in this region.

The midspan refinement effort concentrated on the area from 47 to 61 percent of the span. An inverse design was performed for the target upper surface pressure distribution defined from approximately 1 percent chord to the trailing edge. This solution defined an airfoil that exhibited improved center section flow quality. At this point in the design, the model stress analysis indicated the wing tip area required an increase in thickness from 5 to 7 percent with a linear variation to 5 percent at the midspan. Subsequent analysis of this modification indicated only a minor impact.

A three dimensional finite difference boundary layer analysis (reference 7) was performed at the tunnel test mean aerodynamic chord Reynolds number of 4.1×10^6 to verify fully attached flow would be achieved except inboard near the trailing edge on the upper surface. The airfoils resulting from the potential design were undercut by this boundary layer displacement thickness to minimize weak viscous interaction effects. The resulting trailing edge in the outboard region had insufficient structural thickness. The lower surface was subsequently modified for $x/c > 80$ percent. The increased trailing edge thickness had the additional benefit of reducing the adverse pressure gradients on the lower surface. The final forward wing transonic design geometry is shown on figure 17. The design flow quality is presented on figure 18. Figures 19 and 20 show the boundary layer displacement thickness and undercut airfoils, respectively.

AFT WING

The aft wing was initially modeled as a trapezoidal planform with the candidate airfoil of figure 14 across the entire span. The initial twist is given in figure 9. As a result of not achieving the desired flow quality when matching the linear theory optimum span load shape, several modifications were made to the camber, twist and planform. The camber was decreased at the root and the tip to increase the forward loading of the lower surface. The twist was also adjusted to give the desired sectional lift distribution across the span. The revised planform incorporates an inboard glove to reduce the strength of the flow singularity at the root, and a central body fairing of circular cross section was added due to model structural wing-tail attachment considerations, figures 21a and 21b. The status airfoil at $\eta = 0.04$ (the side of the fairing) is presented in figure 21c. The section varies linearly to the airfoil at $\eta = 0.25$. The airfoil of figure 21d is used from $\eta = 0.25$ to 0.80. The airfoil then varies linearly to that of figure 21e at the tip. Status geometric twist is compared with the linear optimum on figure 21f. Transonic small disturbance (reference 5) span loading and upper and lower surface pressure distribution isometrics are given on figures 21g and 21h respectively. Figures 21i through 21k show sectional pressure distributions at three representative span stations. The inboard span stations still indicated a shock while the midspan region develops the desired flat top pressure distribution with a mild leading edge peak.

Further design effort was directed at eliminating the root shock, reducing the leading edge peak pressure in the center section, and increasing the upper surface leading edge pressure at the tip. A transonic small disturbance inverse (reference 6) analysis was employed to determine changes to the airfoil geometry to eliminate the root shock and used to reduce the upper surface pressure peak at the leading edge of the wing center section. Tip airfoil redesign was directed at increasing the loading in the leading edge region. Since further increase in twist was undesirable based on tip fairing/attachment considerations, effort concentrated on decambering the airfoil section while maintaining the linear optimum sectional normal force coefficient distribution.

A three dimensional finite difference boundary layer analysis (reference 7) was then performed at a test mean aerodynamic chord Reynolds number of 4.1×10^6 to verify fully attached flow was essentially achieved and define associated boundary layer displacement thickness distribution for the upper and lower surfaces. Separation occurs nominally in the last 5 percent on the upper surface and is fully attached on the lower surface. The inviscid design airfoils are corrected for weak viscous interaction effects by undercutting the coordinates by the displacement thickness.

A 7 percent thick tip section was subsequently investigated due to model pressure instrumentation/structural considerations. The design flow quality was not significantly affected. The final design geometry incorporating a 7 percent thick tip section linearly decreasing to a base 5 percent airfoil at 50 percent semispan is summarized in figure 22 and 23. Figure 24 presents the final design loading and flow quality. Figures 25 and 26 present the aft wing boundary layer displacement thickness and undercut airfoils respectively.

THEORETICAL DESIGN PERFORMANCE

A theoretical figure of merit for the joined wing will now be defined. Specifically, it is the highest (or ultimate) L/D that would be expected at the design condition. The evaluation includes fully turbulent skin friction, profile and potential wake losses but does not account for viscous component interference or separation drag. As such the performance is upper bound in nature. Skin friction drag is evaluated (reference 2) for a flat plate condition in conjunction with a component build up approach. The result (figure 27) is corrected to account for the design pressure distribution and sweep using the profile drag method described in appendix B. Induced drag is calculated using trimmed potential theory lifting efficiency. The drag is then the sum of skin friction (C_{D_f}), profile drag (C_{D_p}) and the induced (C_{D_i}) drag.

The constituent drag pieces and the trimmed upper bound L/D at the design lift coefficient are summarized in figure 28.

TRANSONIC REDESIGN

The results of the first wind tunnel test are presented in reference 8, appendices C, D, and E. Pertinent design results are shown in figure 29. Lift curve slope and longitudinal stability were as expected while the intercepts C_{L_0} and C_{M_0} were not matched by linear analysis for the design twist and as built camber. As a consequence self-trim was not achieved.

Examination of the wind tunnel pressure data revealed the forward wing was more heavily loaded and the aft wing more lightly loaded than intended. This resulted in the forward wing developing a swept shock (figure 30) at the design C_L . The front wing center section was intended to operate at lower angle-of-attack and the rear wing airfoils at higher angle-of-attack due to the elastic twist increments (figure 31). When structurally bench tested, (see appendix C) the model was not nearly as flexible as a beam structural analysis had predicted.

Calculations were subsequently performed for the as built (i.e., jig) twist. The linear spanloading (figure 32) showed this was indeed the cause of the loading anomalies observed. The jig twist was then analyzed using transonic small disturbance theory at the wind tunnel angle-of-attack for the design lift coefficient. This result (figure 33) produced the anomalous results that no shocks would be anticipated for either the design or jig twist on the forward wing. Conservative full potential analysis (reference 9) was subsequently performed.

These results (figure 34) indicate an essentially shockless condition on the forward wing with the design twist and angle-of-attack and a shocked flow for the jig twist and test angle-of-attack for $C_L = 0.50$. A comparison of the forward wing numerical shock capturing differences between transonic small disturbances and full potential theory at the design $C_L = 0.50$ for the as built twist are summarized on figure 35. The latter analysis was consequently used for redesign effort. The aft wing flow (figures 36 and 37) was adequately predicted by TSD and verified to be shockless at the design condition.

Differences between design and jig twist for the aft wing are offset by the increased angle-of-attack required to achieve $C_L = 0.50$. The opposite is true for the forward wing. This consideration in conjunction with substantially higher design loading accounts for its elastic sensitivity.

Since the twist of the high strength steel wings could not be readily changed, the use of negative wing incidence to reduce the forward panel loading was examined as an alternative. Linear theory indicated a 1 degree nose down incidence on the forward wing and a 0.25 degree nose up change on the aft wing would approximate the design span load shape. The resources available did not permit incorporation of the aft wing modification. The linear span load for a -1 degree change on the forward wing is presented on figure 38. The predicted longitudinal results are presented on figure 39. The self trim condition at the design C_L is essentially realized. Full potential analysis of the modified design is presented on figure 40 and indicates an essentially shockless flow.

The results of the second wind tunnel test are presented in appendices G, H, and I of reference 8. Pertinent design results are shown in figure 41. Lift curve slope and longitudinal stability were unchanged from previous results. The intercepts, C_{L_0} and M_0 , again were not matched by linear analysis for the jig twist, wing incidence change, and as built cambers. The design is considerably closer to achieving self trim. As before, a swept shock exists on the forward wing but appears to be weaker for the center section due to the forward wing still being more heavily loaded than desired. A detailed discussion of the second test entry surface pressure measurements and associated oil flow data is presented in section VI. Further flow quality progress (i.e., shock weakening) requires achieving the design twist on both the forward and aft panels to realize the intended loading distribution between the two surfaces.

The aft wing flow quality is good and consequently does not require further attention. This is due in part to the panel being more lightly loaded for the design condition.

Section IV

REFERENCE MONOPLANE DESIGN

The reference monoplane of section II was derived from representative geometric data of current fighter aircraft. The resulting arrangement is shown on figure 1. Representative geometric properties included: body length and width to wing span, and horizontal and vertical tail volumes.

LINEAR INITIALIZATION

Necessary monoplane lifting conditions were satisfied by optimizing the far field vortex drag at $M = 0.90$ and $C_L = 0.50$. The drag minimization model uses a flat plate fuselage, wing and horizontal tail components. A vertical tail was not simulated since it has no influence. The arrangement was paneled in a similar manner as the joined wing with 10 uniform chordwise and spanwise finite elements for the wing (see figure 42).

The following constraints were imposed to insure a practical result:

1. $C_M = 0$ at the design C_L
2. Section loadings consistent with moderate upper surface supercritical Mach numbers ($M_2 < 1.30$)
3. No fuselage twist or camber
4. Horizontal tail deflection only (that is, no twist or camber)

The effect of longitudinal balance, on constrained span load efficiency is presented on figure 43. A 20 percent unstable balance was subsequently selected. The section loadings for this case are presented on figure 44.

DESIGN PRESSURE DISTRIBUTION

Evaluation of the design sectional supercritical pressure distribution (figure 45) was performed for the mean chord test Reynolds number of 7.3×10^6 . The reference monoplane operates at a higher Reynolds number due to a longer chord than the joined wing. The sectional lift coefficient for the wing at the design point is 0.55. This pressure distribution corresponds to a near midspan value resulting from the minimization of trimmed vortex drag and is comparable in magnitude and shape to the distribution on the forward panel of the joined wing. A local upper surface Mach number of 1.16 resulted.

A laminar/turbulent yawed wing boundary layer analysis (reference 4) was initially performed for the same unit Reynolds number and a wing mean sweep of 33.6 degrees corresponding to the same leading edge sweep as the joined wing. A revised reference monoplane having the same mean sweep was subsequently analyzed in order to achieve similar transonic perpendicular sectional lift coefficients ($C_{L\perp} = C_L + \cos^2 \Lambda_{c/2}$) and comparable supersonic wave drag which is a function of the maximum thickness line which is approximately equal to the mean sweep line. Transition was enforced at approximately 3.5 percent chord for both cases. The analysis indicated fully attached flow would be expected for the design pressure distribution of figure 45 for either planform. Profile drag results using the analysis of appendix B are summarized below.

Planform	Λ_{LE} (deg)	$\Lambda_{c/2}$ (deg)	Re_c	C_{DF}	C_{Dp}
Initial	45	33.6	7.3×10^6	0.01098	0.01170
Revised	53.2	45	7.3×10^6	0.01098	0.01288

Section V

JOINED WING/REFERENCE MONOPLANE COMPARISON

Theoretical induced drag and fully turbulent profile drag were calculated at $M = 0.90$ and $C_L = 0.50$ for the two configurations for the same wind tunnel test unit Reynolds number. The results are summarized in figure 46a. The joined wing has an 11 percent induced drag advantage compared to the monoplane of the same span due to the nonplanar nature of the arrangement. Viscous comparison indicate the joined wing has 15 percent higher viscous drag than the monoplane as a result of 12 percent higher surface area for the same plan area and a 42 percent lower mean chord Reynolds number. Ultimate L/D's at the design $C_L = 0.50$ for the joined wing and reference monoplane are 12.97 and 13.24, respectively. These levels neglect viscous component interference, separation drag, etc., and consequently are upper bound in nature.

A similar calculation was performed for full scale conditions as a function of flight altitude. The results are presented on figure 46b and indicate the joined wing and reference monoplane have essentially equal upper-bound aerodynamic efficiency between sea level and 50,000 feet altitude. Fixed altitude comparisons correspond to constant normal load factor in order to maintain $C_L = 0.50$.* Constant Reynolds number comparison corresponds to variable load factor due to the change in altitude required to operate at the design lift coefficient.

The previous results do not weigh more extensive passive laminar flow extents for the joined wing relative to the monoplane that may result from operating at lower chord Reynolds number.

*Wing area variations were not considered in the construction of the results of figure 46b.

Section VI

JOINED WING COMPARISON WITH THEORY

FORCE DATA

The chord plane finite element models of figures 3 and 4 were used to predict the longitudinal and lateral-directional characteristics of the joined wing.

LONGITUDINAL

Measured lift and pitching moment are slightly nonlinear in the angle-of-attack range $-4 < \alpha < +10$ degrees. The stall is stable because the outboard section of the forward wing stalls first and is forward of the moment reference point. These characteristics, and the effect of the forward wing incidence change have been presented earlier in figures 29 and 39. The measured longitudinal derivatives of lift curve slope, $C_{L\alpha}$, and pitching moment slope, dC_M/dC_L , are expected to agree most closely with results of linear theory calculations at angle-of-attack and sideslip near $\alpha = 0$ and $\beta = 0$ degrees. These measured derivatives and lift and pitching moment at zero angle of attack are compared on table IV with linear theory calculations. Measured lift curve slopes exceed linear theory calculation by 3 to 9 percent. Measured lift coefficients at zero angle of attack, C_{L0} , are 40 to 60 percent lower than predicted by linear analysis using as-built cambers. The neglect of boundary layer displacement thickness decambering effects for supercritical type pressure distributions is believed to be responsible for this discrepancy. The intent was to select the moment reference point so that the joined wing model is 20 percent unstable at $M = 0.90$. The dC_M/dC_L comparison of table IV shows that the moment reference point should have been selected 4 percent \bar{c} further forward. Measured pitching moment at zero angle-of-attack, C_{M0} , was within 0.008 of linear theory prediction. The boundary-layer induced lift loss is in the same direction on both wings, with the pitching moment contributions being of opposite sign on the two wings.

LATERAL-DIRECTIONAL

Comparisons between linear theory calculation and measurement are shown in figure 47 for a forward wing incidence, i_{w_F} , of -0.27 degree (first test, TWT-438) and on figure 48 for $i_{w_F} = -1.27$ degrees (second test, TWT-487). Yawing moment and side force derivatives $C_{n\beta}$ and $C_{y\beta}$ show weak variations with angle-of-attack and sideslip in the ranges $-4 < \alpha < +8$ and $-10 < \beta < +10$ degrees. Rolling moment derivative $C_{l\beta}$ shows a variation with angle of attack characteristic of a sweptback wing. The measured derivatives $C_{n\beta}$ and $C_{y\beta}$ were within ± 10 percent of the linear theory calculation as shown in table V. The predicted derivative $C_{l\beta}$ at $\alpha = 0$ degrees was satisfactory.

LONGITUDINAL CONTROL

The lift and pitching moment effectiveness of 20 percent chord trailing edge flaps showed relatively weak variations with angle of attack in the range -4 degrees $< \alpha < +8$ degrees and are lower than the linear theory calculation as shown on figures 49 and 50, on tables VI and VII and in reference 8. Measured increments were generally in the range of 60 to 90 percent of linear theory predictions. The difference between calculation and measurement is attributed to viscous and nonlinear compressibility effects.

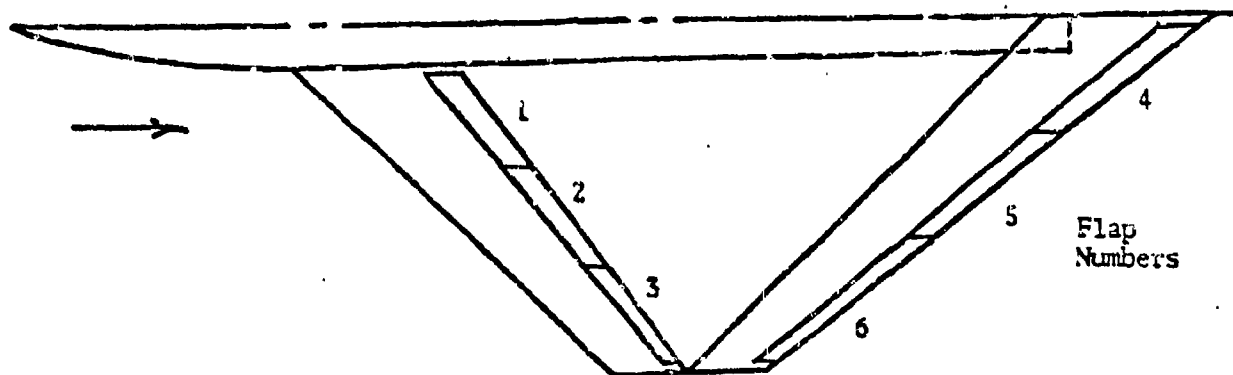
LATERAL CONTROL

The rolling moment effectiveness of various combinations of 20 percent chord trailing edge flaps showed weak variations with angle of attack in the range $-4 < \alpha < +8$ degrees and were substantially lower than the linear theory calculation as shown on figures 51, on table VIII and in reference 8. Measured increments were 41 to 62 percent of the linear theory rolling moment increments.

DIRECT SIDE FORCE

The maximum side force flap configuration is with the trailing edges of all three flaps deflected toward each other on one side of the joined wing and away from each other on the other side, i.e., with:

$$\begin{aligned}\delta_{1L} + \delta_{2L} + \delta_{3L} &= +\delta_{FL} \\ \delta_{1R} + \delta_{2R} + \delta_{3R} &= -\delta_{FR} \\ \delta_{4L} + \delta_{5L} + \delta_{6L} &= -\delta_{AL} \\ \delta_{4R} + \delta_{5R} + \delta_{6R} &= +\delta_{AR}\end{aligned}$$



For $\delta_{F_L} = \delta_{A_R} = +10$ degrees and $\delta_{F_R} = \delta_{A_L} = -10$ degrees, comparisons between linear calculation and measurement are $L(M = 0.90, \alpha = 0$ degrees):

	Linear Theory	Measurement
ΔC_L	0.0	-0.026
ΔC_M	0.0	-0.016
ΔC_Y	+0.0306	+0.018
ΔC_n	+0.0059	+0.0055
ΔC_l	+0.0043	+0.00385

As with other flap deflections, the measured increments are less than calculated by linear theory. Since it is of interest to consider flap deflections to reduce the yawing and rolling moments to zero while maintaining a side force increment, the linear theory results are given in equation form as:

$$\begin{aligned}
 C_L &= +0.005345\delta_{F_L} + 0.005796\delta_{A_L} + 0.005345\delta_{F_R} + 0.005796\delta_{A_R} \\
 C_M &= +0.01060\delta_{F_L} - 0.008435\delta_{A_L} + 0.01060\delta_{F_R} - 0.008435\delta_{A_R} \\
 C_Y &= +0.00073\delta_{F_L} - 0.00080\delta_{A_L} - 0.00073\delta_{F_R} + 0.00080\delta_{A_R} \\
 C_n &= +0.000635\delta_{F_L} + 0.00034\delta_{A_L} - 0.000635\delta_{F_R} - 0.00034\delta_{A_R} \\
 C_l &= +0.00100\delta_{F_L} + 0.000785\delta_{A_L} - 0.00100\delta_{F_R} - 0.000785\delta_{A_R}
 \end{aligned}$$

By inspection it can be seen that the flap deflections

$$\delta_{F_L} = -\delta_{F_R} = -0.553\delta_{A_L} = +0.553\delta_{A_R}$$

give zero yawing moment, and:

$$+\delta_{F_L} = -\delta_{F_R} = -0.787\delta_{A_L} = +0.787\delta_{A_R}$$

give zero rolling moment.

Both of these combinations give positive sideforce. The flap deflections on the aft wing are greater than on the forward wing to produce direct sideforce with either zero yawing moment or zero rolling moment.

SUMMARY

Chord planè linear theory comparisons reported here have successes and deficiencies that are similar to monoplane correlation experience. That is, slopes are satisfactorily predicted and intercepts and control effectiveness are marginal.

SURFACE PRESSURE DATA

Pressure data from the first wind tunnel test with the forward wing at nominal zero incidence ($\alpha_F = -0.27$ degrees) have been discussed for the design condition $M = 0.90$ and lift coefficient 0.50 in the section on transonic redesign. The shock on the upper surface of the forward wing was predicted by the full potential analysis, but was not captured by the transonic small disturbance analysis. With a one degree nose down change in the incidence of the forward wing to $\alpha_F = -1.27$ degrees, the full potential prediction indicated the shock would be eliminated on the forward wing. Surface pressures measured on the forward wing during the second wind tunnel test with this one degree incidence change are compared on figure 52 with calculations. Figure 52a shows that the measured inboard shock was further aft than calculated. Figure 52b indicates that the midspan shock was weakened but not eliminated by the incidence change. Figure 52c shows reasonable agreement between calculation and measurement at the outboard station with a suggestion of trailing edge separation. The measured lower surface pressures were slightly more positive than calculated at all three spanwise stations. Oil flow photographs, figure 53, corroborated the upper surface shock positions at the inboard and midspan stations.

Surface pressures measured on the aft wing are compared on figure 54 with pressures calculated using transonic small disturbance analysis with effective twists considering downwash from the forward wing. The measured pressure data at the inboard station, figure 54a, from the second wind tunnel test are suspect for reasons which will be subsequently stated. Also shown at the inboard station are pressure data from the first wind tunnel test at the same total lift coefficient. To produce a lift coefficient of 0.5, the angle-of-attack was 6.0 degrees during the first wind tunnel test and 6.5 degrees during the second. The measured pitching moment was more negative during the second wind tunnel test so that at the same lift coefficient, the aft wing should carry more lift and the forward wing less lift. The measured pressures at the inboard station on the aft wing show substantially less lift load being carried during the second test and, for this reason, are questionable.

Measured pressure data from the second wind tunnel test are compared with TSD calculation at the midspan and outboard stations on figures 54b and 54c at an angle-of-attack of 6.5 degrees. The mid-span of the aft wing is carrying less lift than calculated, while the outboard station is carrying about the same lift as predicted. Measurement and calculation are in reasonable agreement for the more lightly loaded slightly supercritical aft wing. Both pressure measurements and oil flow observations indicated an absence of shocks on the aft wing at the design condition.

Complete sets of tabulated and plotted pressure data are available in reference 8.

Section VII

CONCLUSIONS

1. The joined wing supercritical design achieved 88 percent of the fully turbulent theoretical upper bound L/D of 12.97 which neglects component viscous interference and separation.
2. Weak drag divergence was achieved at the design condition. A swept shock exists on the forward wing upper surface as a result of not achieving the anticipated twist change due to model elasticity. The impact of this effect is estimated to be 0.5 in L/D and was deduced from the measurements between $M = 0.85$ and 0.90 . Elimination of this decrement results in achievement of 92 percent of the ultimate lift/drag ratio.
3. Theoretical turbulent upper bound aerodynamic efficiency for the reference monoplane and joined wing are essentially the same for the same mean sweep. The vortex drag advantage of the nonplanar joined wing of the same span is offset by viscous penalties resulting from higher surface area for the same plan area and lower chord Reynolds number.
4. Joined wing longitudinal trim is impacted by elastic effects on C_{M_0} resulting from differential twist between the front and aft surfaces. Out of balance pitching moment will be typically reduced at high dynamic pressure for unstable balances.
5. Six component force measurements for the joined wing are well behaved and near linear over an angle-of-attack range of $-4 < \alpha < 10$ degrees. Stable stall is naturally achieved for the arrangement. Weak changes in longitudinal and lateral-directional stability and control with pitch angle exist.
6. Chord plane linear theory comparisons have successes and deficiencies that are similar to monoplane correlation experience. That is, slopes are satisfactorily predicted and intercepts and control surface effectiveness are marginal.
7. Approximate and simplified theoretical structural analyses underestimated the stiffness of the joined wing wind tunnel model.

REFERENCES

1. Wolkovitch, Julian, "Joined-Wing Research Feasibility Study," AIAA Paper 84-2471, November 1984
2. Bonner, E., Clever, W., and Dunn, K., "Aerodynamic Preliminary Analysis System," NASA CR-145284, April 1978
3. Clever, W. C., "Wing Twist and Camber Optimization Program," Rockwell Document TFD-78-532, July 1978
4. Gingrich, P. and Bonner, E., "Prediction of Infinite Yawed Viscous Characteristics at Subsonic Speeds," Rockwell Document NA-74-758
5. Mason, W. H., et. al., "An Automated Procedure for Computing the Three-Dimensional Transonic Flow Over Wing-Body Combinations, Including Viscous Effects," AFFDL TR-77-122, February 1977
6. Shankar, V. and Malmuth, N. D., "Computational Transonic Design Procedure for Three Dimensional Wings and Wing-Body Combinations," AIAA Paper 79-0344, January 1979
7. Nash, J. and Scruggs, R., "An Implicit Method for the Calculation of Three Dimensional Boundary Layers on Finite, Thick Wings," AFFDL TR-77-122, February 1977
8. Clyde, J. A., "Results of the 0.067-Scale Joined Wing Aero Force and Pressure Model Tests Performed in the Rockwell International Trisonic Wind Tunnel (TWT 483 and TWT 487)," TFD-84-1590, June 1984
9. Caughey, D. A., and Jameson, A., "Recent Progress in Finite Volume Calculations for Wing-Fuselage Combinations," AIAA Paper 79-1513, July 1979
10. Siegel, S., "Flutter Analysis of a Joined Wing Wind Tunnel Force Model," Rockwell Document NA-83-715, August 1983



TABLE I AERODYNAMIC CHARACTERISTICS

AERODYNAMIC COEFFICIENT	REFERENCE MONOPLANE				JOINED WING			
	MACH NUMBER							
	0.20	0.90	1.50	0.20	0.90	1.50		
$C_{L\alpha}$ DEG-1	0.064	0.078	0.073	0.059	0.069	0.067		
dC_m/dC_L	0.10	0.090	-0.18	0.10	0.16	-0.13		
C_{mq} RAD/SEC	-3.017	-3.987	-4.205	-10.716	-13.423	-14.445		
C_{Tr} RAD/SEC	-0.261	-0.318	-0.287	-0.343	-0.381	-0.422		
C_{Tp} RAD/SEC	-0.289	-0.328	-0.369	-0.300	-0.333	-0.359		
$C_{n\beta}$ DEG-1	0.0024	0.0033	0.0033	0.0025	0.0029	0.0038		
$C_{L\beta}$ DEG-1	-0.0006	-0.0007	-0.0009	-0.0004	-0.0004	-0.0003		
C_{Dw}	0	0	0.01991	0	0	0.02211		
C_{Df}^*	0.01254	0.00971	0.00879	0.01407	0.01086	0.00984		

*NOMINAL TRISONIC TEST CONDITIONS



TABLE II OPTIMIZATION RESULTS

DESIGN CONDITIONS $M = 0.90$ $C_L = 0.50$

OPTIMIZATIONS	CASE NUMBER	$M_g < 1.30$	dC_m/dC_L	MODERATE TWIST	EFFICIENCY	COMMENT
OPTIMUM C.G.	1	✓	UNACCEPTABLE	✓	✓	SEE FIGS. 5 & 6
$dC_m/dC_L = 0.15$ (LOWSPEED)	2	MARGINAL	✓	MARGINAL	✓	SEE FIG. 7
$dC_m/dC_L = 0.10$ (LOWSPEED)	3	UNACCEPTABLE	✓	MARGINAL	✓	SEE FIG. 7
LOADING SPLIT 10% 45% 45% BODY, FRONT, AFT	4	UNACCEPTABLE	✓	UNACCEPTABLE	UNACCEPTABLE	SEE FIGS. 5 & 7
WING AREA SPLIT 60% FRONT 40% AFT	5	✓	✓	✓	MARGINAL	SEE FIG. 7
LOWER DESIGN C_L	6	✓	✓	✓	✓	SEE FIGS. 5, 6, 7

✓ = ACCEPTABLE

TABLE III JOINED WING AIRFOIL
DESIGN CONDITIONS

M_∞	=	0.90
C_L	=	0.50
$\frac{dC_m}{dC_L}$	=	0.20
$\frac{t}{c}$	=	0.05

FORWARD PANEL

$C_{L\perp}$	=	0.60
$\Lambda c/2$	=	41°
$M_{L\perp}$	=	0.68
$C_{L\perp}$	=	1.5
$\frac{t}{c} _{\perp}$	=	0.66

AFT PANEL

$C_{L\perp}$	=	0.33
$\Lambda c/2$	=	-48°
$M_{L\perp}$	=	0.602
$C_{L\perp}$	=	0.74
$\frac{t}{c} _{\perp}$	=	0.747

Table IV
LONGITUDINAL CHARACTERISTICS

$$\alpha = 0^\circ, \beta = 0^\circ$$

i_{w_F}	M	$C_{L\alpha}$		C_{L_0}		dC_M/dC_L		C_{M_0}	
		Linear Theory	Meas.	Linear* Theory	Meas.	Linear Theory	Meas.	Linear* Theory	Meas.
-0.27	0.90	0.0687	0.071	0.1200	0.0736	0.200	0.243	+0.0030	-0.0041
-1.27	0.90	0.0687	0.075	0.0991	0.0445	0.200	0.236	-0.0635	-0.0569
-1.27	0.40	0.0587	0.061	0.1080	0.0563	0.140	0.164	-0.0510	-0.0439

*As-built camber and twist

Table V
LATERAL DIRECTIONAL STABILITY

$$\alpha = 0^\circ, -5^\circ < \beta < +5^\circ$$

i_{w_F}	M	$C_{Y\beta}$		$C_{n\beta}$		$C_{l\beta}$	
		Linear Theory	Meas.	Linear Theory	Meas.	Linear Theory	Meas.
-0.27	0.90	0.01195	0.012	0.0032	0.0028	-0.00053	-0.00092
-1.27	0.90	0.01195	0.013	0.0032	0.0028	-0.00053	-0.00055
-1.27	0.40	0.0117	0.0116	0.0028	0.0030	-0.00053	-0.00052

Table VI
LIFTING FLAP EFFECTIVENESS

$M = 0.90, \alpha = 0$ degrees

Flap Combination	Flap Deflection* (degrees)	i_{w_F}	Linear Theory	C_{L_0} Measurement
4+5	+10	-1.27	0.00760	0.0047
4+5	+10	-0.27	0.00760	0.0058
4+5	-10	-0.27	0.00760	0.0044
1+2+4+5	+10	-0.27	0.01721	0.0144
1+2	+10	-0.27	0.00961	0.0087

Table VII
PITCHING MOMENT EFFECTIVENESS

$M = 0.90, \alpha = 0$ degrees

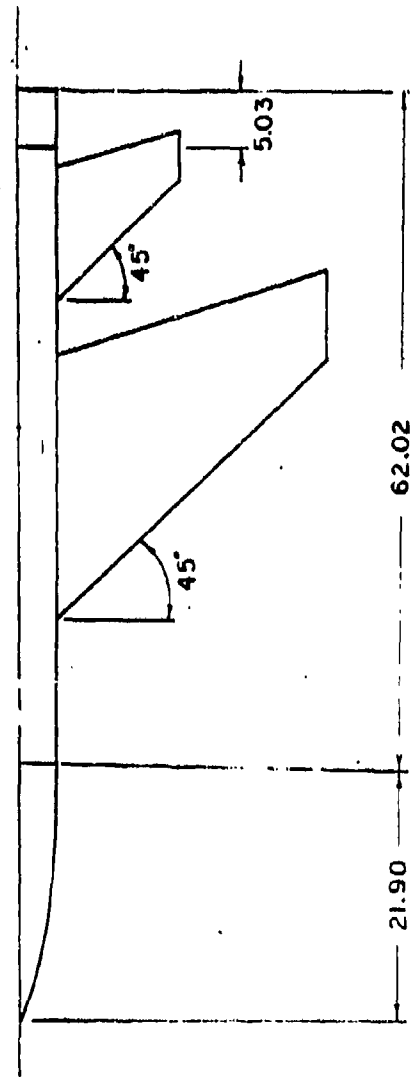
Flap Combination	Flap Deflection* (degrees)	i_{w_F}	Linear Theory	C_{M_0} Measurement
4+5	+10	-1.27	0.01264	0.00780
4+5	+10	-0.27	0.01264	0.00801
4+5	-10	-0.27	0.01264	0.01070
1+2+4+5	+10	-0.27	0.00565	0.00220
1+2	+10	-0.27	0.01829	0.01290

*Perpendicular to hinge line

Table VIII
 ROLLING MOMENT EFFECTIVENESS
 $M = 0.90, \alpha = 0$ degrees

Flap* Combination	Flap Deflection** (degrees)	i_{w_F}	Linear Theory	$C_{l\delta}$ Measurement
3R	+10	-0.27	-0.000310	-0.000127
6R	+10	-0.27	-0.000470	-0.000218
3R + 6R	+10	-0.27	-0.000780	-0.000345
3L + 6L	+10	-1.27	+0.001560	+0.000728
3R + 6R	-10			
2L + 6L	+10	-1.27	+0.00181	+0.001112
2R + 6R	-10			

*R - Right side, L - Left side
 ** Perpendicular to hinge line



REFERENCE MONOPLANE

TRAPEZOIDAL WING

AREA	911.25 IN. ²
ASPECT RATIO	3.20
L.E. SWEEP	45.00 DEG.
TAPER RATIO	0.30
DIHEDRAL	0.00 DEG.
ROOT CHORD	25.96 IN.
TIP CHORD	7.79 IN.
MEAN CHORD	18.51 IN.
SPAN	54.00 IN.

EXPOSED HORIZONTAL TAIL (Projected)

AREA	182.25 IN. ²
ASPECT RATIO	2.50
L.E. SWEEP	45.00 DEG.
TAPER RATIO	0.42
DIHEDRAL	-10.00 DEG.
ROOT CHORD	12.03 IN.
TIP CHORD	5.05 IN.
MEAN CHORD	9.01 IN.
SPAN	10.67 IN.

VERTICAL TAIL

AREA	102.25 IN. ²
ASPECT RATIO	1.25
L.E. SWEEP	51.00 DEG.
TAPER RATIO	0.77
DIHEDRAL	90.00 DEG.
ROOT CHORD	19.02 IN.
TIP CHORD	5.13 IN.
MEAN CHORD	13.41 IN.
SPAN	15.09 IN.

SCALE: 1:10

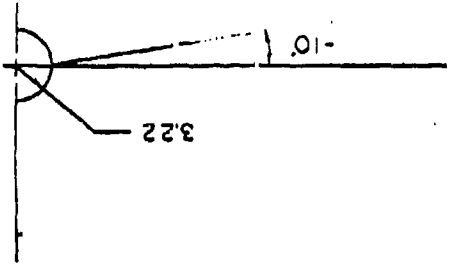
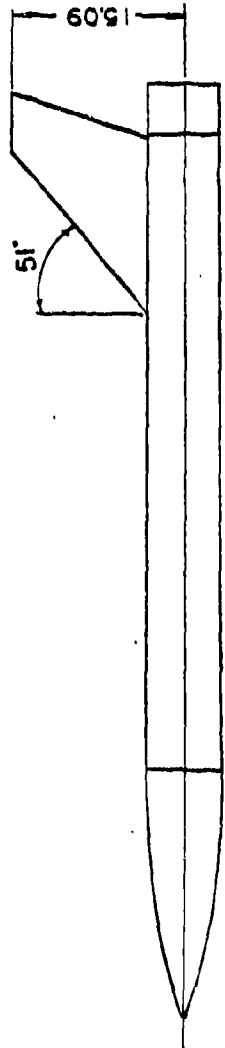
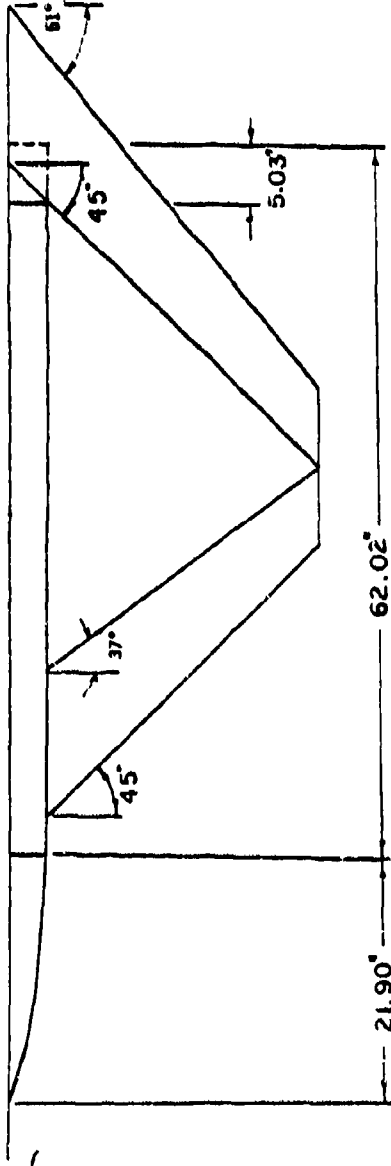


Figure 1. Reference Monoplane Arrangement



JOINED WING

FORWARD WING (Projected)

AREA	546.75 IN. ²
ASPECT RATIO	5.33
L.E. SWEEP	45.00 DEG.*
TAPER RATIO	0.50
DIHEDRAL	18.00 DEG.
ROOT CHORD	13.50 IN.
TIP CHORD	6.75 IN.
MEAN CHORD	10.50 IN.
SPAN	54.00 IN.

AFT WING (Projected)

AREA	546.75 IN. ²
ASPECT RATIO	5.33
L.E. SWEEP	-45.00 DEG.*
TAPER RATIO	0.50
DIHEDRAL	-20.00 DEG.
ROOT CHORD	13.50 IN.
TIP CHORD	6.75 IN.
MEAN CHORD	10.50 IN.
SPAN	54.00 IN.

VERTICAL WING

AREA	189.27 IN. ²
ASPECT RATIO	1.04
L.E. SWEEP	53.07 DEG.
TAPER RATIO	1.00
DIHEDRAL	90.00 DEG.
ROOT CHORD	13.50 IN.
TIP CHORD	13.50 IN.
MEAN CHORD	13.50 IN.
SPAN	14.02 IN.

SCALE: 1:10

*In Wing Plane

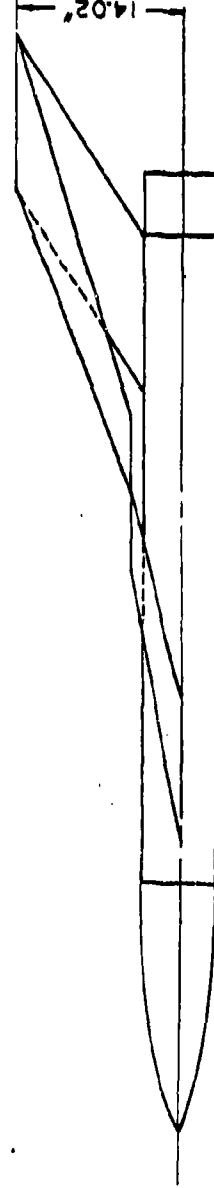
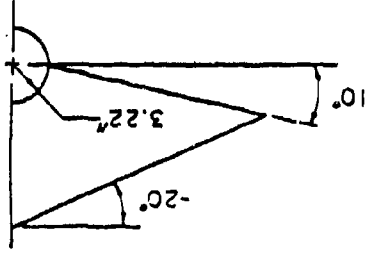
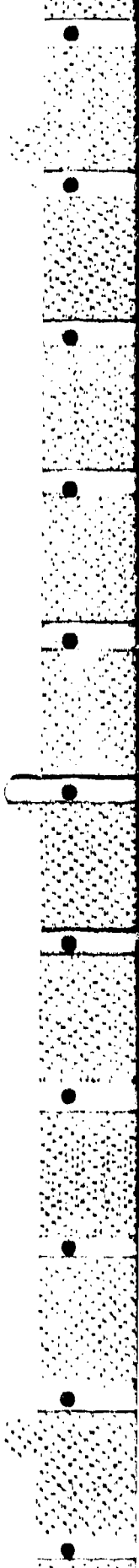
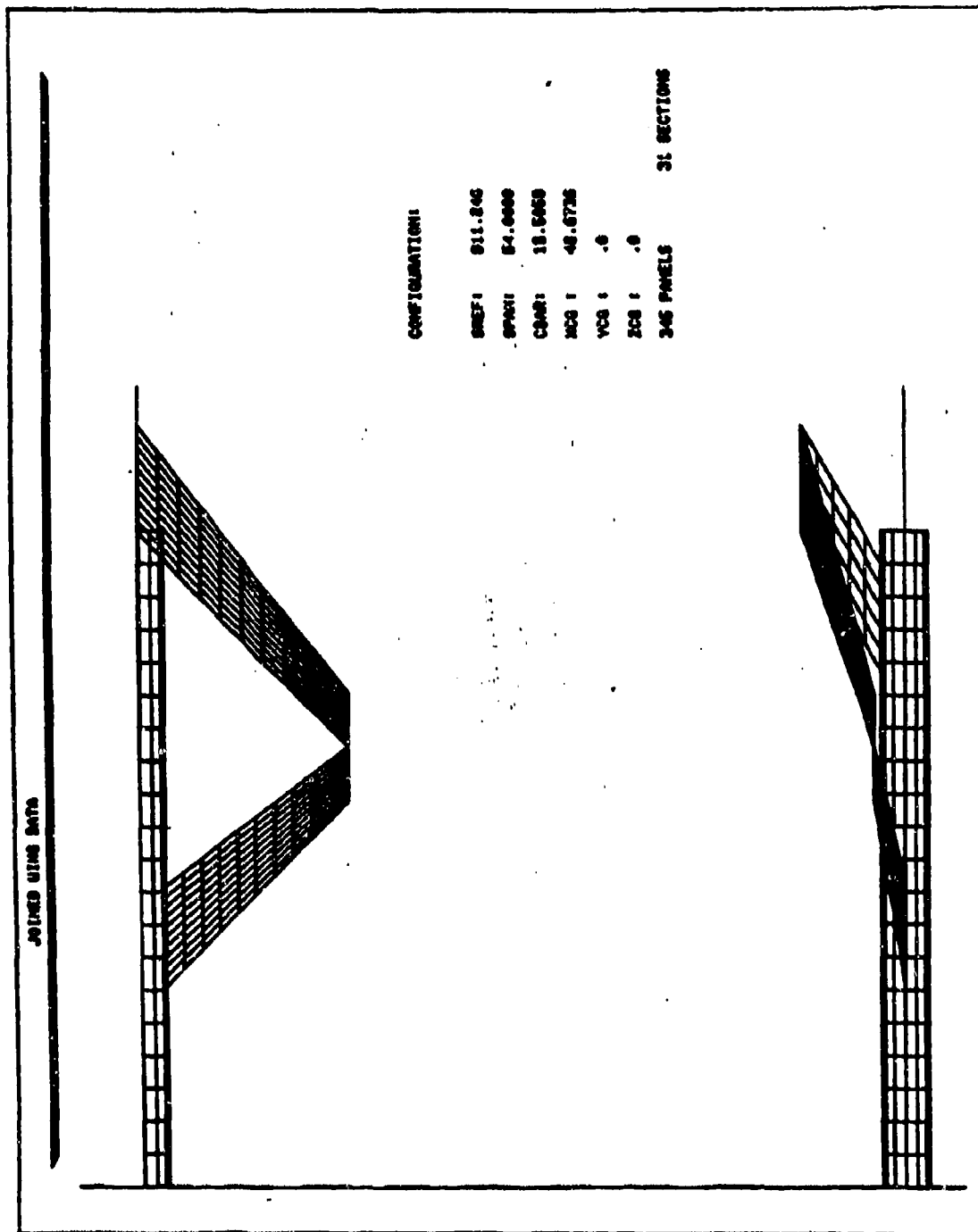


Figure 2. Joined Wing Arrangement



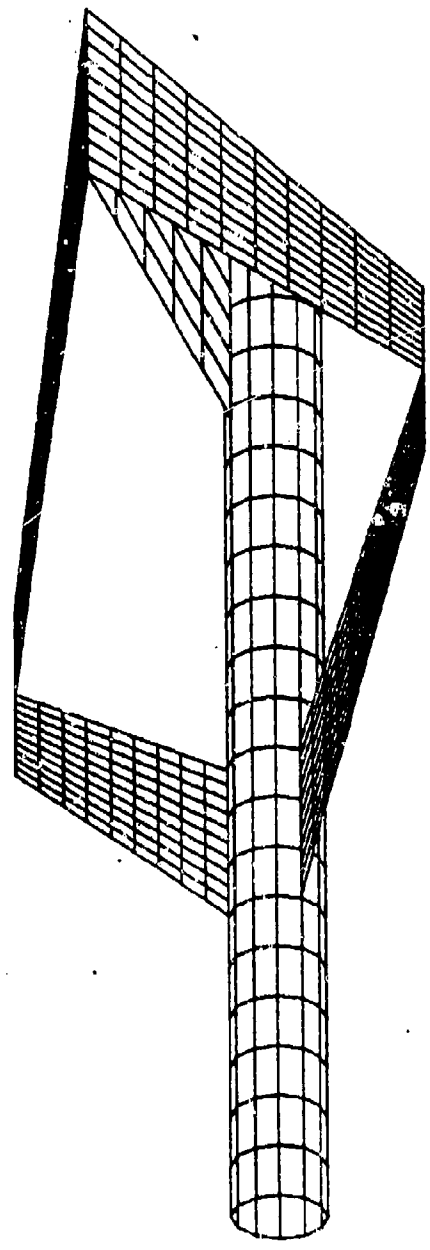


a) Plan View

Figure 3. Joined Wing Linear Finite Analysis Model

DISPLAY ANGLES YAW , PITCH , ROLL
 -120.00 0.0 30.00

PANELS 1 THRU 345



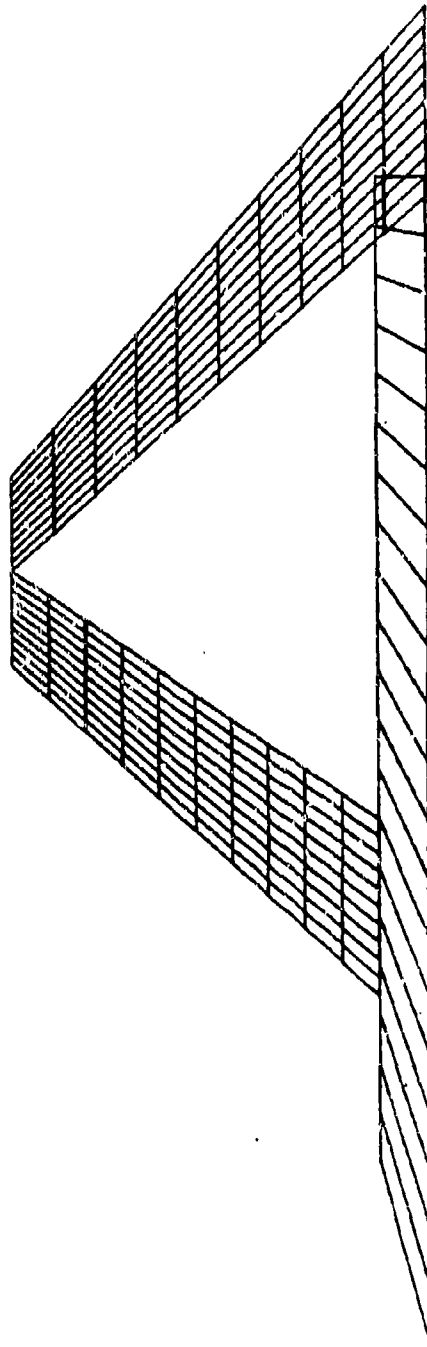
b) Orthographic View

FIGURE 3. COMPLETED

PANELS 1 THRU 228

INPUT DISPLAY ANGLES (YAW, PITCH, ROLL):

7
-08 5 99



a.) Plan View

Figure 4. Joined Wing Linear Vortex Drag Optimization model

PANELS 1 THRU 228

INPUT DISPLAY ANGLES (YAW, PITCH, ROLL):

-00 0 0



b) Side View

FIGURE 4. COMPLETED

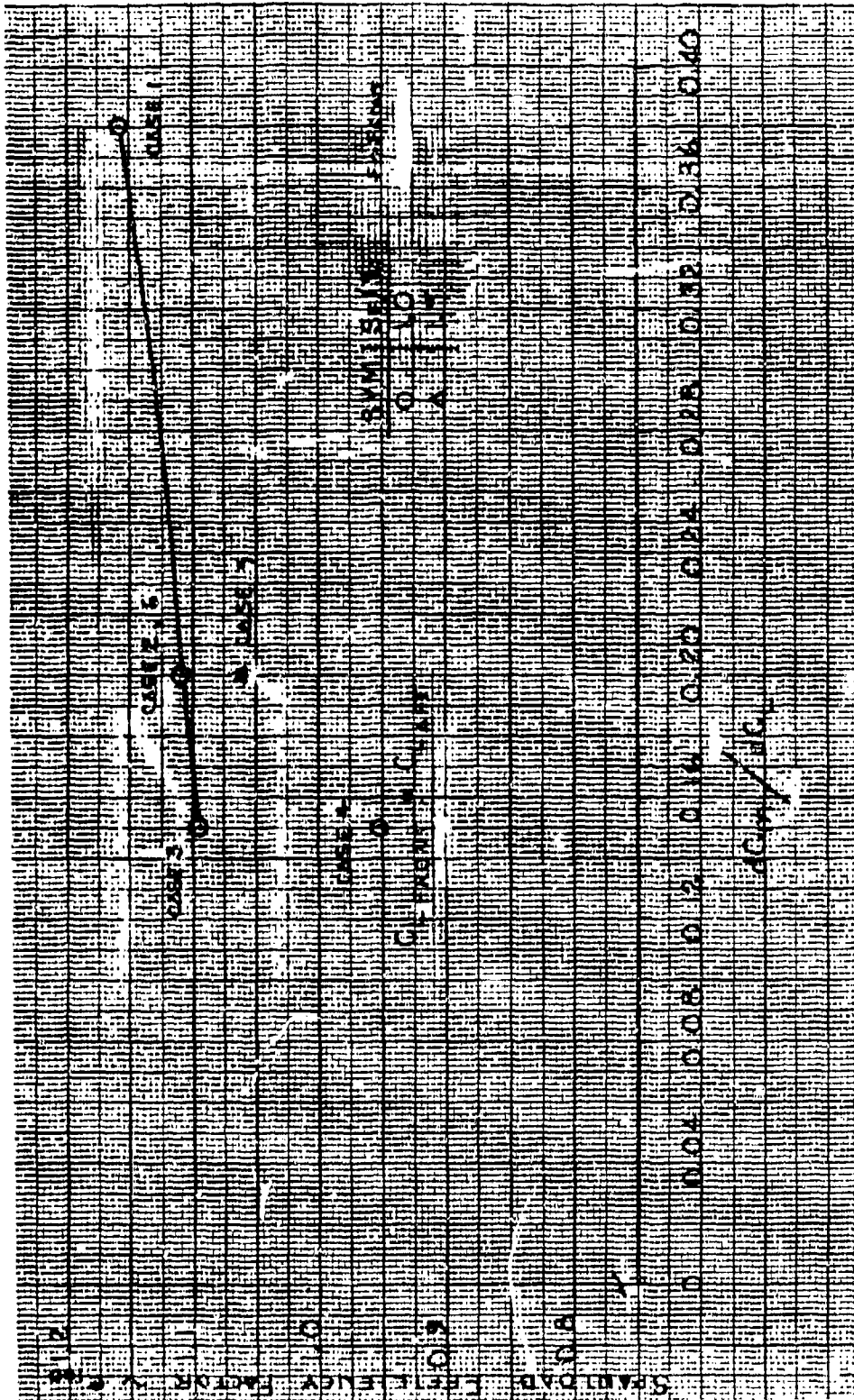


Figure 5. Effect of Longitudinal Stability on Joined Wing Trimmed Span Load Efficiency at $M = 0.90$

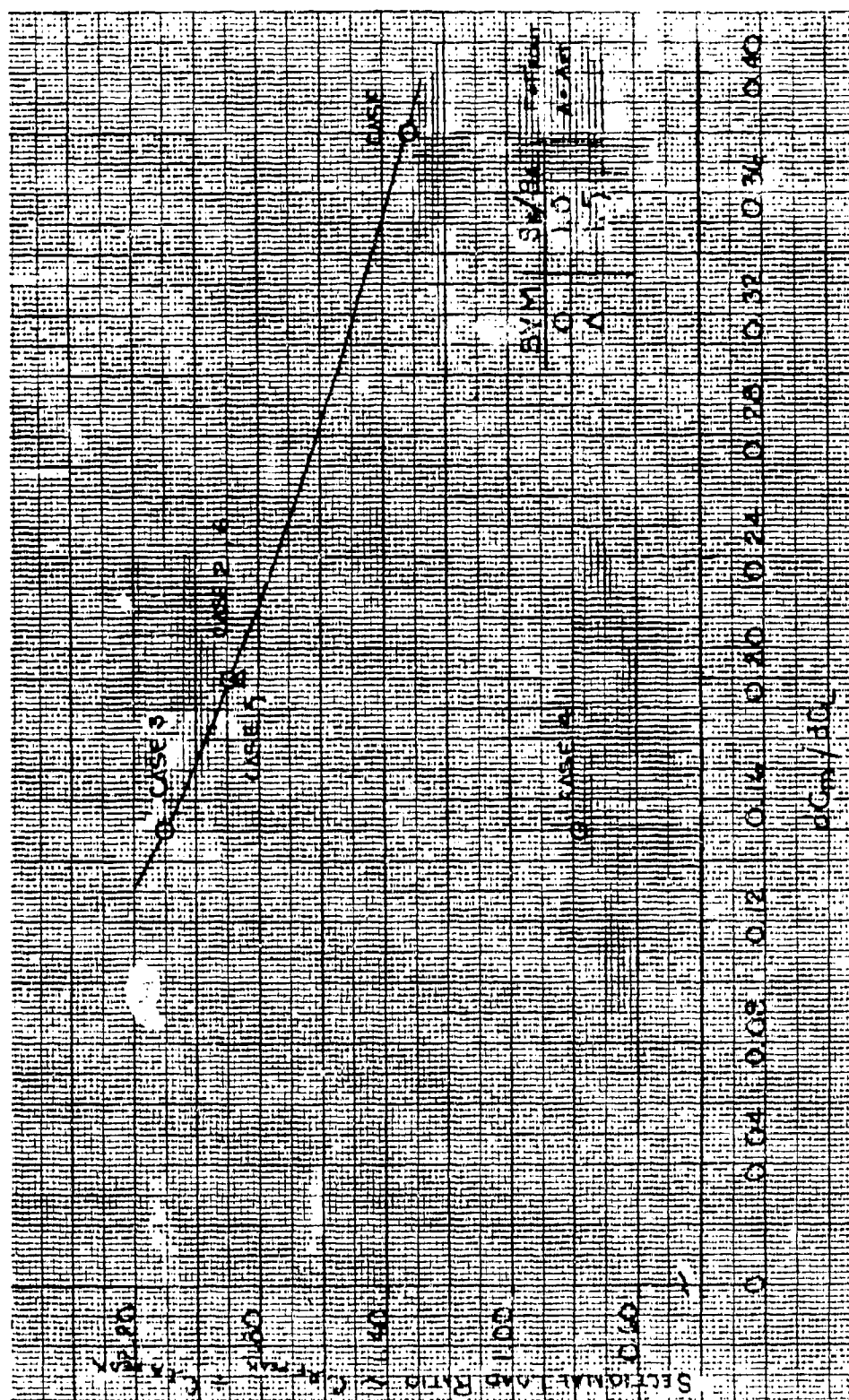


Figure 6. Effect of Longitudinal Stability on Joined Wing Sectional Load Ratio at M = 0.90

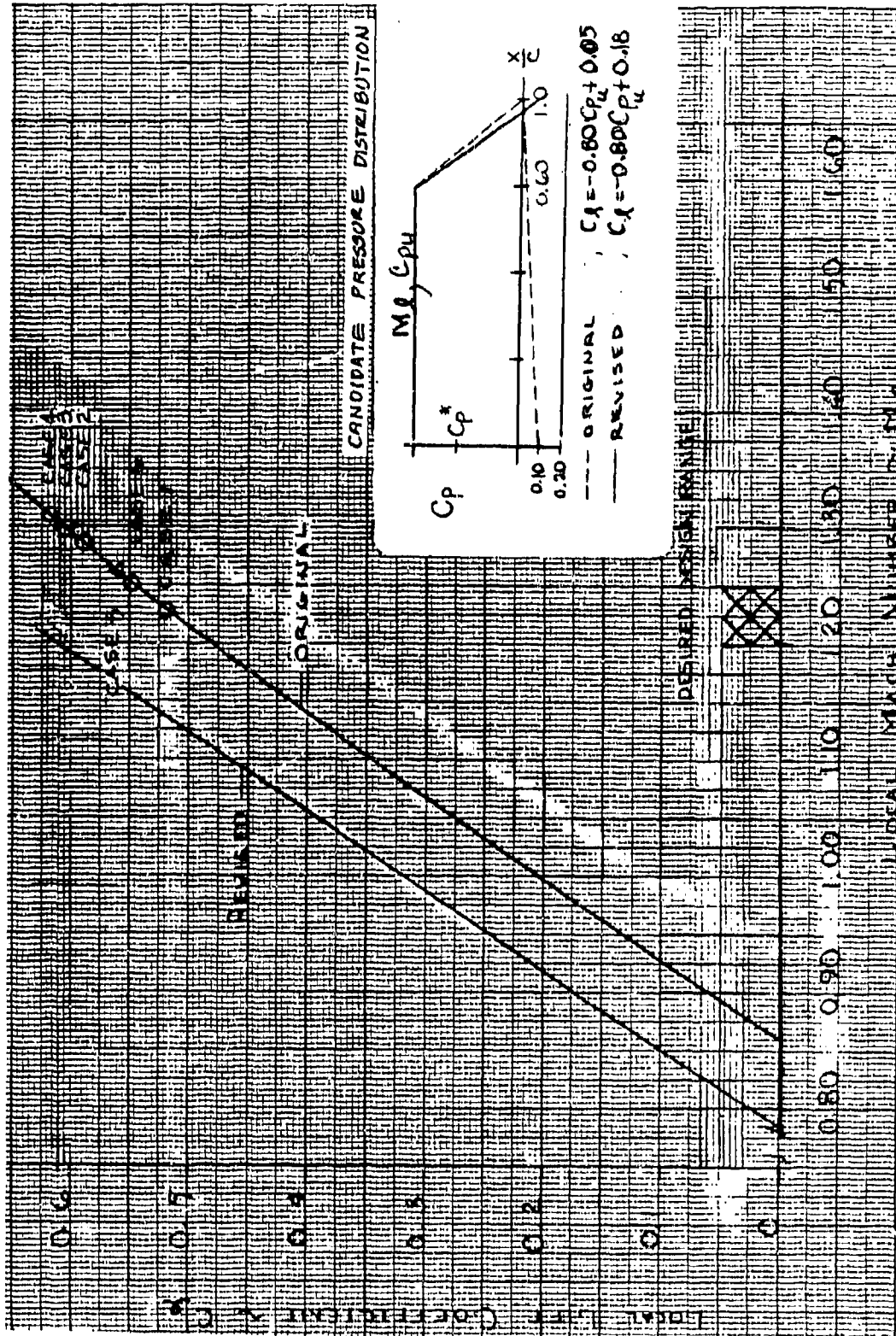
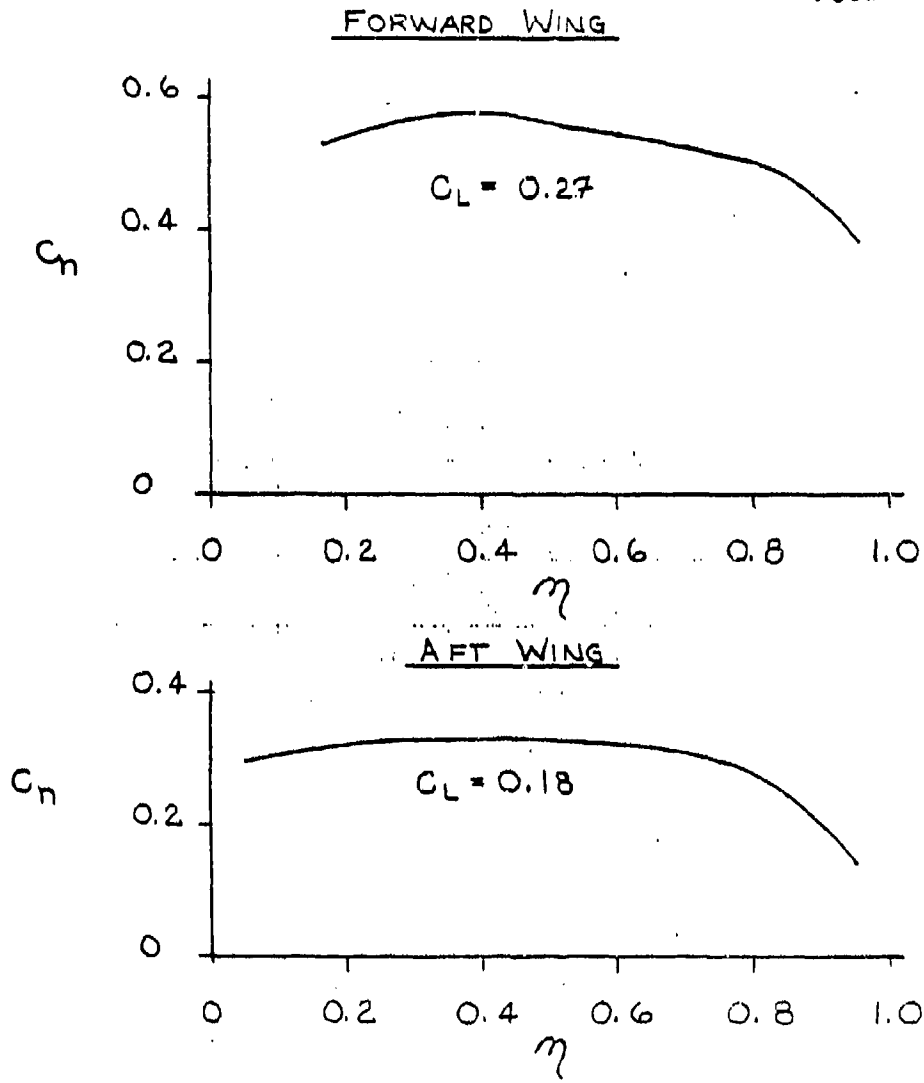


Figure 7. Effect of Forward Wing Section Lift Coefficient on Upper Surface Local Mach Number for a Candidate Supercritical Design Pressure Distribution at $M = 0.90$

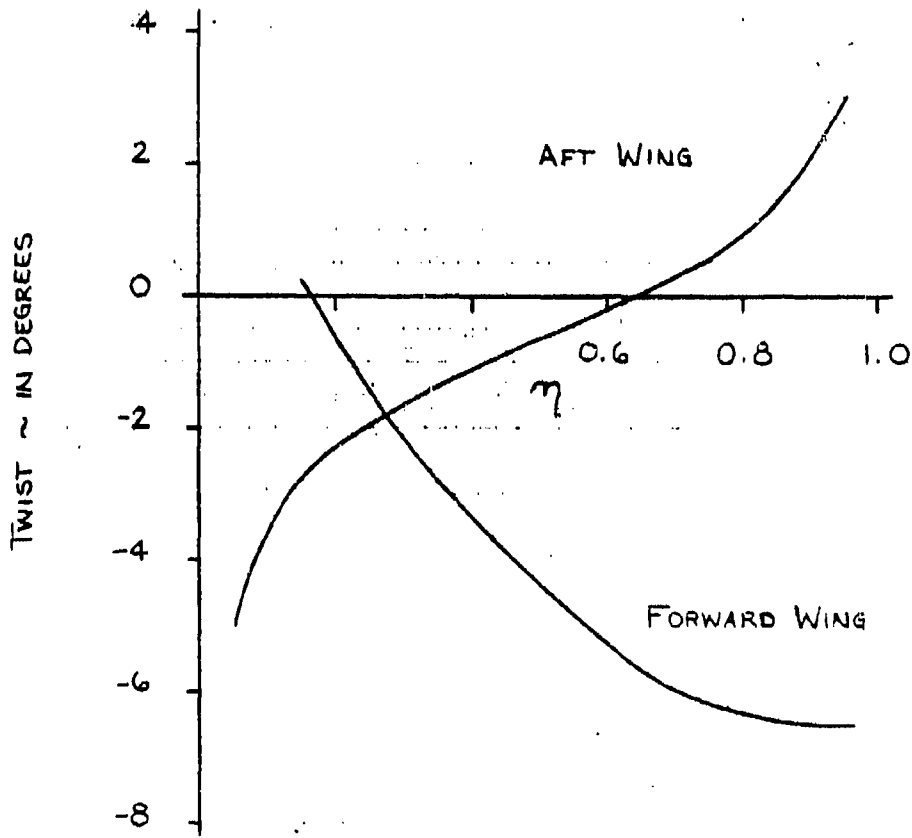
FORM 1

$e_{100} = 1.11$
 $\Delta C_{L_{FUSE}} = 0.05$



a) Span Loading

Figure 8. Candidate Linear Optimum at $M = 0.90$, $C_L = 0.50$



b) Twist

FIGURE 8. CONTINUED

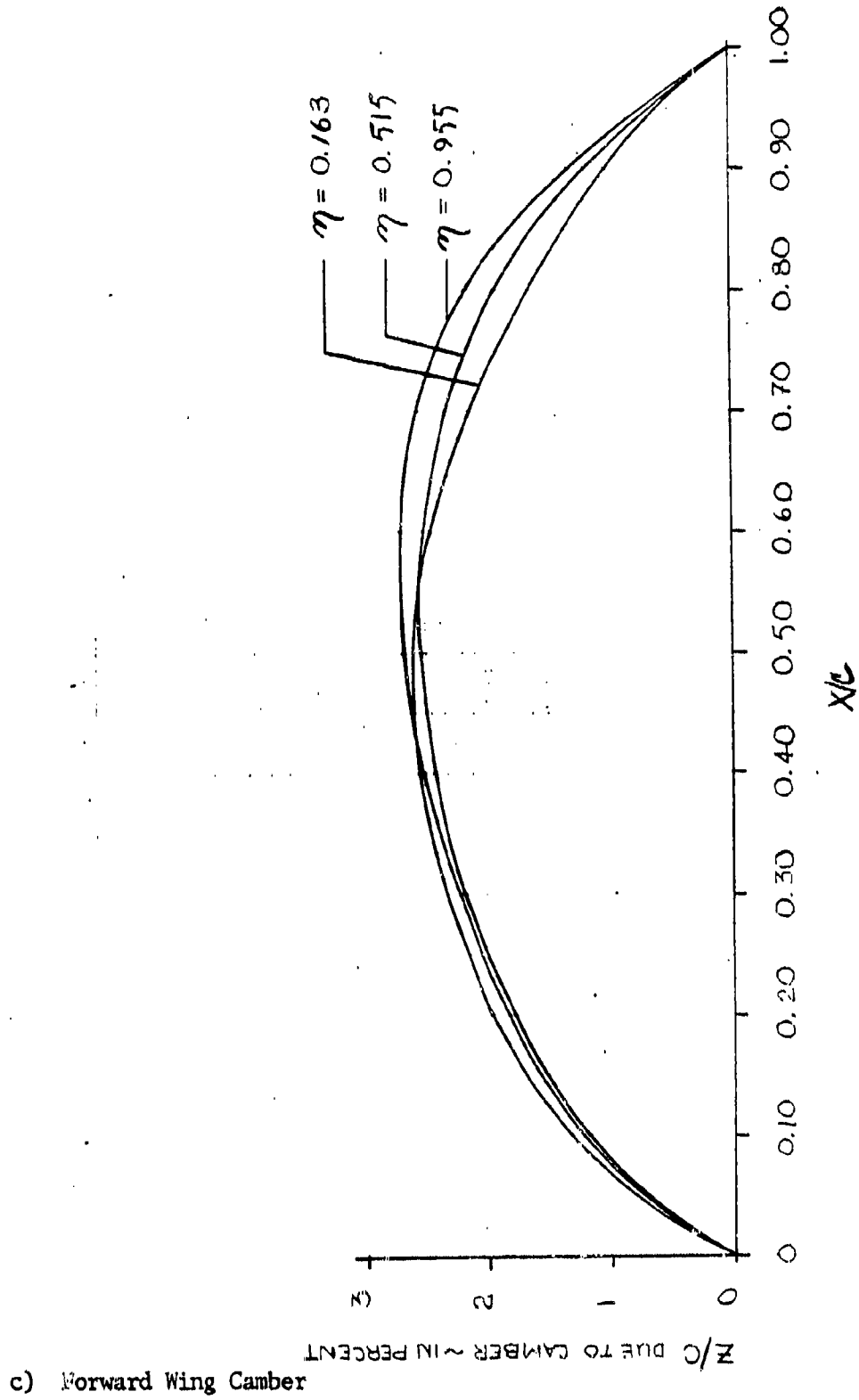
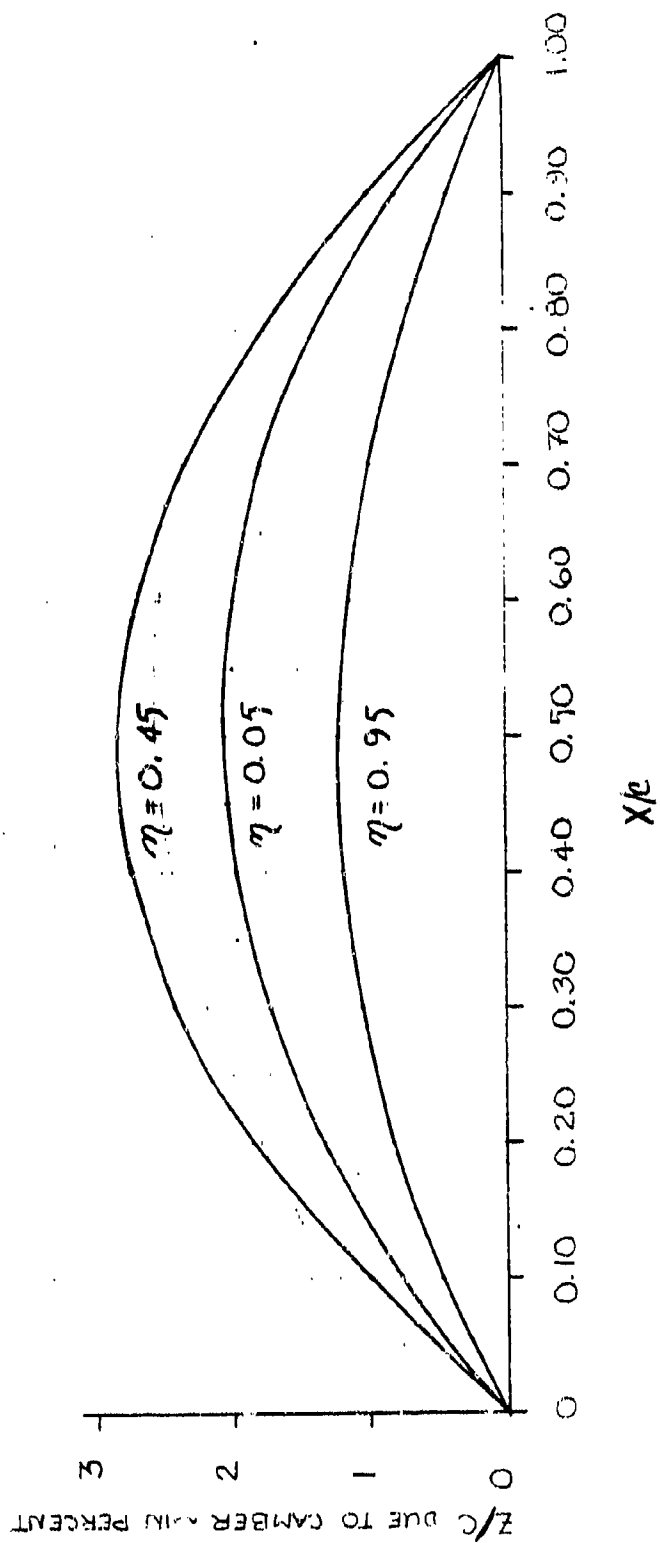


FIGURE 8. CONTINUED

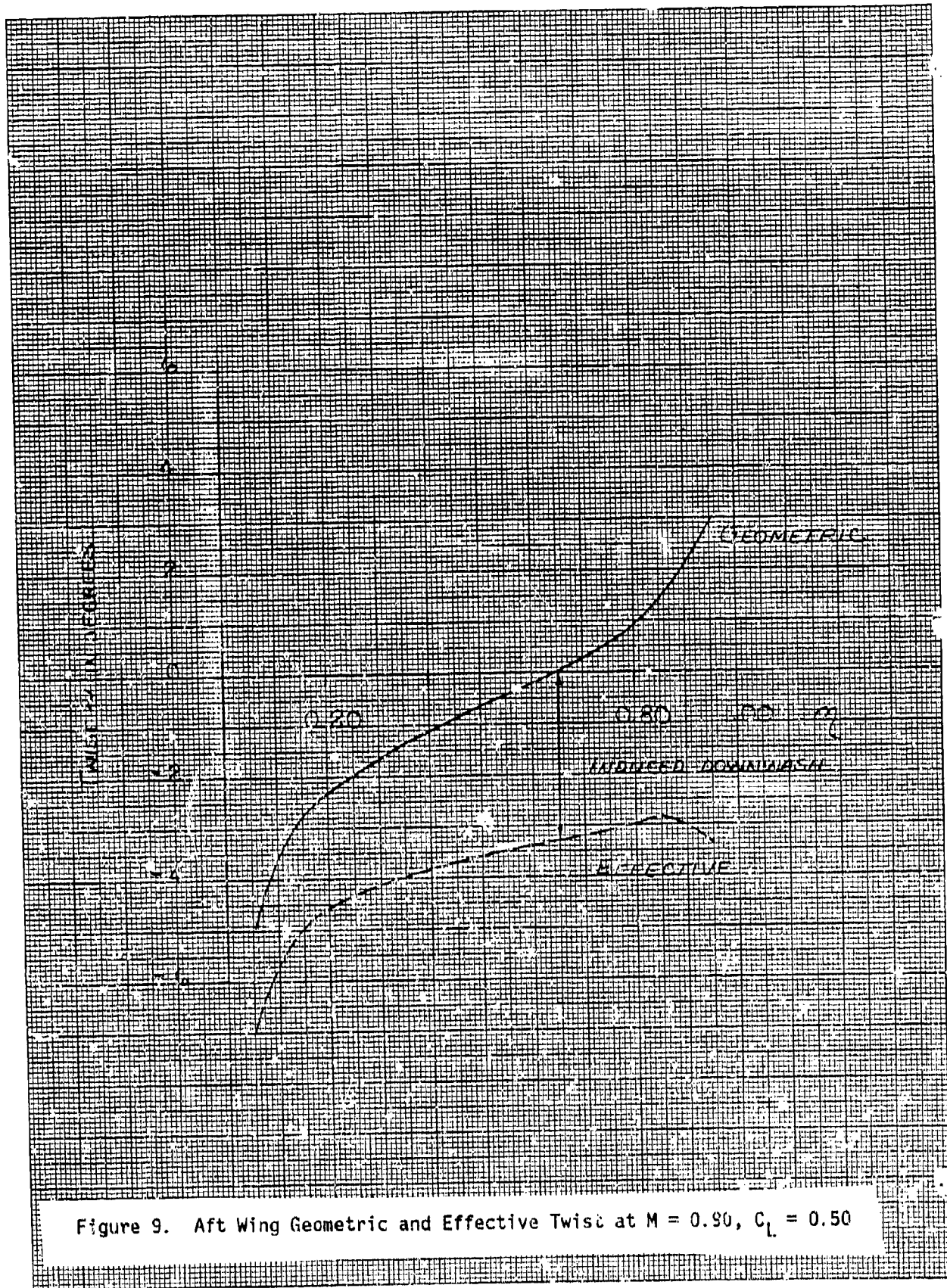


d) Aft Wing Camber

FIGURE 8. COMPLETED

46 1513

K&E 10 X 10 TO THE CENTIMETER 18 X 25 CM.
KROFFEL & ESSER CO. MILWAUKEE WIS.



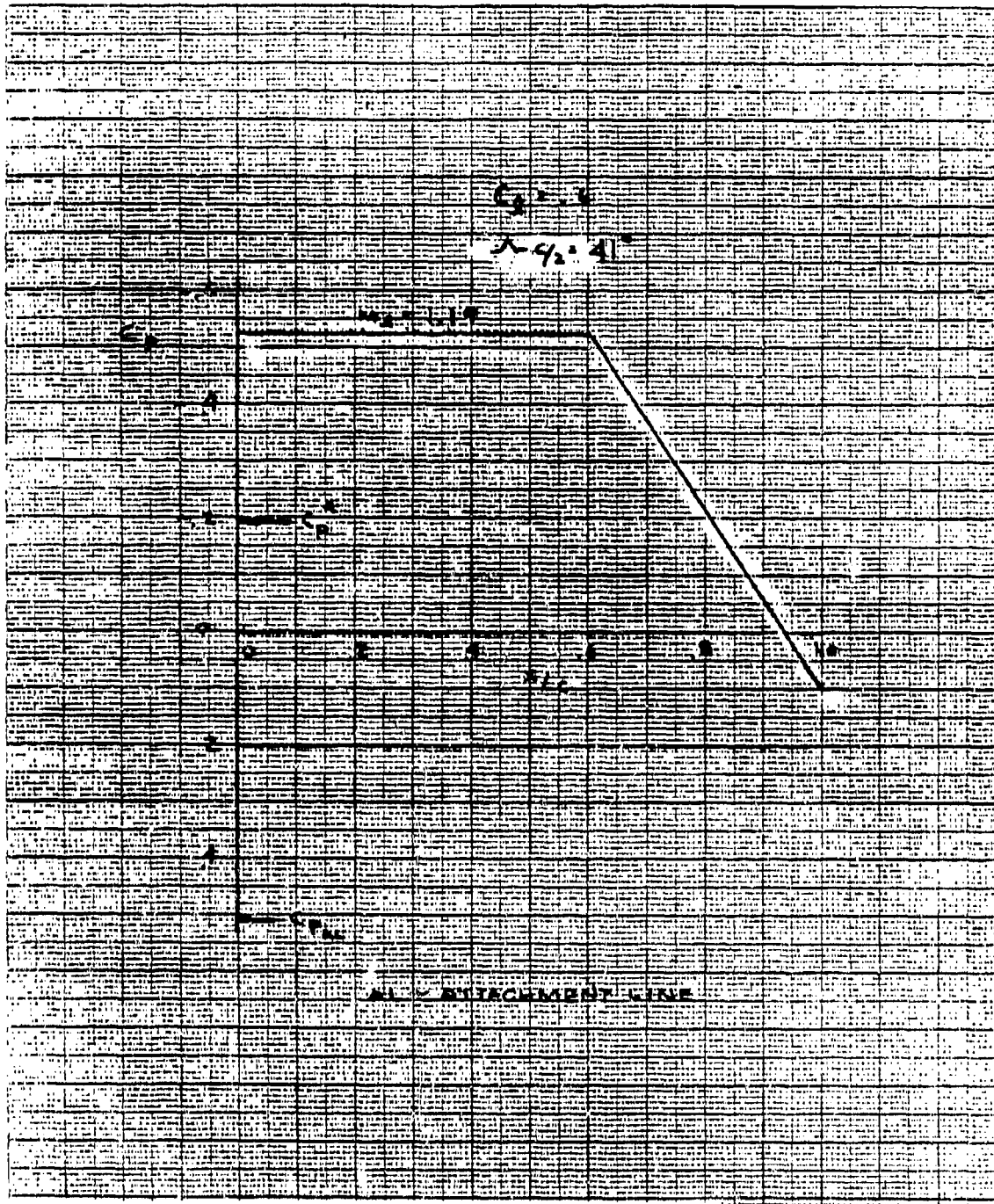


Figure 10. Forward Joined Wing Design Pressure Distribution at $M = 0.90$

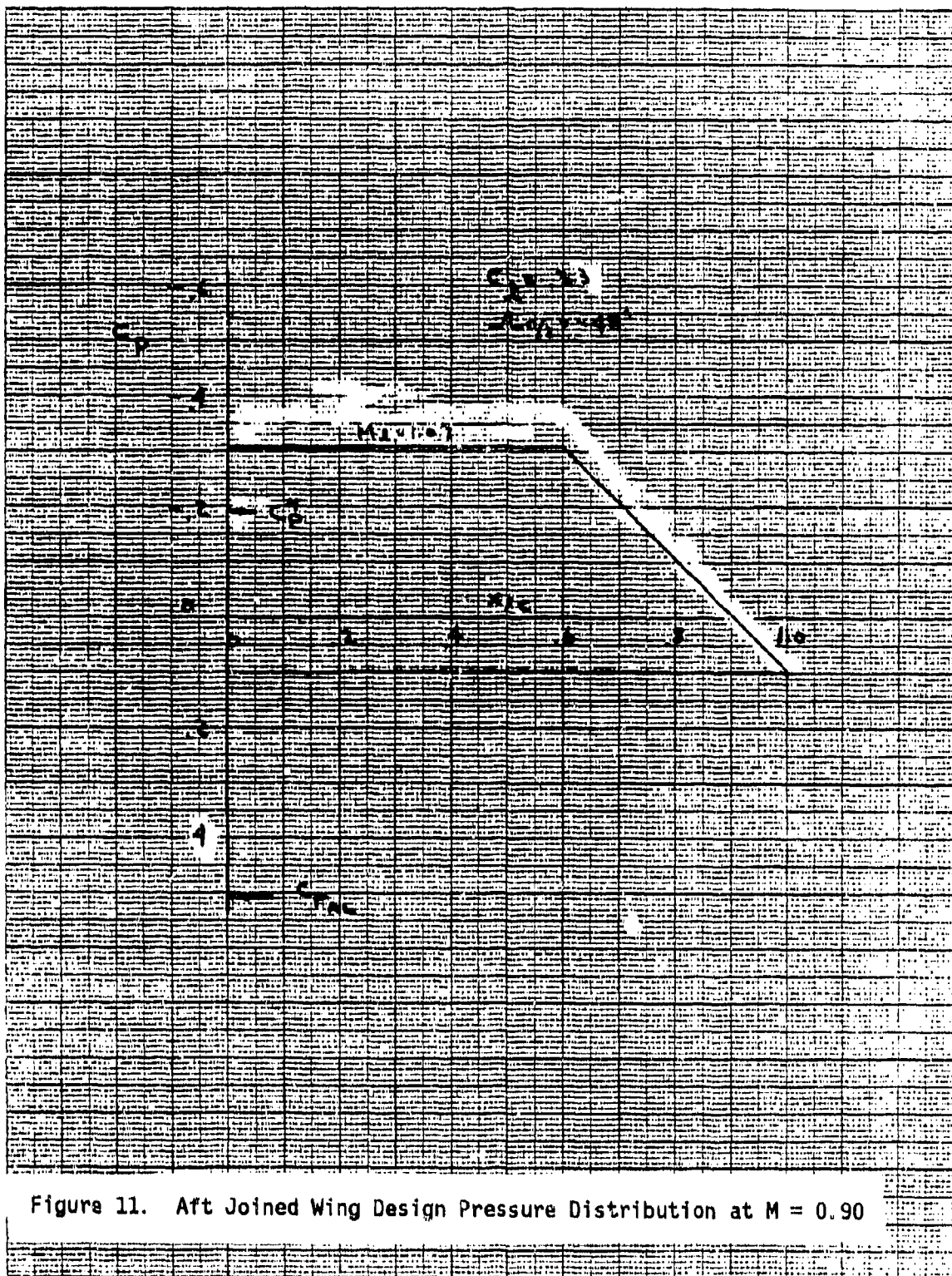


Figure 11. Aft Joined Wing Design Pressure Distribution at $M = 0.90$

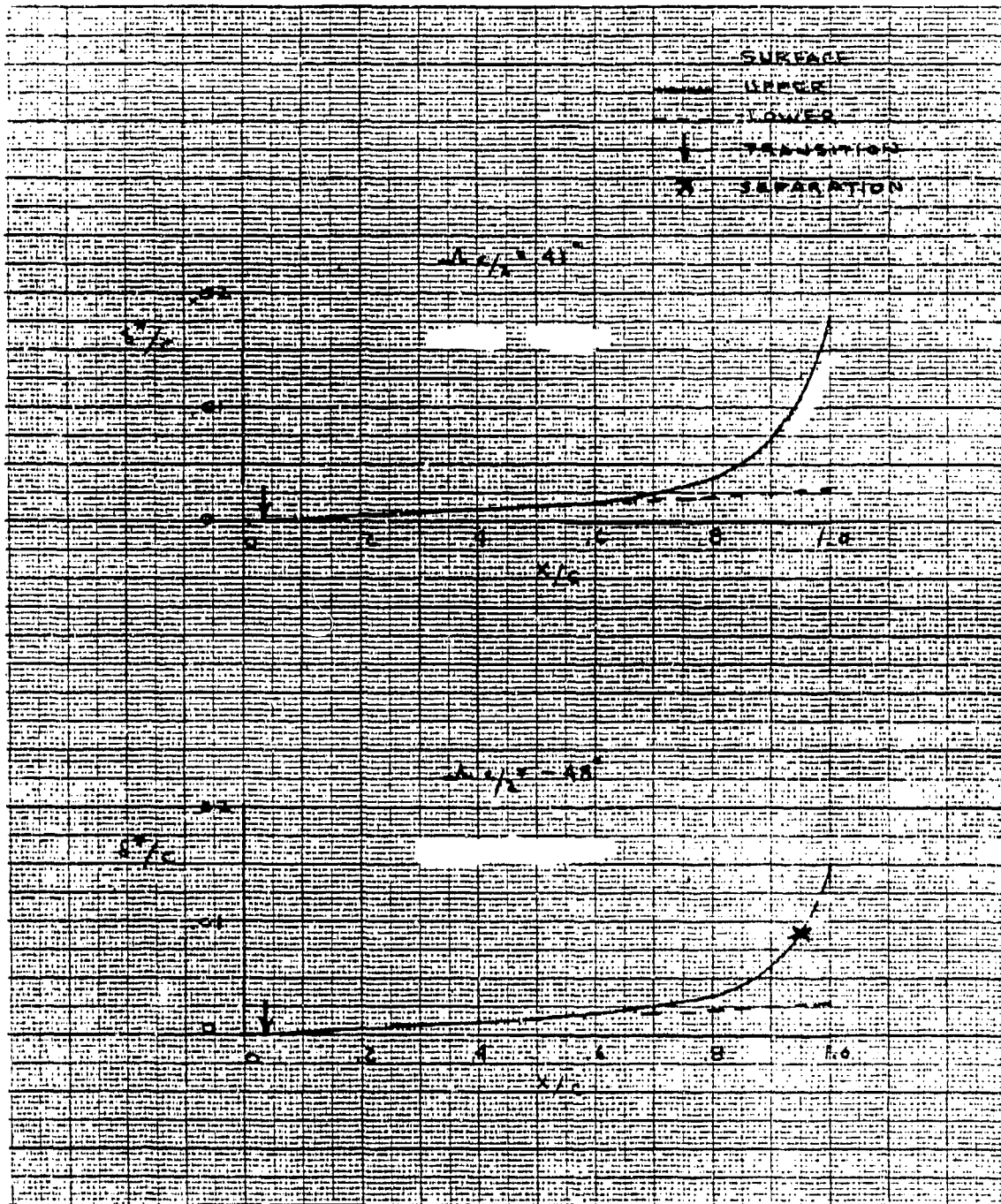


Figure 12. Yawed Wing Boundary Layer Analysis of Design Pressure Distribution

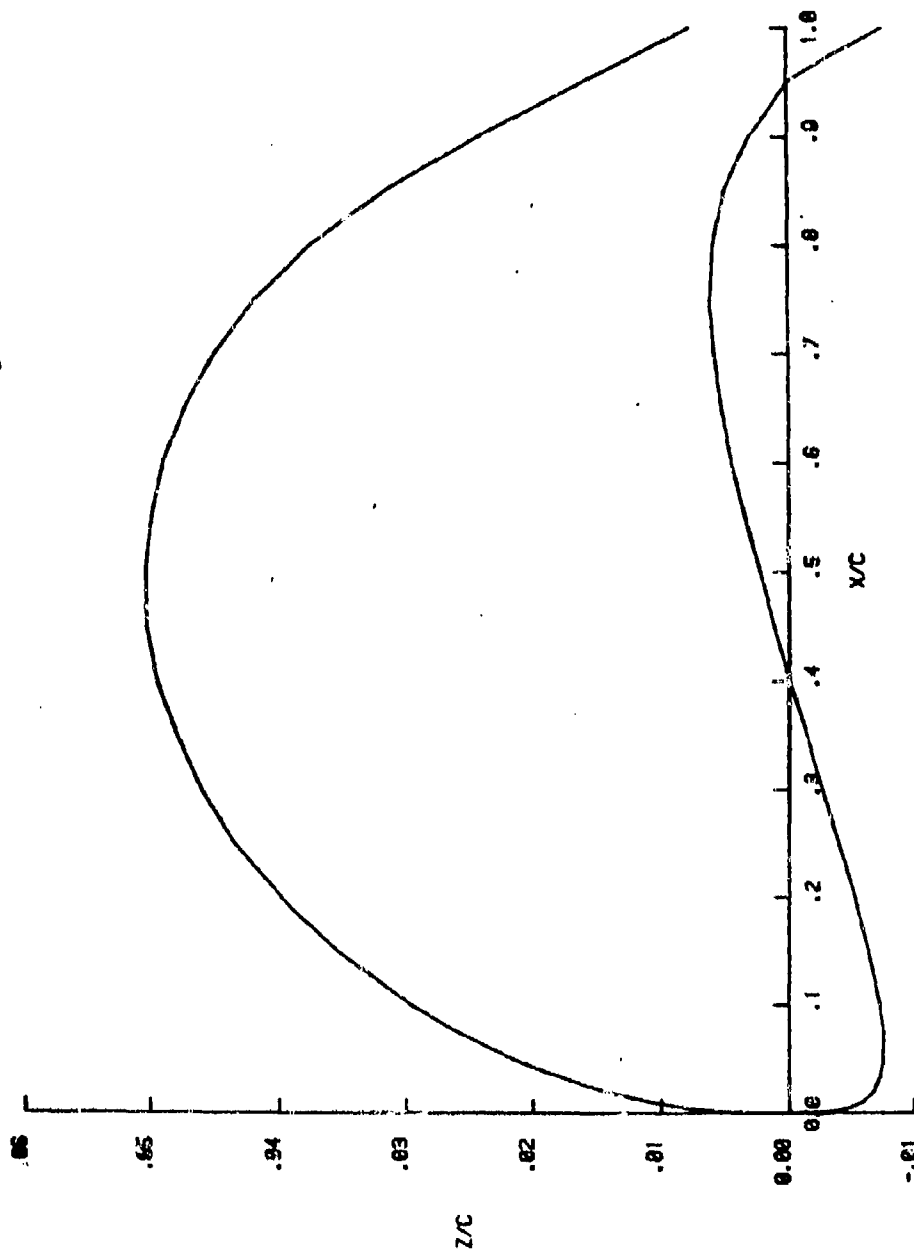


Figure 13. Forward Joined Wing Candidate Streamwise Airfoil

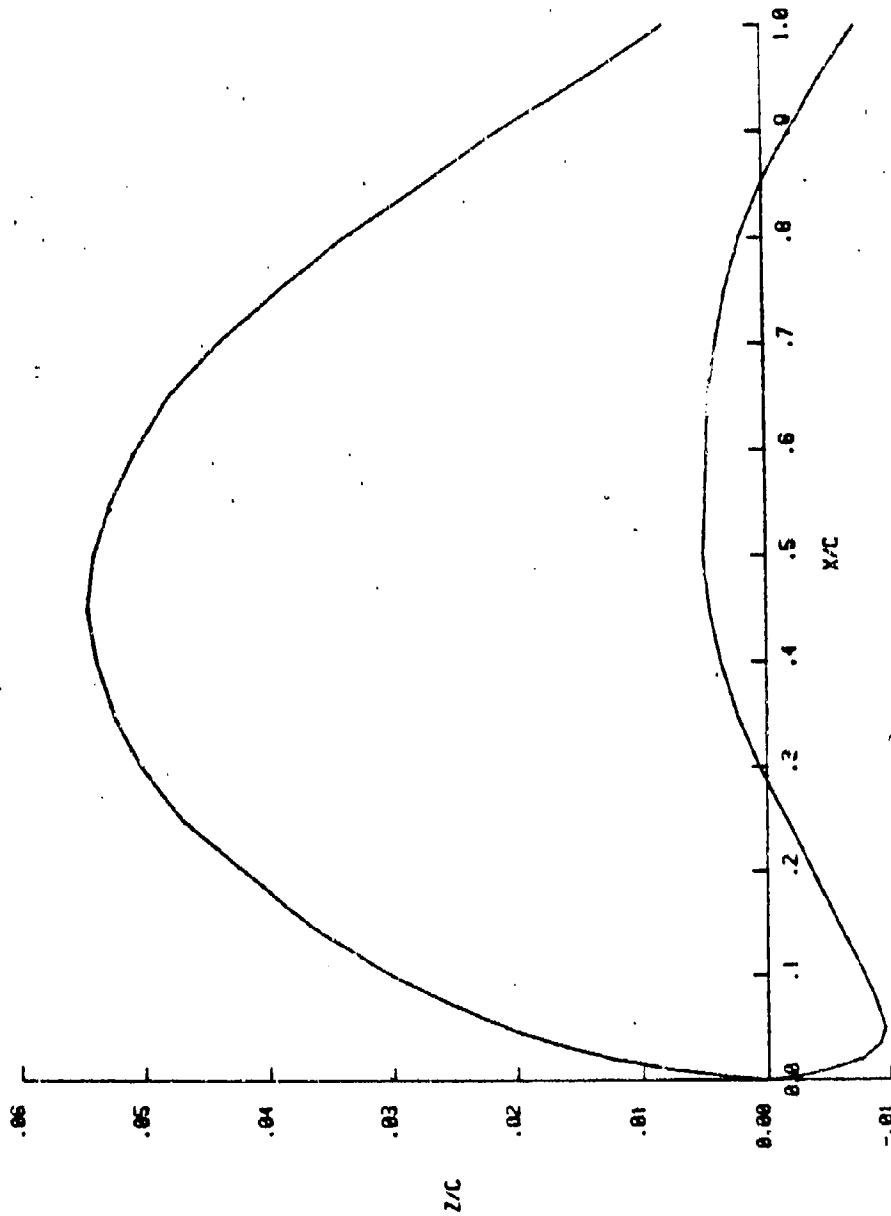
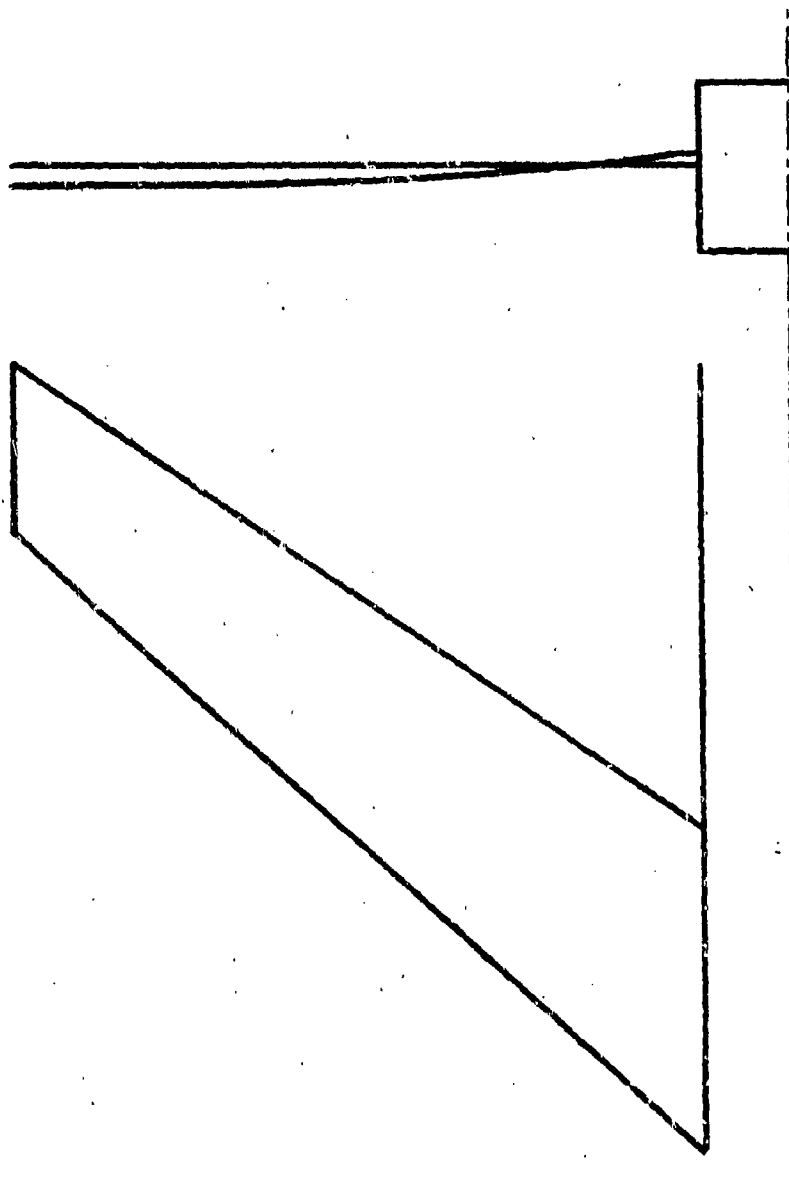


Figure 14. Aft Joined Wing Candidate Streamwise Airfoil

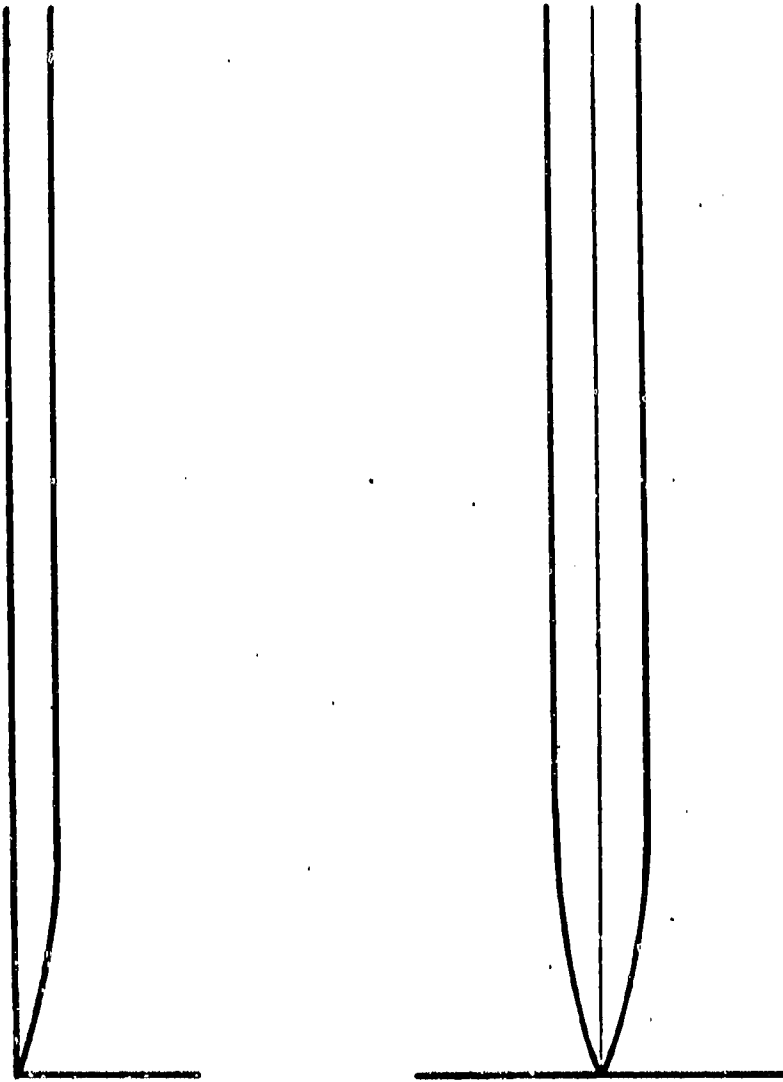
PLANFORM



a) Plan View

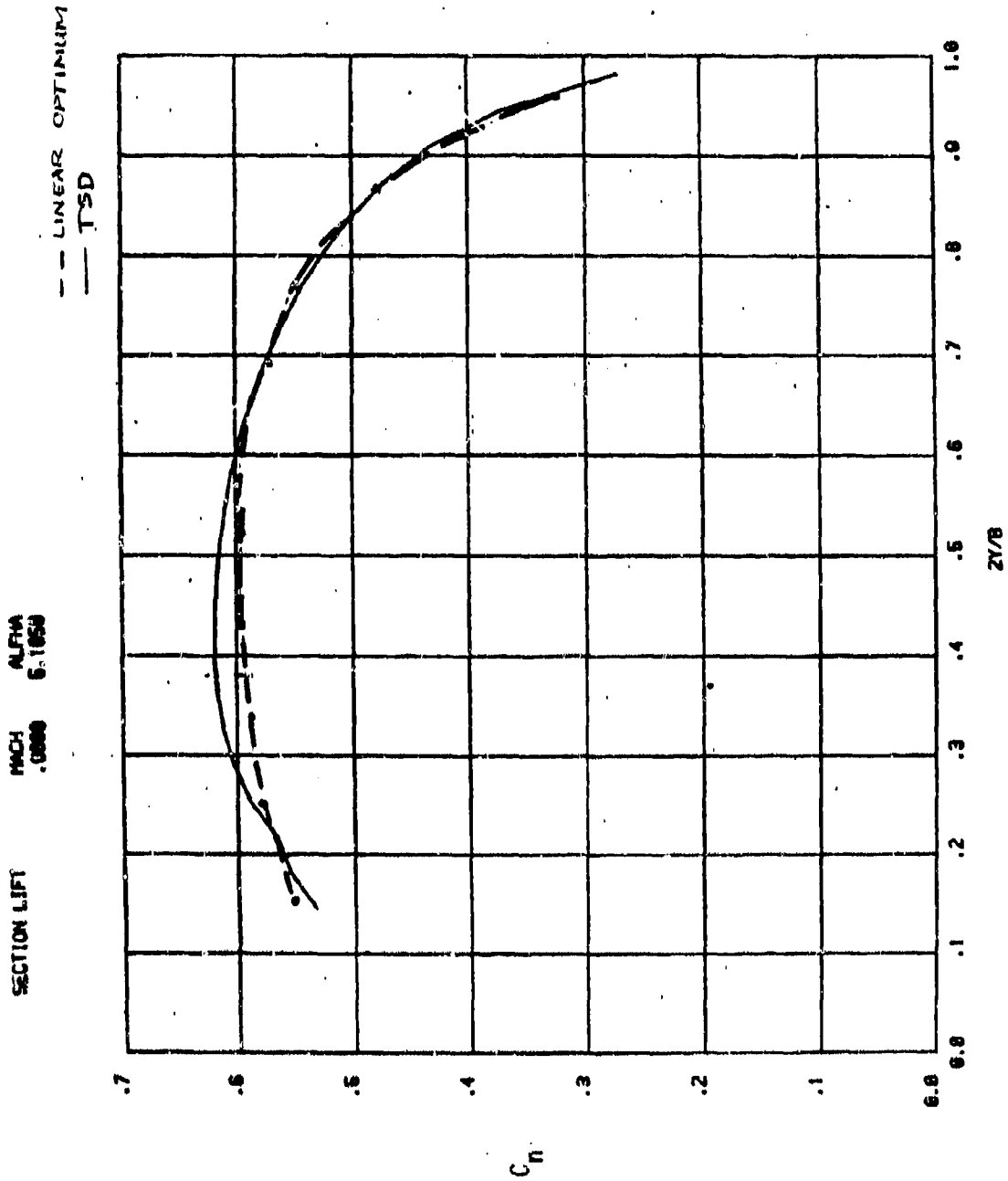
Figure 15. Transonic Forward Wing-body Prism Model

F. JSEL AGE



b) Body

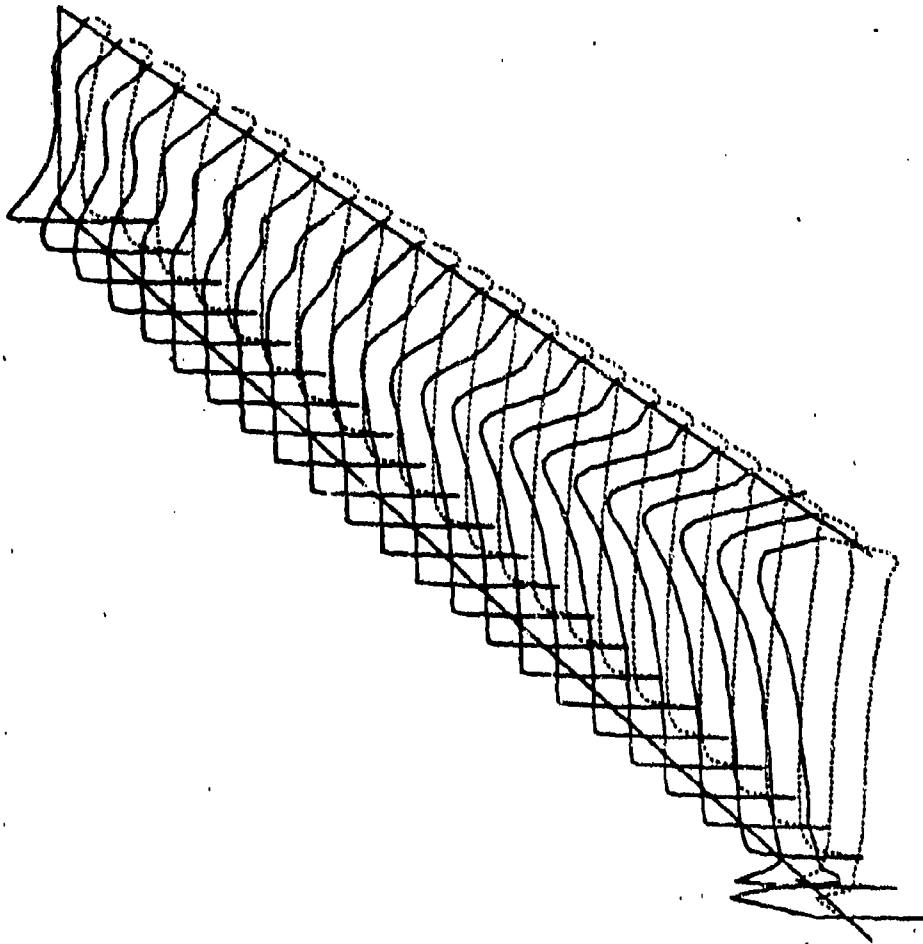
FIGURE 15. COMPLETED



a.) Span Load

Figure 5 Initial Transonic Forward Wing Analysis at $M = 0.90$,
 $C_L = 0.50$

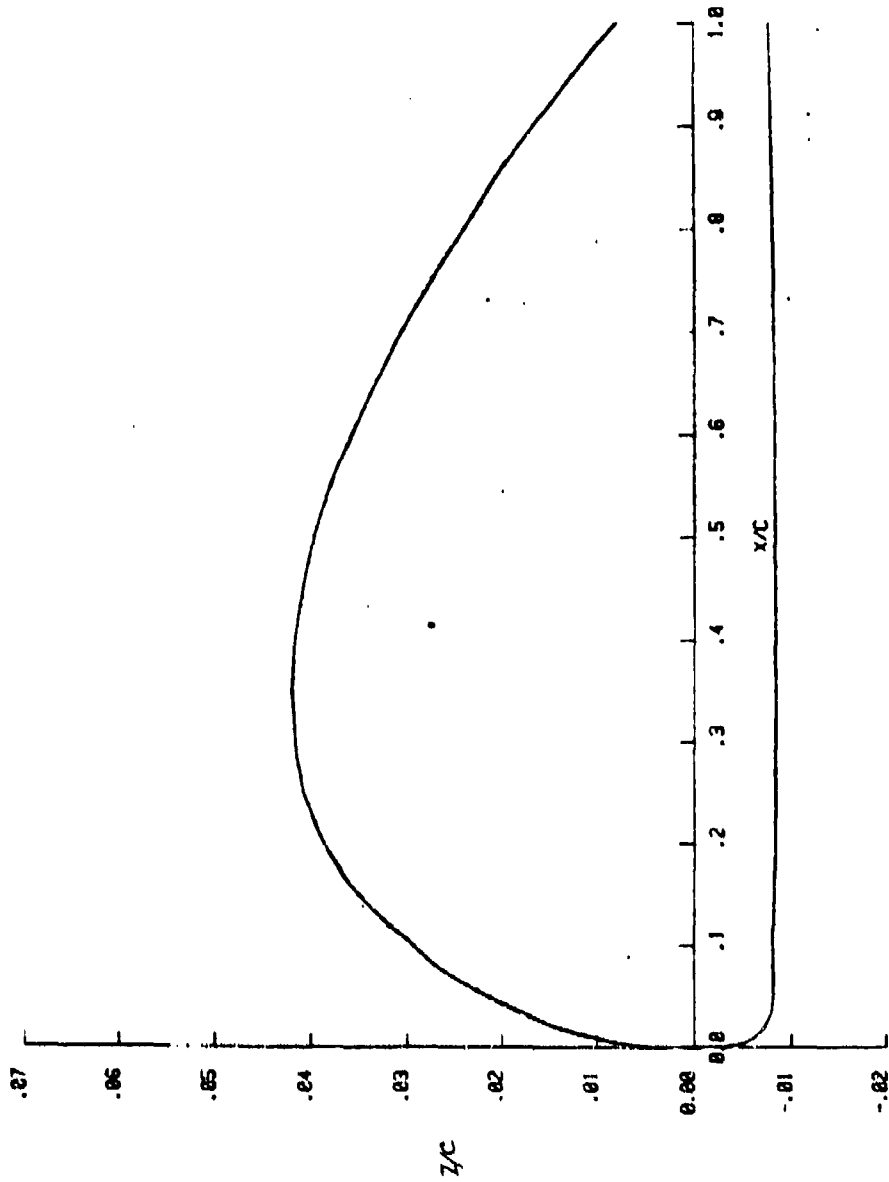
SURFACE PRESSURE
INCH .000
ALPHA 5.165



b) Surface Pressure Isometric

FIGURE 16. COMPLETED

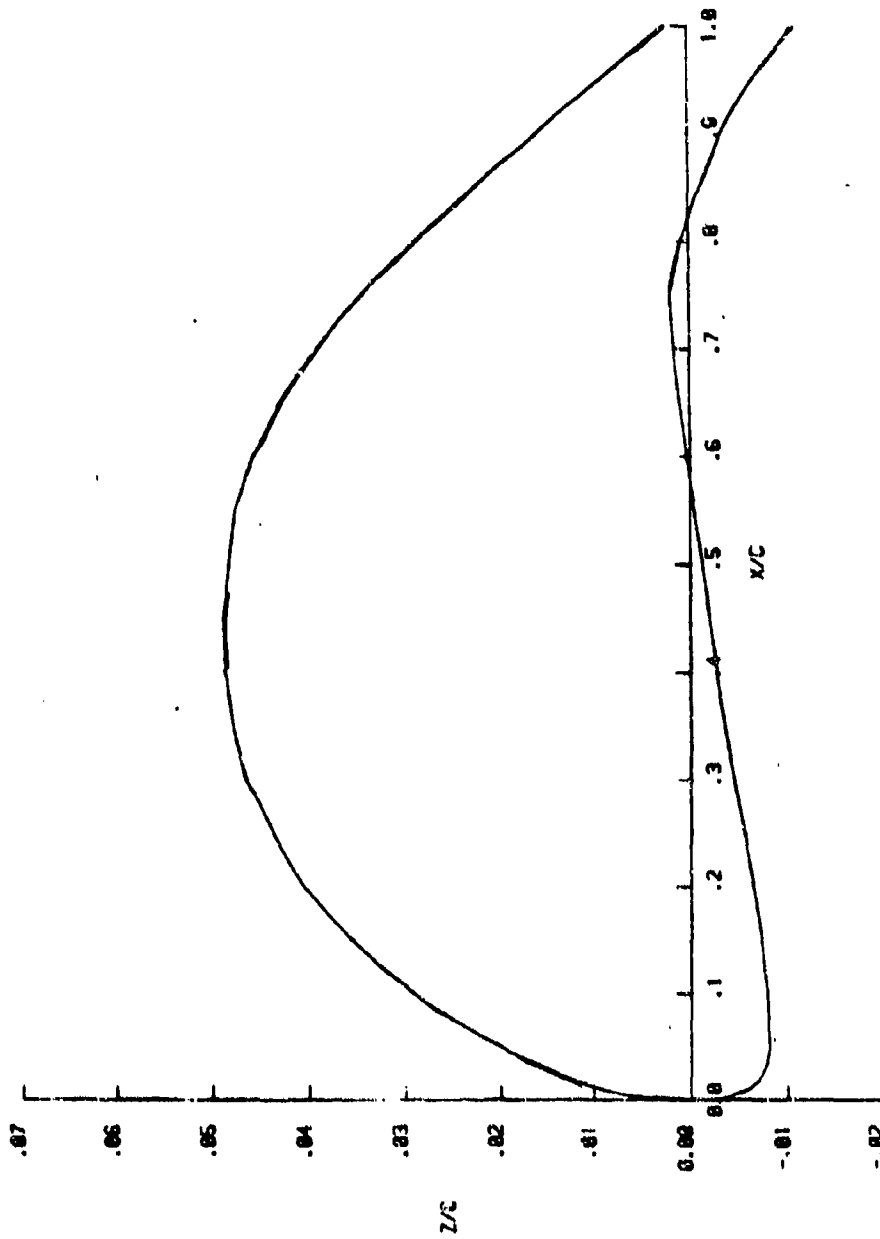
21/8
,1198



a) Root Airfoil

Figure 17. Final Forward Wing Transonic Design Geometry

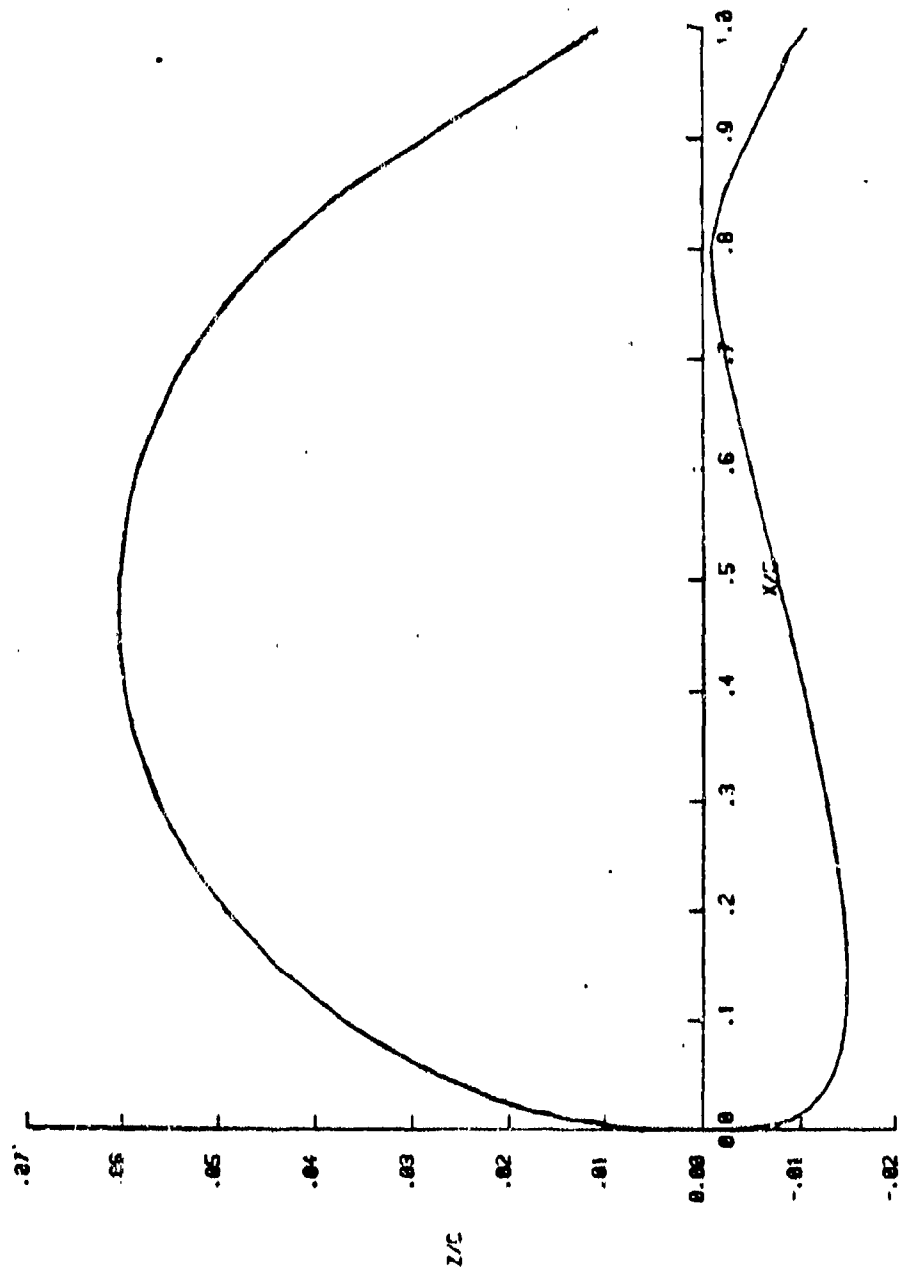
21/8
.5152



b) Mid-Span Airfoil

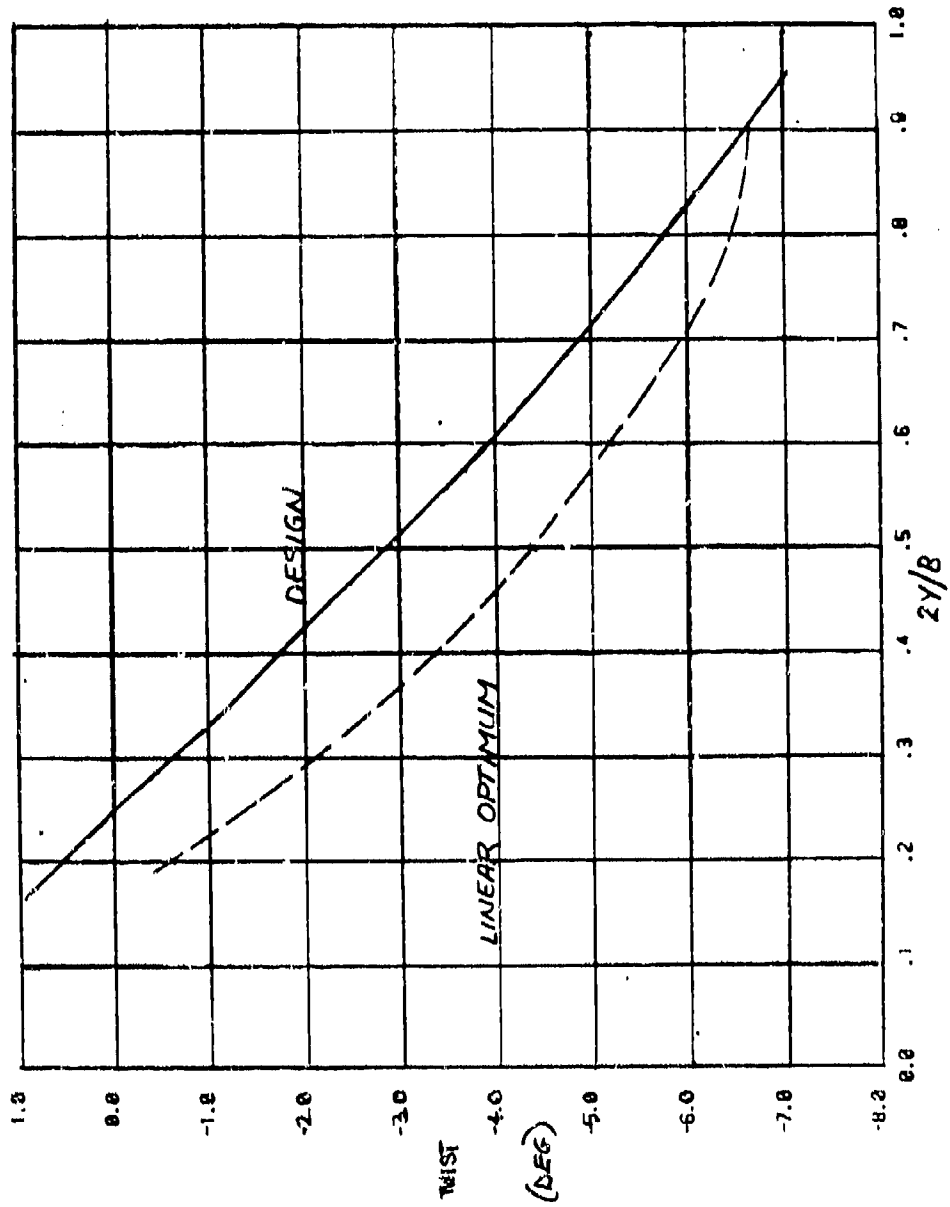
FIGURE 17. CONTINUED

27/0
1.0000



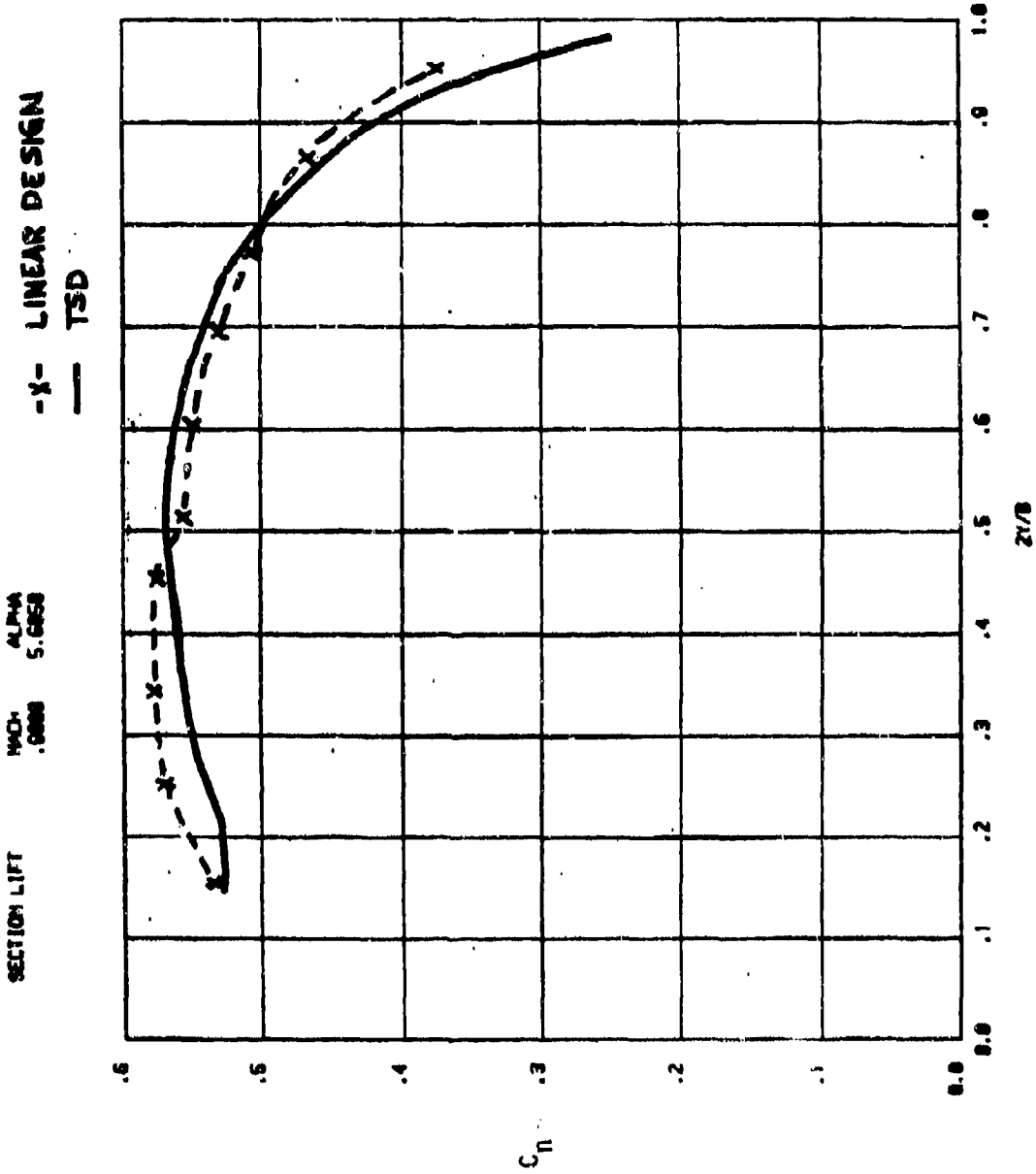
c) Tip-Airfoil

FIGURE 17. CONTINUED



d) Twist

FIGURE 17. CONCLUDED



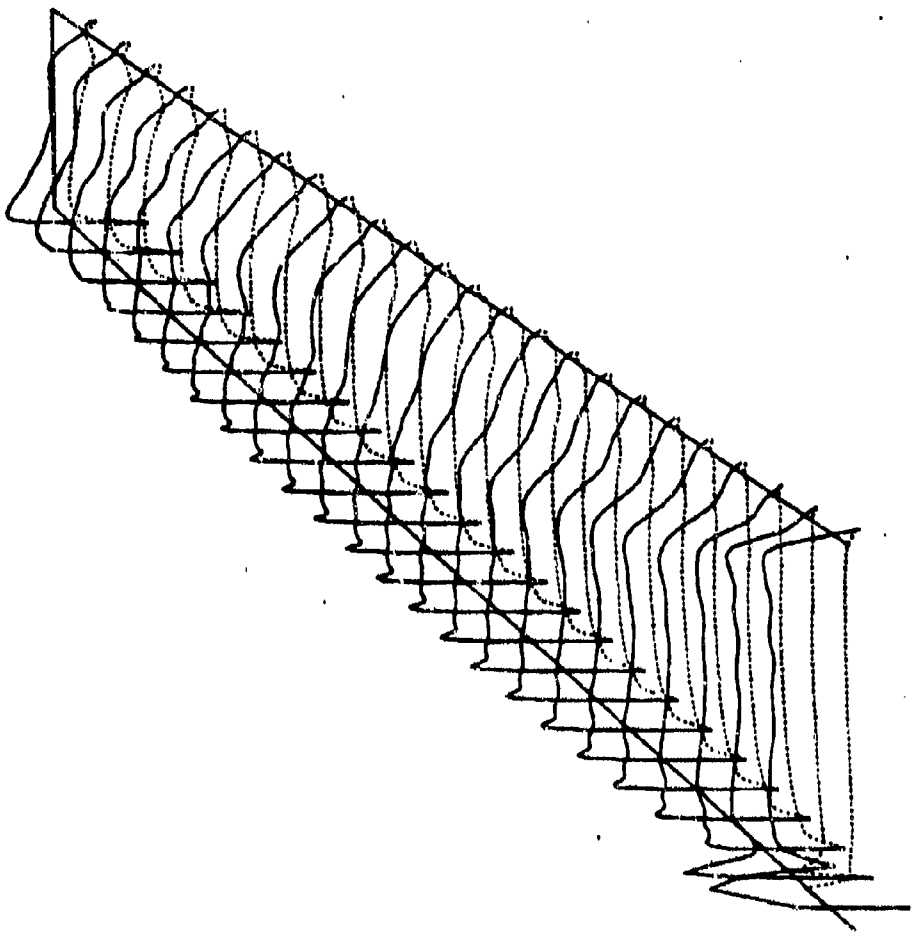
a) Span Load

Figure 18. Final Forward Wing Transonic Design Flow Quality

SURFACE PRESSURE INCH ALPHA

.000

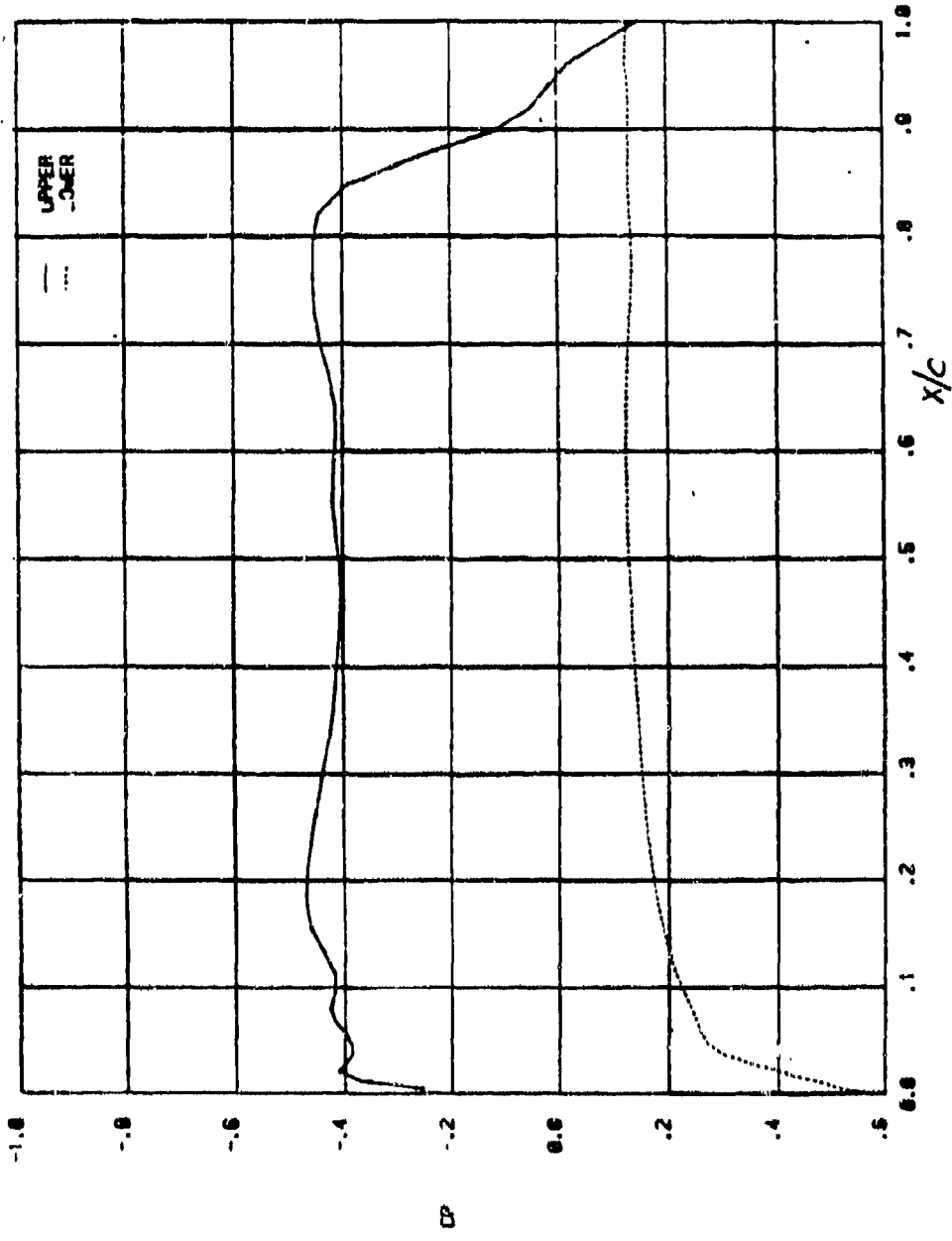
5.385



b) Surface Pressure Isometric

FIGURE 18 - CONTINUED

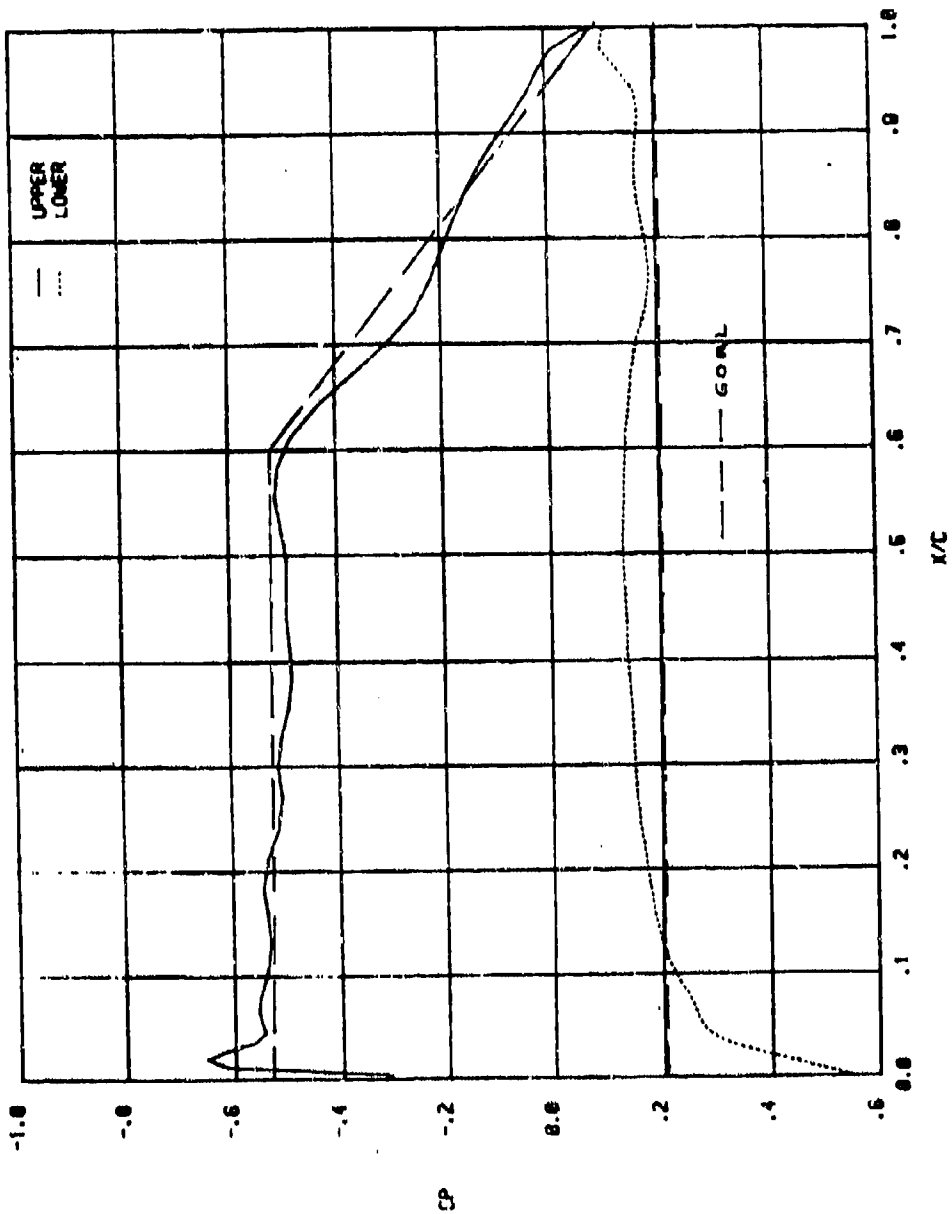
K 4 Z 5.0006 MACH .0008 ALPHA 5.0558 CL .5312 CD .0635 XCP .4362



c) Pressure Distribution at $\eta = 0.22$

FIGURE 18. CONTINUED

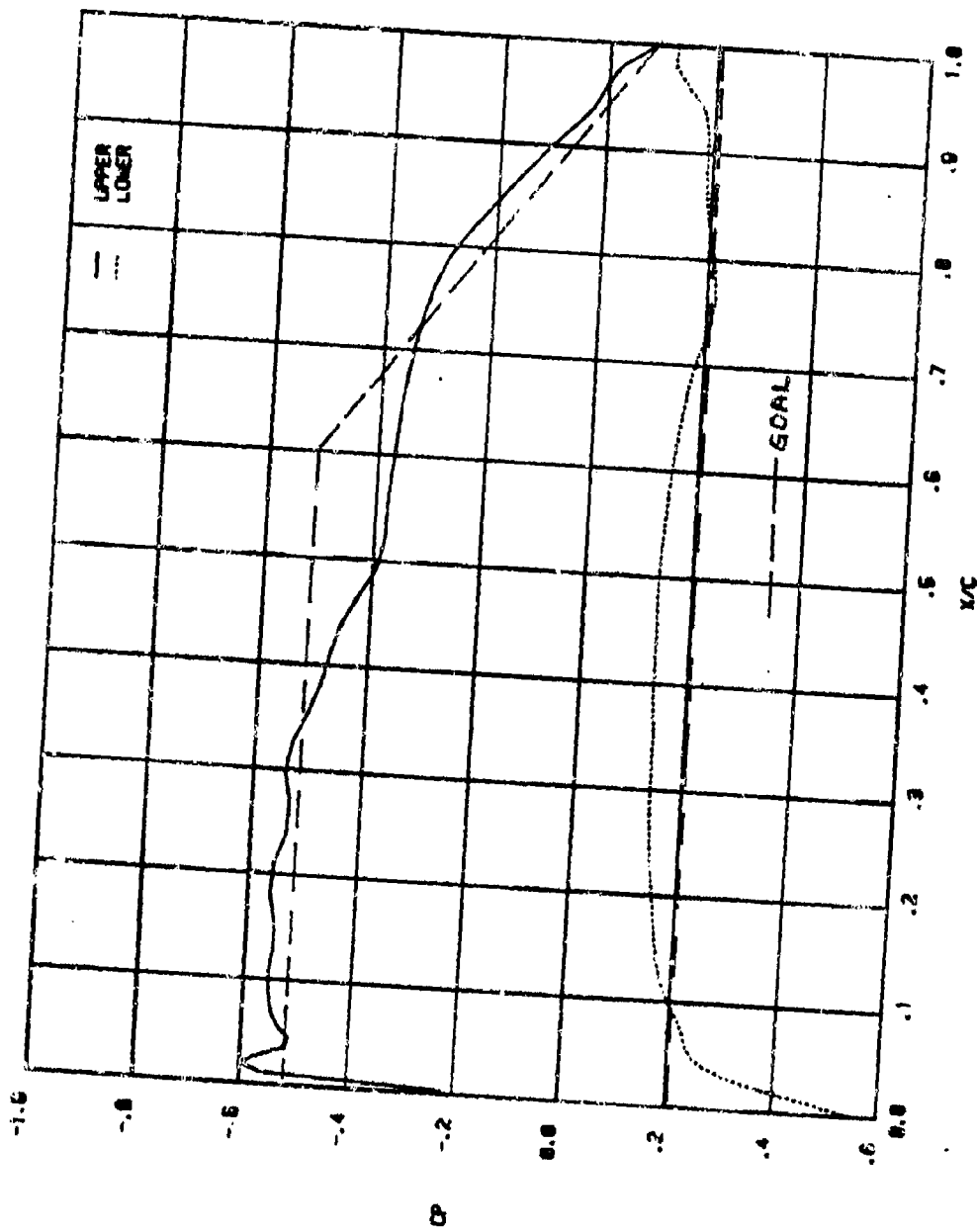
K 10 Z 11.7818 MACH 5.6568 ALPHA 5.6556 CL .6235 CD .4854 XCP .4854



d) Pressure Distribution at $\eta = 0.44$

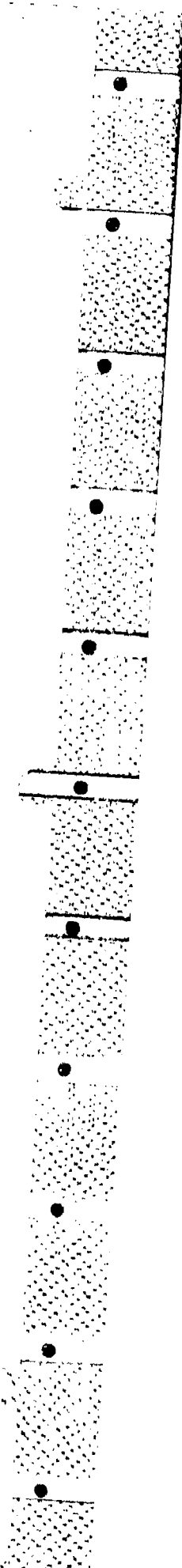
FIGURE 18. CONTINUED

K 15
 16.5000
 $MACH$.0000
 α .0000
 CD .0030
 CD .0030
 XCP .4171

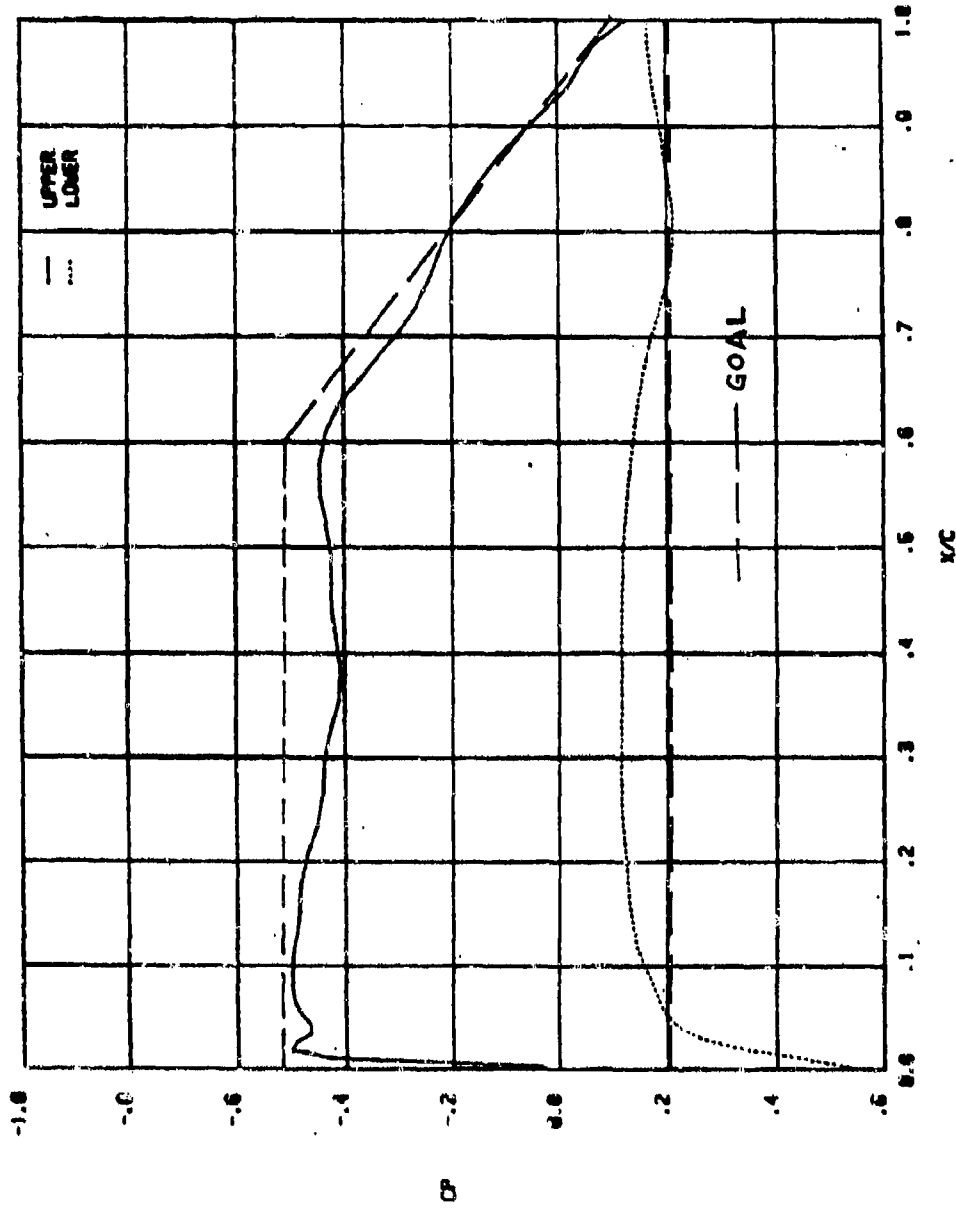


e) Pressure Distribution at $M = 0.62$

FIGURE 18. CONTINUED

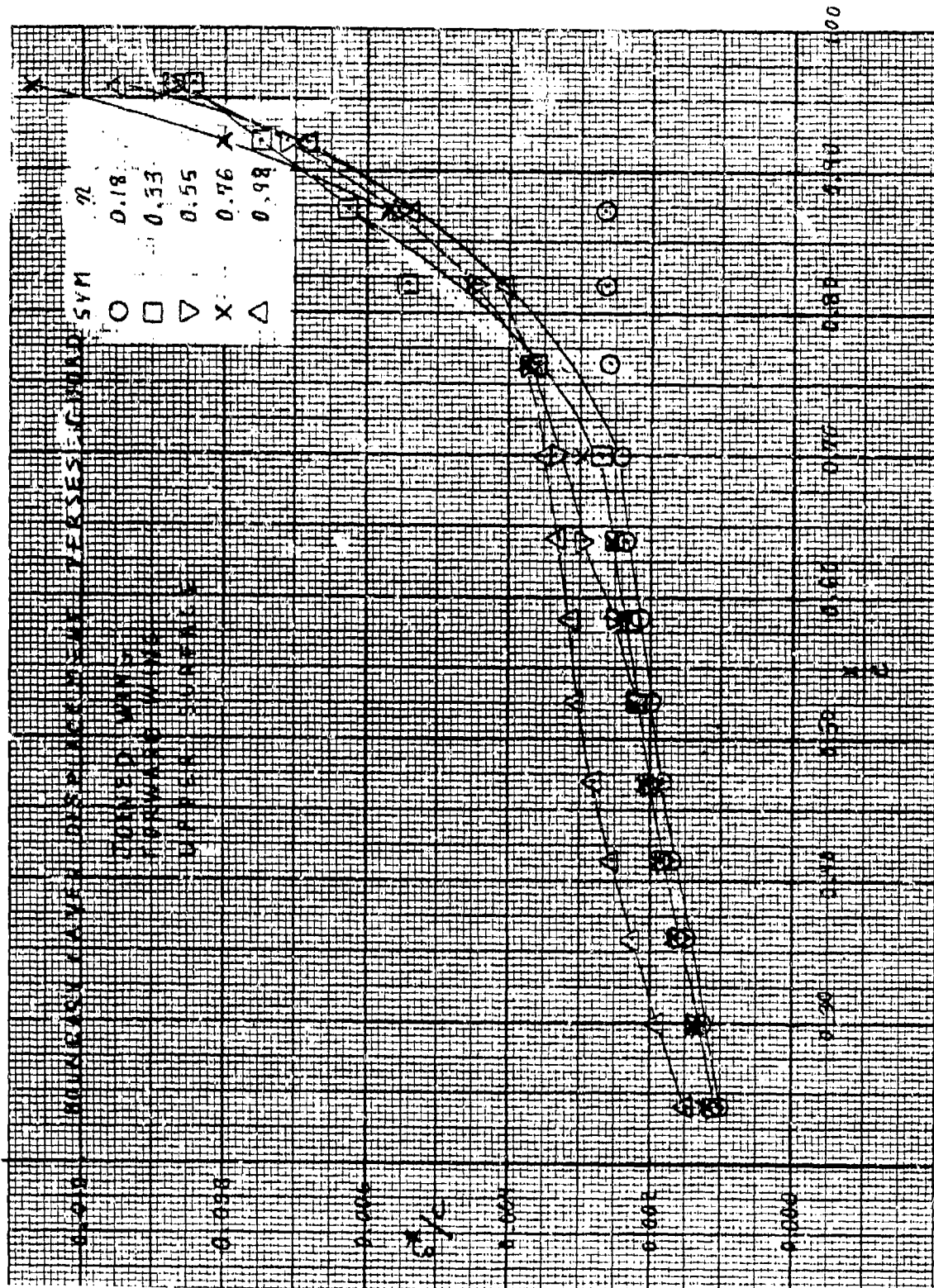


K 28 Z 21.638 MACH .0902 ALPHA 5.5852 CL .5817 CD -.8116 XCP .4254



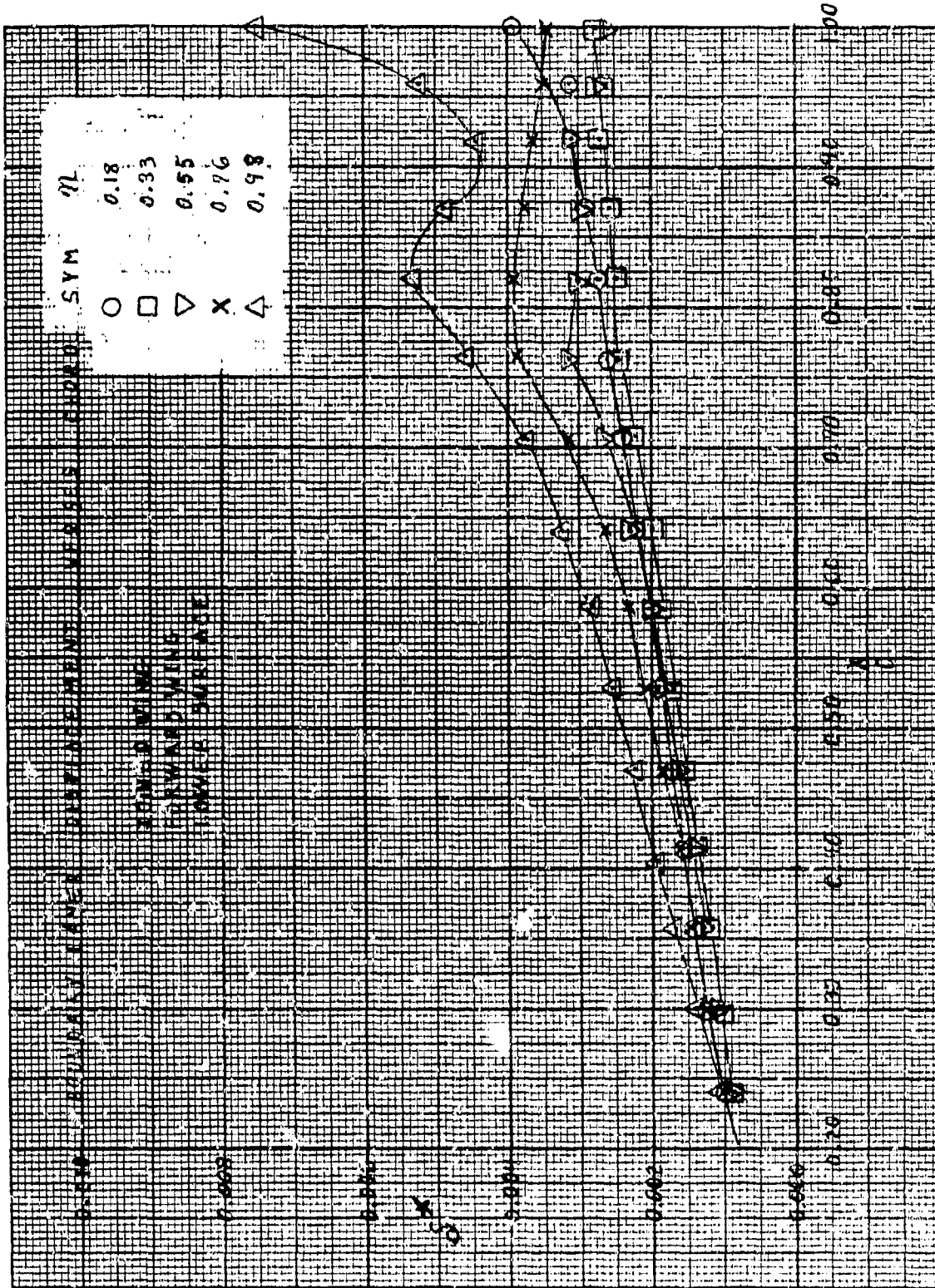
f) Pressure Distribution at $\eta = 0.80$

FIGURE 18. CONCLUDED



a) Upper Surface, $R_{N_c} = 4.1 \times 10^6$

Figure 19. Final Forward Wing Transonic Boundary Layer Displacement Thickness



b) Lower Surface, $R_{NC} = 4.1 \times 10^6$ FIGURE 19. CONCLUDED

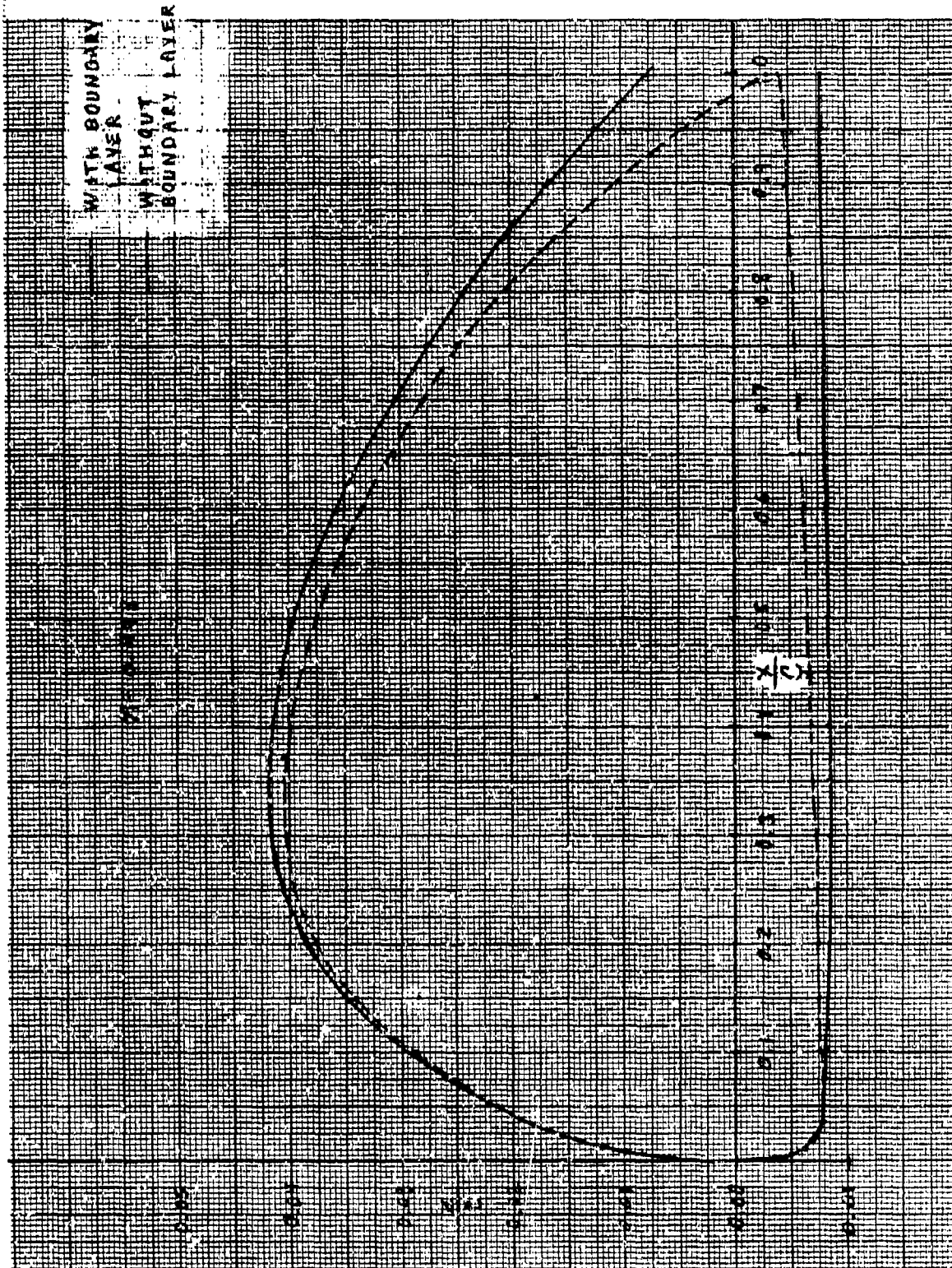
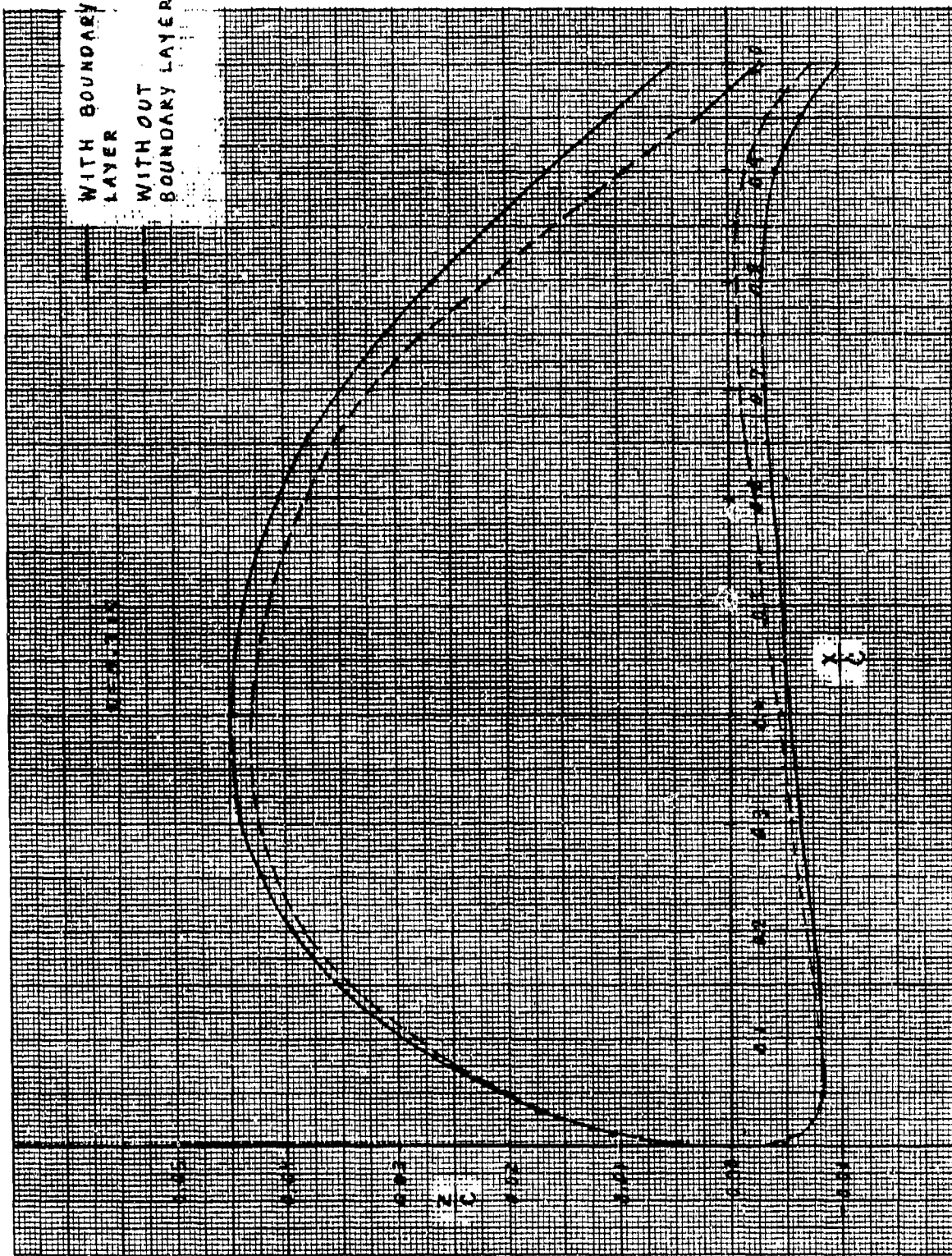


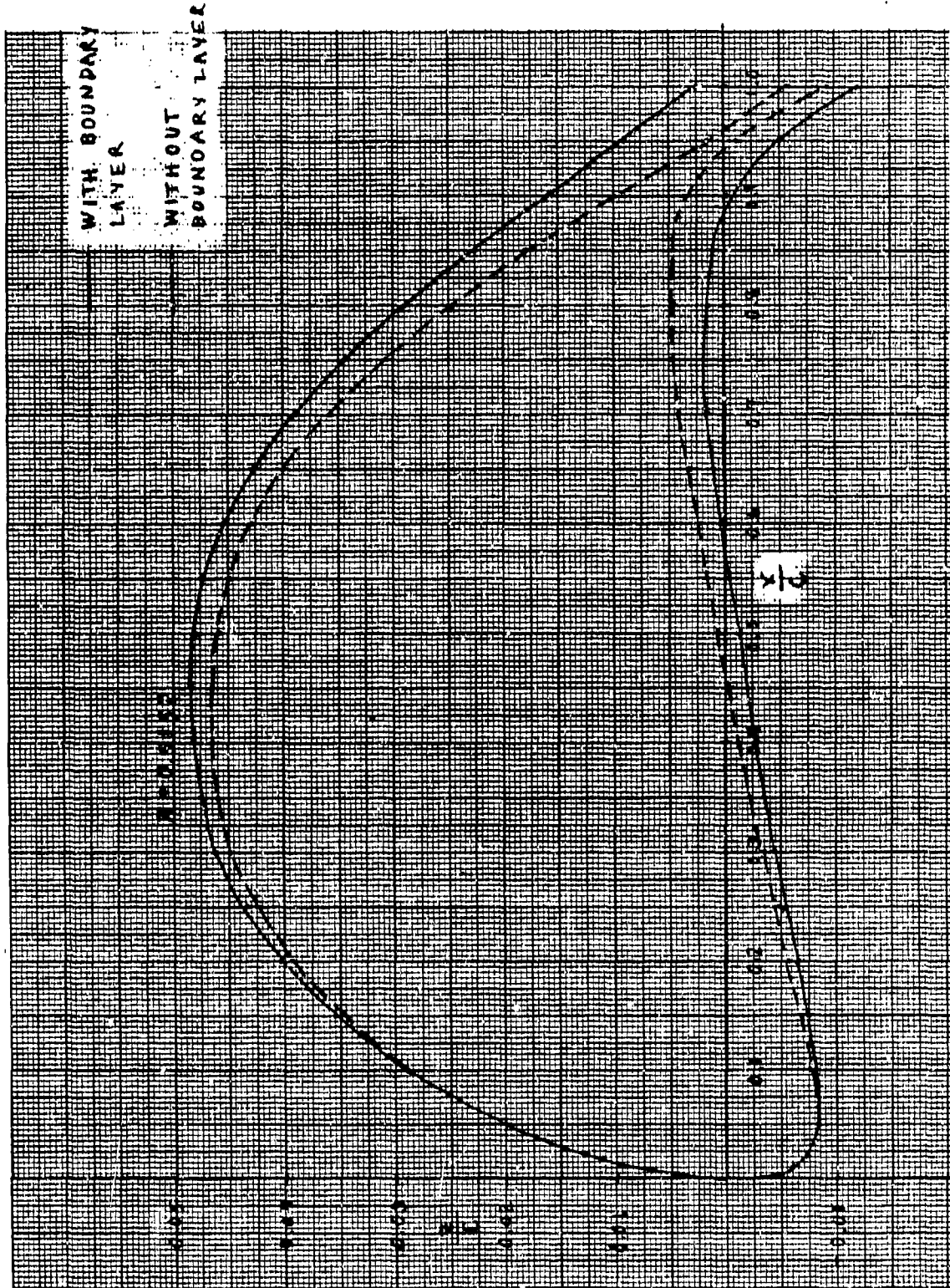
Figure 20. Forward Wing Airfoils with/without Boundary Layer Displacement Thickness

a) Airfoil at $n = .12$



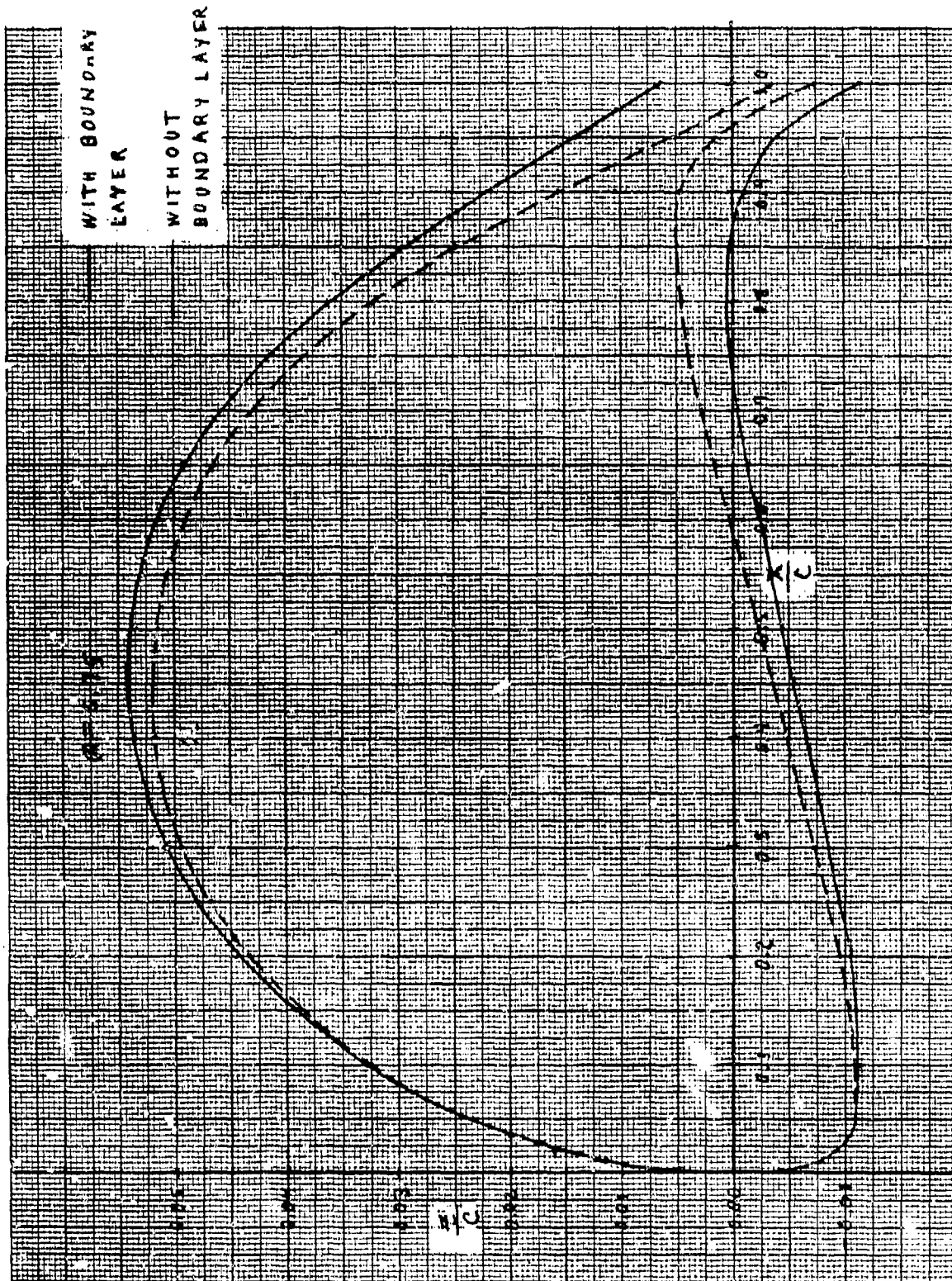
b) Airfoil at $\eta = 0.32$

FIGURE 20. CONTINUED



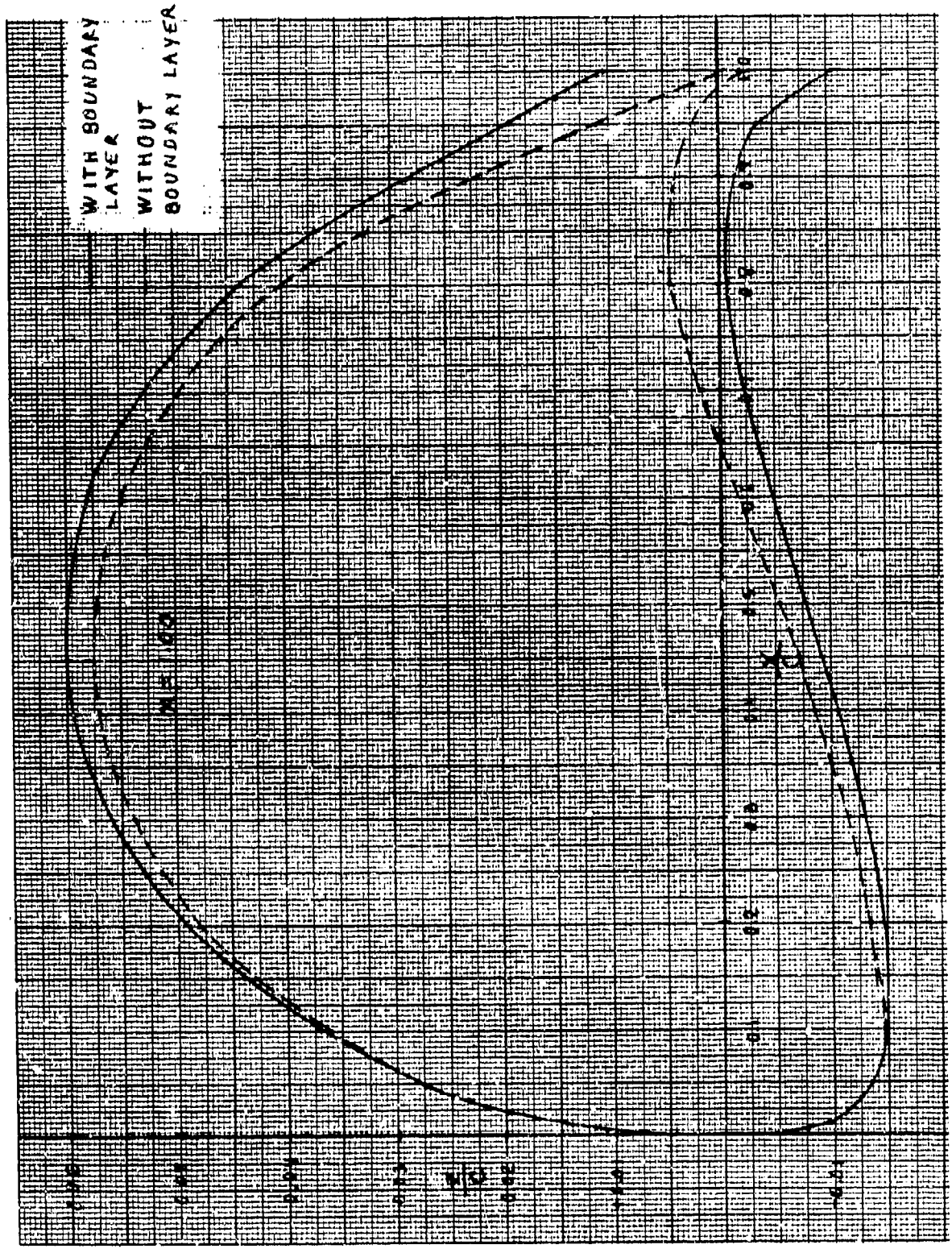
c) Airfoil at $\eta = 0.52$

FIGURE 20. CONTINUED



d) Airfoil at $\eta = 0.75$

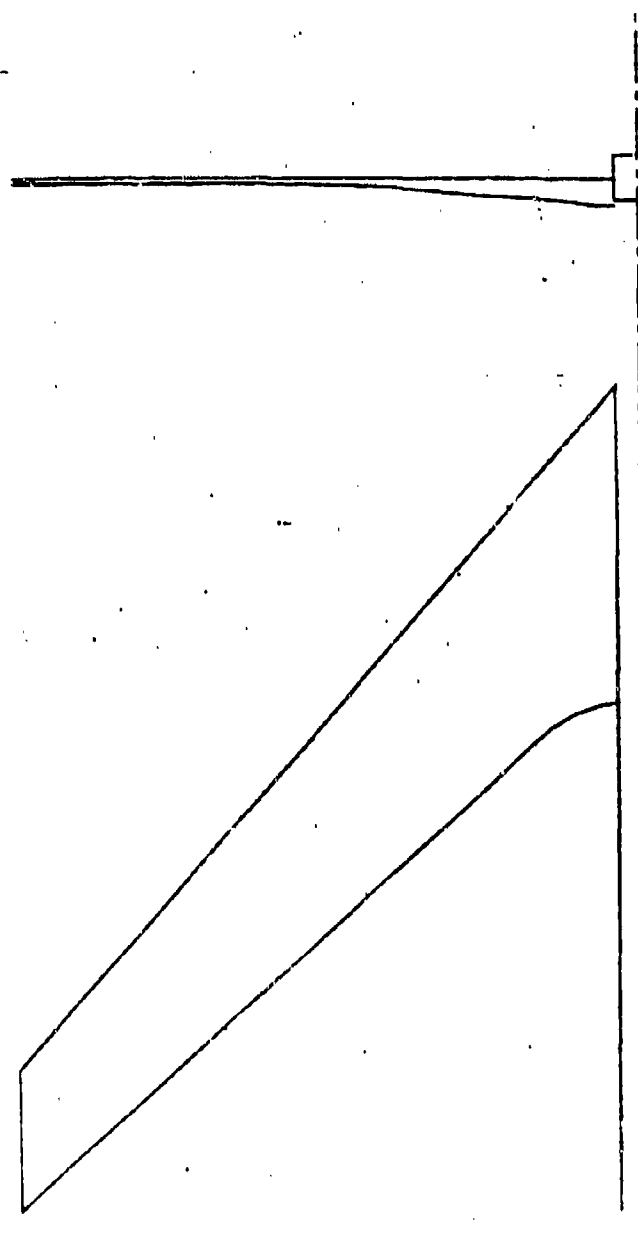
FIGURE 20. CONTINUED



e) Airfoil at $n = 1.00$

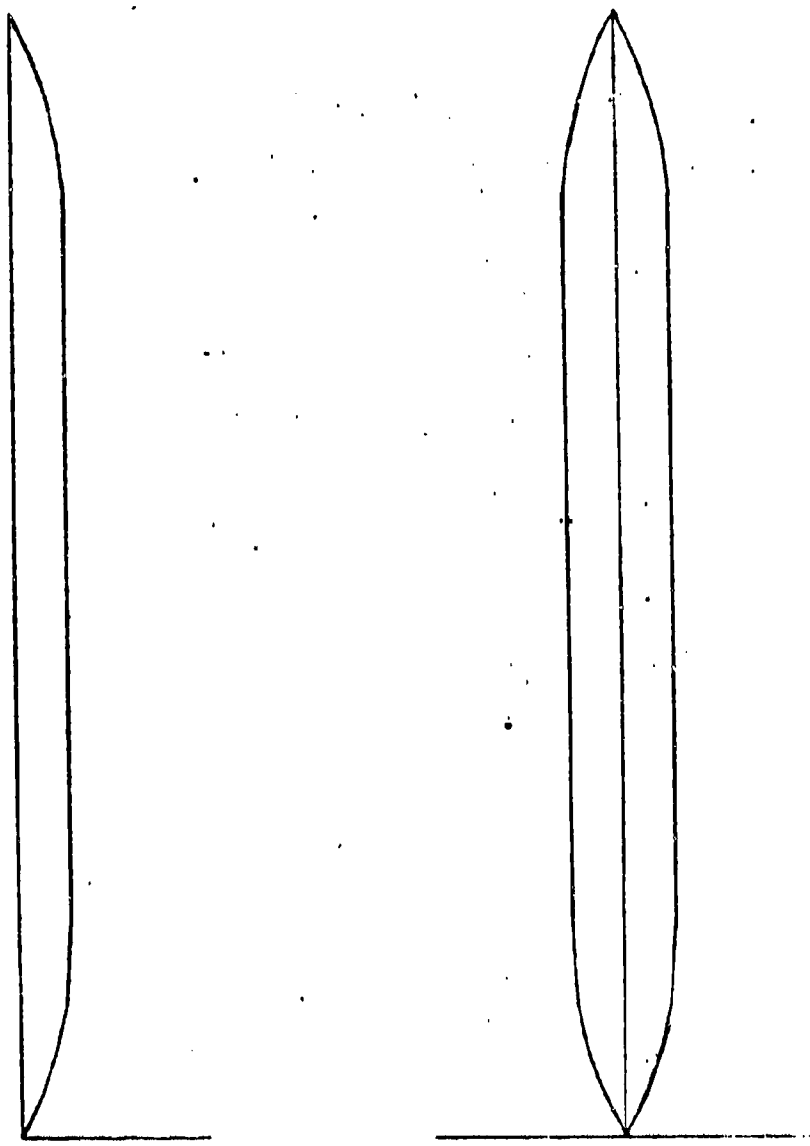
FIGURE 20. CONCLUDED

PLANFORM



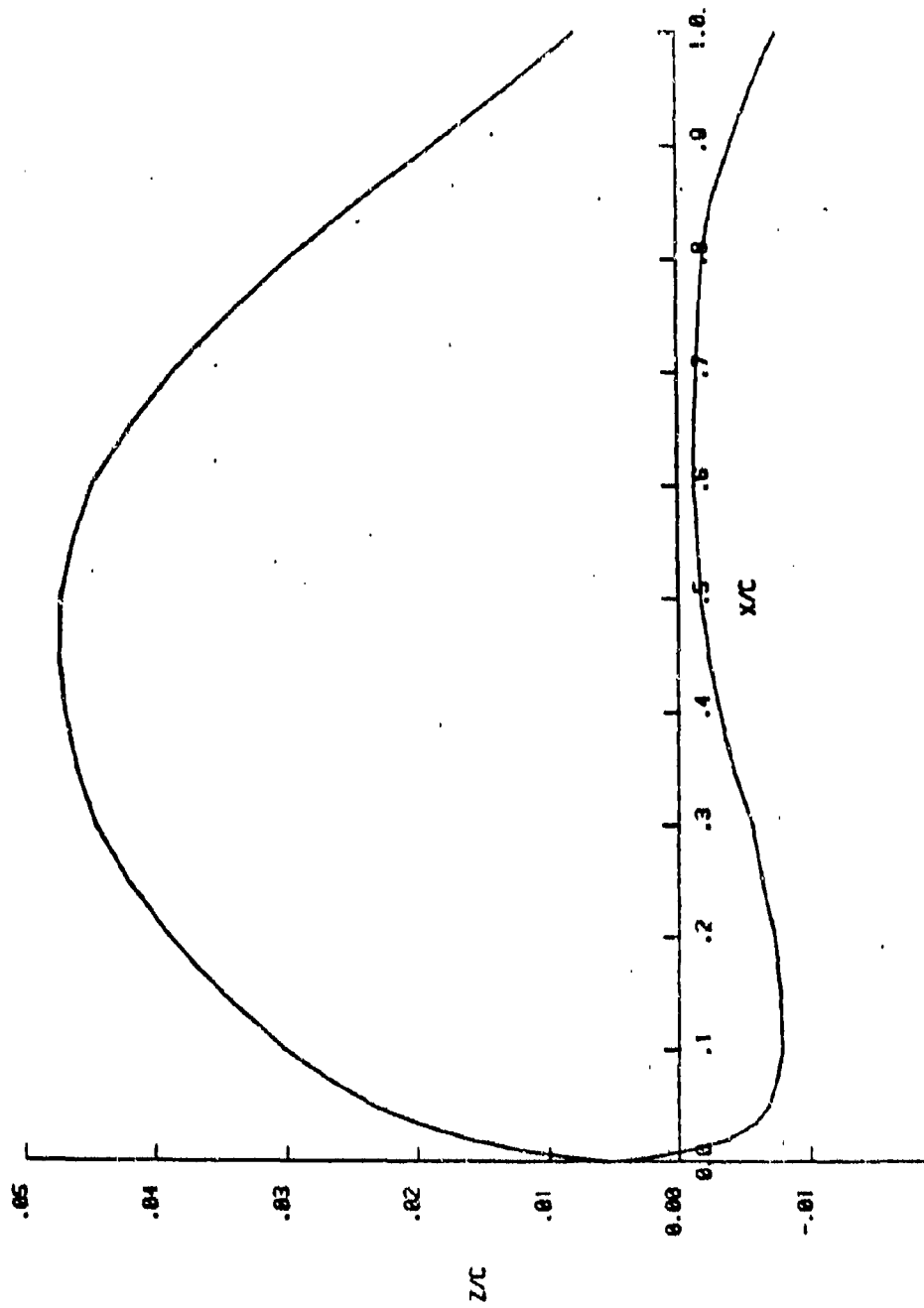
a) Planform Modification

Figure 21. Aft Wing Transonic Model



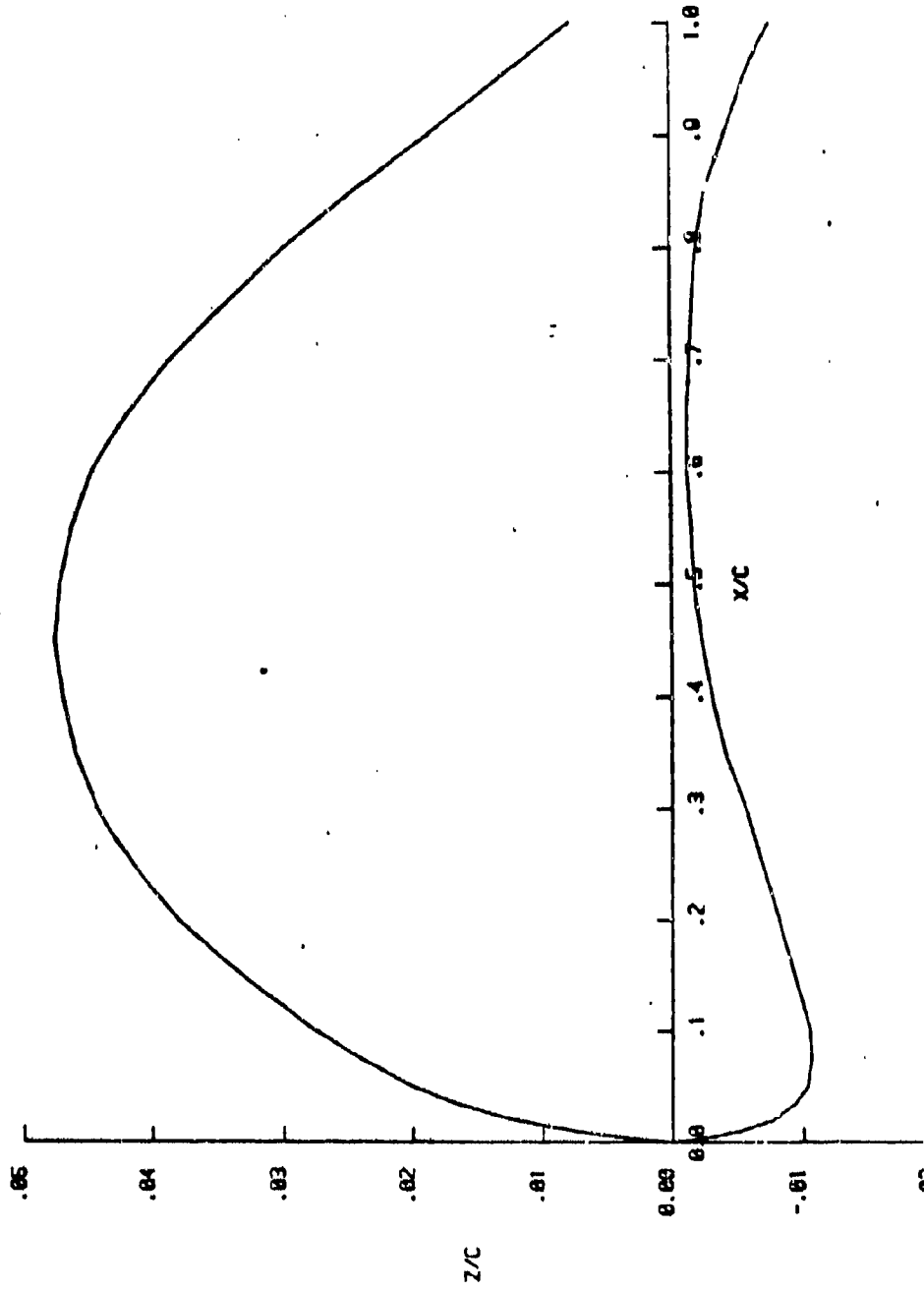
b) Wing-Tail Structural Attachment

FIGURE 21. CONTINUED



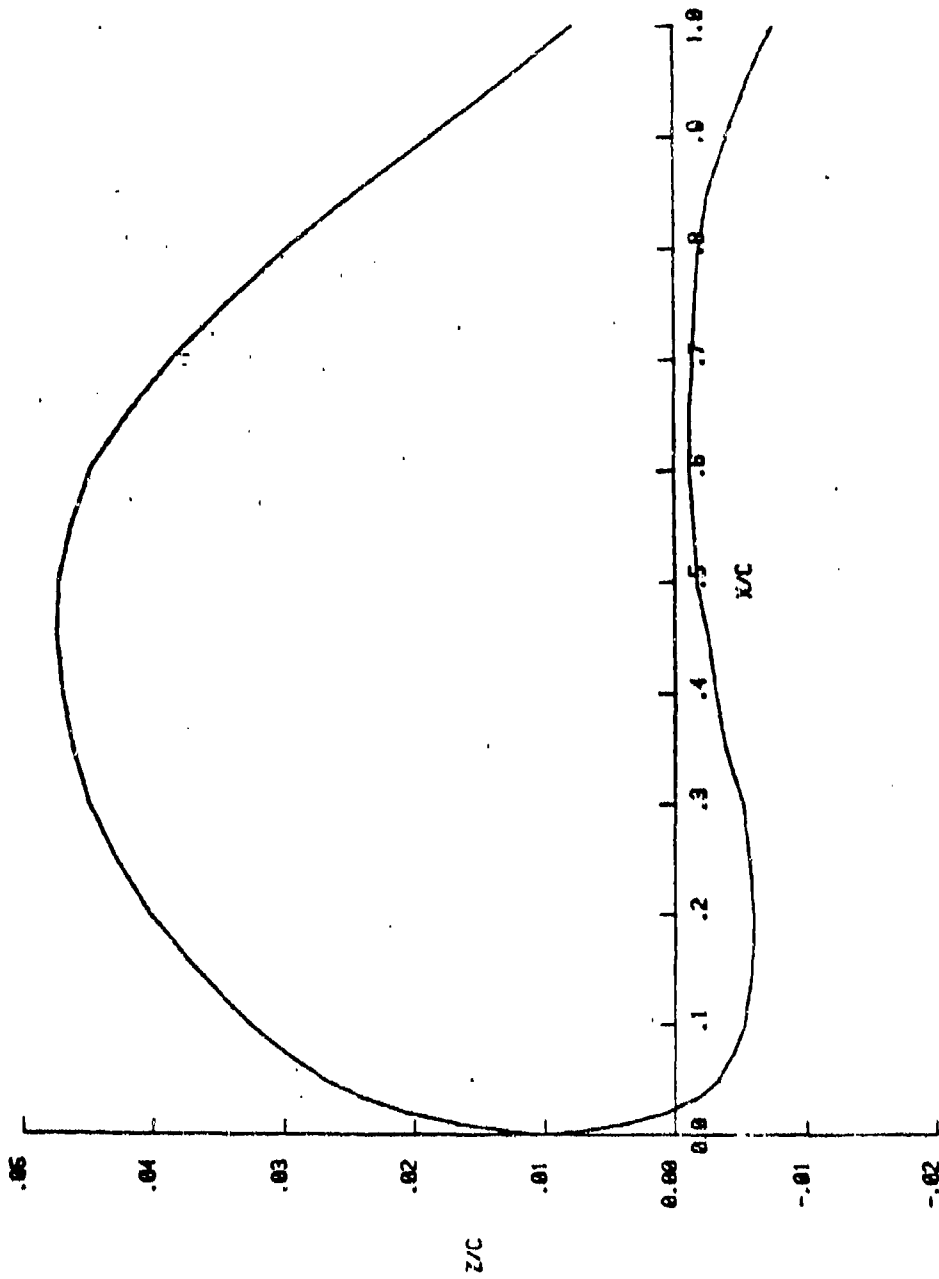
c) Airfoil at $\eta = 0.04$

FIGURE 21. CONTINUED



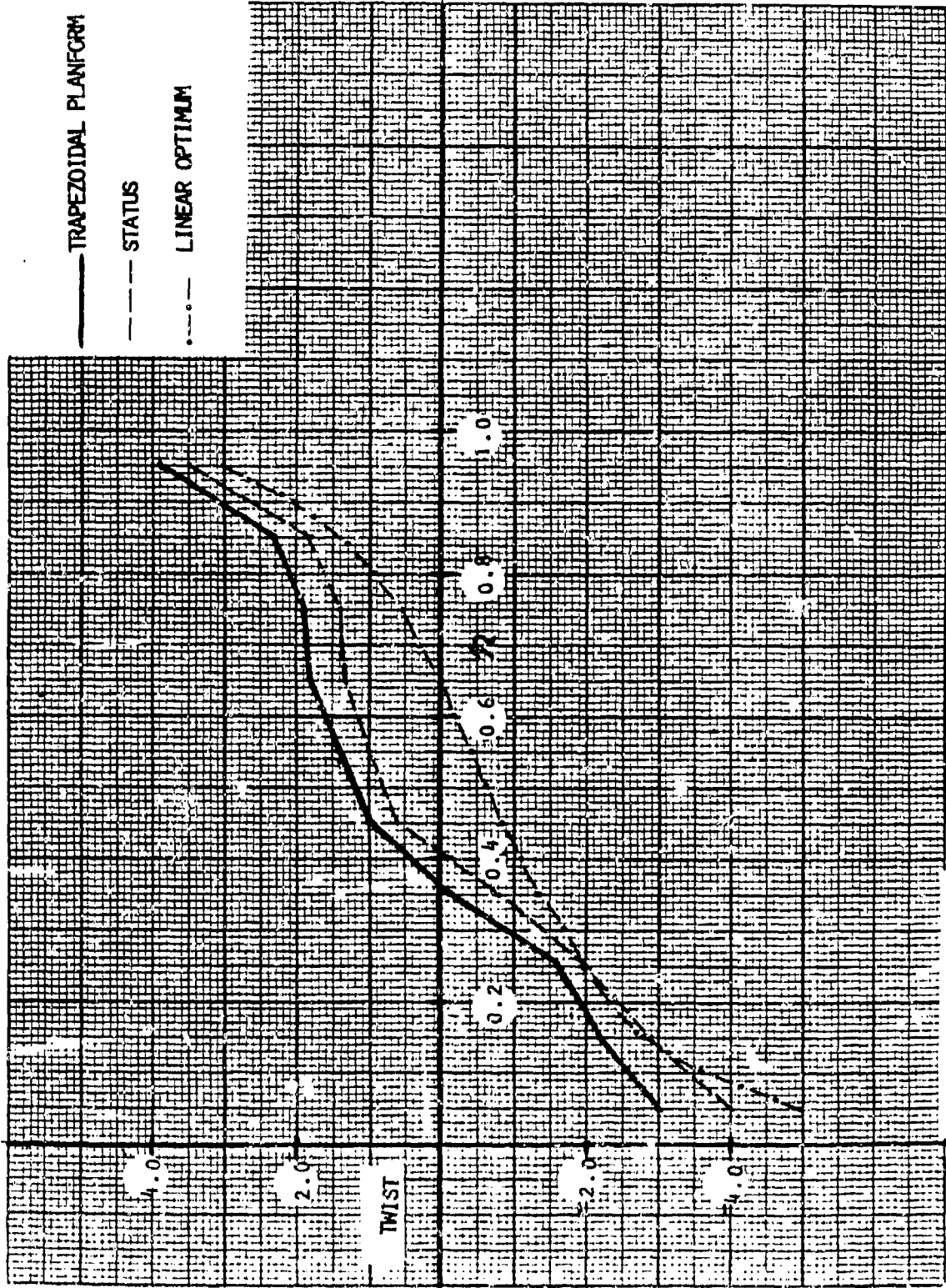
d) Airfoil at $\eta = 0.25 - 0.80$

FIGURE 21. CONTINUED



e) Airfoil at $\eta = 0.80$

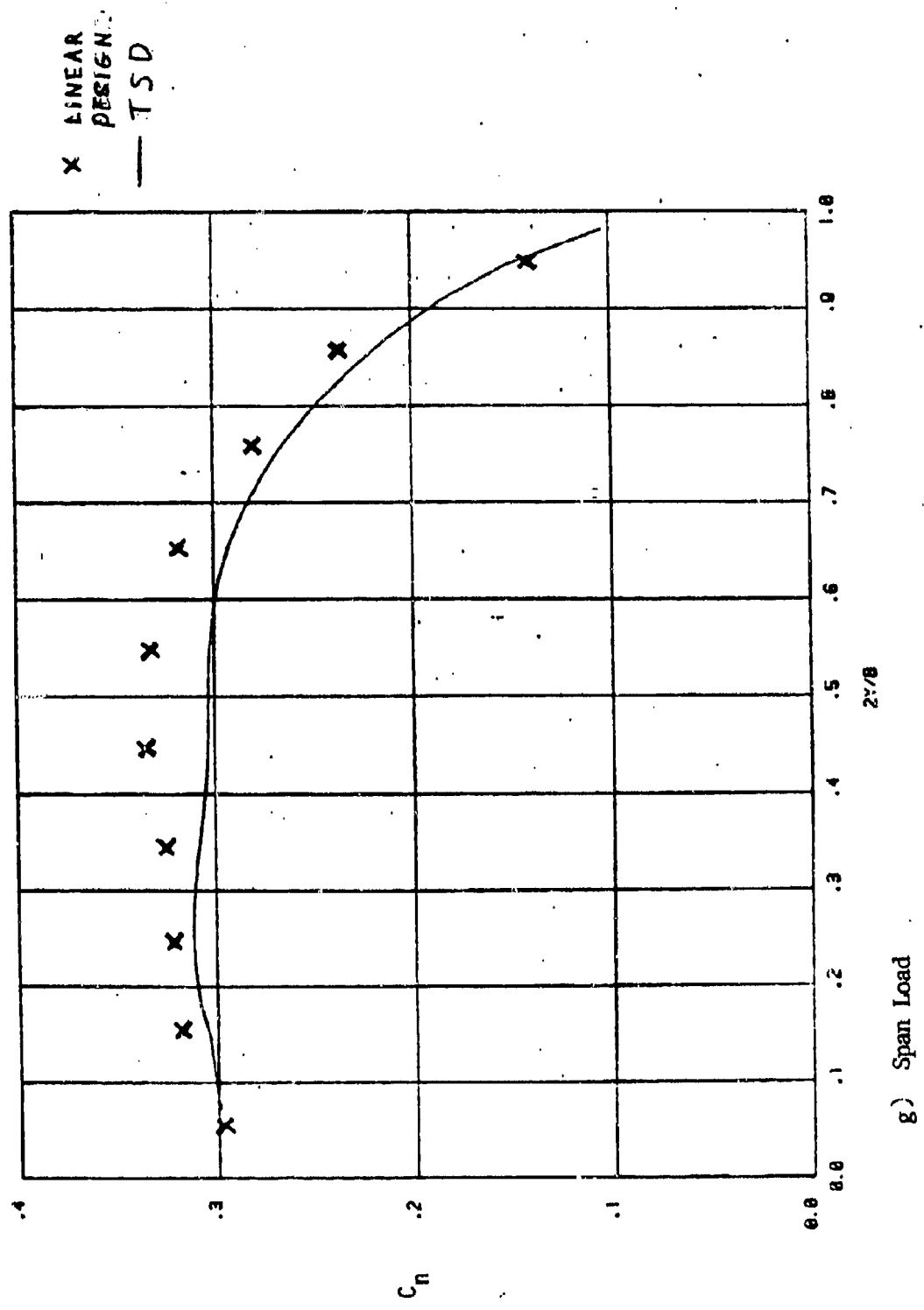
FIGURE 21. CONTINUED



f. geometric twist

FIGURE 21 CONTINUED

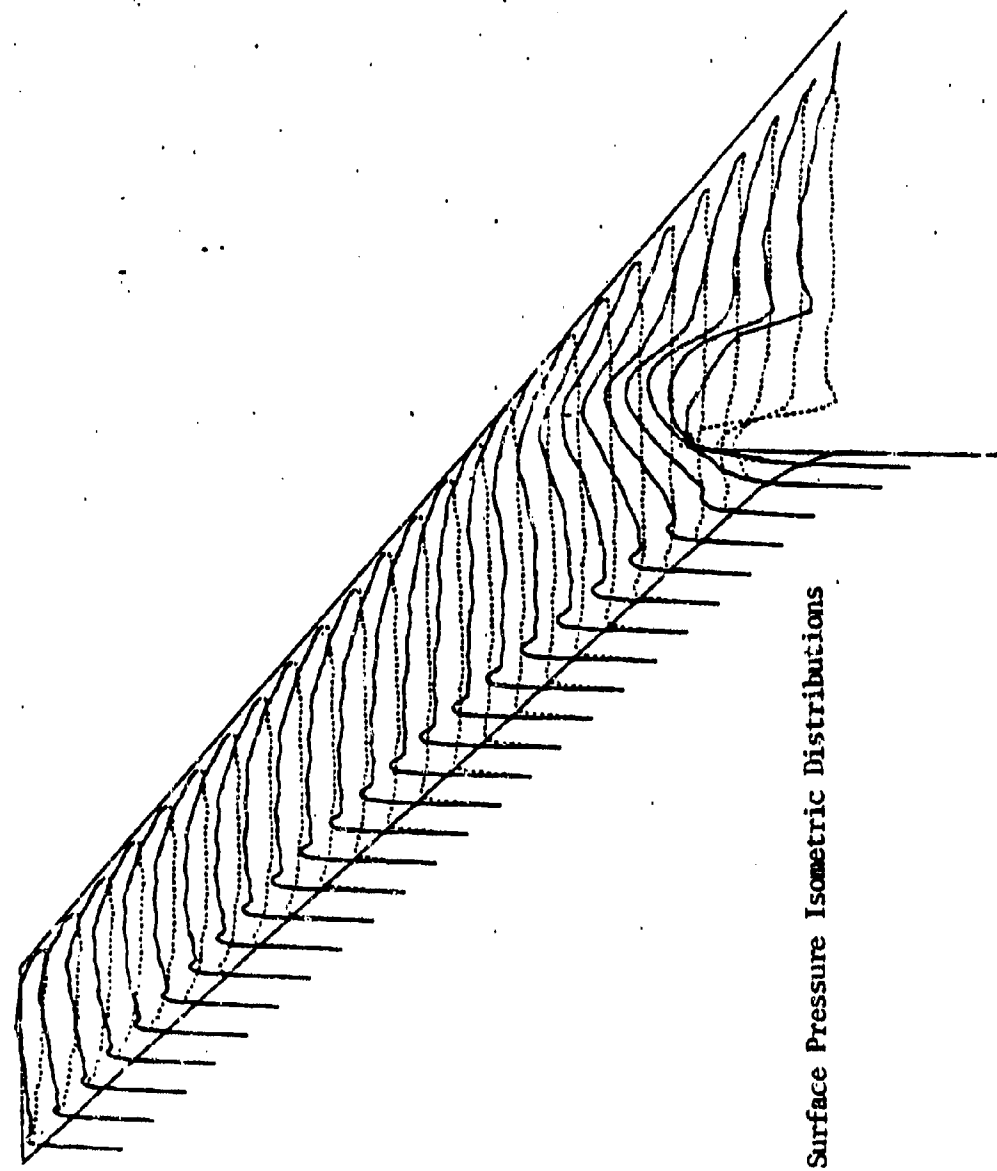
SECTION LIFT MACH ALPHA
.0000 5.1658



g) Span Load

FIGURE 21. CONTINUED

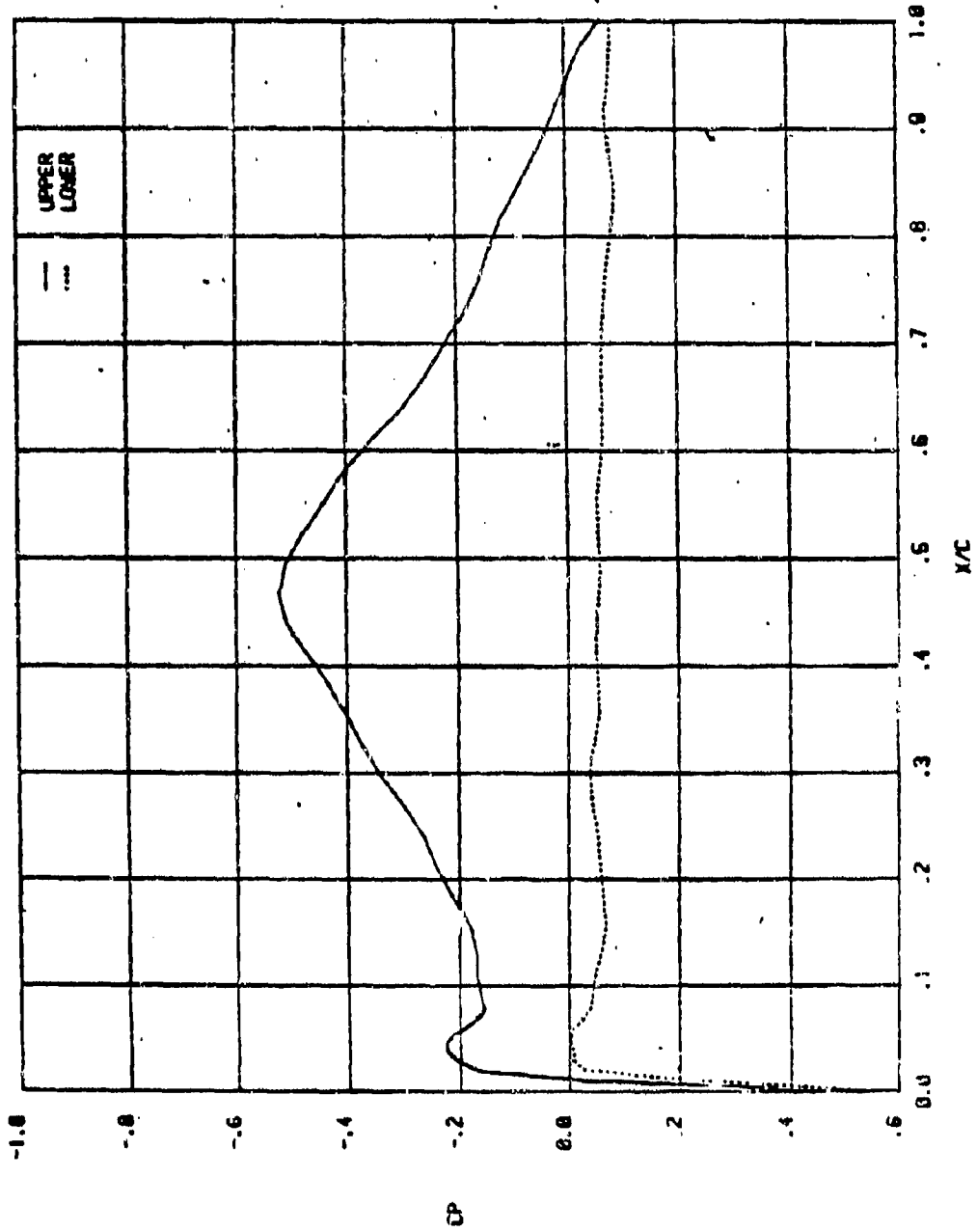
SURFACE PRESSURE MACH ALPHA
 .008 5.185



h) Surface Pressure Isometric Distributions

FIGURE 21. CONTINUED

K 7
 Z 6.8727
 MACH .9668
 ALPHA 6.1858
 CL .3115
 CD .0030
 MCP .4628

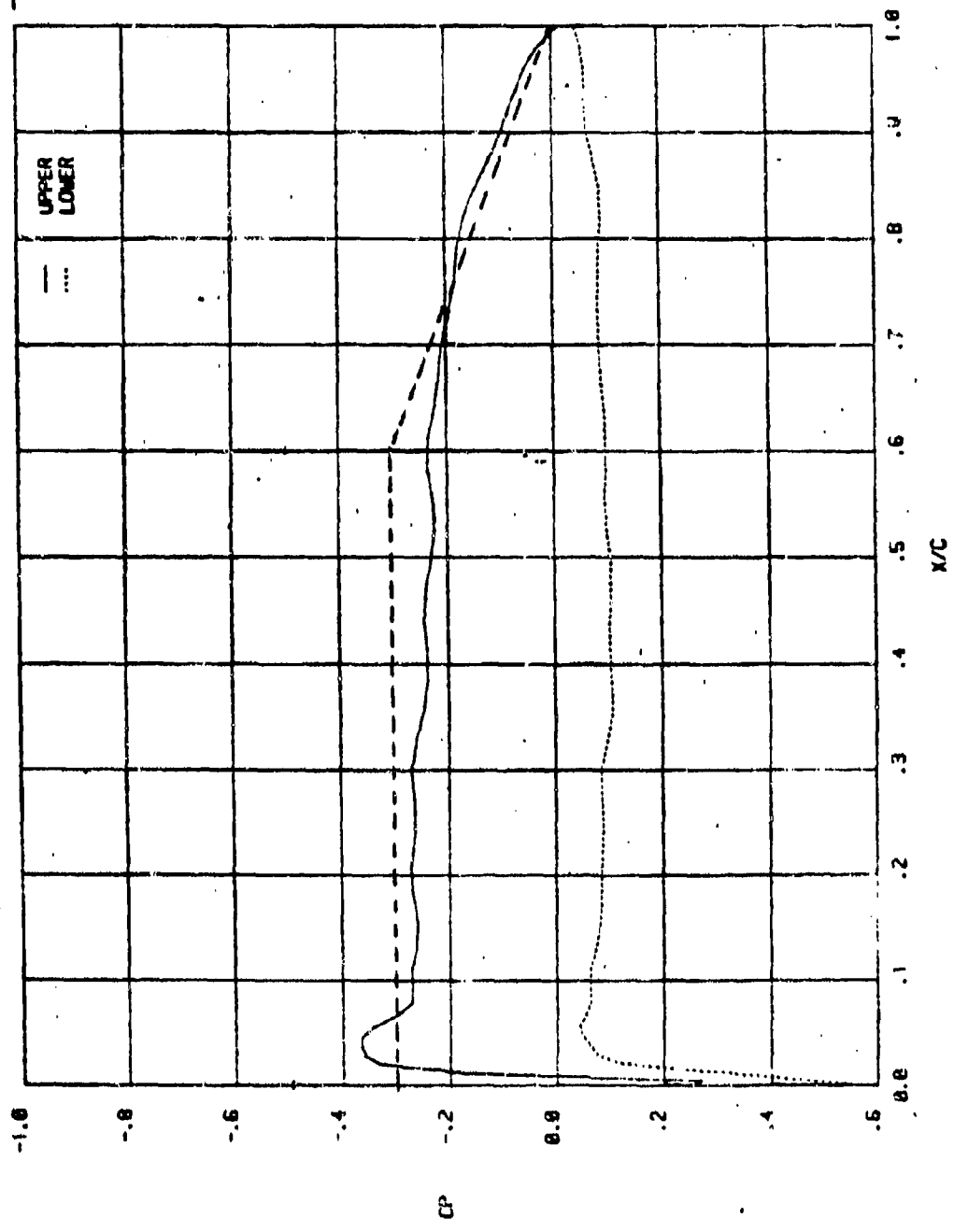


i) Pressure Distribution at $\eta = 0.25$

FIGURE 21. CONTINUED

K 13 Z 12.7636 MACH .0000 ALPHA 5.1850 CL .3035 CD .0121 XCP .4350

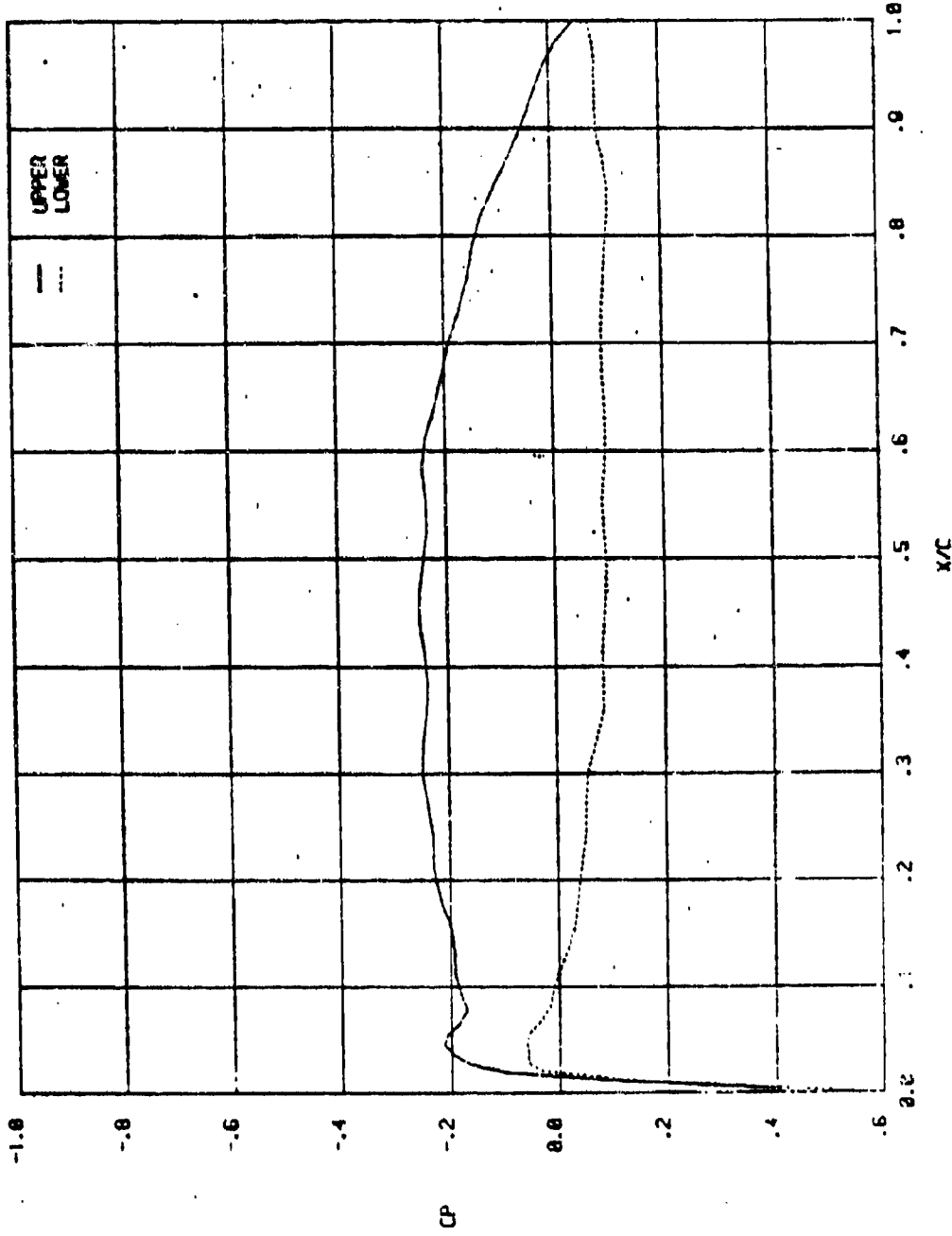
-----Goal
Pressure
Distribution



j) Pressure Distribution at $\eta = 0.47$

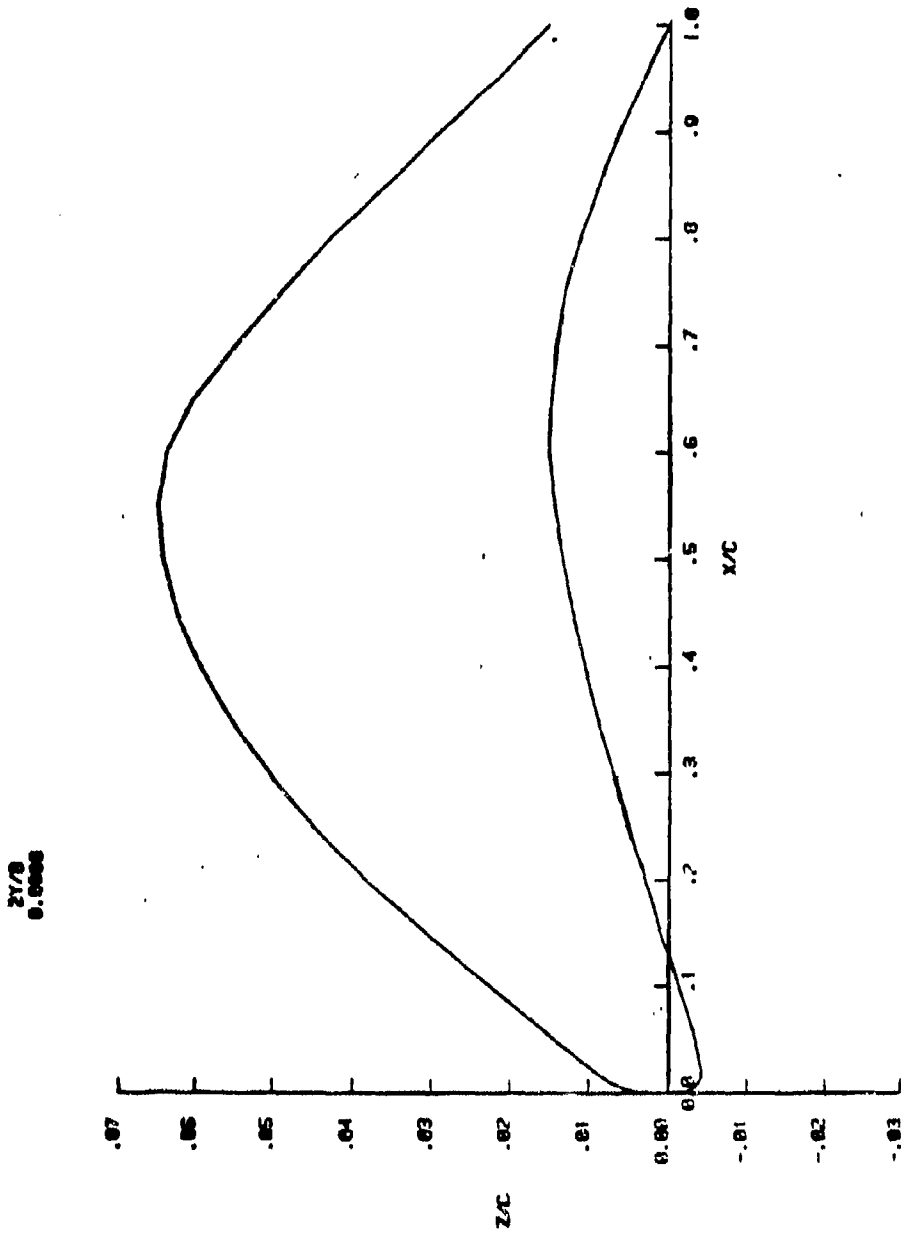
FIGURE j. CONTINUED

K 32 Z 21.6000 MACH .0000 ALPHA 5.1658 CL .2402 CD .0120 XDP .4881



k) Pressure Distribution at $\eta = 0.80$

FIGURE 21. COMPLETED



a) Root Airfoil

Figure 22. Final Aft Wing Transonic Design Geometry

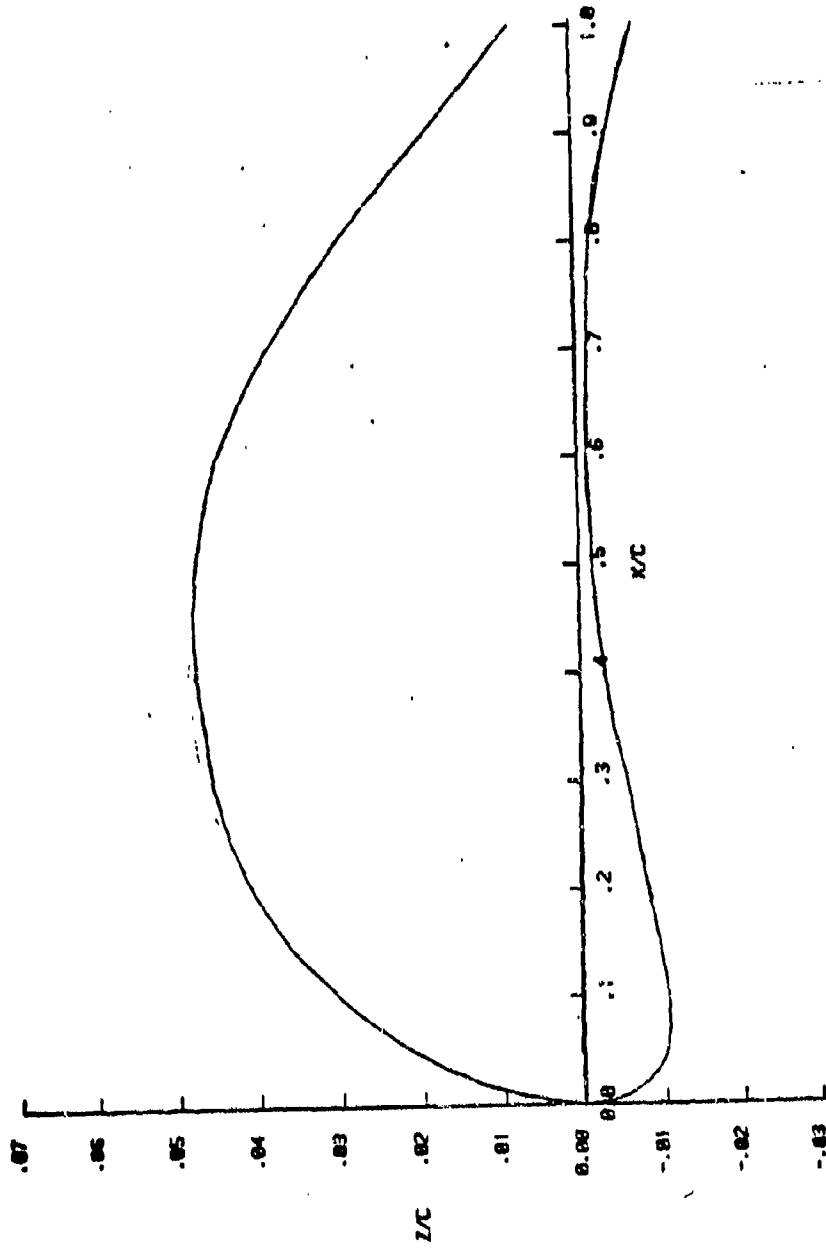
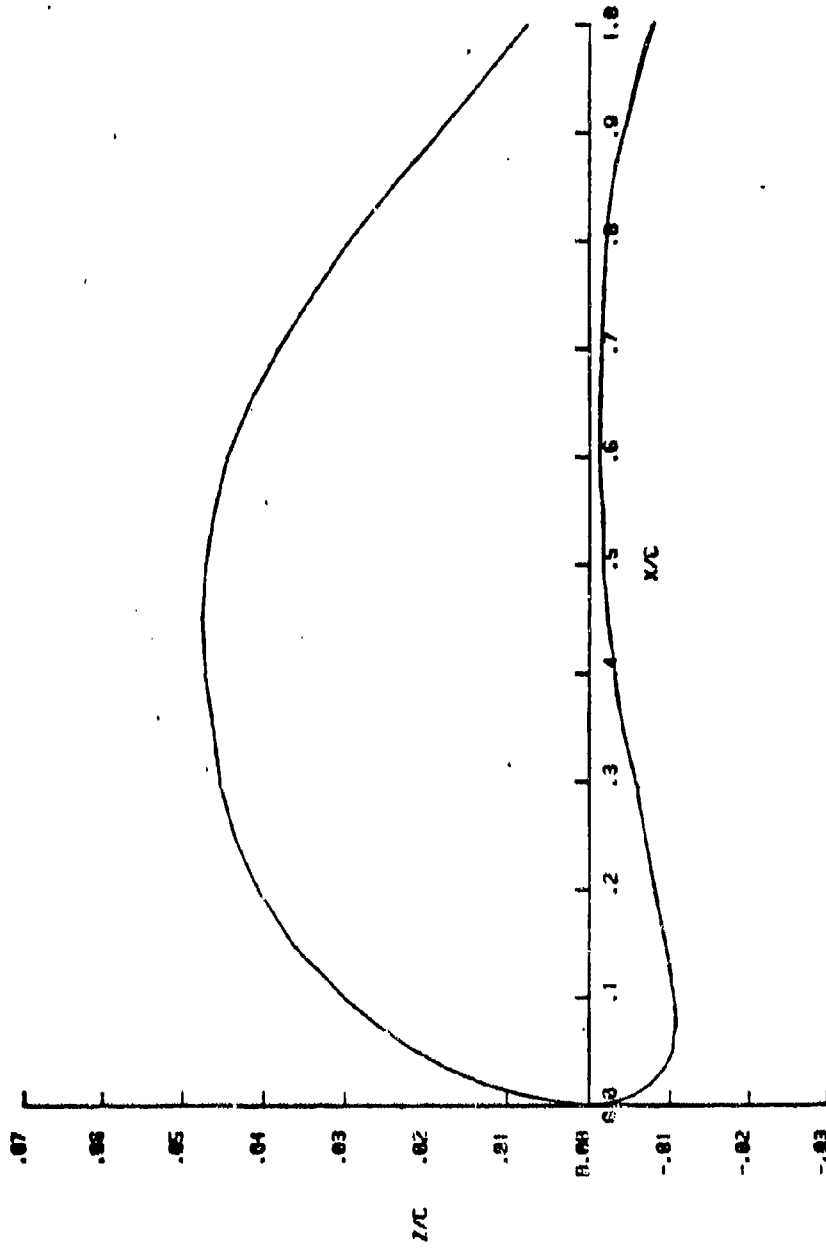
b) Airfoil at $\eta = 0.25$

FIGURE 22 CONTINUED

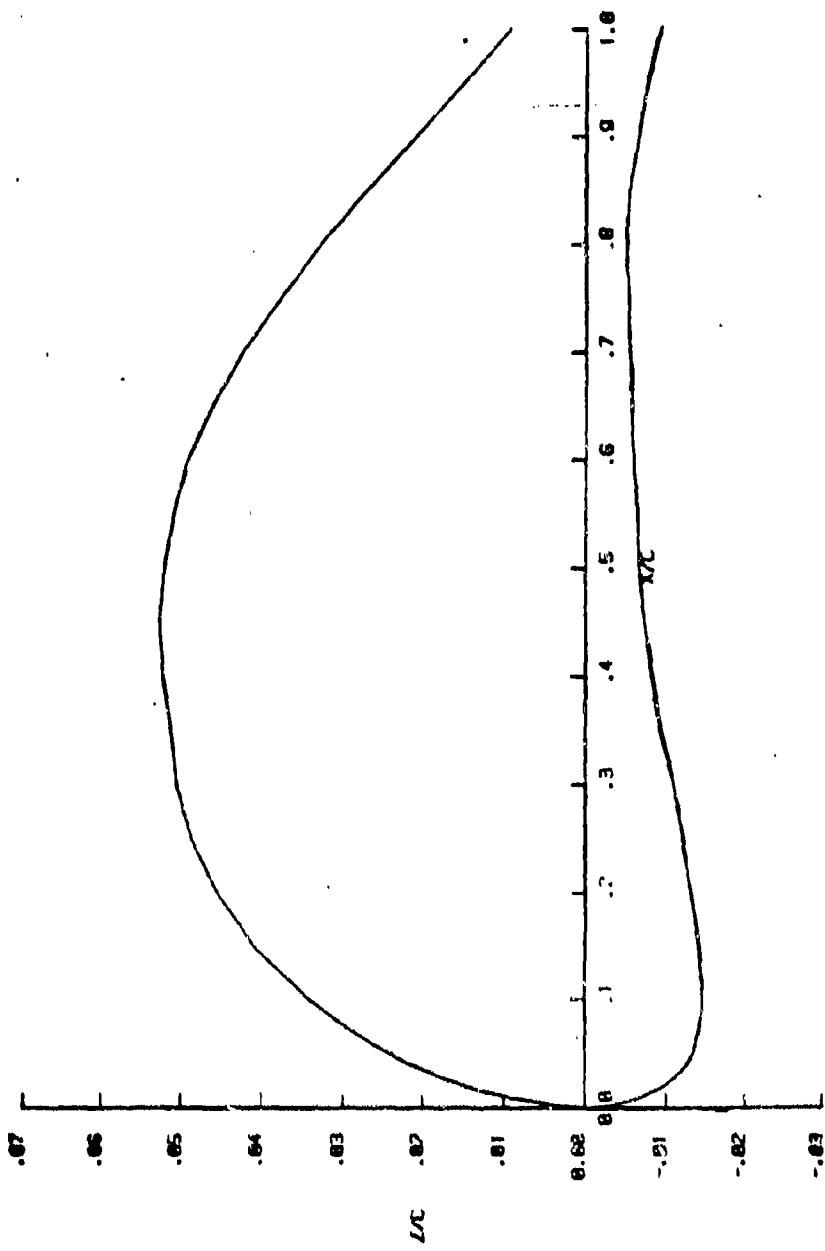
21/8
.5638



c) Airfoil at $\eta = 0.50$

FIGURE 22 CONTINUED

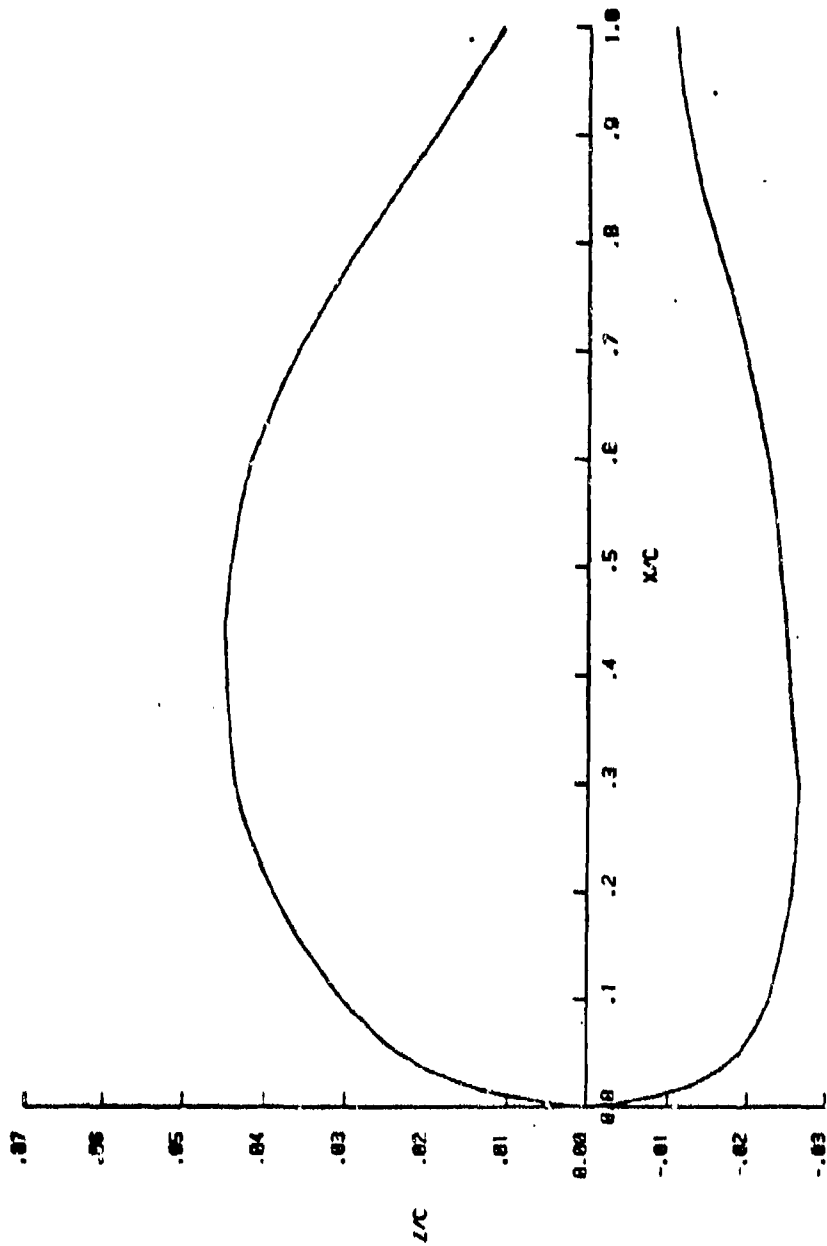
21/8
.0000



d) Airfoil at $h = 0.80$

FIGURE 22 CONTINUED

21/3
0.022
1.0020



e) Tip Airfoil

FIGURE 22 CONTINUED



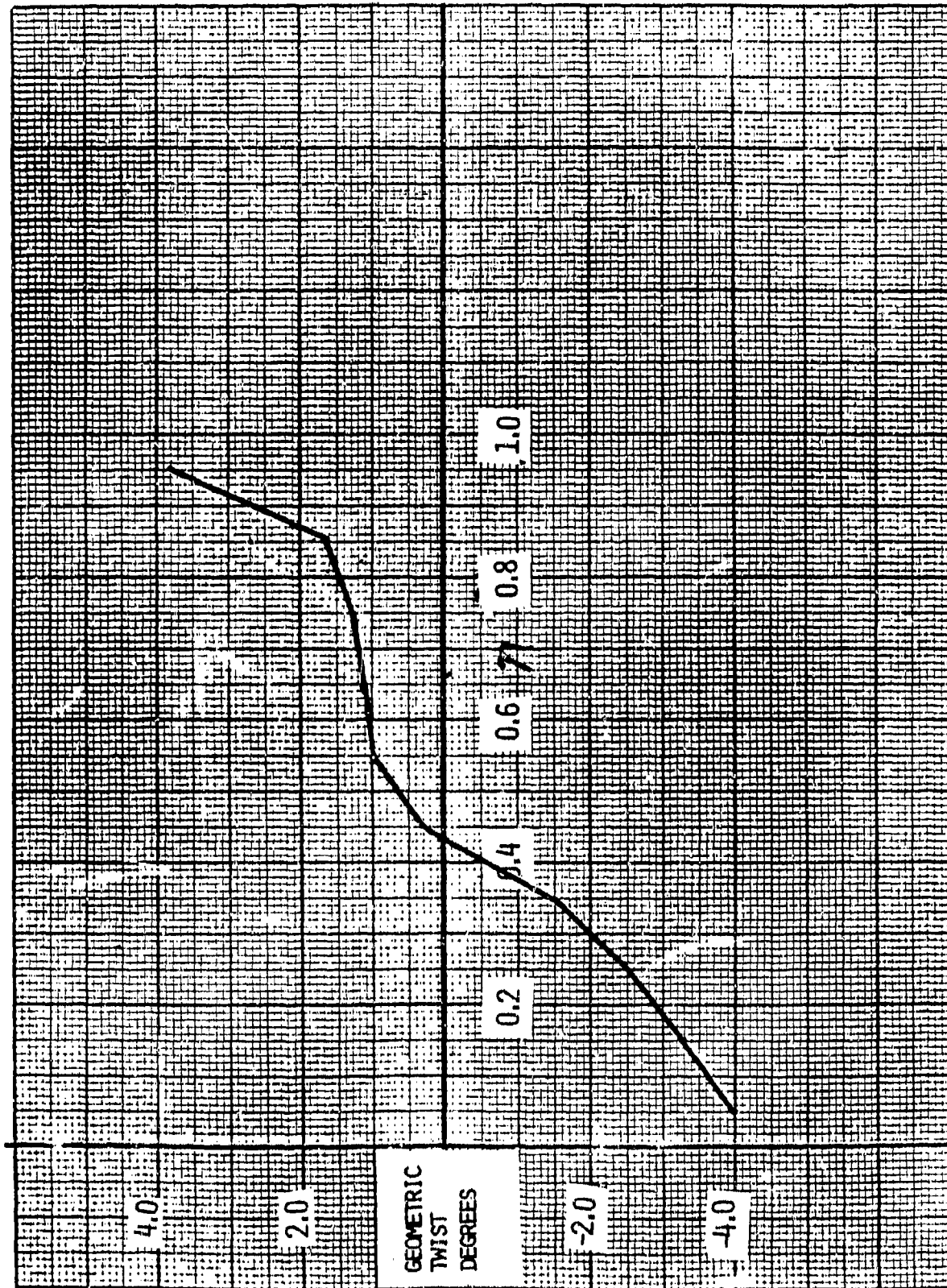
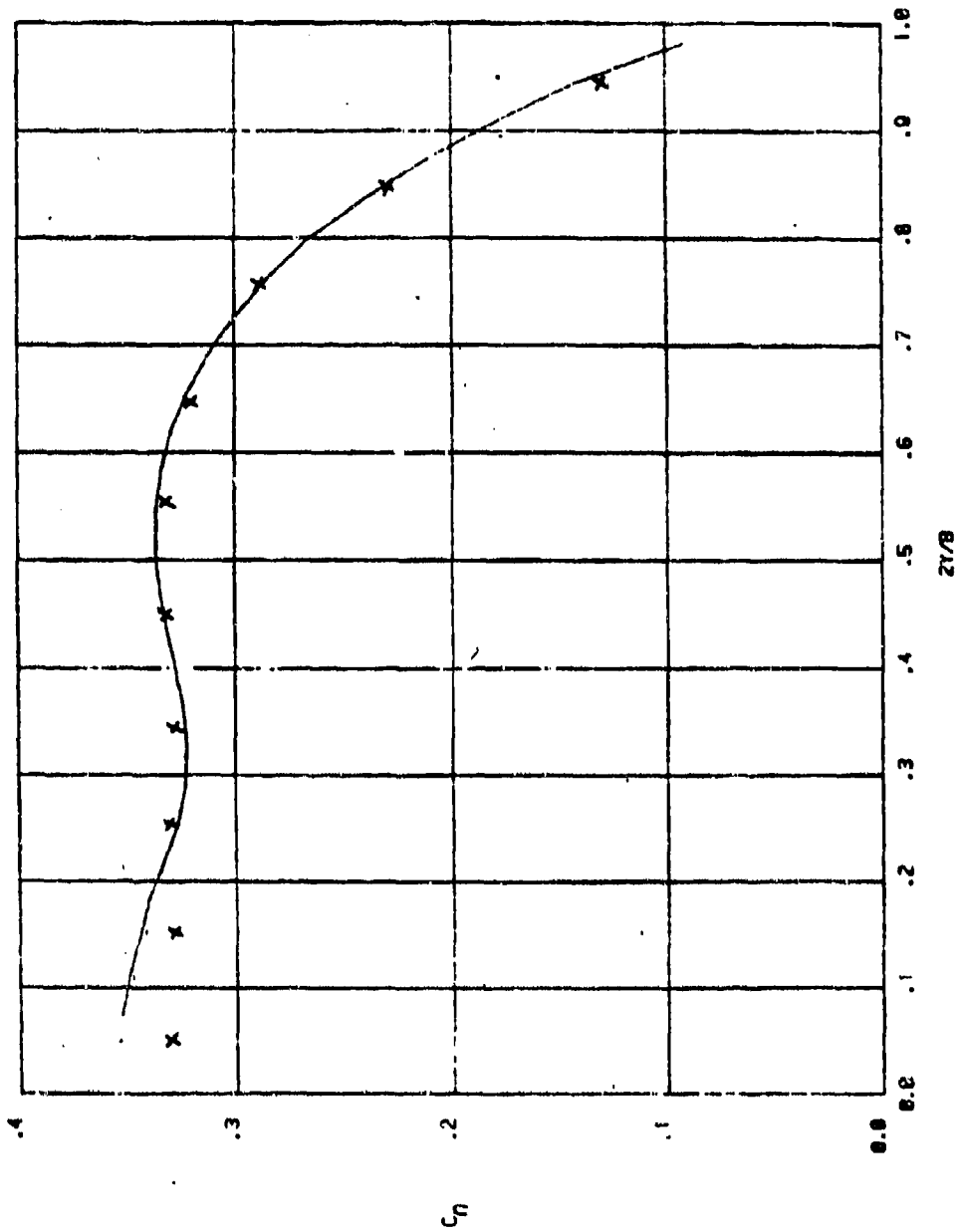


Figure 23. Final Aft Wing Transonic Design Twist

X LINEAR
DESIGN
TSD

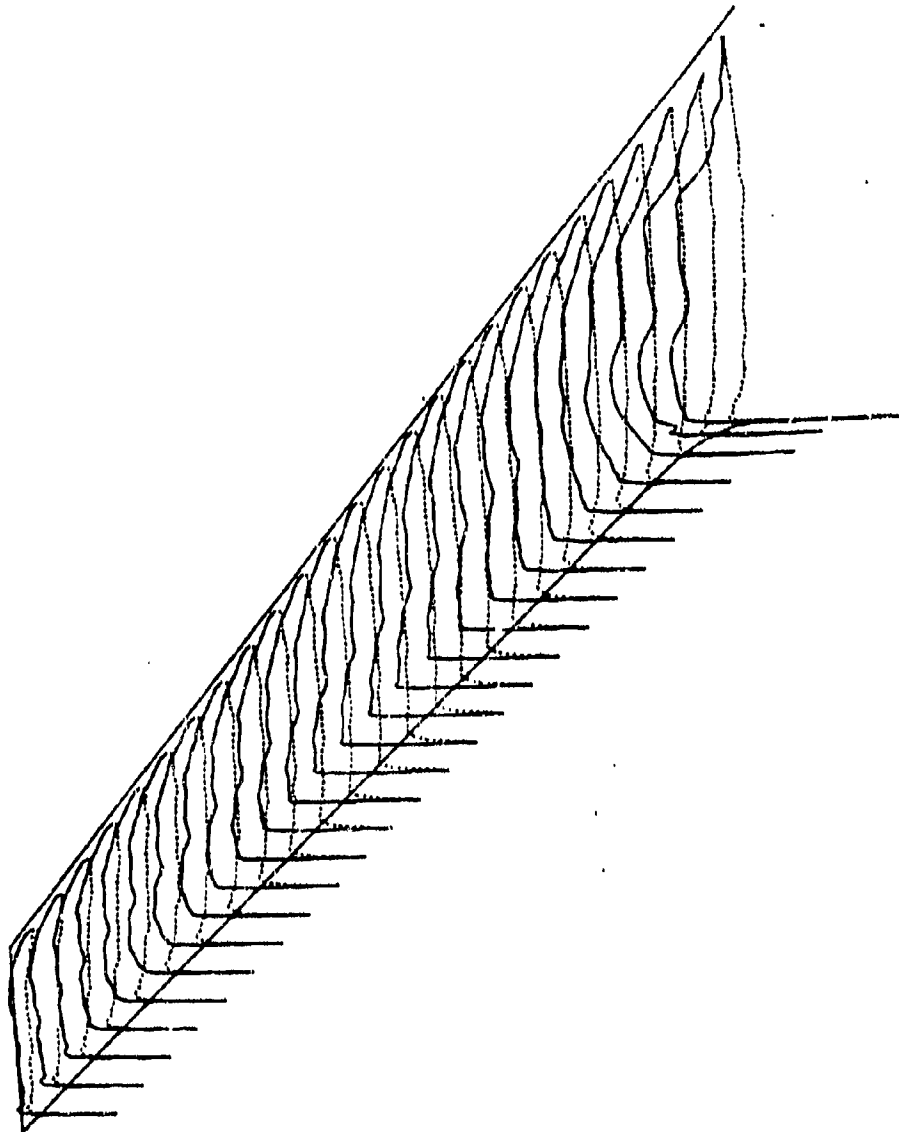
SECTION LIF MACH ALPHA
.0088 .5.6852



a) Span Loading

Figure 24. Final Aft Wing Transonic Design Flow Quality

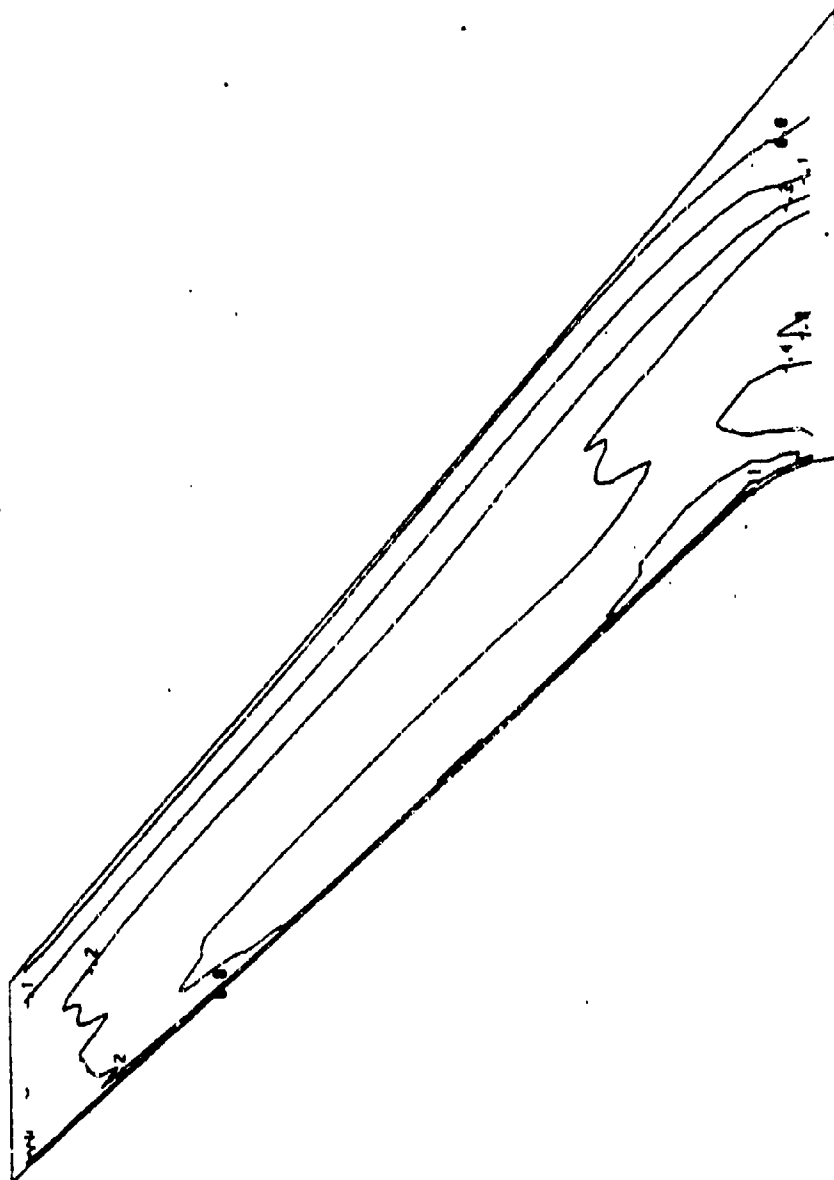
SURFACE PRESSURE MACH .000 ALPHA 5.000



b) Surface Pressure Isometric Distributions

FIGURE 24. CONTINUED

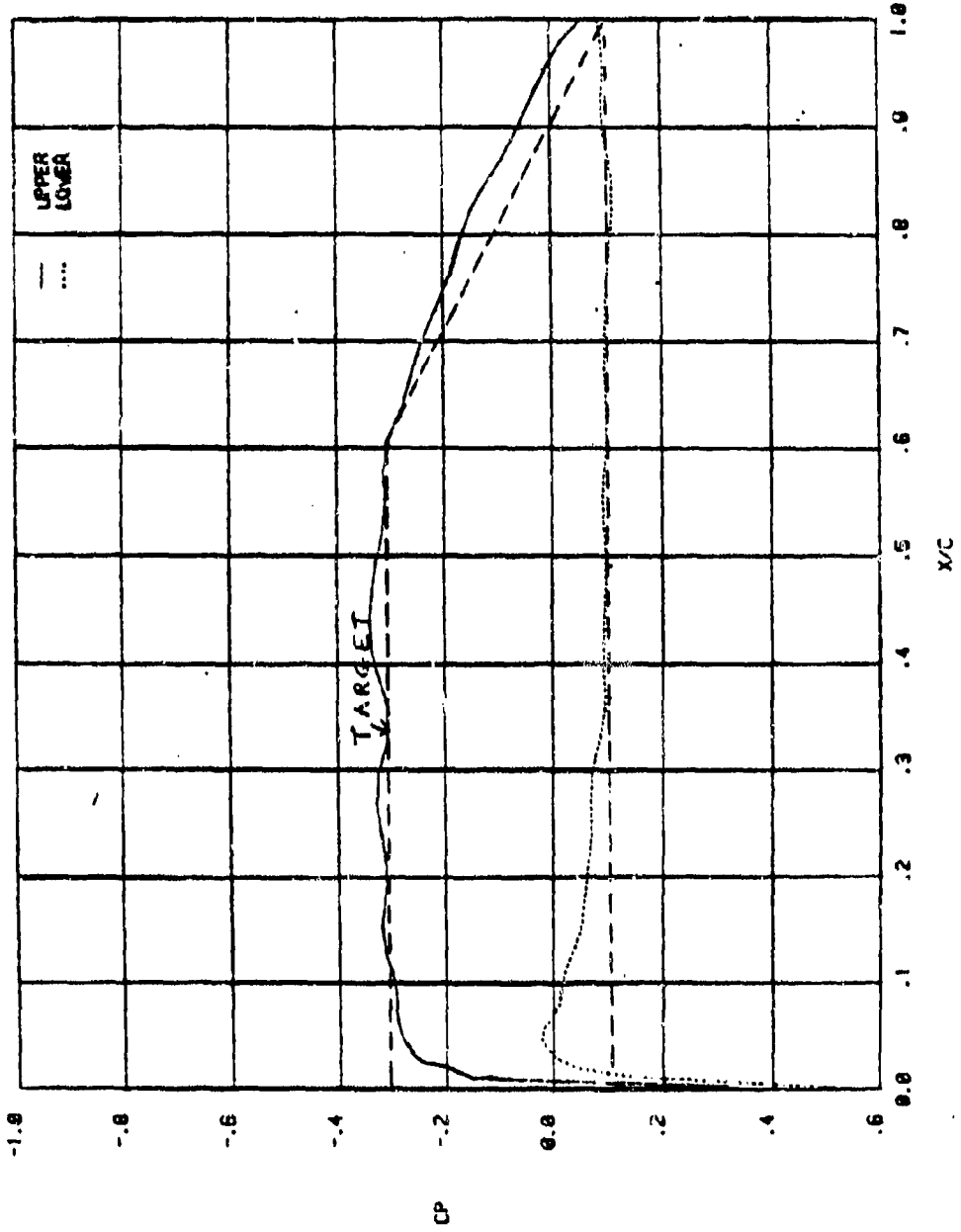
UPPER SURFACE ISOBARS
 MACH .988
 ALPHA 5.685



c) Upper Surface Isobars

FIGURE 24. CONTINUED

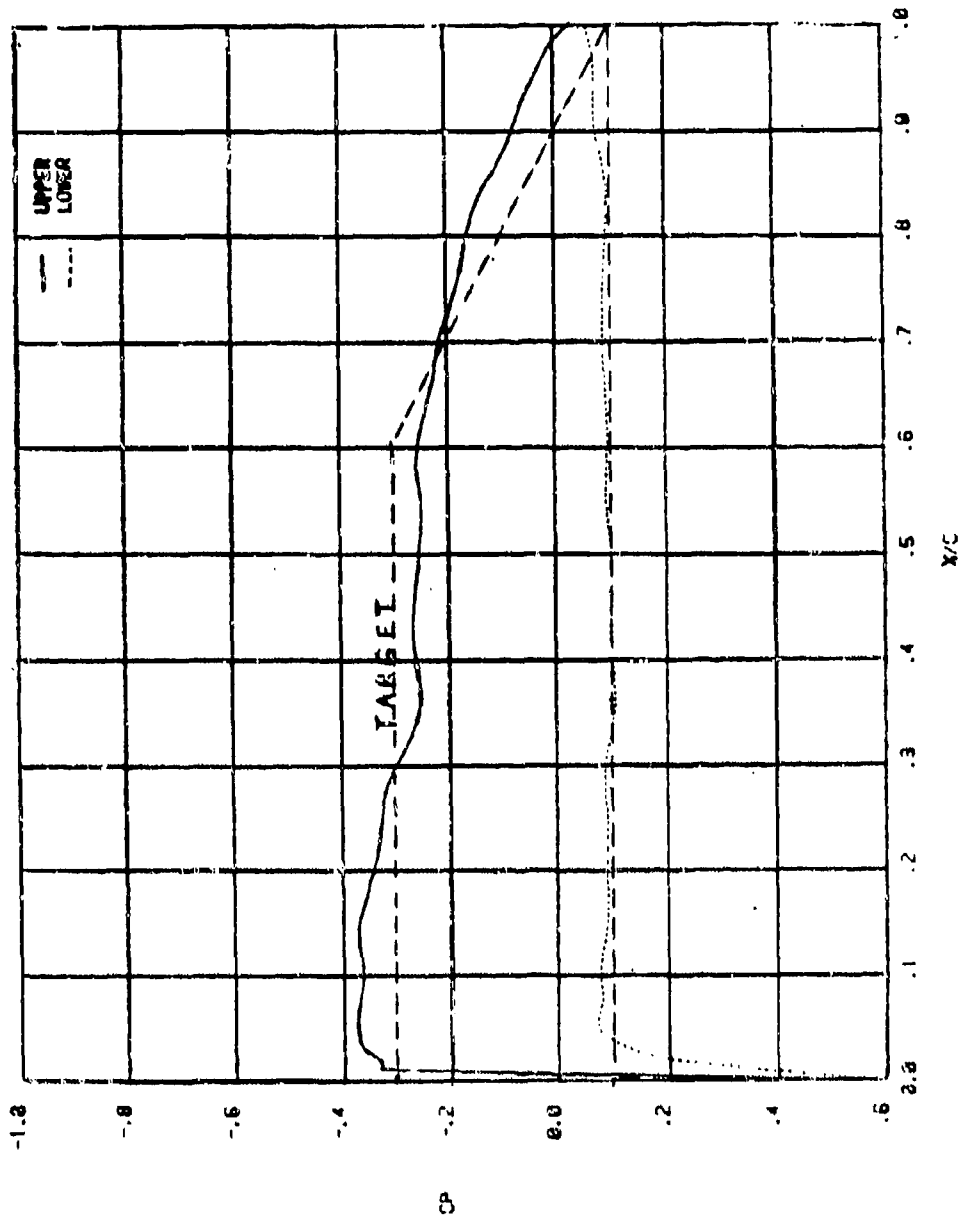
K 7
 Z 6.8727
 MACH .0080
 ALPHA 5.6850
 CL .3260
 CD .2387
 XCP .4557



d) Pressure Distribution at $\eta = 0.25$

FIGURE 24. CONTINUED

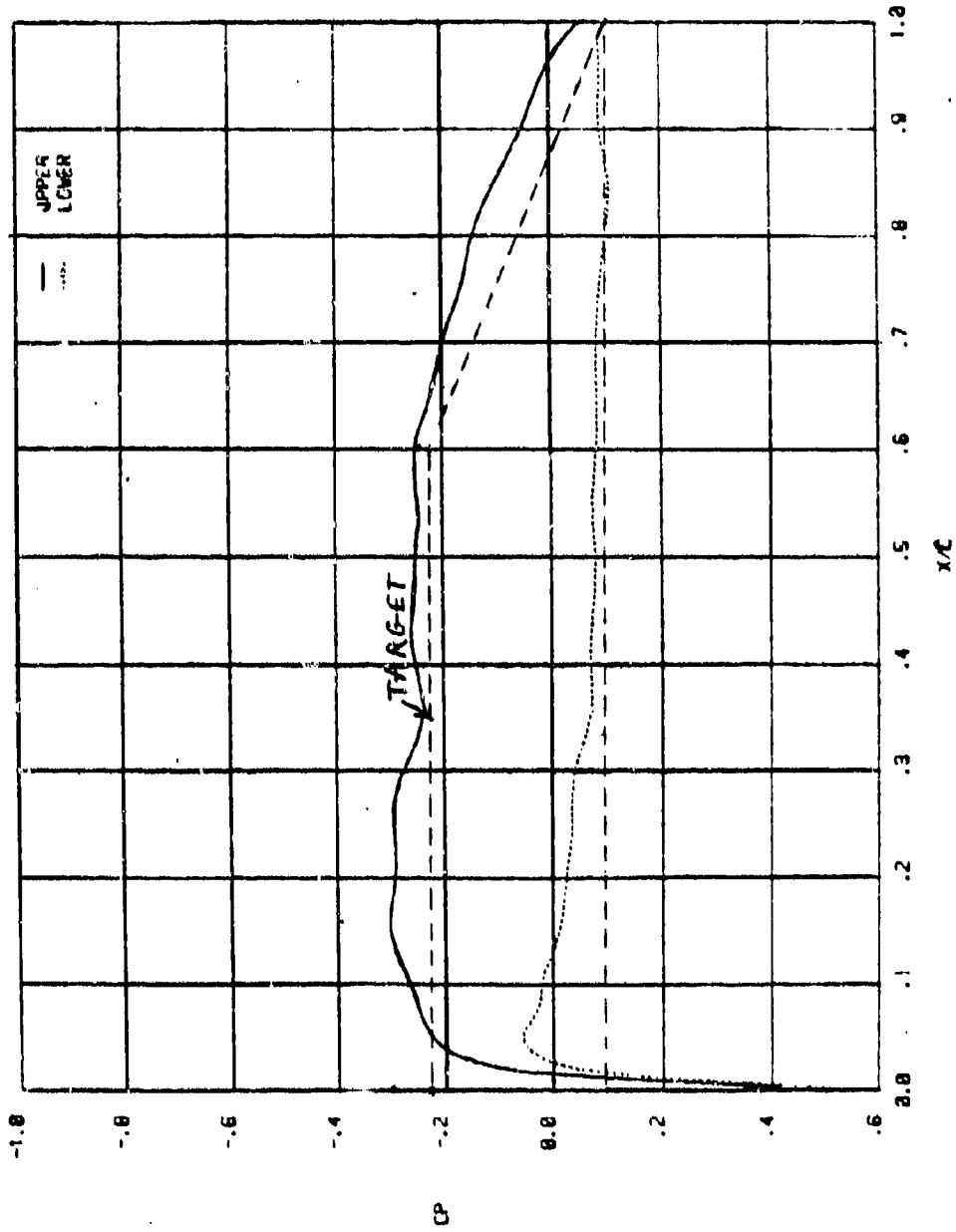
K 19 \bar{z} 2.7636 MAC-1 .2030 ALD-4 5.6858 CL .334 CD .0835 SFP .4711



e) Pressure Distribution at $\eta = 0.47$

FIGURE 24. CONTINUED

κ 22
 Z 2'.6820
 $MACH$.0008
 α 5.6053
 C_d .2847
 CD .8143
 XCP .4726



f) Pressure Distribution at η 0.80

FIGURE 24. CONTINUED

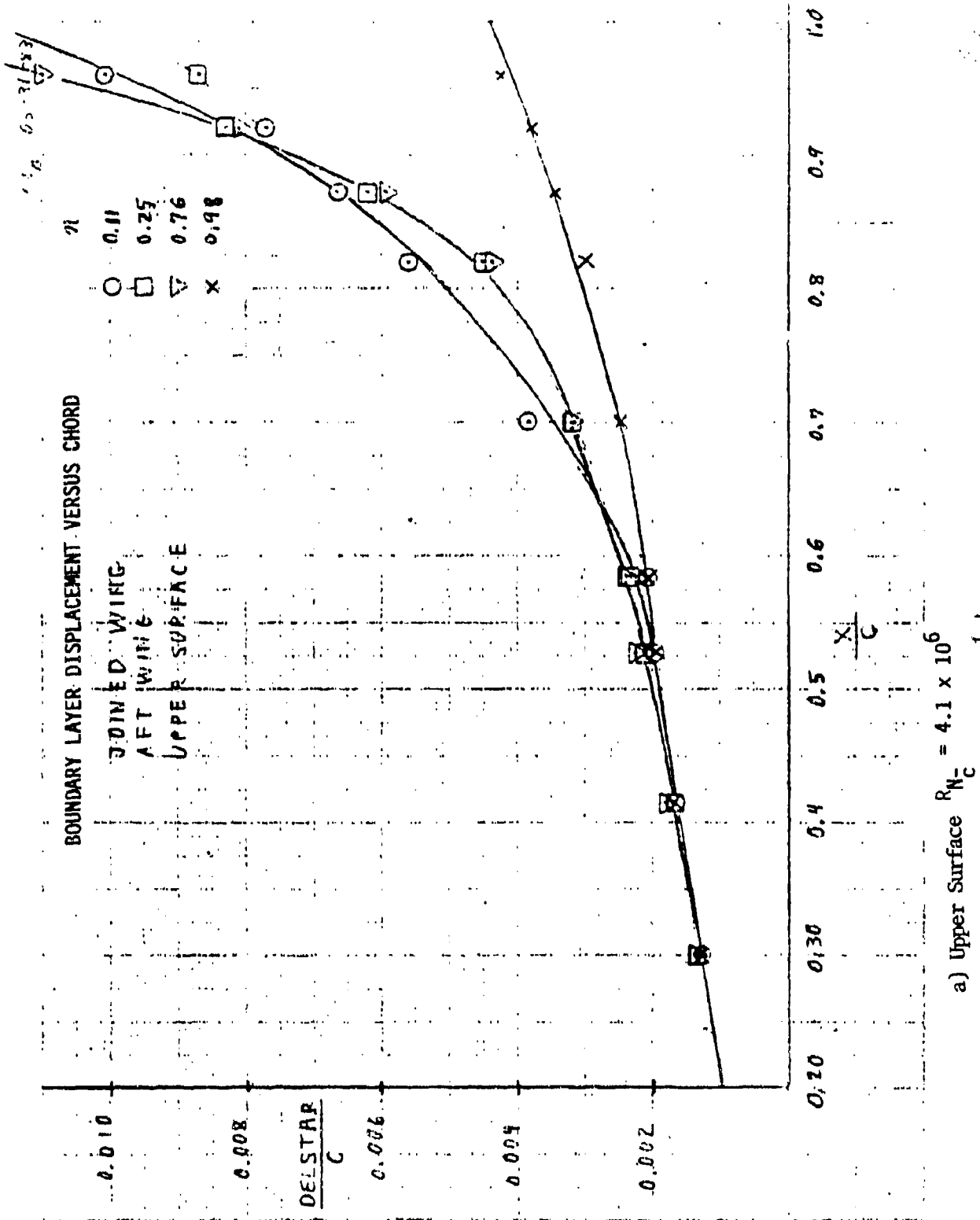
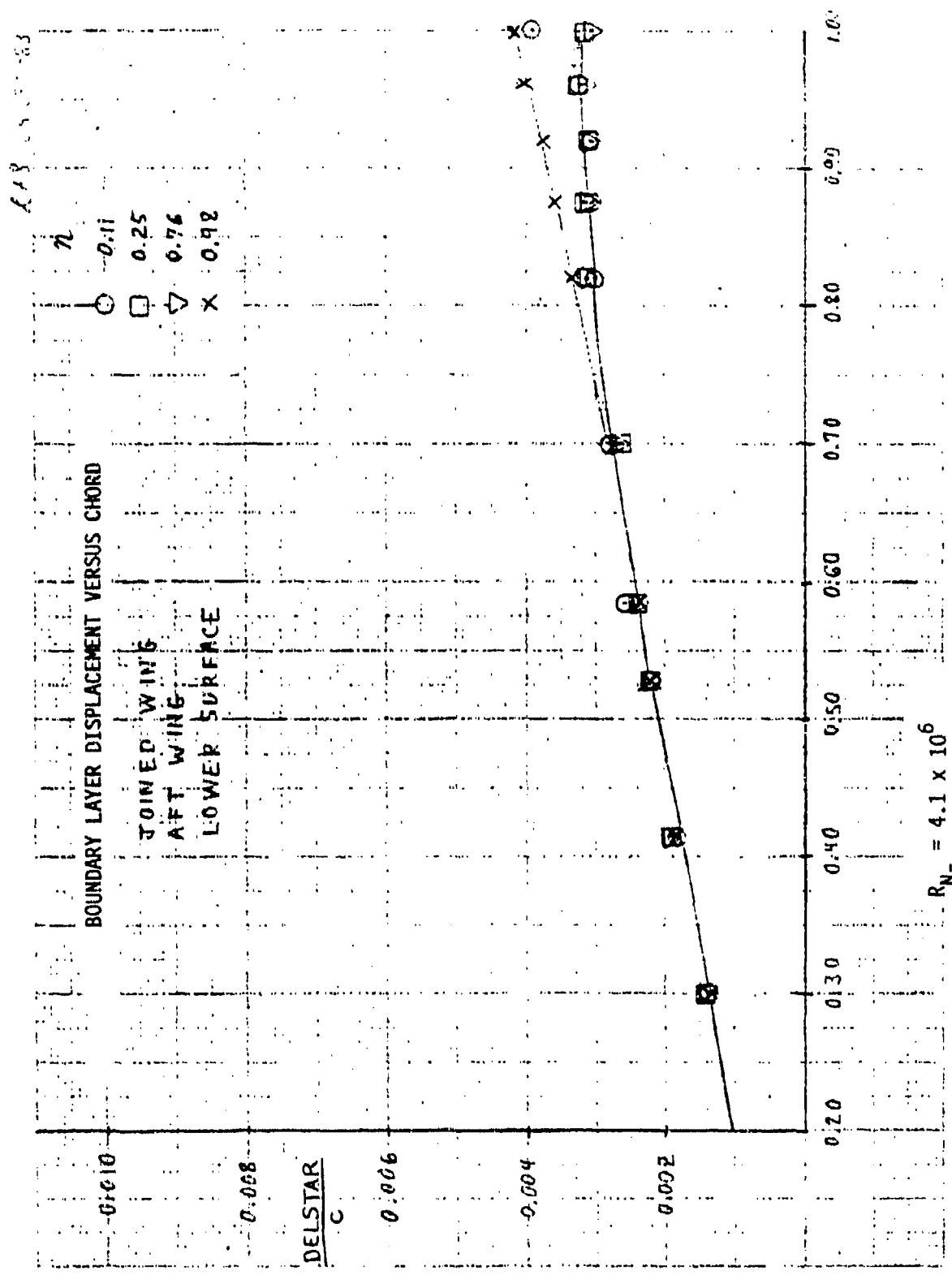


Figure 25. Final Aft Wing Transonic Boundary Layer Displacement Thickness



b) Lower Surface

FIGURE 25. CONCLUDED

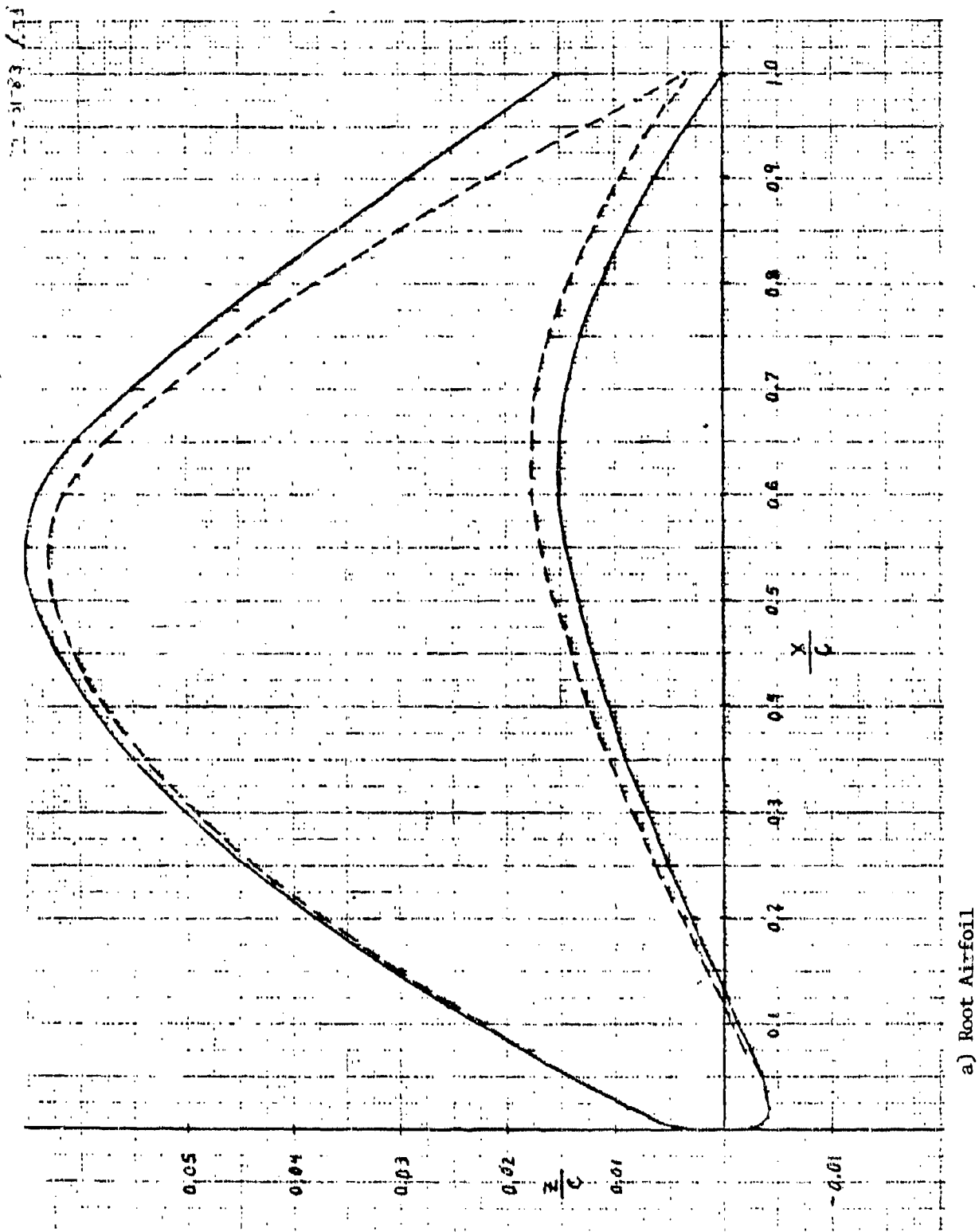
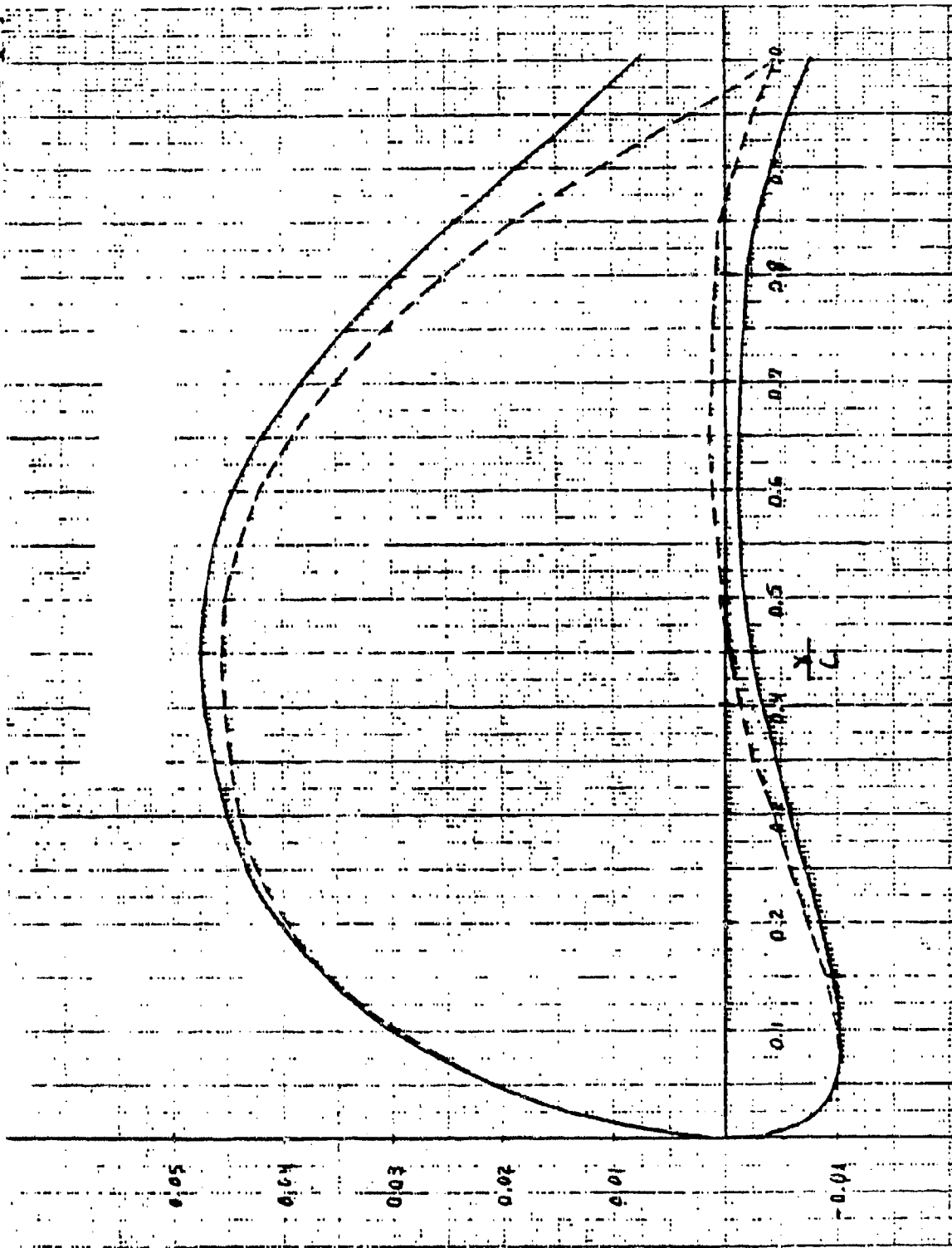
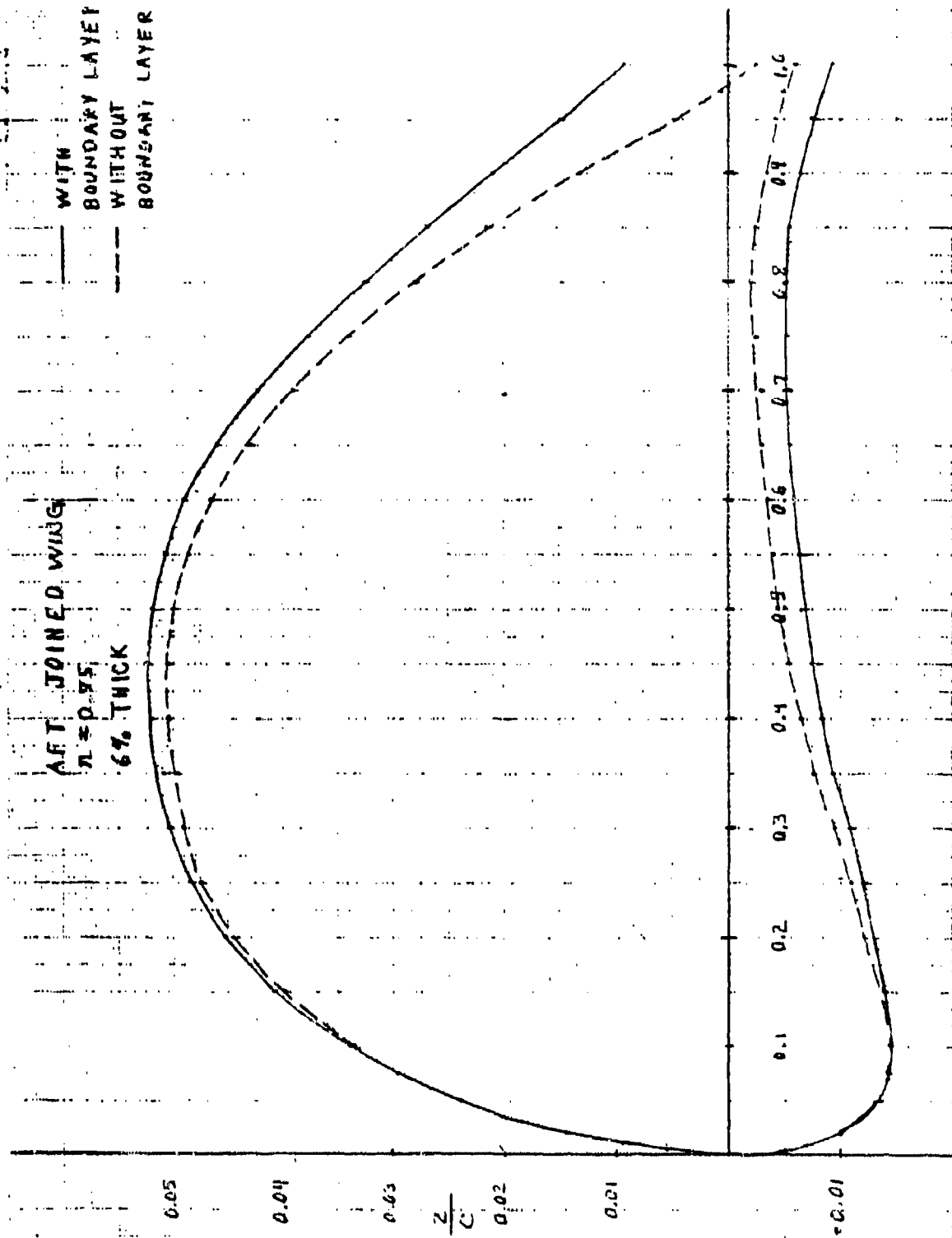


Figure 26. Aft Wing Airfoils With/Without Boundary Layer Displacement Thickness



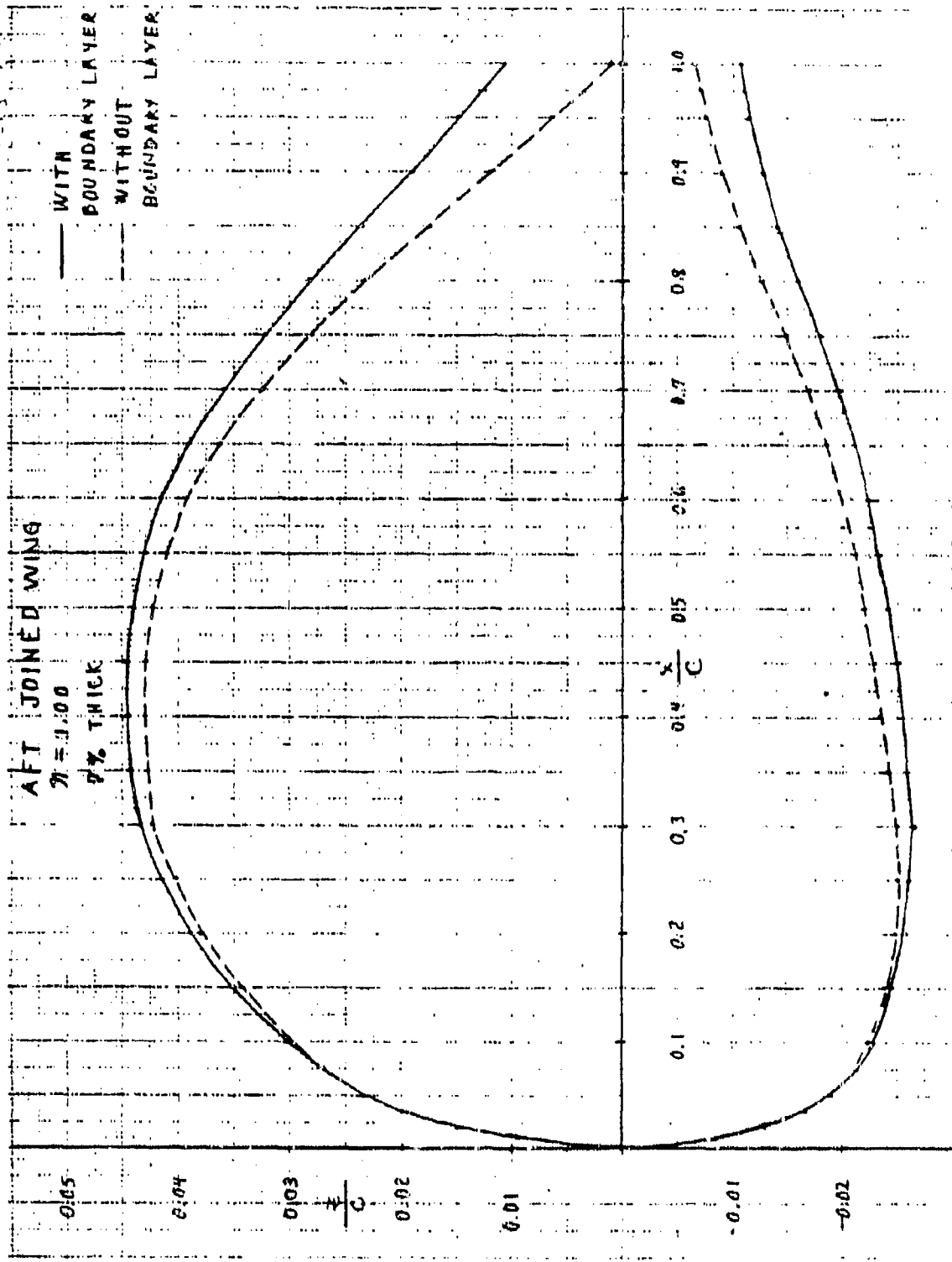
b) Airfoils from $0.25 \leq n \leq 0.50$

Figure 26 Continued



c) Airfoil With/Without Boundary Layer Displacement Thickness; $\eta = 0.75$

FIGURE 26. CONTINUED



d) Airfoil With/Without Boundary Layer Displacement Thickness; $\eta = 1.00$

FIGURE 26. CONCLUDED

JOINED WING 10TH SCALE MODEL

MACH: 0.000	PRESS: 1316.015	455.110 R	SREF: 6.328 FT2	KS: 0.0	FT	USED			
COMPONENT	SURF/PLAN AREA FT2	PFS LENGTH FT	TEMP: COMP	FF	X/L TRANS.	REYNOLDS NO.	SMOOTH CDF	ROUGH CDF	USED
FUSELAGE	10.8	6.003	1.095	1.000	0.050	3.28206E+07	0.00389	0.0	0.00389
HALF TAIL FAIRING	1.0	2.003	1.043	1.000	0.050	0.77704E+08	0.00046	0.0	0.00046
WING TIP FAIRING	1.2	1.958	1.022	1.000	0.050	0.18730E+08	0.00054	0.0	0.00054
PANEL FWD WING	0.8	1.833	1.000	1.000	0.050	4.04906E+06	0.00040	0.0	0.00040
PANEL FWD WING	0.8	0.984	1.000	1.000	0.050	4.61666E+06	0.00038	0.0	0.00038
PANEL FWD WING	0.8	0.934	1.000	1.000	0.050	4.36335E+06	0.00037	0.0	0.00037
PANEL FWD WING	0.7	0.884	1.000	1.000	0.050	4.15120E+06	0.00035	0.0	0.00035
PANEL FWD WING	0.6	0.835	1.000	1.000	0.050	3.91693E+06	0.00034	0.0	0.00034
PANEL FWD WING	0.6	0.785	1.000	1.000	0.050	3.68548E+06	0.00032	0.0	0.00032
PANEL FWD WING	0.5	0.735	1.000	1.000	0.050	3.45365E+06	0.00030	0.0	0.00030
PANEL FWD WING	0.4	0.681	1.000	1.000	0.050	3.24100E+06	0.00024	0.0	0.00024
PANEL FWD WING	0.4	0.650	1.000	1.000	0.050	3.04966E+06	0.00023	0.0	0.00023
PANEL FWD WING	1.1	0.611	1.000	1.000	0.050	2.88572E+06	0.00020	0.0	0.00020
PANEL AFT INBD W	1.1	1.145	1.000	1.000	0.050	5.37528E+06	0.00053	0.0	0.00053
PANEL AFT INBD W	1.1	1.016	1.000	1.000	0.050	4.78883E+06	0.00052	0.0	0.00052
PANEL AFT OUTBD	0.8	0.955	1.000	1.000	0.050	4.78883E+06	0.00044	0.0	0.00044
PANEL AFT OUTBD	0.8	0.903	1.000	1.000	0.050	4.24046E+06	0.00038	0.0	0.00038
PANEL AFT OUTBD	0.8	0.852	1.000	1.000	0.050	4.0007E+06	0.00037	0.0	0.00037
PANEL AFT OUTBD	0.7	0.799	1.000	1.000	0.050	3.74018E+06	0.00036	0.0	0.00036
PANEL AFT OUTBD	0.6	0.745	1.000	1.000	0.050	3.40615E+06	0.00034	0.0	0.00034
PANEL AFT OUTBD	0.6	0.695	1.000	1.000	0.050	3.20068E+06	0.00029	0.0	0.00029
PANEL AFT OUTBD	0.4	0.652	1.000	1.000	0.050	3.0003E+06	0.00022	0.0	0.00022
PANEL AFT OUTBD	0.4	0.613	1.000	1.000	0.050	2.87810E+06	0.00022	0.0	0.00022
PANELED VERTICAL	1.0	1.125	1.000	1.000	0.050	5.20010E+06	0.00042	0.0	0.00042
PANELED VERTICAL	1.0	1.125	1.000	1.000	0.050	5.28066E+06	0.00050	0.0	0.00050

** TOTAL WET SURFACE AREA = 28.56 FT2
 ** TOTAL SKIN FRICTION DRAG = 0.01252

Figure 27. Joined Wing Estimated Turbulent Friction Drag

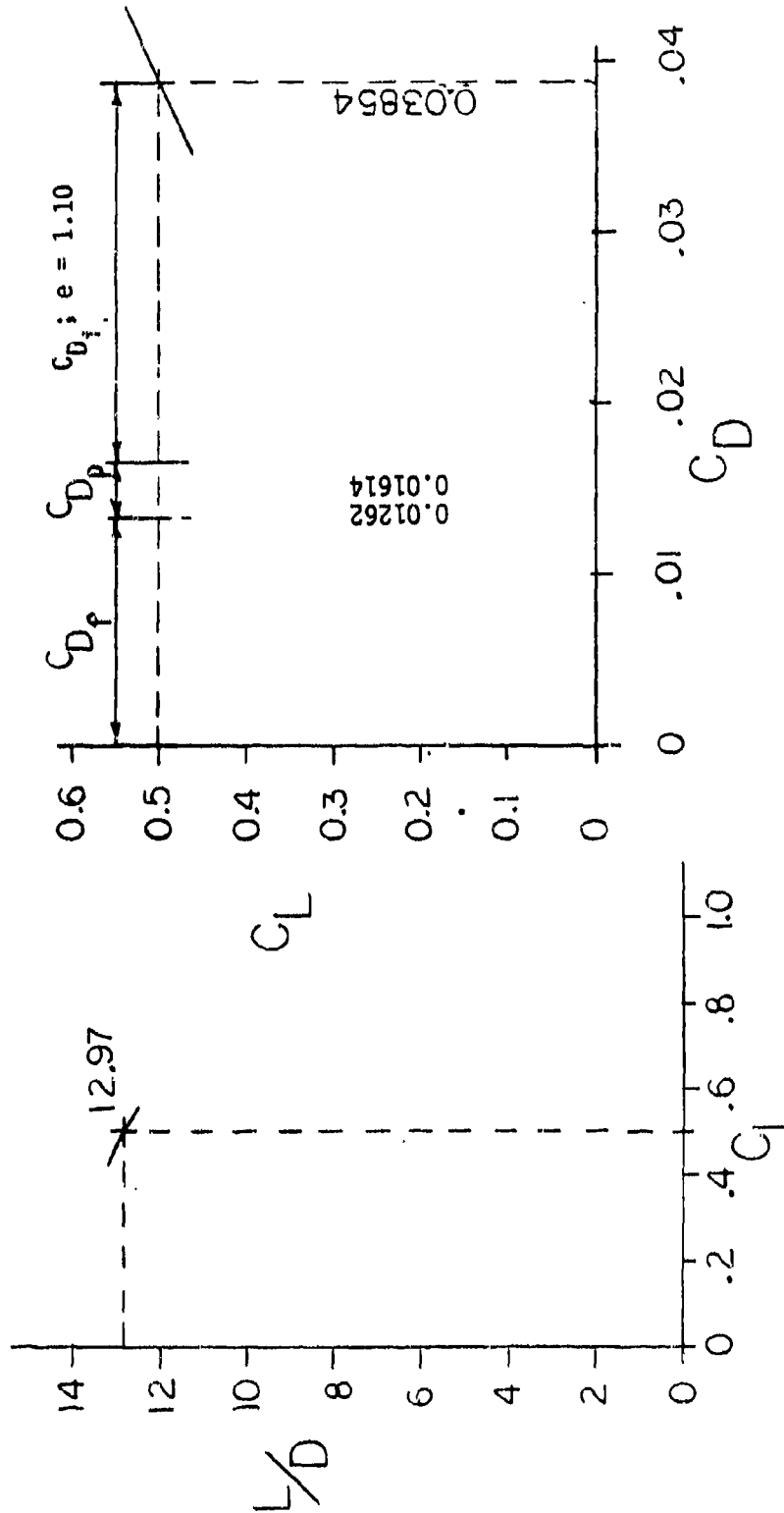


Figure 28. Joined Wing Trimmed Theoretical Design Performance at $M = -.90, C_L = 0.50$

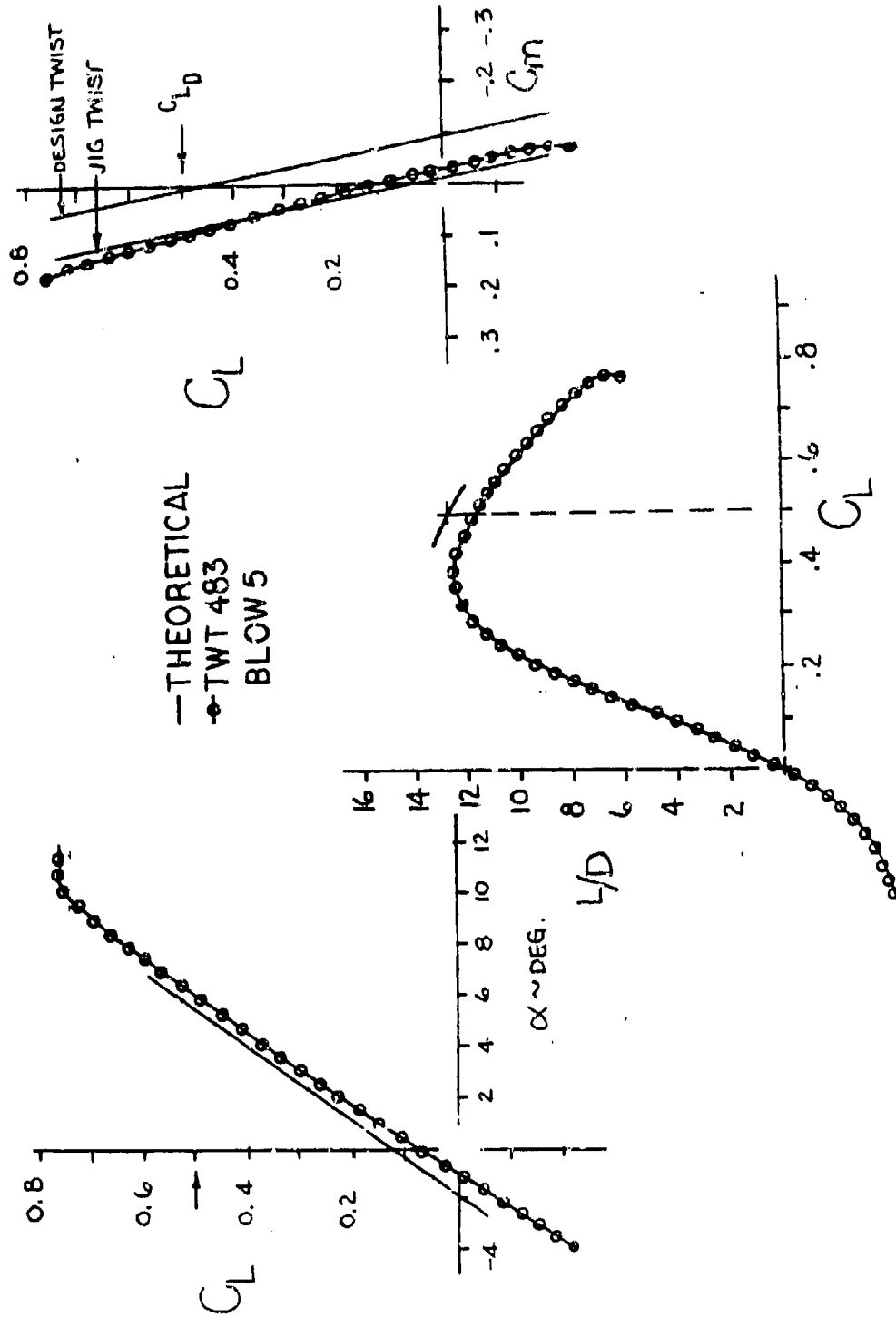


Figure 29. Joined Wing Force Results, First Test Entry, M = 0.90

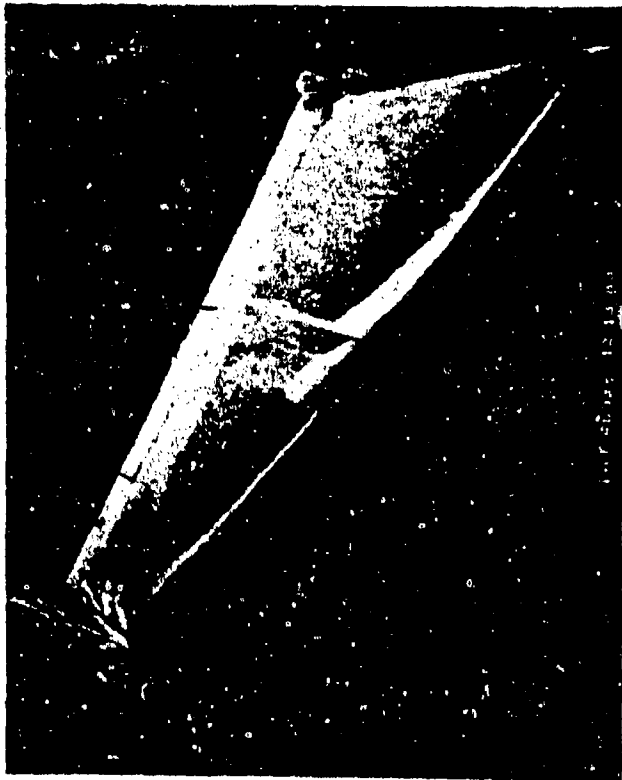


Figure 30. Joined Wing Oil Flow Photographs, First Test Entry, Forward Wing, $M = 0.90$

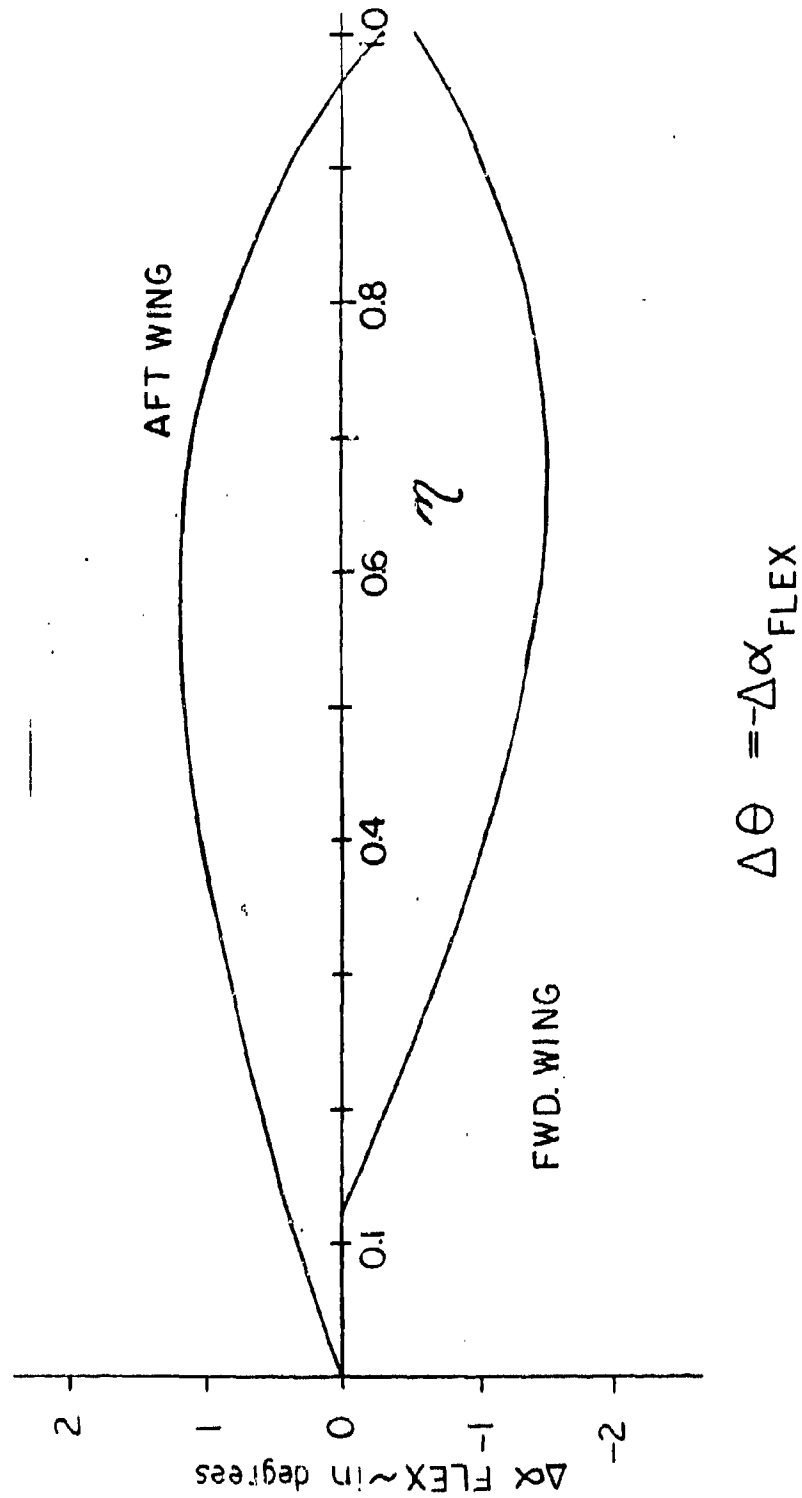


Figure 31. Joined Wing Theoretical Elastic Twist Increments, $M = 0.90$,
 $C_L = 0.50$, $q = 1120$ psf

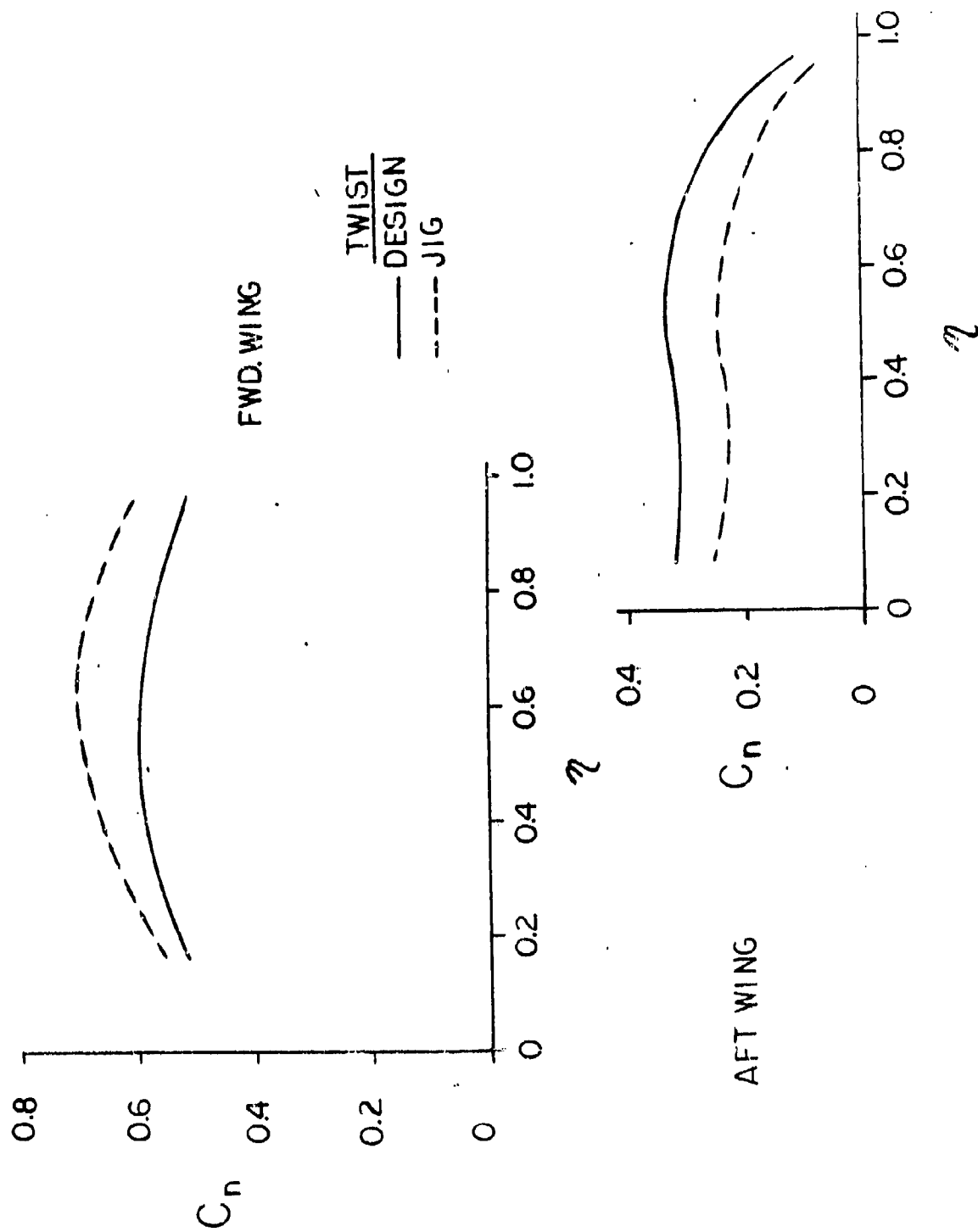


Figure 32. Joined Wing Linear Spanload for Design and Jig Twist at $M = 0.90$

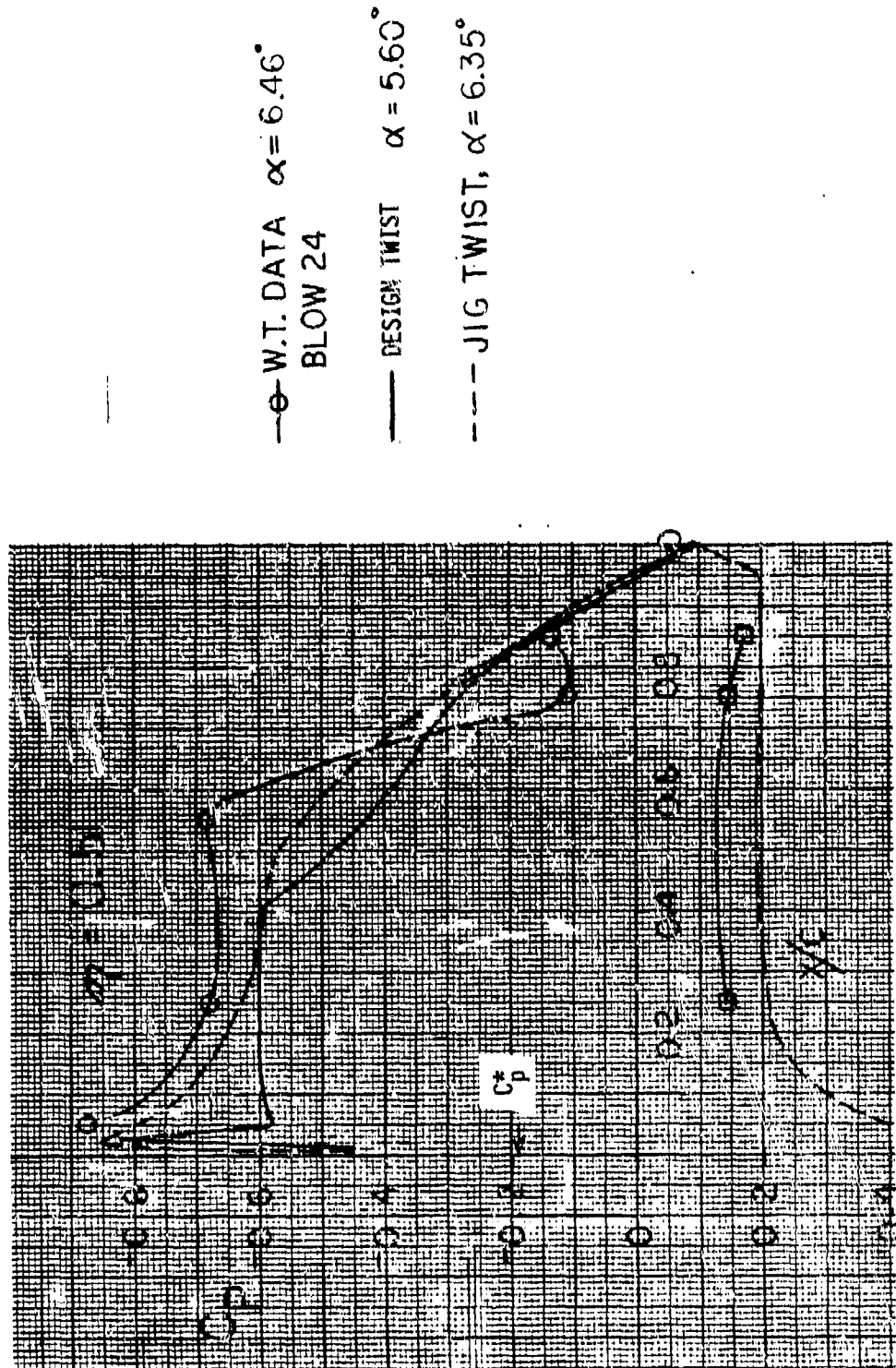
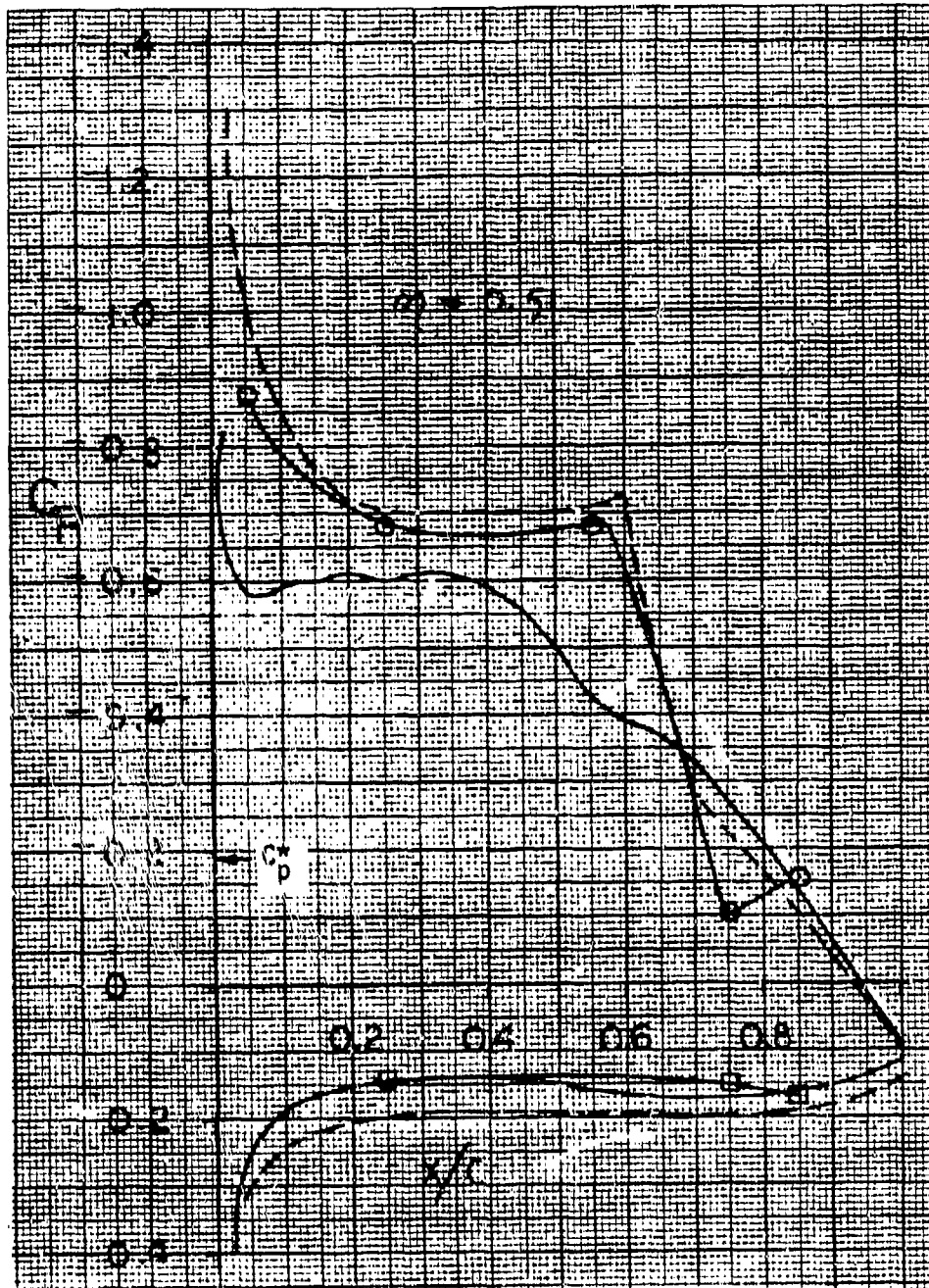


Figure 33. Joined Wing Transonic Small Disturbance Pressure Distribution Comparison, Forward Wing, $M = 0.90$



—○— W.T. DATA BLOW 24 $\alpha = 6.46^\circ$
 ——— DESIGN TWIST $\alpha = 5.60^\circ$
 - - - JIG TWIST $\alpha = 6.35^\circ$

Figure 34. Joined Wing Full Potential Pressure Distribution Comparison, Forward Wing, $M = 0.90$

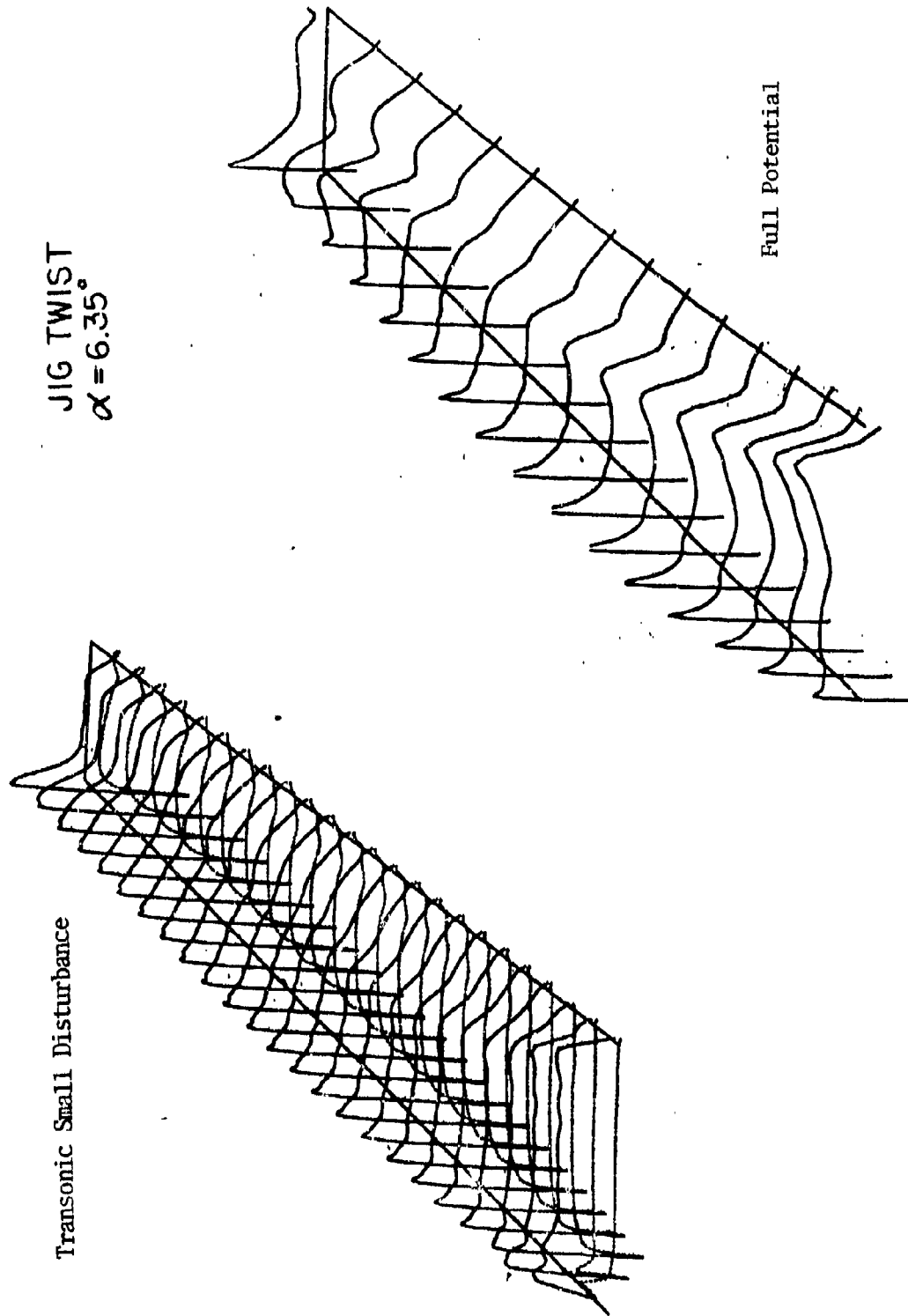
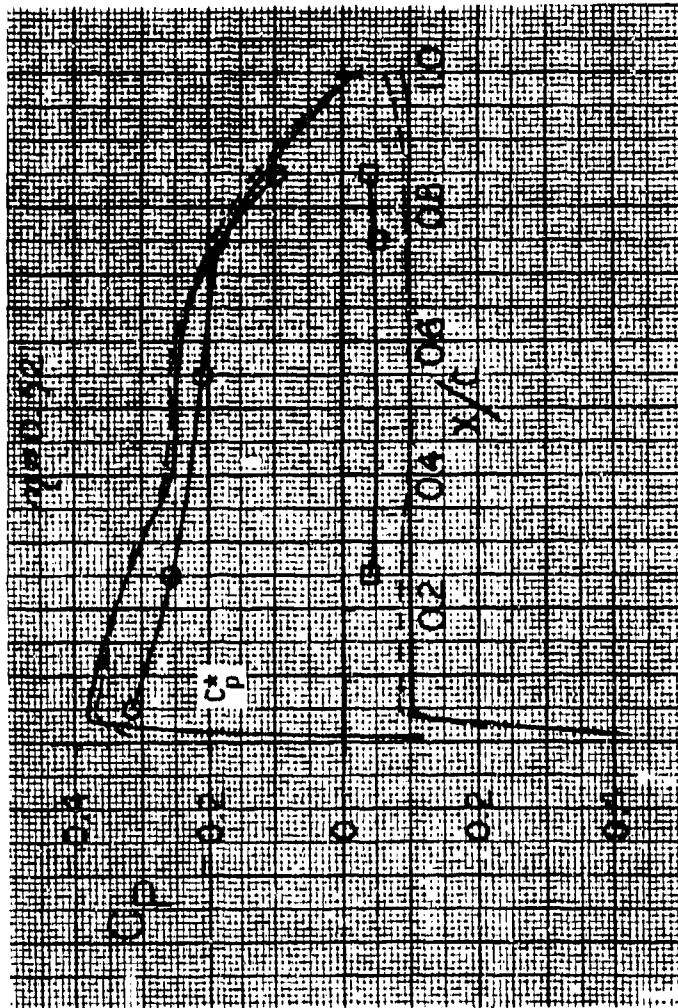


Figure 35. Joined Wing Transonic Small Disturbance and Full Potential Pressure Distribution Comparison, Forward Wing, $M = 0.90$, $C_L = 0.50$



—○— W.T. DATA BLOW 24 $\alpha = 6.46^\circ$
 ——— DESIGN TWIST $\alpha = 5.60^\circ$
 - - - JIG TWIST $\alpha = 6.50^\circ$

Figure 36. Joined Wing Transonic Small Disturbance Pressure Distribution Comparison, Aft Wing, $M = 0.90$, $C_L = 0.50$

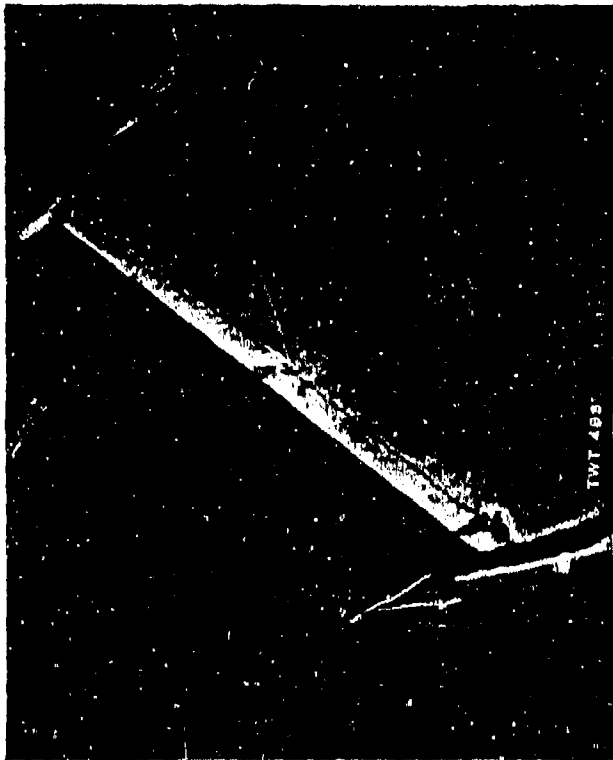


Figure 37. Joined Wing Oil Flow Photographs, First Test Entry, Aft Wing,
 $M = 0.90$

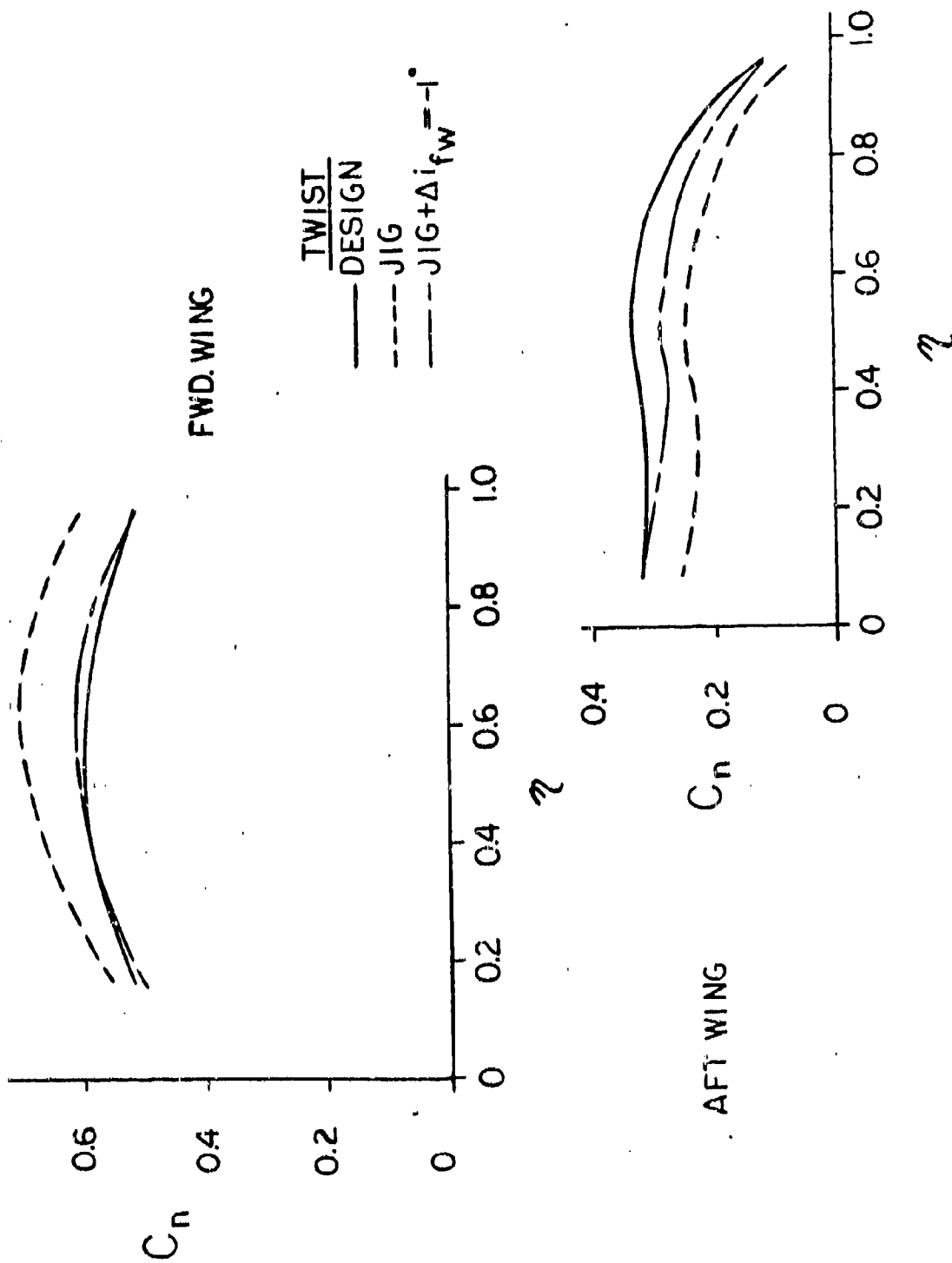


Figure 38. Effect of Jointed Wing Incidence Change on Linear Spanload Distribution at $M = 0.90$, $\alpha = 5.60^\circ$

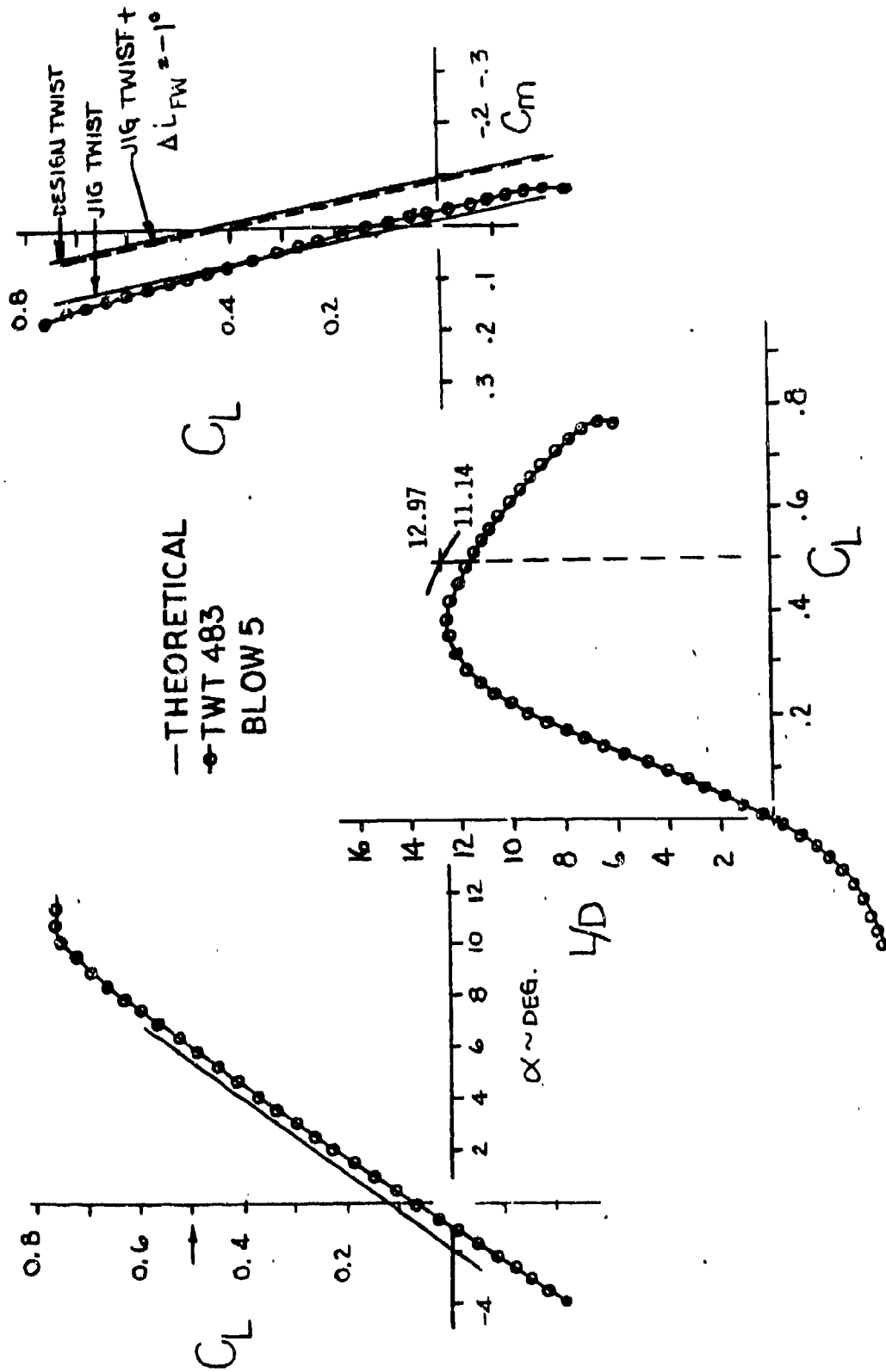


Figure 39. Effect of Joined Wing Incidence Change on Predicted Longitudinal Characteristics at $M = 0.90$

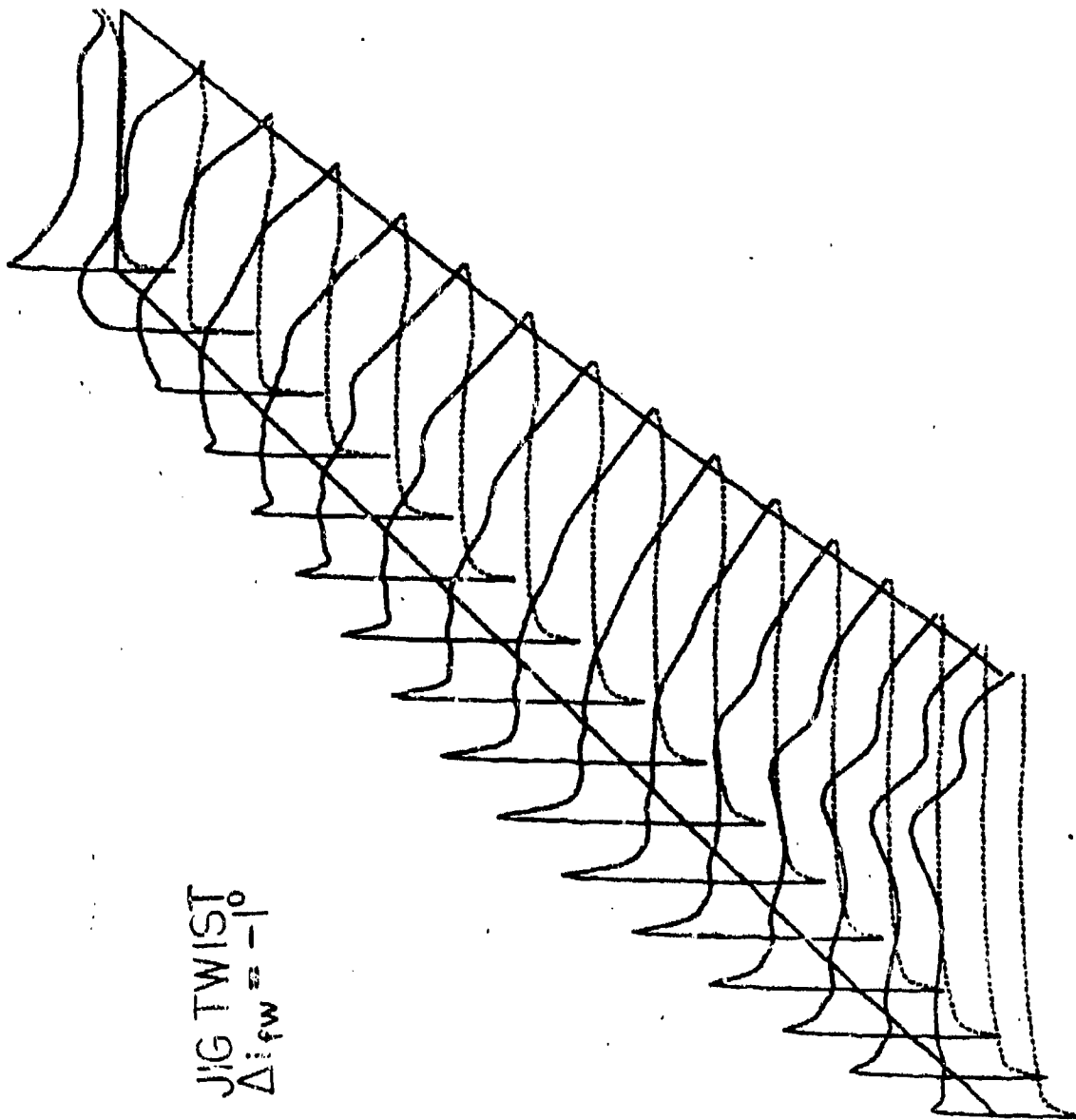


Figure 40. Redesign Full Potential Transonic Flow Quality, $M = 0.90$, $\alpha = 6.35^\circ$

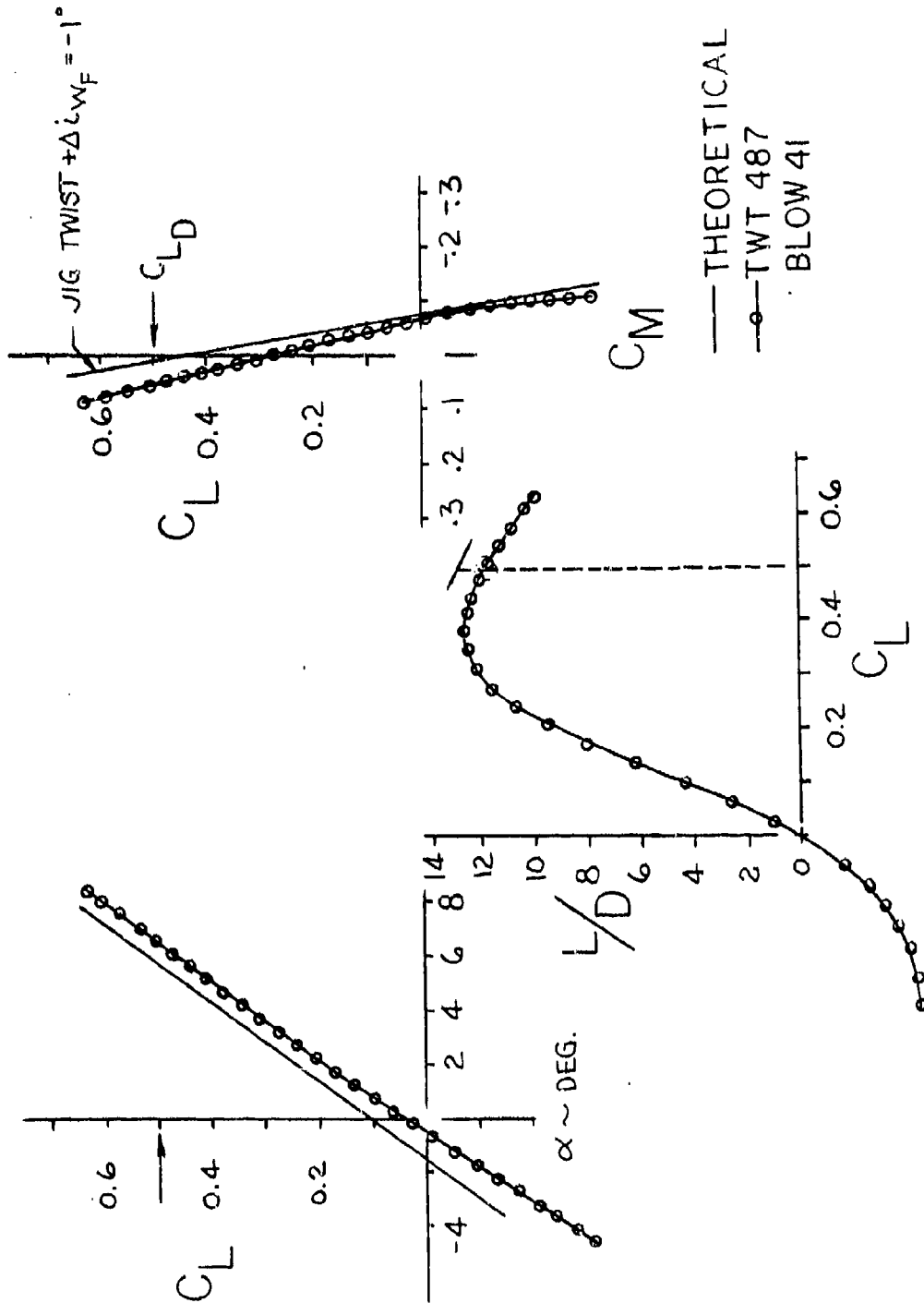


Figure 41. Joined Wing Force Results, Second Rest Entry, $M = 0.90$

INPUT DISPLAY ANBLES (YAW,PITCH,ROLL):
-08 6 00
PANELS 1 THRU 146

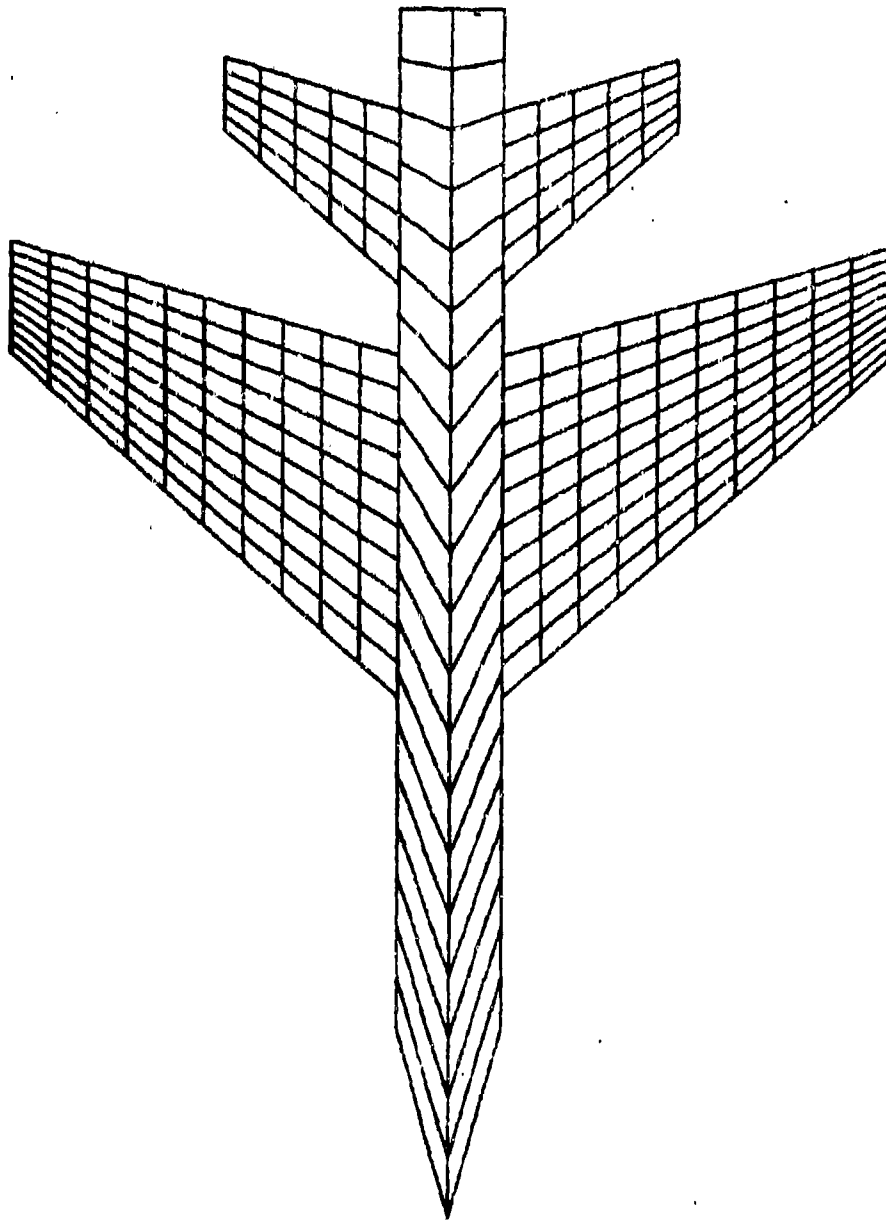


Figure 42. Reference Monoplane Linear Finite Element Analysis Model

46 1513

K&E 10 X 10 TO THE CENTIMETER 10 X 25 CM.
KEUFFEL & ESSER CO. MADE IN U.S.A.

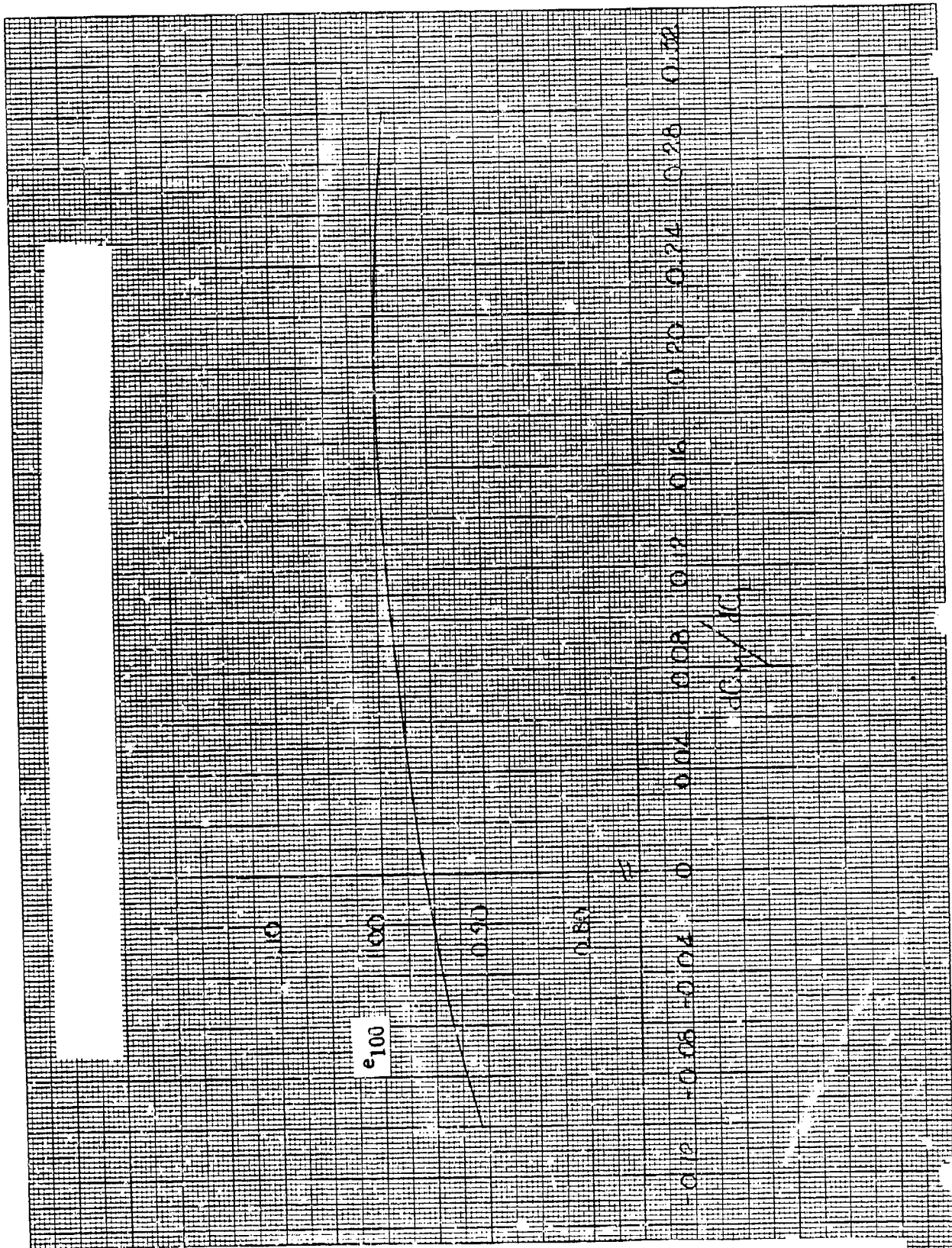


Figure 43. Effect of Longitudinal Stability on Reference Monoplane Span Load Efficiency at M = 0.90

46 1513

K&E 10 X 10 TO THE CENTIMETER 38 X 35 CM.
 KEUFFEL & ESSER CO. MADE IN U.S.A.

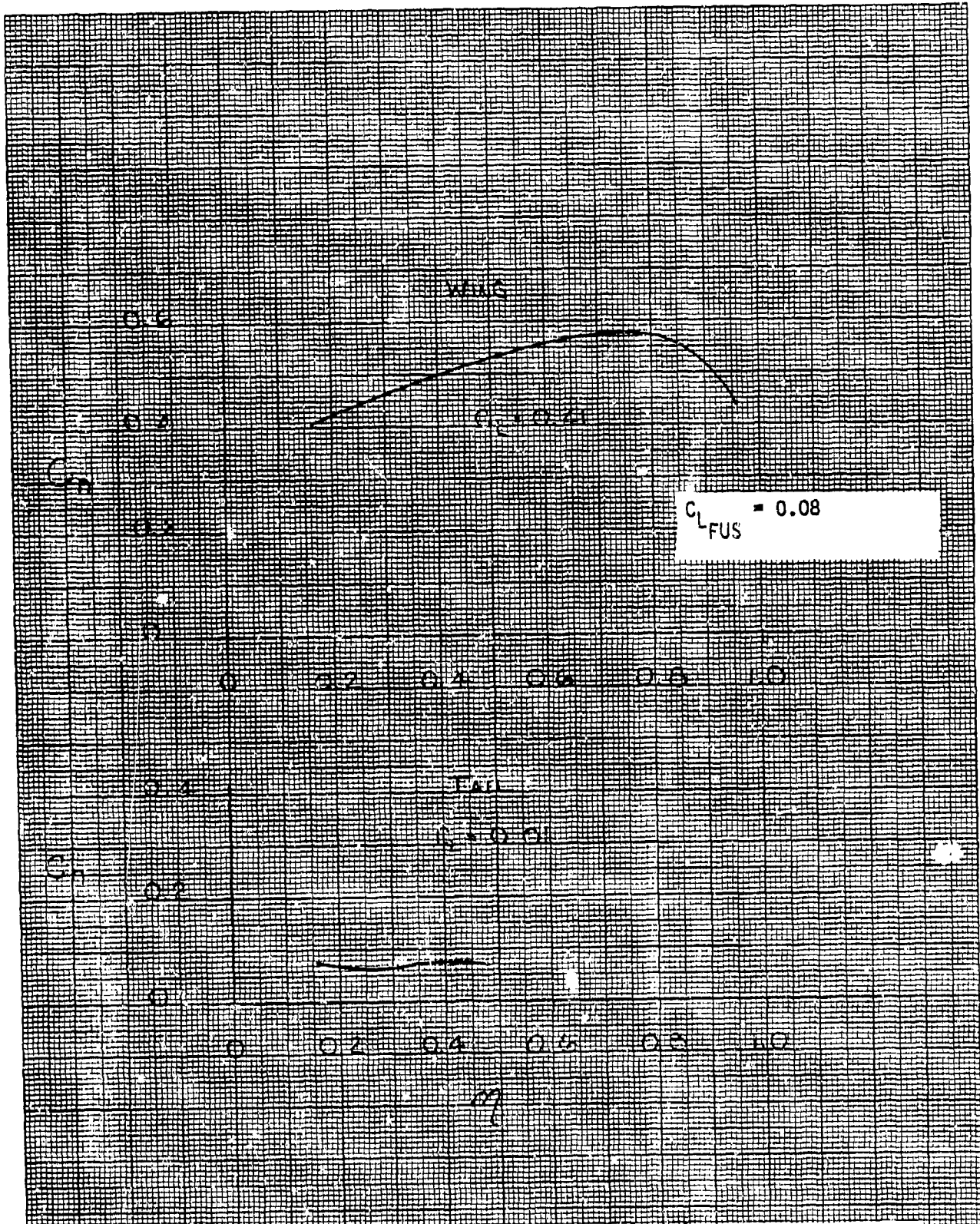


Figure 44. Reference Monoplane Wing Sectional Loading at $M = 0.90$, $C_L = 0.50$

46 1513

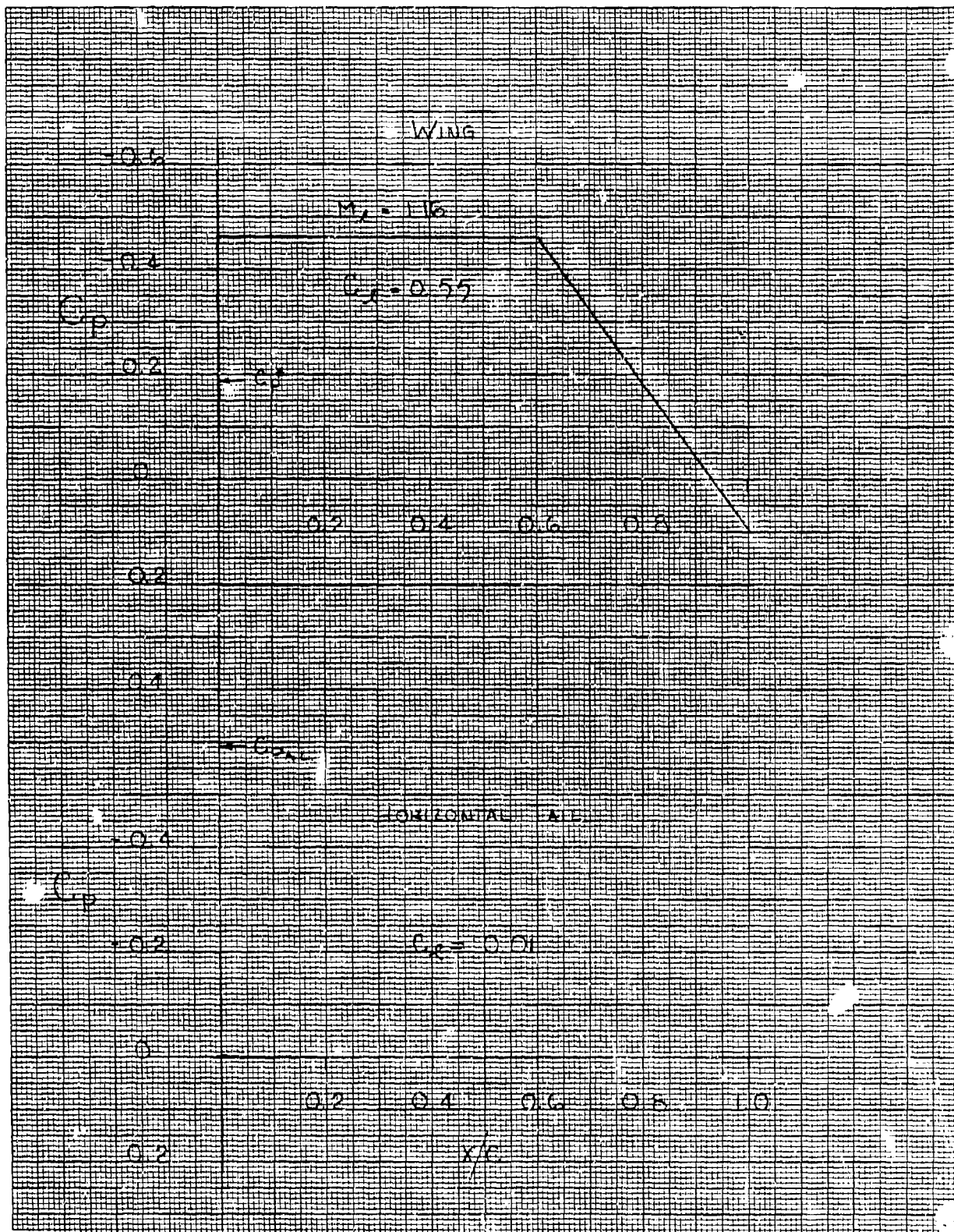
K&E 10 X 10 TO THE CENTIMETER 11 X 25 CM.
KEUFFEL & ESSER CO. MADE IN U.S.A.

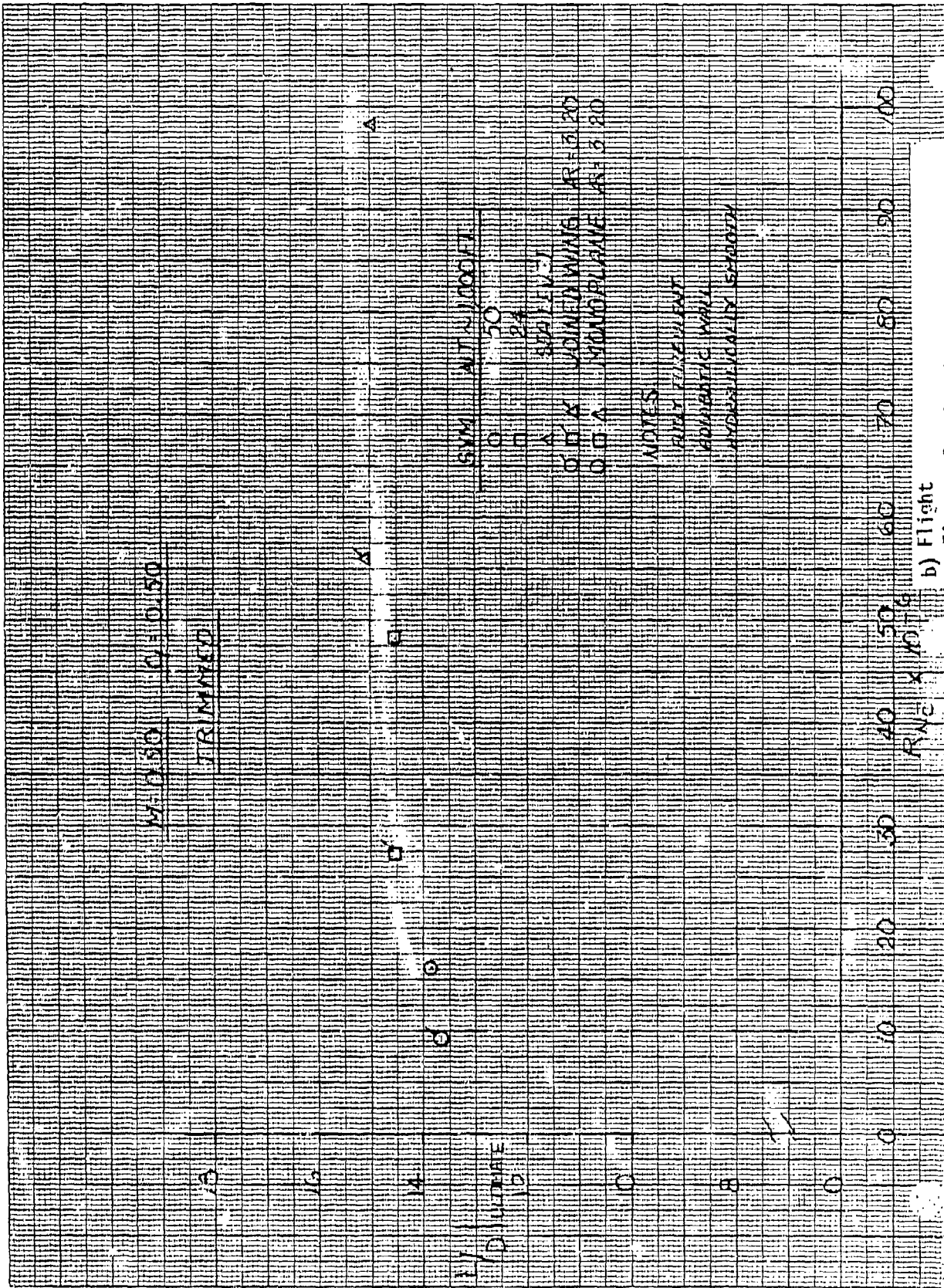
Figure 45. Reference Monoplane Design Pressure Distribution at $M = 0.90$,
 $C_L = 0.50$

Config	$\Lambda_{c/2}$ (deg)	e	C_{D_i}	$\frac{S_{MET}}{S_{REF}}$	R_{E-6} $\times 10^{-6}$	$C_{D_F}^*$	$C_{D_p}^*$	$C_{D_i + C_{D_p}^*}$	L/D
Joined Wing	41/-38	1.11	0.0224	4.51	4.1	0.01262	0.01614	0.03854	12.97
Reference Monoplane	45	1.00	0.0249	4.03	7.3	0.01098	0.01288	0.03778	13.24

* $Re_{FT} = 7.1 \times 10^6$

a) Wind tunnel

Figure 46. Upper Bound Joined Wing/Reference Monoplane Lift/
Drag Ratio Comparison at $M = 0.90$, $C_L = 0.50$



b) Flight

Figure 46. Continued

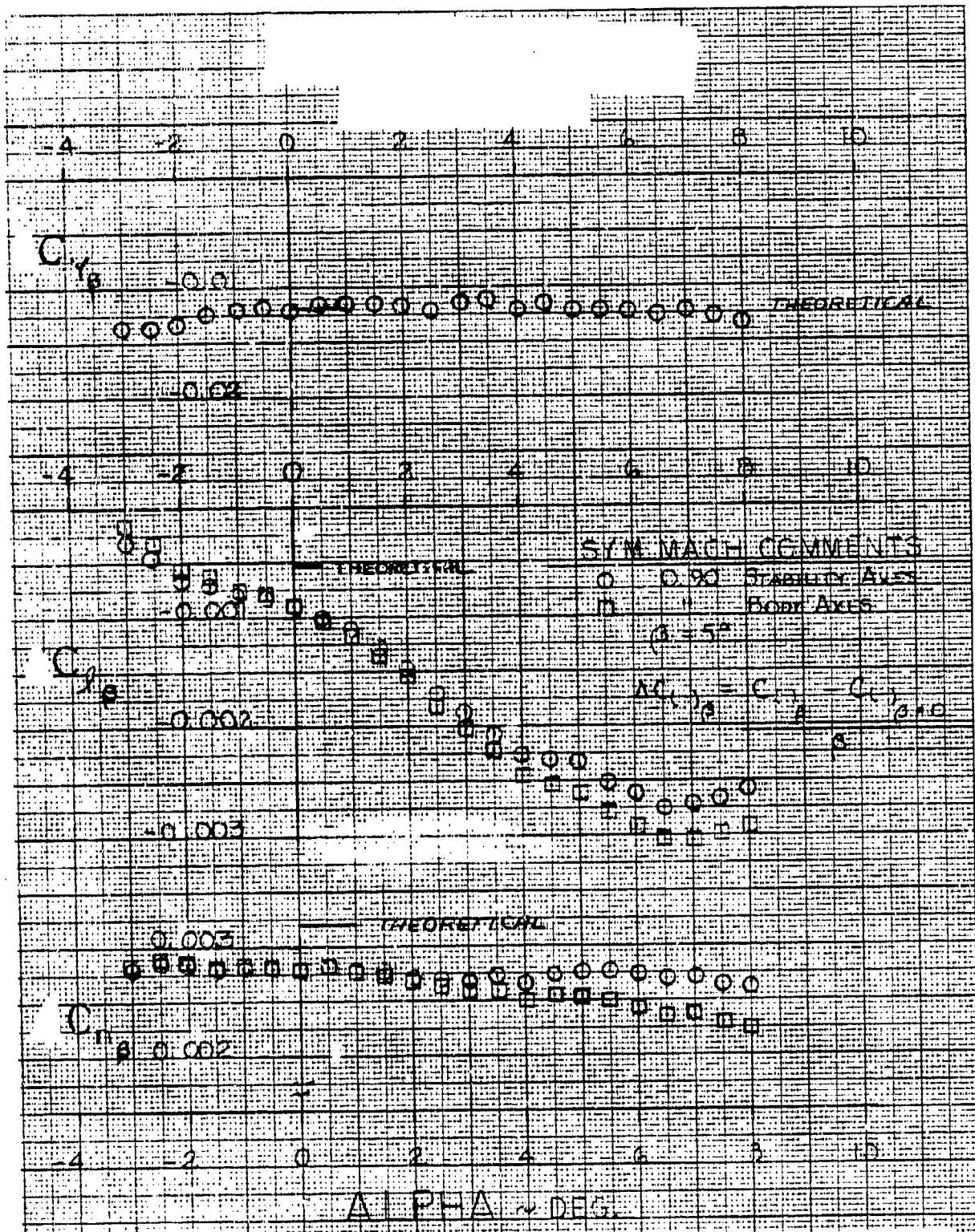


Figure 47. Joined Wing Lateral-Directional Comparison, First Test Entry,
 $M = 0.90$

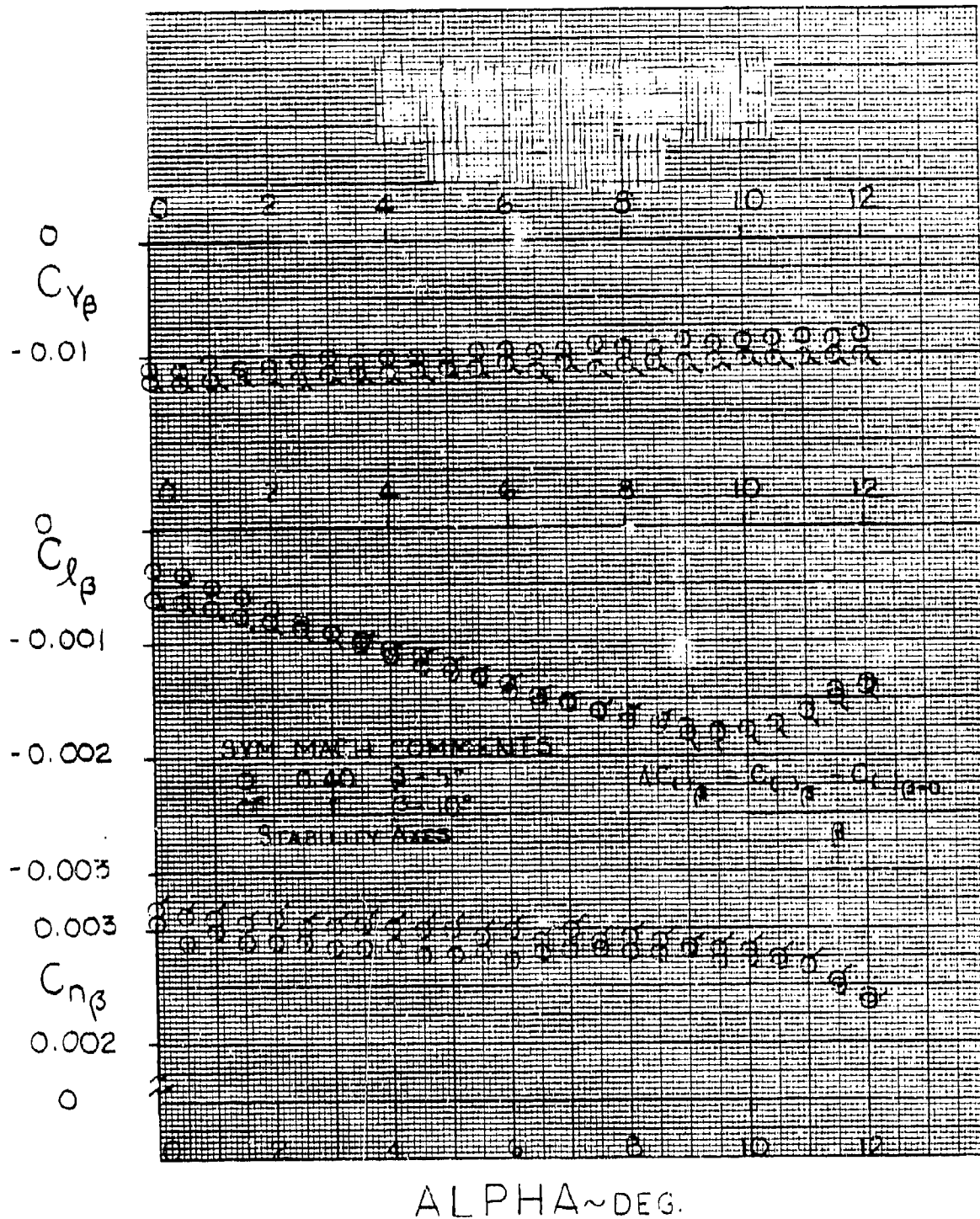


Figure 48. Joined Wing Lateral-Directional Comparison, Second Test Entry,
 M = 0.40

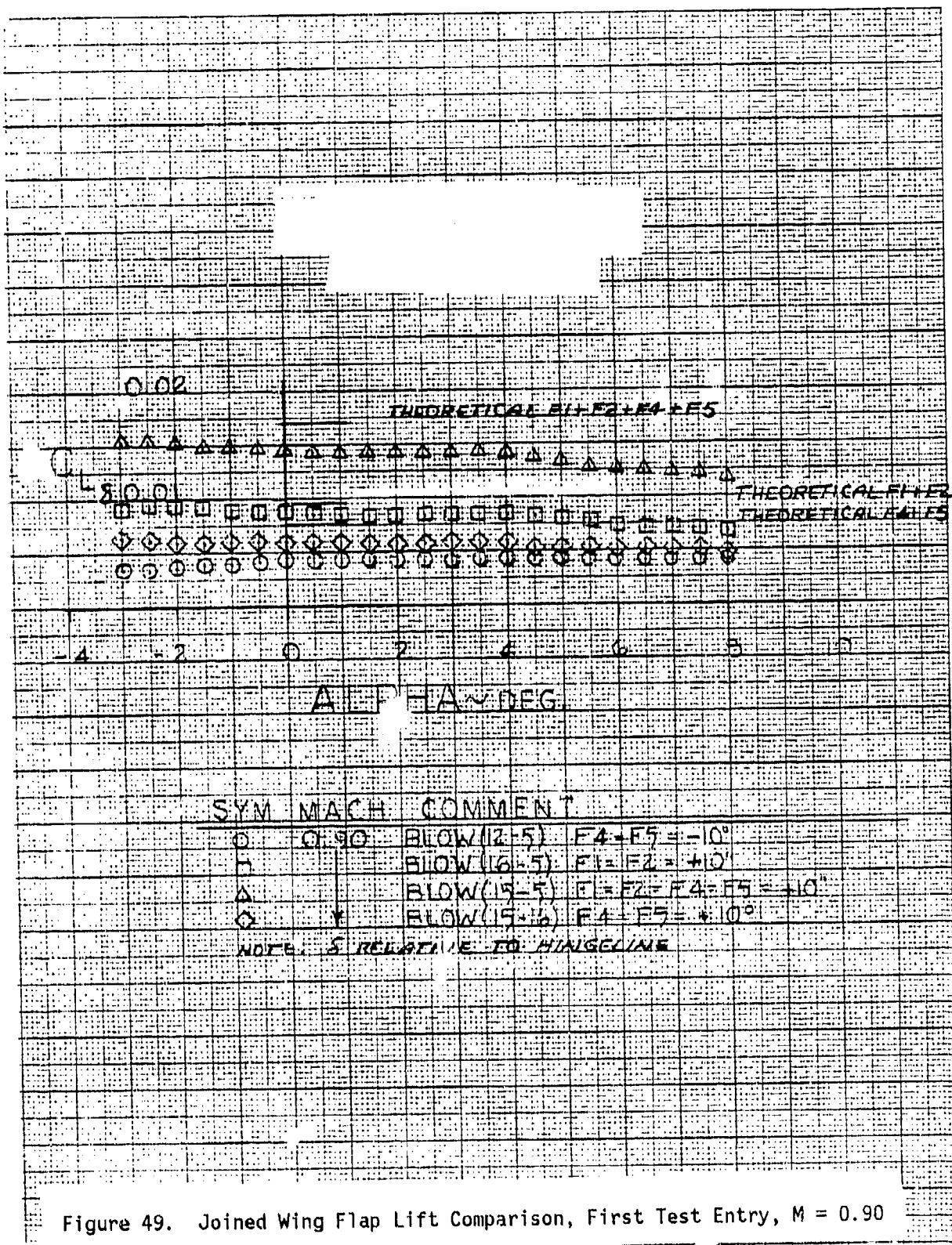


Figure 49. Joined Wing Flap Lift Comparison, First Test Entry, M = 0.90

SYM MACH COMMENT

- 0.90 BLOW(12-5) F4=F5 = +10°
- BLOW(16-5) F1=F2 = -10°
- △ BLOW(15-5) F1=F2=F4=F5 = -10°
- ◇ BLOW(15-16) F4=F5 = -10°

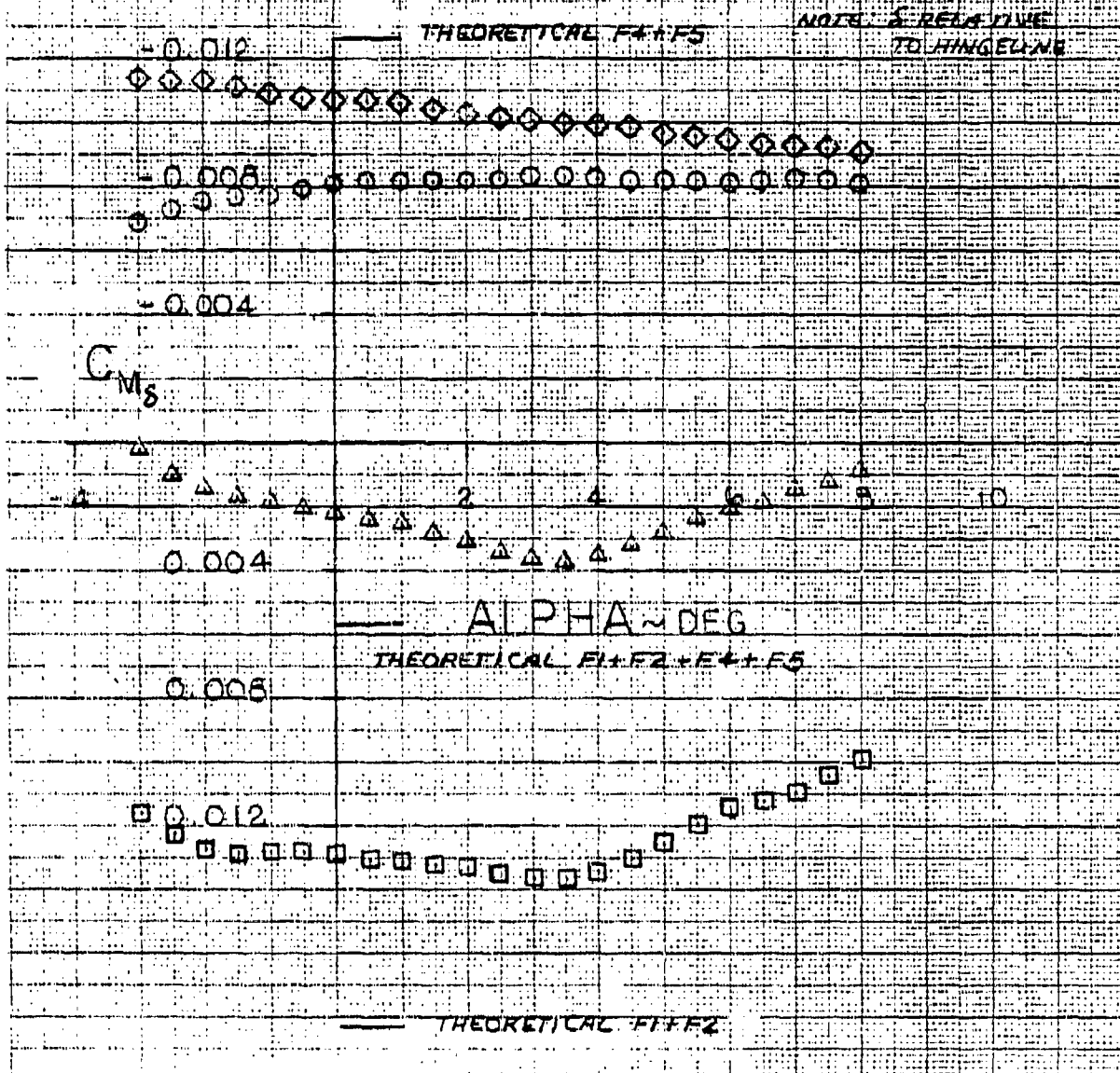


Figure 50. Joined Wing Flap Pitching Moment Comparison, First Test Entry, M = 0.90

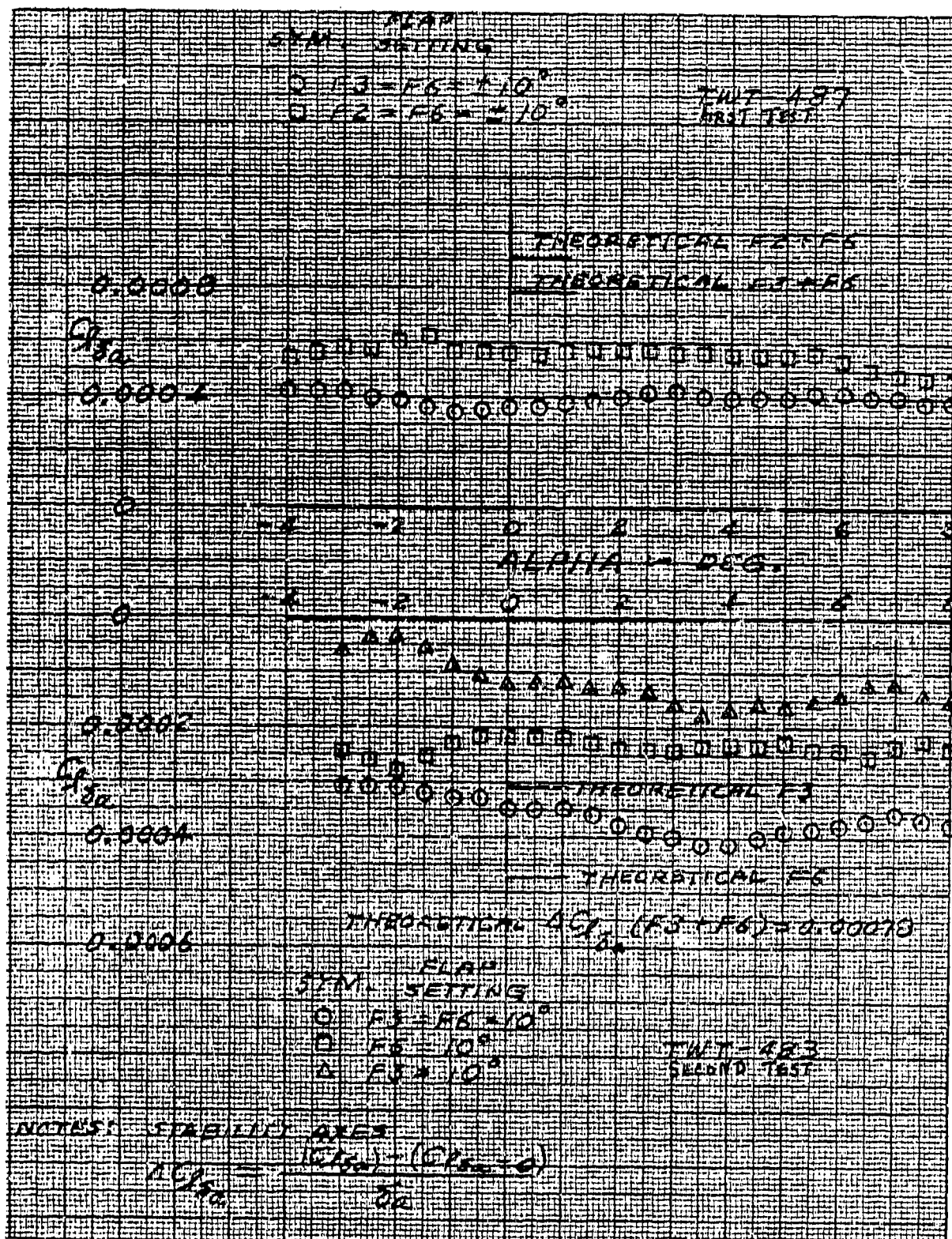


Figure 51. Joined Wing Aileron Comparison, First and Second Test Entry, M = 0.90

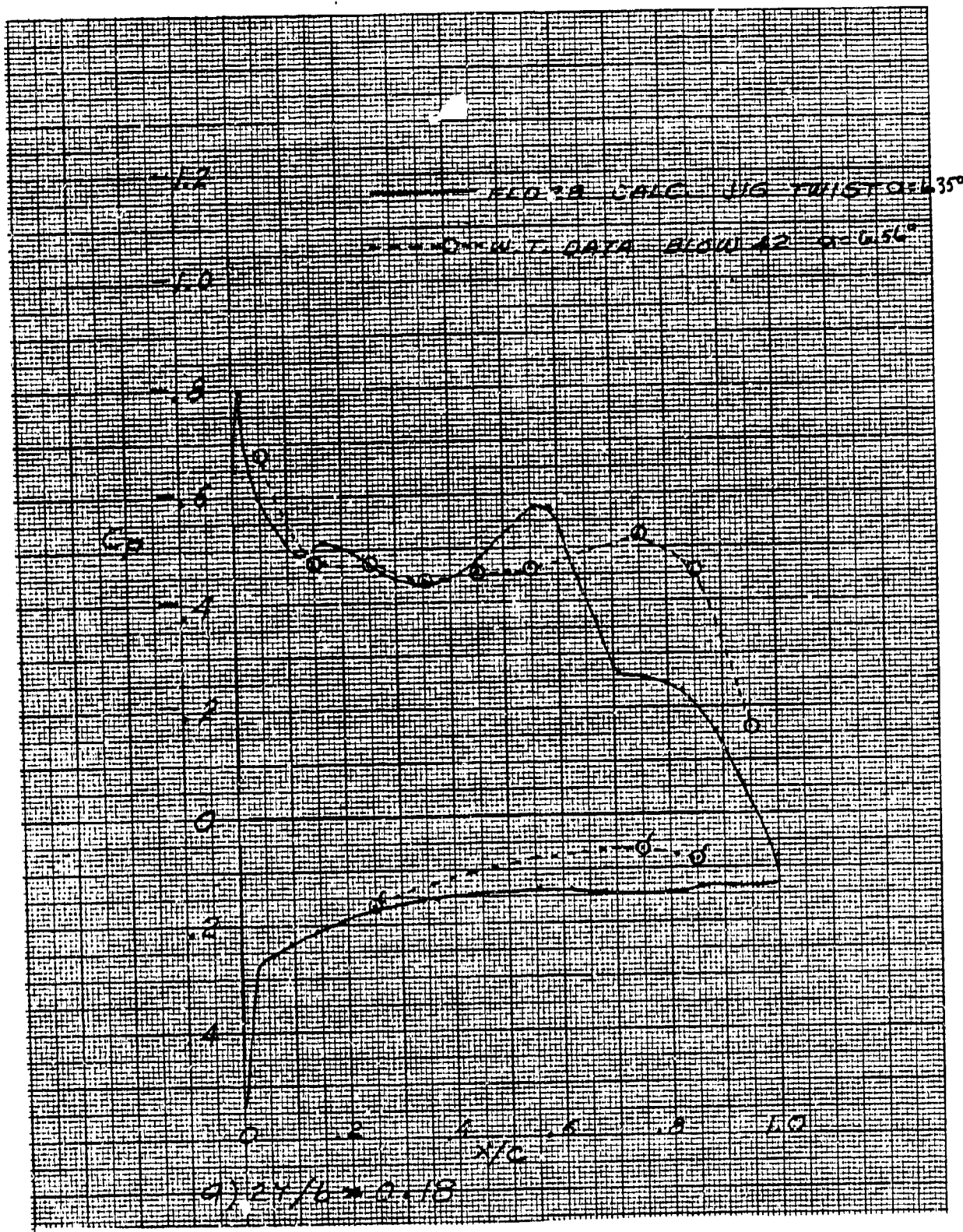


Figure 52. Comparison of Measured and Full Potential Forward Wing Pressure Distributions at $M = 0.90$, $C_L = 0.50$

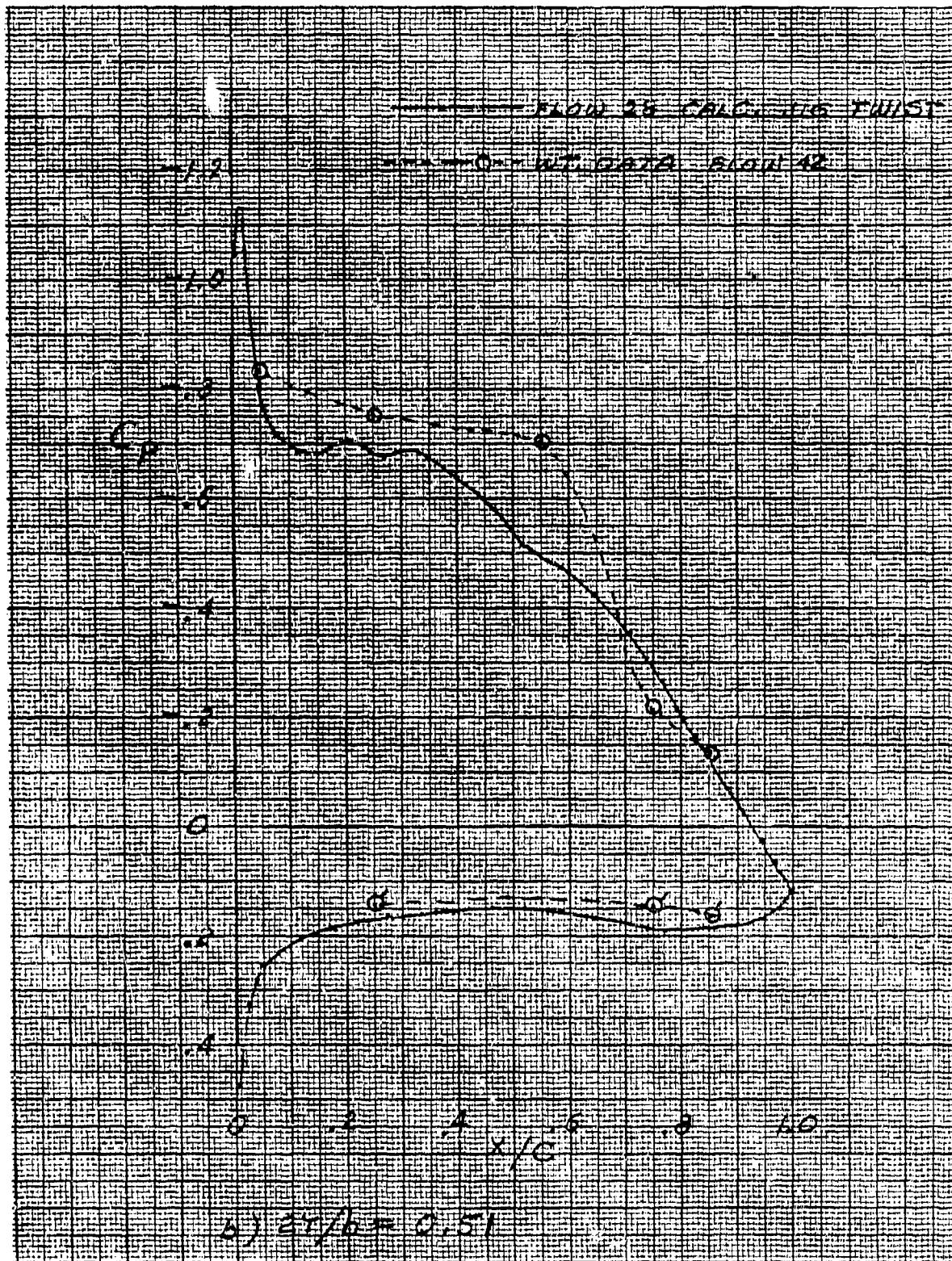


FIGURE 52 CONTINUED

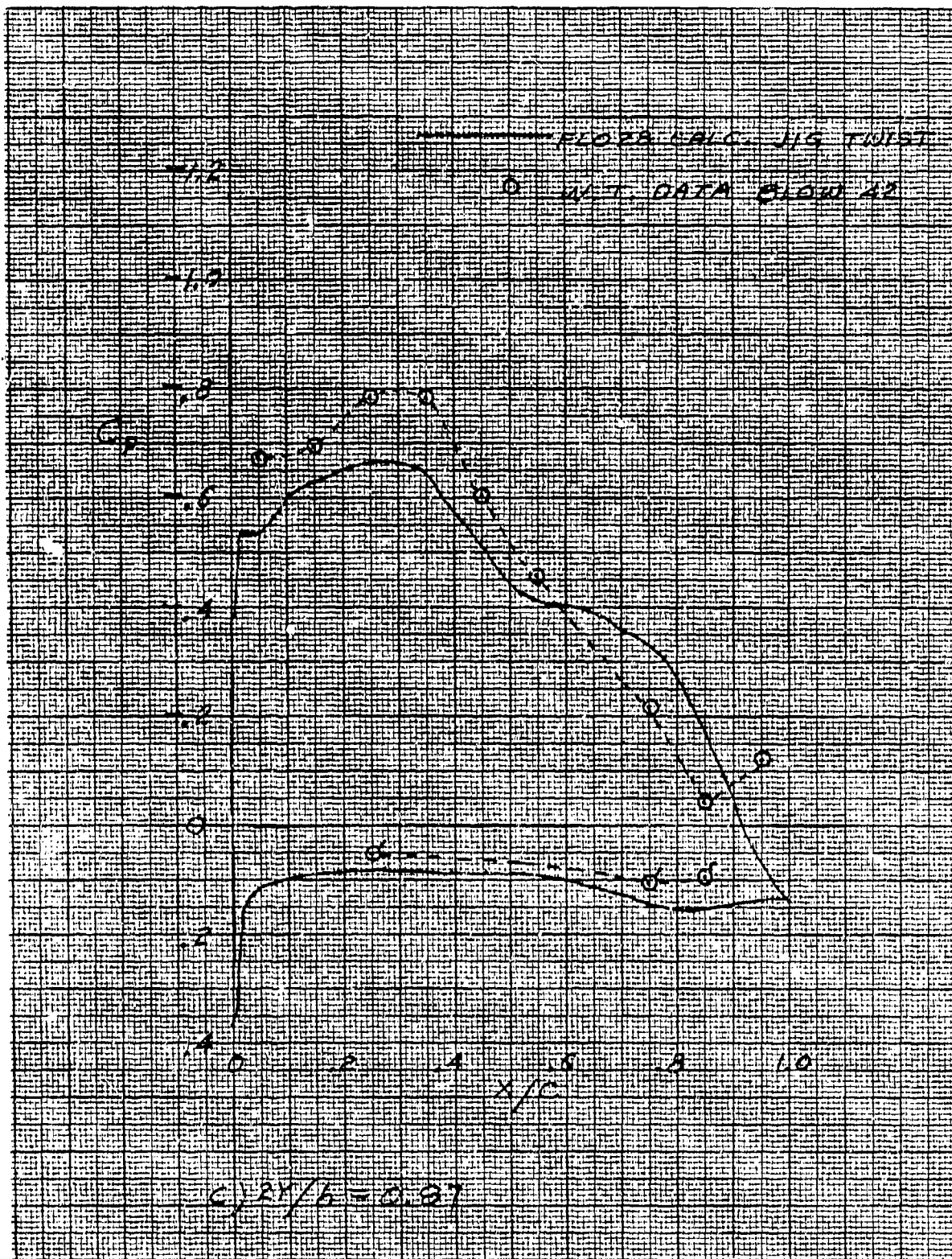
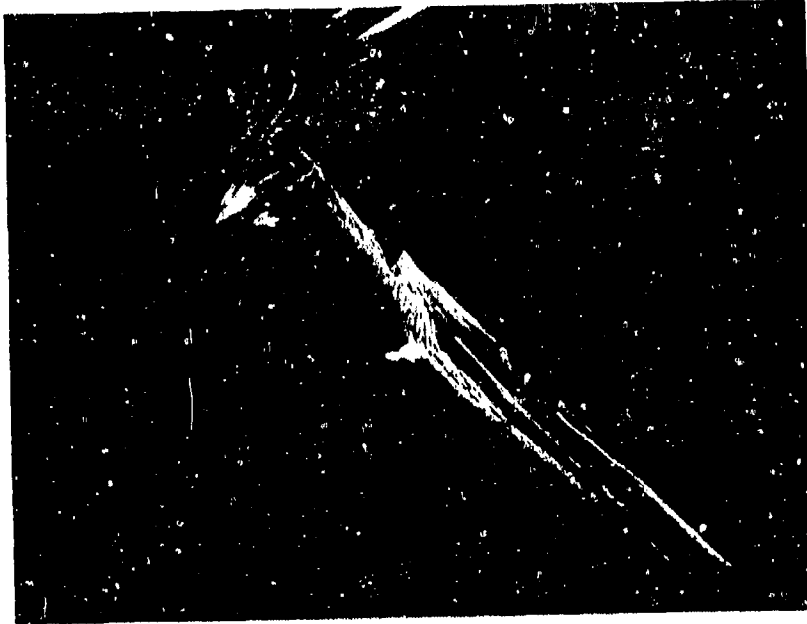


FIGURE 52 CONCLUDED



a) FORWARD WING OUTBOARD



b) FORWARD WING INBOARD

Figure 53. Upper Surface Oil Flow Photographs $M = 0.90$, $Re_c = 4.1 \times 10^6$,
 $C_L = 0.507$, $i_w = -1.27$ degrees

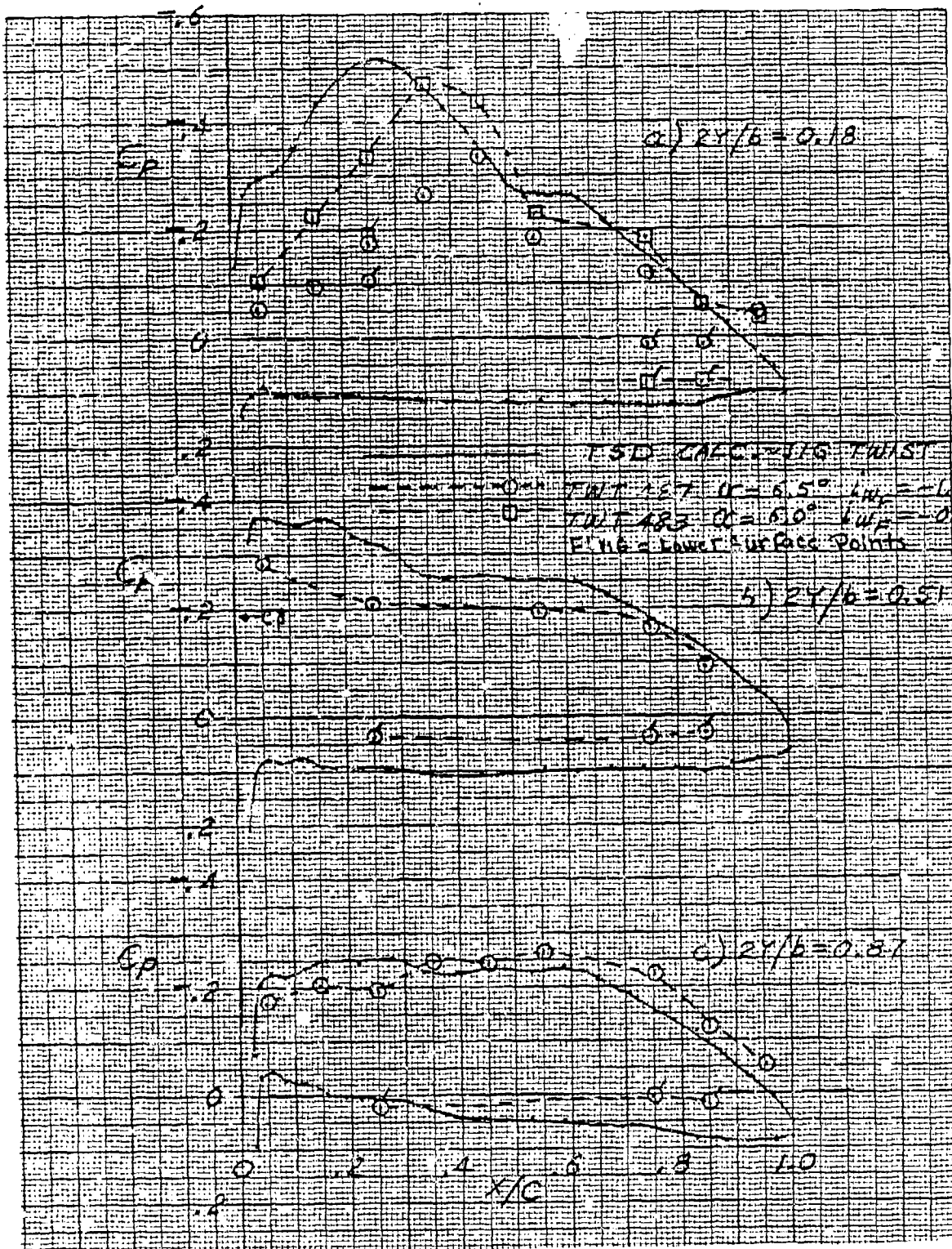


Figure EA. Comparison of Measured and Transonic Small Disturbance Aft Wing Pressure Distribution at $M = 0.90$, $C_L = 0.50$

Appendix A
AERODYNAMIC METHODOLOGY

LINEAR DESIGN AND ANALYSIS

The initial design and analysis tool used is the unified distributed panel method (reference 2). The linearized small disturbance equation

$$(1 - M_{\infty}^2) \phi_{xx} + \phi_{yy} + \phi_{zz} = 0$$

is numerically solved for arbitrary configurations by a superposition of chord plane and body singularities in conjunction with an interference shell to account for surface-body inductions. Surface lifting effects are represented by constant-pressure panels. Surface thickness effects are represented by chordwise linearly varying source panels. The analysis is applicable to multiple-surface nonplanar configurations at subsonic or supersonic speeds. Longitudinal and lateral-directional forces and rotary derivative characteristics are evaluated.

Inverse lifting solutions are obtained by specifying the net loads at the panel centroids and determining the boundary conditions by matrix multiplication. Problems where boundary conditions are given in one region and net loads are prescribed in the remainder can also be treated. Wing-on-wing inductions in the presence of the body are established by this analysis for subsequent use in the transonic codes to approximately account for surface interactions (by use of an effective twist and camber philosophy) not directly modeled.

Linear analysis is also used in conjunction with structural influence coefficients to estimate static aeroelastic deflections of the model wing panels.

In the design mode, lifting surface theory is used to minimize (reference 3) the far-field (i.e., Trefftz plane) vortex drag and define the optimum surface span loads and candidate twist distributions.

SUPERSONIC PRESSURE DRAG

The technique used to evaluate wave drag is the supersonic area rule. The spatial singularities which are a solution to the linearized equation of motion are reduced to a series of equivalent linear distributions by application of the cutting plane concept. The 3-D distribution is surveyed longitudinally at fixed roll angles by an oblique plane. The drag is then evaluated with slender body theory.

$$C_{D_W} = \frac{1}{4\pi^2 S} \int_0^{2\pi} \int_0^L \int_0^L S''(x_1, \theta) S''(x_2, \theta) \ln|x_1 - x_2| dx_1 dx_2 d\theta$$

where S is the oblique projected cross-sectional area cut by the system of Mach planes.

TRANSONIC DESIGN AND ANALYSIS

The methods used to derive supercritical forward and aft wing contours in the presence of each other and the body are described in the following paragraphs. Experience with transonic methods indicates that the initial supercritical contours be defined with the transonic small disturbance formulation because of its design capability. The result is subsequently evaluated and refined using a full-potential analysis.

TRANSONIC SMALL DISTURBANCE THEORY

TSD theories are extensions of the classical small disturbance formulation. The modifications involve the retention of higher order terms, principally to capture swept shocks. The governing equation is solved by a mixed elliptic-hyperbolic, relaxation algorithm applied to a finite-difference approximation. The boundary conditions are linearized and applied on the surface chord plane and fuselage shell.

The wing-body code (reference 5) uses an embedded fine-grid structure with sweep and taper transformations in addition to a crude Cartesian outer grid. This feature increases computational efficiency by a factor of five over earlier small disturbance solutions of the same resolution. The equation used for computing transonic flow is:

$$\begin{aligned} & [1 - M_\infty^2 - (\gamma + 1) M_\infty^2 \phi_x] \phi_{xx} - 2 M_\infty^2 \phi_y \phi_{xy} \\ & + [1 - (\gamma - 1) M_\infty^2 \phi_x] \phi_{yy} + \phi_{zz} = 0 \end{aligned}$$

The underlined terms are those added to the classical small disturbance formulation.

Rockwell's wing-body inverse code (reference 6) is used to define the wing contours for specified design pressure distributions.

FULL POTENTIAL ANALYSIS

The Jameson FL028 transonic wing-body (reference 9) code solves the exact potential equation.

$$\phi_{x_1} \phi_{x_j} \phi_{x_1 x_j} - a^2 \phi_{x_j x_j} = 0$$

$$i, j = 1, 2, 3$$

using a conservative rotated differencing scheme for a surface fitted grid system obtained from a series of analytic mappings.

WING BOUNDARY-LAYER ANALYSIS

A yawed wing integral laminar/turbulent boundary layer analysis (reference 4) is used to assess candidate sectional design pressure distributions from an attached flow viewpoint at the test condition. The solution is also used to estimate transition point location considering cross flow vorticity due to sweep and streamline instability. Finally, the evaluation is used to estimate the magnitude of the displacement thickness correction that will be required to eliminate weak viscous boundary layer interaction effects by undercutting the design section geometry.

The three dimensional laminar and turbulent boundary layer analysis developed by Nash (reference 7) is applicable to finite swept wings. An orthogonal surface coordinate system is used, and the equations are solved with an efficient difference scheme. The analysis is used to verify that the final wing design pressure distributions produce attached flow at the test Reynolds number and estimate potential separation problems due to adverse pressure gradients and shock boundary-layer interactions which can not be fully controlled. For the design case the inviscid/viscous interaction is minimized by removing the three dimensional displacement thickness from the wing sections.

Appendix B

VISCOUS DRAG ANALYSIS

Standard techniques (reference 2) for the evaluation of turbulent flat plate skin friction at compressible speeds are used in conjunction with a component buildup approach. Fuselage, empennage, and wing fairing component thickness effects were approximated using experimental data correlations. An integral infinite yawed boundary layer analysis (reference 4) is used to correct the flat plate wing analysis for the effect of thickness, lift and sweep as follows

$$C_{Dp} = \sum_i 2 C_{F_i} \frac{\Delta S_i}{S_{REF}} \left. \frac{C_{dp}}{C_{dF}} \right|_i$$

$$\approx \left. \frac{C_{dp}}{C_{dF}} \right|_{\bar{c}} \sum_i C_{DF_i}$$

The mean chord sectional profile drag C_{Dp} is evaluated by relating the wake momentum thickness at infinity to the momentum thickness at the trailing edge using a Squire-Young analysis appropriately extended for the effect of sweep. That is

$$C_{dp} = \frac{2\theta_{11\infty}}{\theta_{11TE}} \frac{\theta_{11TE}}{c}$$

where

$$\frac{\theta_{11\infty}}{\theta_{11TE}} = \frac{U'_{TE}}{U'_{\infty}} \frac{Q_{\infty}}{Q_{eTE}} \left[\frac{M_{eTE}}{M_{\infty}} \right] \frac{(H_{TE} + H_{\infty} + 4)}{2} \left[\frac{T_{eTE}}{T_{\infty}} \right] \left[\frac{H_{TE} + H_{\infty}}{4} + \frac{\gamma}{\gamma-1} \right]$$

$$\frac{U'_{TE}}{U'_{\infty}} = \frac{U'_{TE}/Q_{\infty}}{U'_{\infty}/Q_{\infty}} = \frac{[Q_{eTE}/Q_{\infty}]^2 - \sin^2 \Lambda_c/2}{\cos \Lambda_c/2}$$

$$\text{and } H_{\infty} = 1 + (\gamma-1) M_{\infty}^2$$

The trailing edge properties are evaluated for the design pressure distribution of figures 10, 11, and 44 at the test Reynolds number. A summary of the results is presented in tables B1 and B2.

This calculation is performed for the upper and lower surface, and summed i.e., $C_{dp} = C_{d,upper} + C_{d,lower}$. This mean chord sectional flat plate skin friction drag coefficient C_{df} is evaluated using the standard techniques described previously.

Considerations such as separation and component interference are not accounted for in the present analysis. The evaluation in conjunction with potential vortex drag is consequently referred to as ultimate, upper bound, etc. condition.

Table 81
 JOINED WING SECTIONAL BOUNDARY LAYER AND
 PROFILE DRAG CHARACTERISTICS

$M = 0.90$, $RN/FT = 7 \times 10^6$

Config	$A^{\circ}c/2$	$R_c^{\circ} \times 10^{-6}$	Surface	θ_{11}/c	θ_{11}/e_{11}	Q_{TE}/Q_{∞}	Me_{TE}/M_{∞}	H_{TE}	U'_{TE}/U'_{∞}	$C_{d,p}$
Joined Wing	41	4.1	Upper	0.004697	0.814	0.9497	0.9422	2.495	0.9099	0.00765
	41	4.1	Lower	0.00134	0.831	0.9497	0.9422	1.5726	0.9099	0.00223
	-48	4.1	Upper	0.004501	0.796	0.9497	0.9422	2.2615	0.8838	0.00716
	-48	4.1	Lower	0.001683	0.897	0.9497	0.9422	1.6426	0.8838	0.00302
Flat Plate	0	4.1	Either	0.001600	1.0	1.0	1.0	---	1.0	0.0064

Table B2
 MONOPLANE SECTIONAL BOUNDARY LAYER
 AND PROFILE DRAG CHARACTERISTICS
 $M = 0.90, RN/FT = 7 \times 10^6$

Config	$\Lambda_{c/2}$	$R_c \times 10^{-6}$	Surface	$\frac{\theta_{11}}{c}$	$\frac{\theta_{11\infty}}{\theta_{11TE}}$	$\frac{Q_{eTE}}{Q_{\infty}}$	$\frac{M_{eTE}}{M_{\infty}}$	H_{TE}	$\frac{U'_{TE}}{U'_{\infty}}$	C_{dp}
Reference Monoplane	33.5	7.2	Upper	0.003164	0.8385	0.9267	0.9423	2.0709	0.9267	0.0053
	33.6	7.2	Lower	0.000788	0.8526	0.9267	0.9423	1.4255	0.9267	0.0013
	45	7.2	Upper	0.00436	0.80513	0.9497	0.9423	2.3667	0.8966	0.00703
	45	7.2	Lower	0.000631	0.82507	0.9497	0.9423	1.4185	0.8966	0.00104
Flat plate	0	7.2	Either	0.00145	1.0	1.0	1.0	---	1.0	0.00583

NOMENCLATURE

C_{dF}	Sectional flat plate skin friction drag coefficient
C_{dp}	Sectional profile drag coefficient
C_{DF}	Strip flat plate skin friction drag coefficient
C_{Dp}	Profile drag coefficient
C_F	Average flat plate skin friction coefficient
\bar{c}	Mean aerodynamic chord
H	Boundary layer form factor. $\delta^*_{1/\theta_{11}}$
M	Mach number
Q	Total velocity
S_{ref}	Reference area
ΔS	Strip area
T	Static temperature
γ	Ratio of specific heat, 1.4
δ^*	Boundary layer displacement thickness in potential streamline direction
θ_{11}	Boundary layer momentum thickness in potential streamline direction
Λ	Wing sweep

SUBSCRIPTS

$c/2$	Half chord
e	Edge of boundary layer
i	Wing strip i
TE	Trailing edge
∞	Free stream

Appendix C

MODEL DESIGN AND CONSTRUCTION

STRESS AND FLUTTER ANALYSES

Air loads for the 1/10th scale joined wing arrangement of figure 2 exceeded available force balance capacity so the model scale was reduced to 1/15th. This changed the overall span of both the reference monoplane and the joined wing from 54 inches to 36 inches. Corresponding reductions in reference area were from 911.25 square inches down to 405.00 square inches and the reference mean aerodynamic chord (m.a.c) from 18.51 inches to 12.34 inches. A limit condition of Mach number 0.9, angle of attack 10 degrees, lift coefficient 0.785 and dynamic pressure 1120 pounds/square foot gave a limit lift load on the model of 2500 pounds.

The redundant structure of the joined wing model required special stress, flutter and deflection analyses. Simple beam model stress analyses indicated excessive stress levels near the wing tips where the two wings joined. To relieve this stress problem and to provide adequate thickness for installation of pressure orifices near the tips, the thickness ratio at the wing tips was increased from 0.05 up to 0.07, varying linearly to 0.05 at the model midspan.

A finite beam element flutter theoretical analysis was conducted, reference 5, and it was concluded that wing tip fairings of either aluminum or steel, must have a width of at least 5 percent the joined wing semispan, to provide good bearing surfaces and rigid wing-to-fairing attachment for adequate flutter margin.

AEROELASTIC ANALYSIS

The structural finite beam element model created for the flutter analysis was adapted to the calculation of static aeroelastic deflections by eliminating the sting and balance flexibilities, first two. The spanwise design load distributions on the two wings were segmented to give a series of concentrated loads at the control points of the structural finite element model. The resulting angle-of-attack change due to flexibility ($\Delta\alpha_{flex}$) is presented on figure C1 and was subtracted from the design twist distribution to give the jig shape for model construction. The intent was at the design point, the model would flex into the designed twist distribution.

MODEL LOFT GEOMETRY

Lofted model drawings are presented in figures C2 through C8. Figure C2 presents the configuration two view and figure C3 the forward wing detail, Figures C4 and C5 show the aft wing detail and rigging respectively. Figure C6 presents the vertical tail and wing tip fairing details.

MODEL FABRICATION

Templates were constructed from the lofted model drawings. The model was machined to template contours. Both wings and the aft-wing-to-vertical attach fitting were built of high strength steel. The fuselage and wing tip center sections were built of regular strength steel. The nose fairing of the fuselage and the nose and tail portions at the wing tip center fairings were built of aluminum. During model assembly, it became evident the original wing tip fairings of circular cross section lacked sufficient depth for an adequately stiff wing tip joining. The circular cross section of 0.90 inch diameter was changed to a rounded rectangular cross section of 0.95 inch width and 1.21 inch depth. The forebody lengths of the wing tip fairings were increased from 1.79 inches up to 2.40 inches and the afterbody lengths from 2.69 inches up to 3.60 inches in order to maintain an equivalent forebody fineness ratio of 2.0 and afterbody fineness ratio of 3.0.

CONTOUR CHECKS

Static pressure orifice's were installed in the right forward and aft joined wings at spanwise at stations $2Y/b$ of 0.18, 0.51 and 0.87. After model assembly, the twist angles of the wings were measured at the spanwise stations of pressure measurement and found to be within 0.05 degrees of the lofted twist on the forward wing and within 0.24 degrees of the lofted twist on the aft wing. The upper surface contour of the forward wing was measured with a cordax machine and found to agree with the template contour within less than a line width on the lofted drawing.

AEROELASTIC MEASUREMENT

Strain gauges to measure bending moment and torque were installed on the lower surface of the left forward wing at spanwise stations 8 and 12 inches off the model centerline. These gauges were calibrated by applying known loads to the isolated forward wing mounted in a test rig. Then with the model completely assembled, known 100 pounds down loads were applied 11.08 inches off the model centerline at $x/c = 0.45$ perpendicular to the planes of the wings as shown on figure C7. Deflections and twists of the wings relative to the fuselage were measured at the midspan and at the tip. A comparison of measured and calculated deflections and twists is presented on table C1. The "as built" model was substantially stiffer than calculated by the finite-beam-element theoretical calculations and the bending moments and torques measured during the known loading and during wind tunnel test were substantially lower than calculated (figures C8 and C9). These differences were attributed to inaccuracies in the calculated stiffness coefficients and to inadequacies in the theoretical formulation (for example, longitudinal deflections were neglected). Substantial hysteresis was observed in the measured bending moments and torques due, apparently, to adjustments in the tightness of the screw and bolt fasteners at the model joints.



Table C1

DEFLECTIONS AND TWISTS DUE TO 100 LB. DOWN LOAD
APPLIED AT $y = 11.08$ IN., $x/c = 9.45$

	CALCULATED	MEASURED
FW'D	δ_H	-.016 IN.
	δ_L	.034 IN.
	$\Delta\alpha$.14° NOSE UP
	δ_H	-.002 IN.
	δ_L	.045 IN.
	$\Delta\alpha$	-.02° NOSE DOWN
AFT	δ_L	.072 IN.
	$\Delta\alpha$	-.23° NOSE DOWN
	δ_L	.053 IN.
	$\Delta\alpha$.24° NOSE UP
	δ_H	X DEFLECTION PARALLEL TO WING PLANE POSITIVE FORWARD
	δ_L	DEFLECTION PERPENDICULAR TO INITIAL WING PLANE

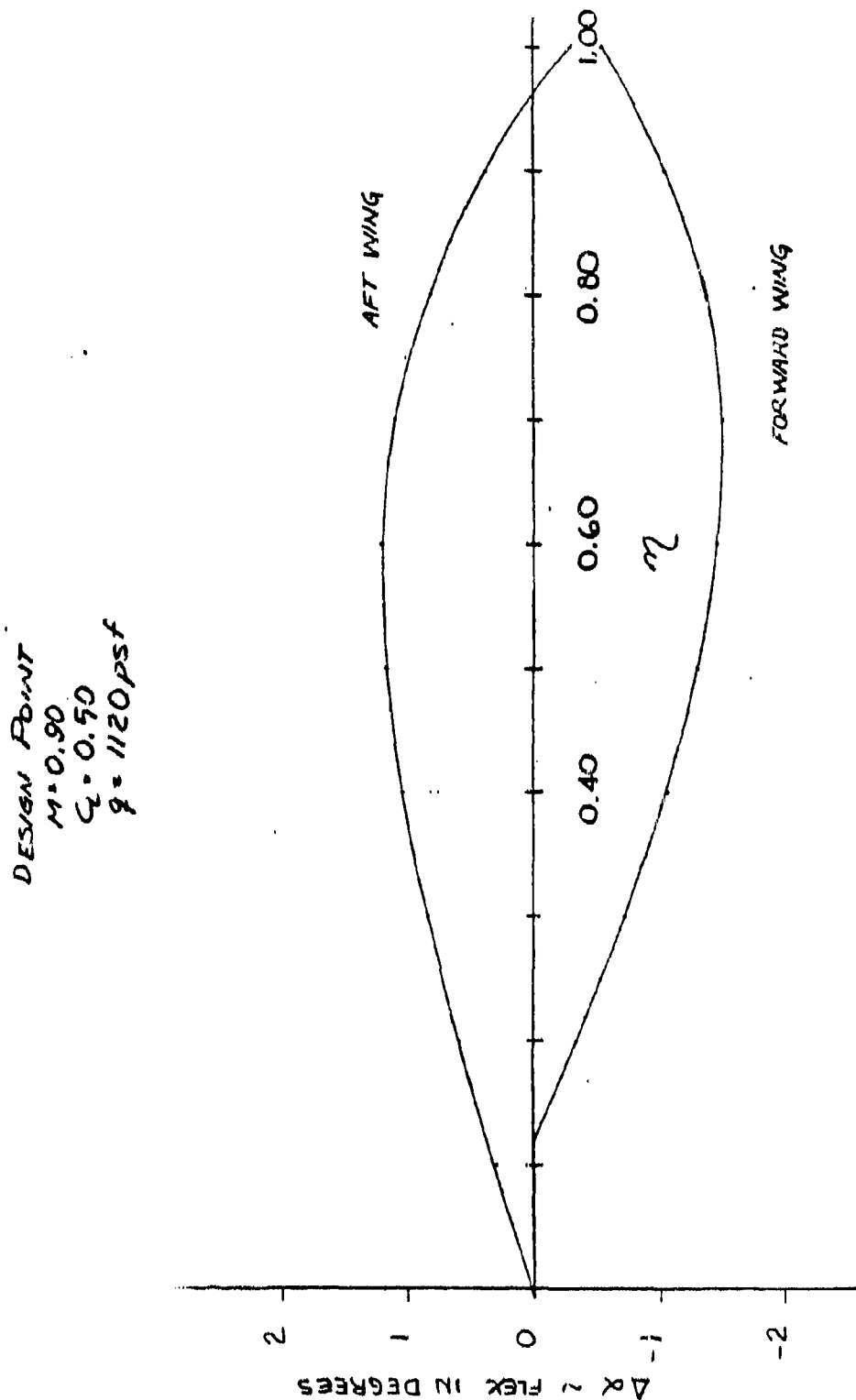


FIGURE C1 THEORETICAL FORWARD AND AFT WING AEROELASTIC TWIST AT $M = 0.9$, $C_L = 0.5$, $q = 1120 \text{ psf}$

NA-84-1434

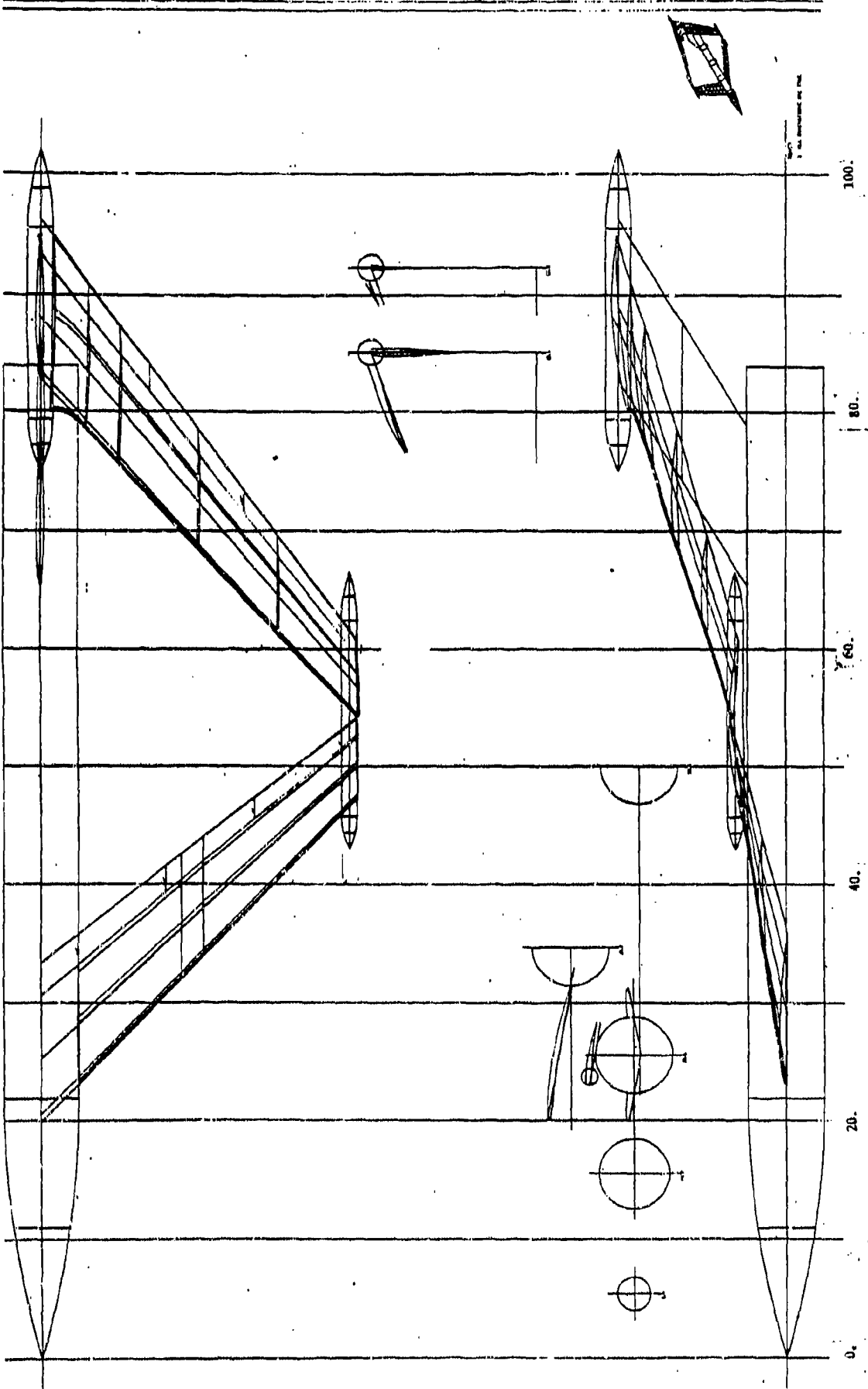


FIGURE C2 JOINED WING LOFTED TWO VIEW

C-5

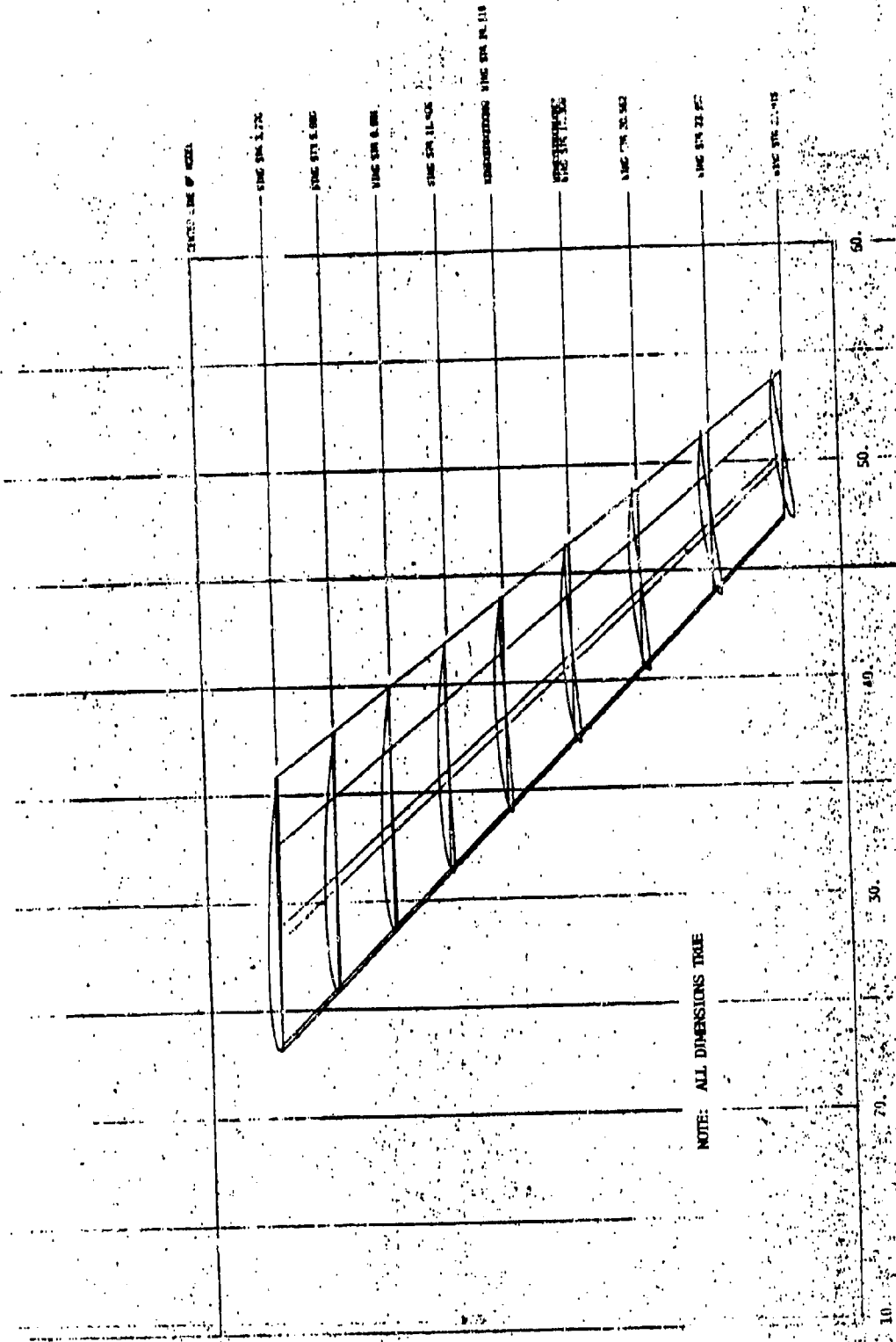


FIGURE C3 JOINED WING FORWARD WING DETAIL

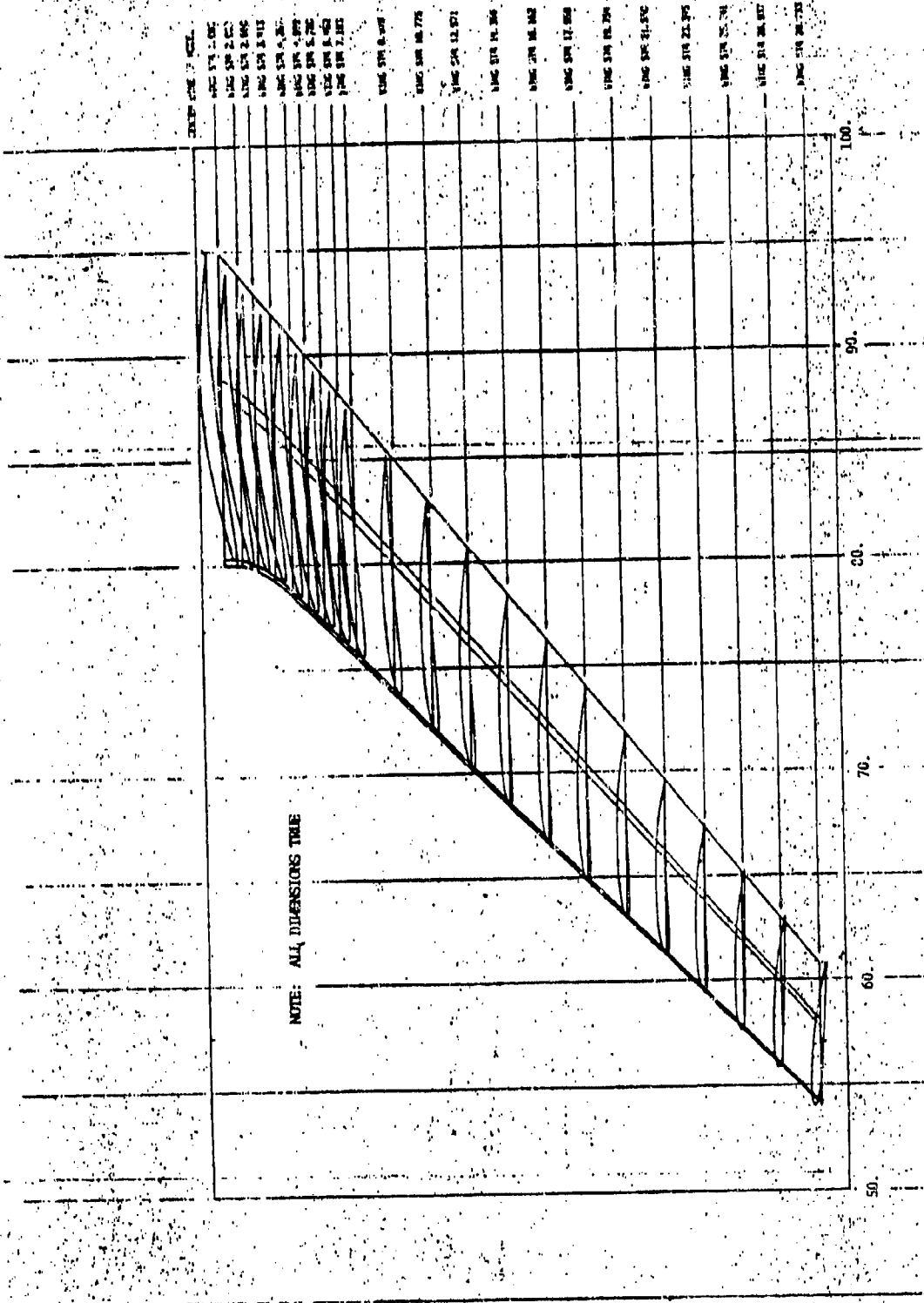
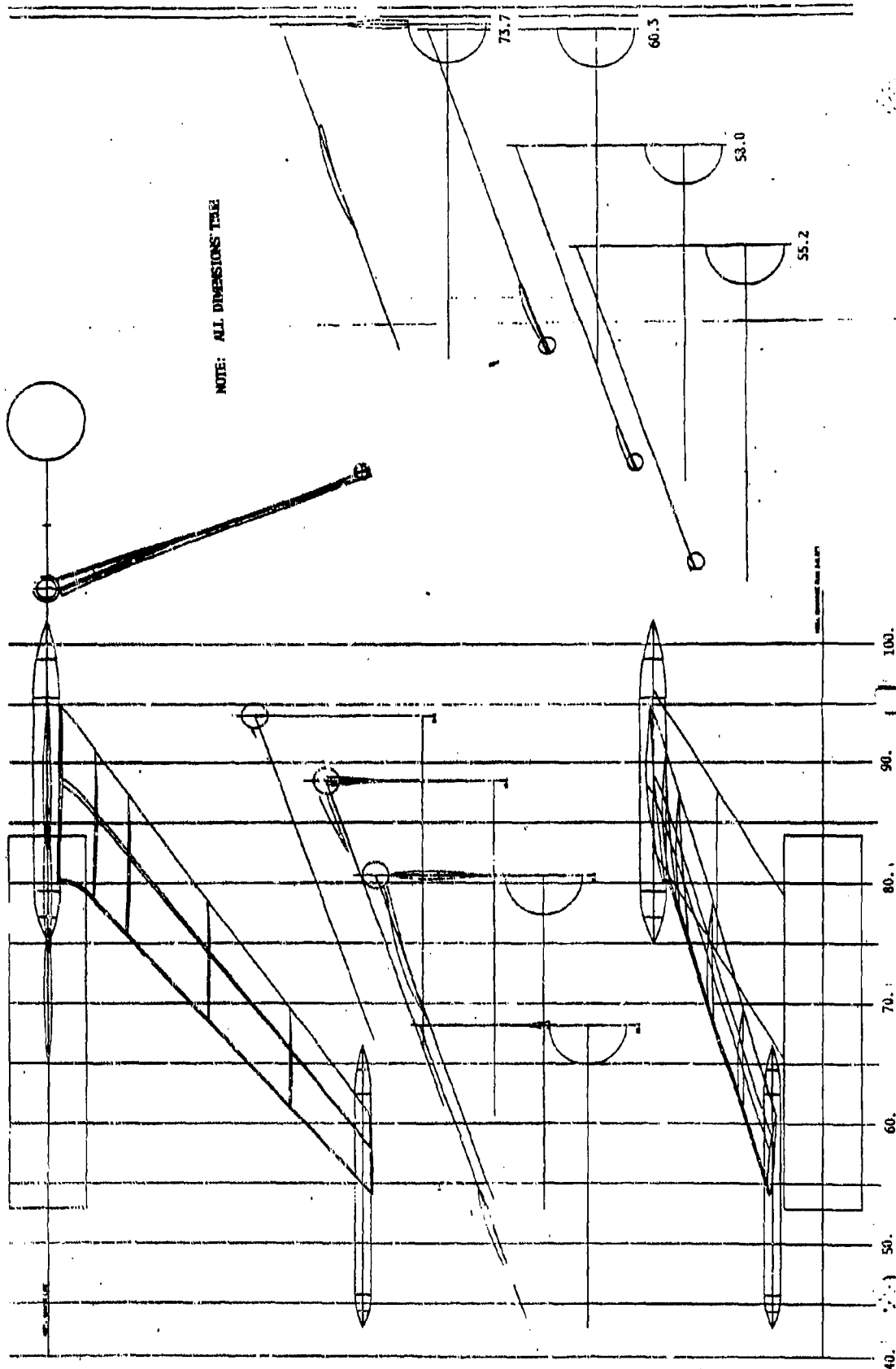


FIGURE C4 JOINED WING AFT WING DETAIL

MA-84-1A34

NOTE: ALL DIMENSIONS ARE IN INCHES



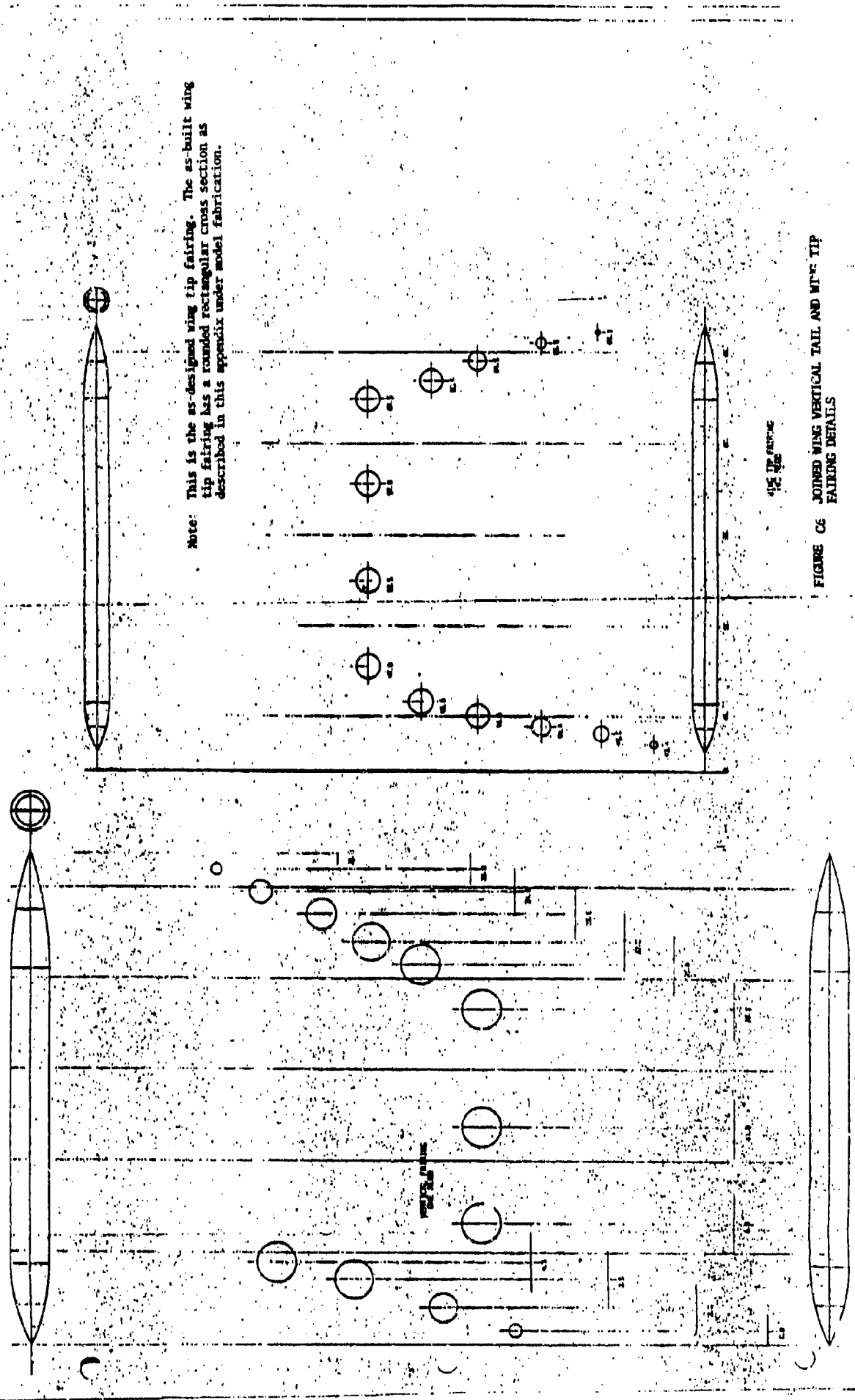


FIGURE C6 JOINED WING VERTICAL TAIL AND WING TIP FAIRING DETAILS

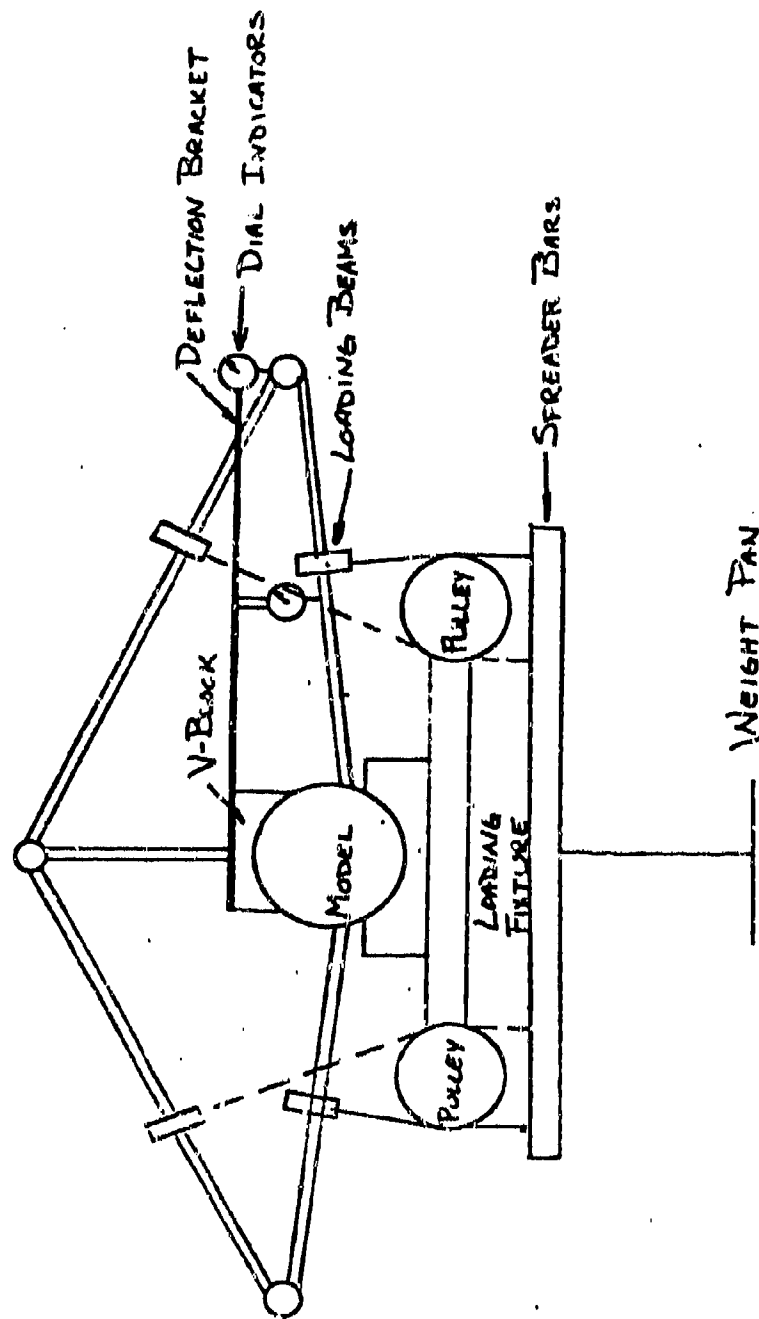


FIGURE C7 WING DEFLECTION CALIBRATION

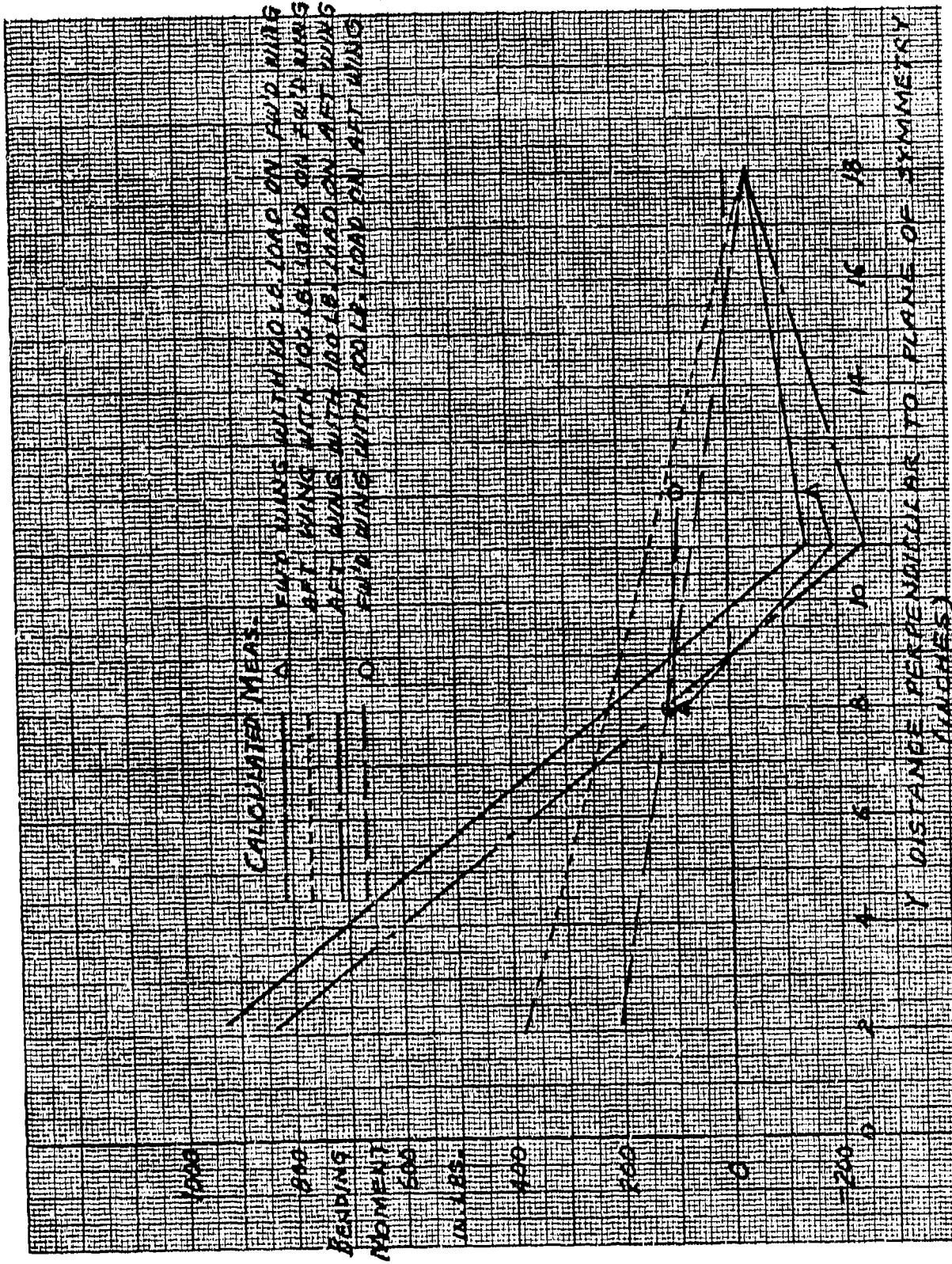


Figure C8. Bending Moment Distribution with 100 Pounds Loads
at $y = 11.08$ in. and $x/c = 0.45$

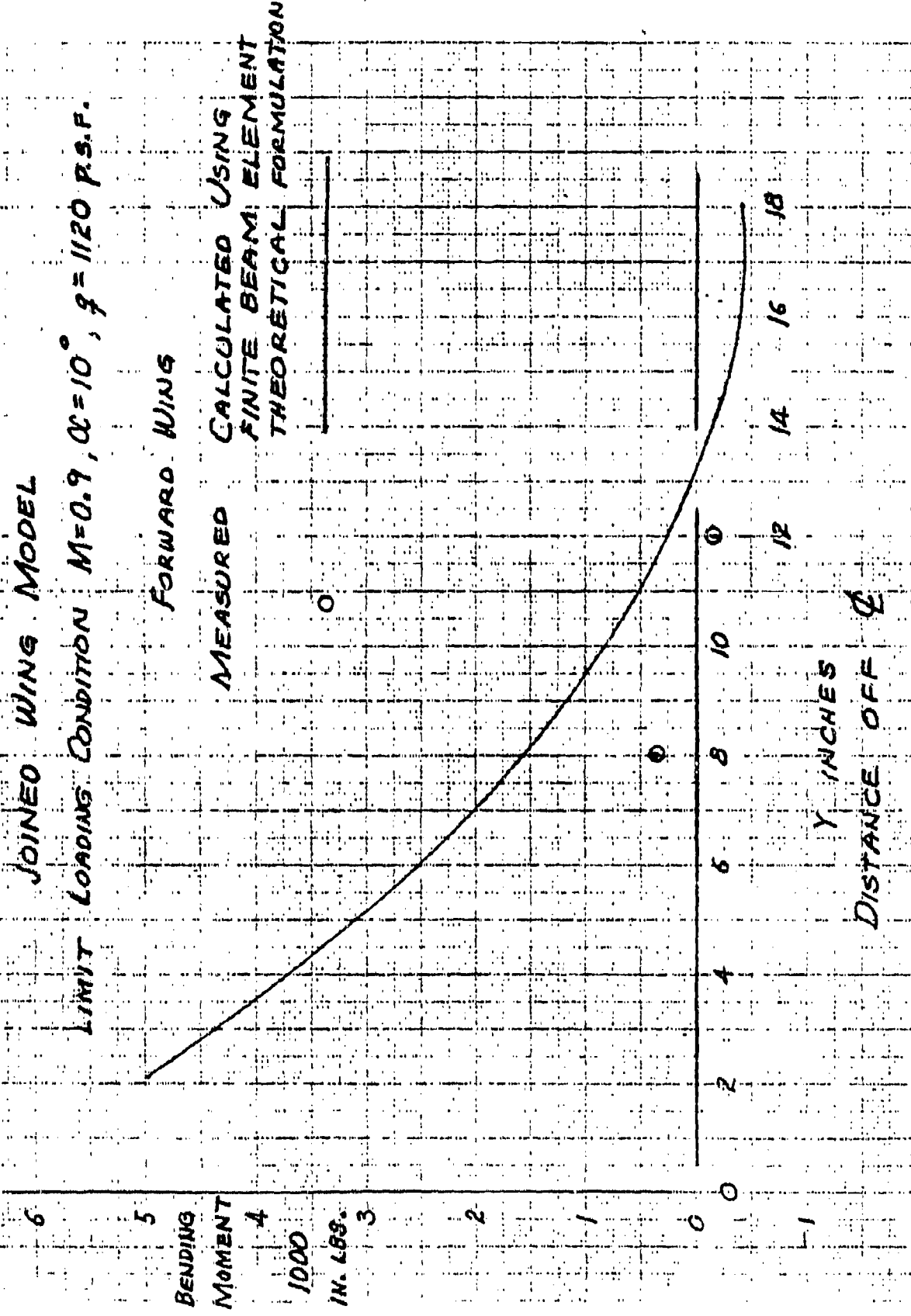


FIGURE C9 BENDING MOMENT DISTRIBUTION AT LIMIT LOADING CONDITION